Rheological characterisation of biofilms in both linear and nonlinear viscoelastic regimes

A thesis submitted to the Faculty of Science, Agriculture and

Engineering for the Degree of Doctor of Philosophy

by

Sam Charlton

School of Engineering

Newcastle Upon Tyne

August, 2019

Abstract

Biofilms are a ubiquitous mode of bacteria proliferation found within aqueous environments. The structure and architecture that a biofilm self assembles into confers mechanical resistance against shear forces. A characteristic trait of biofilm is the production of extra cellular materials which act as the “glue” in the ECM/bacteria composite. The myriad physical properties of biofilm systems result in highly variable mechanical properties, which are studied using rheology. Previous studies about biofilm mechanics were mainly focused on linear viscoelastic regions. However the linear region is unable to provide information regarding the dynamics of deformation and structural rearrangement. Probing the biofilm nonlinear viscoelastic regime and yielding dynamics opens a window to access how the rearrangement behaviour of the EPS network and bacterium network are impacted by EPS composition and bacterial network topology.

In addition, to determine the rheological properties of biofilms within the linear viscoelastic regime using the rotational rheometer, this thesis sheds light on utilising high fidelity non-linear rheological techniques and advanced imaging techniques to produce a framework explaining the emergence of characteristic biofilm mechanical behaviours across an array of species, chemical environments and genetic mutations. I have demonstrated the applicability of three types of large amplitude oscillatory shear (LAOS) analysis methodologies to *Pseudomonas fluorescens* biofilms and the rheological effects of divalent cations and a chaotropic compound. It was shown that by increasing ionic concentration the characteristic behaviour changes from a repulsive glass to an attractive glass. To understand the rheological and architectural effects of capsular polysaccharide secretion in biofilms, I selected the bacterium *Pantoea* sp. I revealed how the secretion of amylovoren and stewartin causes a characteristic rheological change from viscoelastic liquid to glass and how this is primarily driven by changes in EPS polymer concentration and packing fraction. Finally, I investigated the yielding behaviours across a range of bacteria with different geometries (rods/cocci) and EPS compositions. I identified four different types of yielding behaviour across the tested bacterial strains and used a range of rheological and microscopy data to identify the extent of short- and long-range polymer networks which determine the viscoelastic response of bacterial biofilms.

In summary, this thesis demonstrates how contemporary rheological methods and soft matter physics can be used in a reductive approach towards linking biofilm mechanics, microstructure and phenomenology.

Acknowledgements

I have been at Newcastle University for 7 years and during that time I've met a wide range of people who have assisted my personal and professional development.

I would like to thank my supervisor Dr Jinju Chen for her advice and guidance during my PhD studies. I would also like to thank Dr Saikat Jana who has provided me with pearls of wisdom and helped formulate my outlook on the research world, as well as being there as a friend.

I'd like to thank the NUFEB research group for their support and wisdom on all things biofilm. In particular Prof Tom Curtis, who has provided words of wisdom throughout my PhD. I'd also like to thank Dr Matthew Brown, Dr Ben Allen and Dan Curtis who I've had the pleasure of working with on a couple of projects which do not feature in this thesis.

I've had the pleasure of working amongst some great fellow PhD candidates in the Stephenson building; of particular significance are Yunyi Cao, Kegan Bannon and Babis Tzivelekis.

I'd also like to thank Prof Grant Burgess and Cassie Bakshani for their friendship and advice. I would like to acknowledge Dr Nick Jakubovic for providing some bacteria strains.

In addition, I have had the fortune in working with Dr Alex Laude, Dr Rolando Berlinguer- Palmini and Dr David Bulmer in the Bioimaging unit. I thank them for helping to fuel my enthusiasm for microscopy techniques.

I would also like to thank EPSRC DTP for my scholarship and funding throughout my PhD.

Finally, I'd like to thank by family and friends for bearing with me and supporting me as I have travelled through the inevitable peaks and troughs of PhD life.

Contents

List of Figures

List of Tables

Nomenclature

A	Spatial coordinate
B	Binormal vector
D	Bacteria diameter
De	Deborah Number
e_n	Elastic Chebychev harmonic
G	Shear modulus
G_{cage}	Cage modulus
$G_{1,2}$	Burger elastic coefficients
G_∞	Long term relaxation elastic moduli
G^*	Complex modulus
G_n^*	Higher order complex moduli
G'	Elastic modulus
G''	Viscous modulus
G''_{NORM}	Viscous modulus normalized
G_n'	Higher order elastic moduli
G_{n}''	Higher order elastic moduli
G_M'	Minimum elastic modulus
G_L'	Large strain elastic modulus
G_t'	Transient elastic modulus
G_t''	Transient viscous modulus
G_t^*	Transient complex modulus
h	Height
$I_{\frac{3}{1}}$	Intrinsic nonlinearity parameter
J	Compliance
l	Wave propagation length
r	Contact angle radius
R	Cell radius
r_L	Localization length
S	Stiffening ratio

T	Thickening ratio
T_n	Chebychev polynomial
t_0	Initial time
t	Time
φ	Cone angle
γ	Shear strain
$\dot{\gamma}$	Shear strain rate
γ_C	Crossover shear strain
δ	Phase angle
δ_t	Transient phase angle
ε	Strain
ε_0	Step strain
η	Viscosity
$\eta_{1,2}$	Burger viscous coefficients
η'_M	Minimum viscous modulus
η'_L	Large strain rate modulus
η''_n	Higher order viscosity
η'_n	Higher order viscosity
θ	Displacement
$\dot{\theta}$	Displacement velocity
λ	Relaxation time
λ_t	Experiment time
σ	Stress
σ_0	Initial stress
v_n	Viscous Chebychev harmonic
υ'	Elastic modulus power law coefficient
υ''	Viscous modulus power law coefficient
ϕ	Packing fraction
ω	Frequency

List of Abbreviations

AFM	Atomic force microscope
AU	Arbitrary units
C-di-GMP	Cyclic diguanylate

CLAHE	Contrast limited adaptive histogram equalization
CMT	Combined motor transducer
CP	Cone and plate
EPS	Extracellular polymeric substances
FT	Fourier transform
DMA	Dynamic mechanical analysers
FOV	Fields of view
LAOS	Large amplitude oscillatory shear
LB	Lissajous Bowditch
LoG	Laplacian of Gaussian
LVER	Linear viscoelastic region
MAOS	Medium amplitude oscillatory shear
MSCRAMM	Microbial surface components recognising adhesive matrix molecules
NMCT	Naïve Mode coupling theory
PFS	Perfect focus system
PGPR	Plant growth promoting rhizobacteria
PP	Parallel plate
OCT	Optical coherence tomography
SAOS	Small amplitude oscillatory shear
SMT	Separate motor transducer

Chapter 1 Introduction

Bacteria along with archaea are the foundational forms of life (Hug et al., 2016). Estimated to number in the range of 10^{30}, bacteria play a predominant role in the global ecosystem (Kallmeyer et al., 2012). Bacteria drive the biogeochemical cycling of nutrients such as carbon, nitrogen and sulphur (Hofer, 2018; Kuypers et al., 2018). Bacteria have evolved to thrive in almost all environmental conditions. For example, extremophiles can survive extremes in temperature, pH and salinity. Until the 1970's it was believed that bacteria primarily lived in a planktonic state. However, over the past few decades this assumption has been replaced by the framework that most bacteria (40-80%) live communally through symbiotic, antagonistic and consummate interactions within structures termed biofilms (Donlan, 2002; Flemming & Wuertz, 2019).

The biofilm mode of growth confers bacteria various biological advantages over planktonic growth: increased resistance to chemical challenges such as antibiotics (Høiby et al., 2010) and pH fluctuations (Tasaki et al., 2017), closer intracellular proximity increasing the transfer rate of genetic information through horizontal gene transfer (Madsen et al., 2012), division of labour strategies (Dragoš, Kiesewalter, et al., 2018), symbiotic interspecies interactions (M. Cao & Goodrich-Blair, 2017; Meera et al., 2009), resistance to shear forces (A. Park et al., 2011) and increased protection from bacteriophage attack (Meera et al., 2009; Vidakovic et al., 2018). The chemical, biological and physical interactions occurring within a biofilm are complex and myriad. Therefore, biofilm research requires a multidisciplinary approach to reveal the rich physical, chemical and biological interactions which govern the biofilm lifestyle.

Biofilm formation has widespread consequences from both the medical and environmental perspective. Biofilms are the leading cause of hospital infections and contribute to antibiotic resistance in harmful pathogens, reducing antibiotic efficacy. Mutation rates in biofilm bacteria selecting for antibiotic resistance occur at an increased rate through horizontal gene transfer. Biofilms also cause persistent infections in burn victims and cystic fibrosis sufferers and are responsible for surgical site infections and catheter associated urinary tract infections. In the environment biofilm formation on ship hulls and within pumping systems increases hydrodynamic drag, resulting in increased carbon emissions and economic expense (Schultz et al., 2011). Biofilms are also a major cause of corrosion and membrane biofouling in

reverse osmosis water treatment (Maddah & Chogle, 2017). Thus, a greater understanding of biofilm mechanical properties is a necessary in the design and evaluation of disruption and dispersal strategies, to assist in combatting antibiotic resistance and reducing global emissions.

An improved understanding of the biofilm lifecycle can be beneficially harnessed and applied within various industries. For decades biofilm formation has been exploited in biological wastewater treatment filters to remove excessive nutrients and micro pollutants. Electroactive biofilms are used within biological fuel cells, taking advantage of bacterial electrocatalytic reactions to produce electricity (Angelaalincy et al., 2018). The increasing sophistication and availability of synthetic biology techniques is now enabling biofilm to be viewed as a programmable material (C. Zhang et al., 2019). Potential promising applications for biofilm based living materials include the construction of responsive materials, environmental detoxification and materials processing (Balasubramanian et al., 2019; Schaffner et al., 2017).

The resistance of a biofilm to physical forces is determined by its architecture and EPS composition, which are described using rheology (William N. Findley, 1989). Rheology is the study of how matter deforms and flows and investigates how micro and macro interactions within material structures influence multiscale mechanical behaviour (Tanner, 2000). Biofilm rheology is transient and varies from species to species and with environmental physicochemical conditions. The adaptability of biofilm rheology to specific environments is increasingly being recognised as a potential virulence factor for pathogenic biofilms and is one of the governing factors affecting the stable operation of wastewater treatment filters (Gloag et al., 2018). Therefore, an understanding of the structure function relationships which govern biofilm rheology is an important step in understanding how biological function, physical arrangement and chemical conditions link together to determine the mechanical properties of a biofilm.

In this project I propose to investigate multiple single species biofilms using advanced rheological characterisation and mathematical analysis. To better understand the mechanisms underpinning different rheological properties of biofilms, the biofilm structures have been studied by high-resolution imaging techniques (brightfield and confocal laser scanning microscopes). Furthermore, the key principles of soft matter physics have been adopted to better understand the nature of different biofilm rheological fingerprints.

1.1 Aim and objectives of the project

This project aims to explore biofilm mechanics and structure relationships across a range of bacterial species and physicochemical environments by using high fidelity non-linear rheological characterisation and advanced imaging techniques. The specific objectives are:

- Develop a methodology for testing the rheology of bacterial biofilms with high fidelity non-linear rheological techniques.
- Study how physicochemical environments affect biofilm rheology.
- Investigate how the secretion of hydrophilic polysaccharides within the extracellular polymeric substances (EPS) impacts biofilm rheology.
- Explore how different cell morphologies and EPS compositions influence biofilm rheology and microstructure.
- Determine how the nonlinear rheological behaviour of bacterial biofilms can be used to characterise the presence of long- and short-range interactions within a biofilm structure.

1.2 Thesis structure

In order to achieve the aims of this project this thesis is split into seven chapters:

In **Chapter 1** a brief introduction to the motivation behind this project is provided. The aims and objective are also stated.

Chapter 2 provides a comprehensive literature review. It provides background information into the biofilm lifecycle and provides an overview of the mechanical interactions involved in biofilm formation. It then moves onto focus on the EPS matrix. I then describe our current understanding of biofilm rheology and the different multiscale techniques which can be adopted to study biofilm rheology. Finally, I move on to explaining the concepts behind linear rheology, rheometers and I provide mathematical background for the non-linear rheological techniques which will be used throughout this thesis.

Chapter 3 presents a proof of concept study demonstrating the applicability of nonlinear rheological techniques towards the characterisation of bacterial biofilms. This study investigates the rheology of *P. fluorescens* and effect of chemical treatment with; urea, $CaCl_2$ and $FeCl_2$. I show that addition of divalent cations causes

P. fluorescens to change from a repulsive glassy system to an attractive glassy system.

In **Chapter 4** I investigate the non-linear rheology of *Pantoea* sp. and *Pantoea* sp. UDP, a genetic mutant which has reduced production of amylovaroan and stewartin, EPS polysaccharides. I show how EPS secretion can drive changes in cellular packing causing a transition from viscoelastic liquid behaviour to glassy behaviour. To investigate the effect of EPS volume on biofilm rheology I combine *Pantoea* sp. and *Pantoea* sp. UDP in different ratios to control biofilm packing fraction. This system is then used to investigate the transitionary regime between viscoelastic liquid and glassy behaviour.

In **Chapter 5** I investigate the rheology of 4 different biofilm forming strains, *C. denitrificans*, *P. fluorescens*, *S. epidermidis* and *N. polysaccharea*. I compare the rheology of rod and cocci strains and show how cocci biofilm strains consistently exhibit two-step yielding, a property known to occur in attractive glassy materials. I also investigate the unusual rheology of *C. denitrificans*, a bacterial strain which displays short range attractive behaviour and autoaggregates to produce a large interconnected fractal network.

In **Chapter 6** I discuss the findings from this work and position the significance of this work towards assisting biofilm computational modelling and how rheological finger printing could be used in the future with genomic sequencing in order to construct a rheology – genotype database. I also discuss how biofilm non-linear rheology could be used to assist in the processing of artificial functional biofilm structures and how bacterial systems be used to answer fundamental soft matter physics questions.

Chapter 2 Literature review

2.1 The biofilm lifecycle

For aqueous environments within the natural ecosystem bacteria predominantly exist as a biofilm, a complex three dimensional structured community of single or multi species cells bound within a hydrated extra polymeric substance (EPS) secreted by cells and attached to exposed surfaces (Flemming, 2011). Principally the mechanistic aspects of biofilm growth can be reduced to four fundamental stages: reversible and irreversible attachment, maturation and detachment, *Figure 2-1*.

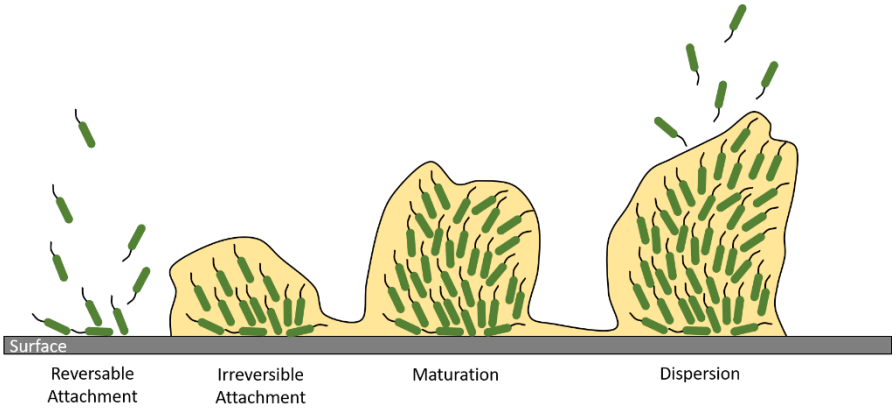

Figure 2-1: The biofilm life cycle begins with reversable attachment of planktonic bacteria to a solid-liquid interface. In this regime bacteria explore the surface through surface motility and remove attached bacteria are removed by shear forces. In the next stage strongly attached bacteria switch to the biofilm phenotype and begin to secrete EPS substances. The secretion of EPS substances and cellular growth leads to formation of mature biofilm structures such as mushrooms and towers. Dispersion is the final stage of a biofilm, here bacteria are released due to the self-induced breakdown of the EPS structure.

Surface attachment is the first stage of biofilm formation and a crucial step for a bacterium to transition from planktonic to a sessile biofilm forming phenotype. Bacteria interact with surfaces through a range of different biophysical and chemical pathways. The decision for a bacterium to adhere or reject a surface is regulated through feedback from sensing mechanisms. Bacteria can mechanosense surfaces using appendages such as flagella and pili and through contact stress using periplasmic stress pathways (Belas, 2014; Ellison et al., 2017; Otto & Silhavy, 2002). For example, type IV pili are bacterial motors which mediate twitching motility in bacteria such as *Pseudomonas aeruginosa* by extending, binding to the surface and then retracting (Burrows, 2012). Crawling bacterial motility facilitates surface exploration and migration towards regions of higher nutrient concentration (Ni et al., 2016; Yi Shen et al., 2012). Adhesion occurs through activation of EPS secretion

pathways which are activated through signalling chemicals, the most widely studied being cyclic diguanylate (C-di-GMP) (Hengge, 2009). Certain species use EPS substances, such as eDNA and specific proteins such as Bap (Biofilm associated protein), to condition surface for attachment (Cucarella et al., 2001; Pakkulnan et al., 2019). The process of initial adhesion is adaptive. Recent studies have shown how bacteria sense and adapt to abiotic surfaces, retaining an integrated memory of previous adhesion events (C. K. Lee et al., 2018). Irreversible attachment occurs when attached bacteria can no longer be easily removed by shear forces and provide an initial layer of bacteria conditioning the surface for further aggregation. Aggregation and attraction of planktonic bacteria is controlled through quorum sensing; which involves the release of chemical messengers called autoinducers, creating chemotactic gradients (Humphries et al., 2017; Miller et al., 2002). After initial colonisation and aggregation, biofilm structures begin to form through a series of physical interactions mediated by the secretion of EPS. Bacterial colonies display a wide array or morphologies and arrangements, *Figure 2-2*. Depending upon the bacterial strain and environmental conditions, various complex patterned structures

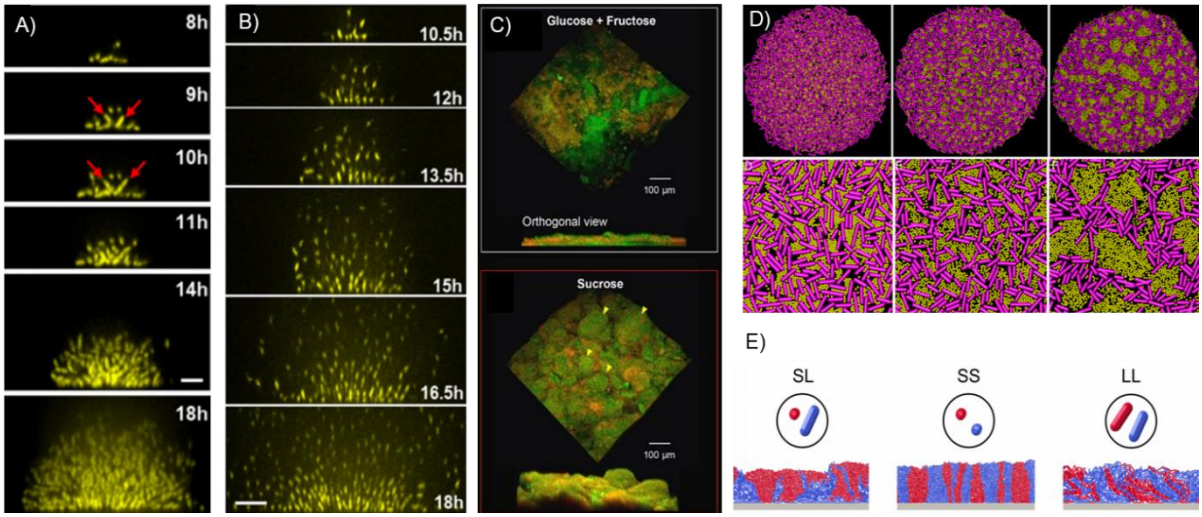

Figure 2-2: The morphology and microstructure of biofilm is influenced by a variety of parameters such as the cellular packing, nutrient conditions, EPS secretion and bacterium shape. (A) When biofilm growth enters the irreversible attachment stage the initial bacteria monolayers buckles this causes the verticalization of some bacteria within the monolayer (red arrow). (B) Deletion of cell-cell attachment proteins leads to less dense biofilm structures (J Yan et al., 2016). (C) Matured biofilm morphology is influenced by the nutrients bacteria consume, here Pseudomonas aeruginosa biofilms produce mushroom features with the addition of sucrose (Xiao et al., 2017). (D) The volume of secreted EPS has been shown computationally to induce phase separation in biofilm monolayers (Ghosh et al., 2015). (E) Bacteria cell shape has been computationally shown to influence the packing and population distribution within bacterial colonies (Smith et al., 2017).

can form (Kundukad et al., 2016). During early stage maturation when still only a few cell layers are attached, colony morphology is driven by mechanical instabilities, such as buckling, which can result in verticalisation (Beroz et al., 2018). At this early stage, cell orientations have a reduced nematic order, and preferential patterns can form due to differences in cell shape and aspect ratio (Boyer, Mather et al. 2011). The order and orientation of rod-shaped bacteria colonies, for instance, varies as a function of growth and stage of division. Early cellular organisation is also controlled via the production of EPS. High levels of non-absorbent EPS increase aggregation through the depletion interaction resulting in phase separation (Ghosh et al., 2015). Verticalisation results in cellular alignment as daughter cells orient with mother cells. This leads to higher cellular packing as the biofilm grows away from the surface (Drescher et al., 2016). Beside mechanical contact forces, the specific types of EPS secreted during biofilm formation have a large impact on how bacteria self-assemble, deletion of cell-cell adhesion proteins can lead to swollen structures with reduced packing density (Genovese, 2012; J Yan et al., 2016). As the biofilm community matures, increased cell number and biofilm thickness cause diffusion fluxes from the surface of the biofilm to the substratum. This results in the formation of chemical, nutrient, pH and O_2 gradients, *Figure 2-3*. The presence of gradients through the depth of biofilm results in the formation of heterogeneous microenviroments and causes the emergence of distinct subpopulations in multispecies biofilms. Subpopulations within biofilms can display antagonistic or consummate relationships, where production of secreted compounds, such as siderophores or enzymes, are used to harm or benefit other species (Nadell et al., 2016; Orazi & O'Toole, 2017). Biofilms exhibit long range collective dynamics with increasing biofilm size. *Bacillus. subtilis* coordinates fluctuations in growth rate to minimise the formation of nutrient poor regions, a process known as nutrient time sharing (Martinez-Corral et al., 2018). The production of EPS has also been demonstrated to be influenced by collective behaviour, where division of labour strategies reduce the metabolic burden on bacteria (Dragoš, Kiesewalter, et al., 2018; Dragoš, Martin, et al., 2018).

Dispersion and detachment are the final process in the biofilm lifecycle. Dispersion is regulated through several different molecular mechanisms activated in response to various environmental stimuli. Dispersion can occur in nutrient and O_2 depleted conditions where a transition to the planktonic state enables recolonization in more favourable regions (Gjermansen et al., 2010; Sauer et al., 2004). Dispersion is also a reaction to variations in cell density, which can be a major cause of virulence in pathogenic species (Rutherford & Bassler, 2012). The main molecular mechanisms currently known to control dispersion relate to quorum sensing pathways and reductions in concentration of cyclic diguanylate (C- di –GMP), which results in a reduction in the production of biofilm related matrix polysaccharides (Ha & O'Toole, 2015). To enable biofilm dispersion, bacteria disrupt the extracellular matrix, this is achieved through the production of various nucleases, glycosides and proteases (Beenken et al., 2012; Fleming et al., 2017; Mitrofanova et al., 2017). In some cases, dispersion can be controlled through cell autolysis of bacteria subpopulations resulting in the formation of cavities which disrupts the biofilm architecture and provide neighbouring live cells with additional nutrients which may be used for growth. Autolysis has also been shown to result in increased metabolic activity of

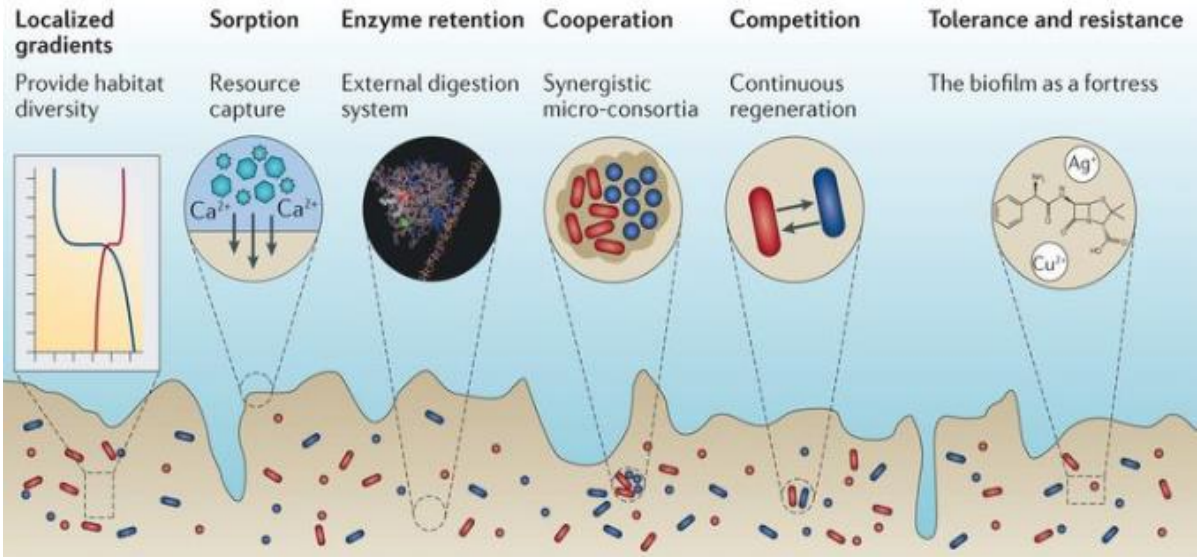

Figure 2-3: The EPS matrix has a lower diffusion coefficient in comparison to water which results in the formation of physicochemical gradients with increasing depth. Within multispecies biofilms localised gradients can result in the formation of microenviroments with distinct community compositions. Nutrients absorbed at the biofilm liquid interface which are consumed by proximate bacteria cause nutrient gradients, starving deeply imbedded bacteria of resources. The sorption of antibiotic molecules in the upper portion of the biofilms and slow diffusion through the biofilm protect bacteria towards the base of the biofilm from antibiotic attack. The gradient is signified by the transition from dark brown to light brown (Flemming & Wingender, 2010).

dispersed cells which may confer an advantage upon recolonization (Guilhen et al., 2016).

Mature biofilms can also be disrupted mechanically through hydrodynamic shear forces, The morphological structures which occur due to hydrodynamic shear include streamer formation, sloughing, rolling and rippling (B. N. Anderson et al., 2007; Rupp et al., 2005), *Figure 2-4*. Streamer formation has been noted to occur in several biofilm strains. In the presence of secondary flows, streamers nucleate from the bulk biofilm surface and extend away, forming fine filaments of bacteria and EPS (Rusconi et al., 2011; X. Wang et al., 2016). Post formation, streamer morphology and distribution are influenced by a combination of surface geometry, chemistry and flow conditions (Jayathilake et al., 2017; Kevin Kim et al., 2014; Valiei et al., 2012). The rapid growth of streamers causes the clogging of pipe systems and are also hypothesised to assist in the spreading and recolonization of new surfaces (Drescher et al., 2013; Sherman et al., 2019). Besides large-scale detachment mechanisms, small scale detachment mechanisms also occur at the biofilm fluid boundary. Individual cells on the periphery of the biofilm can detach through abrasion and

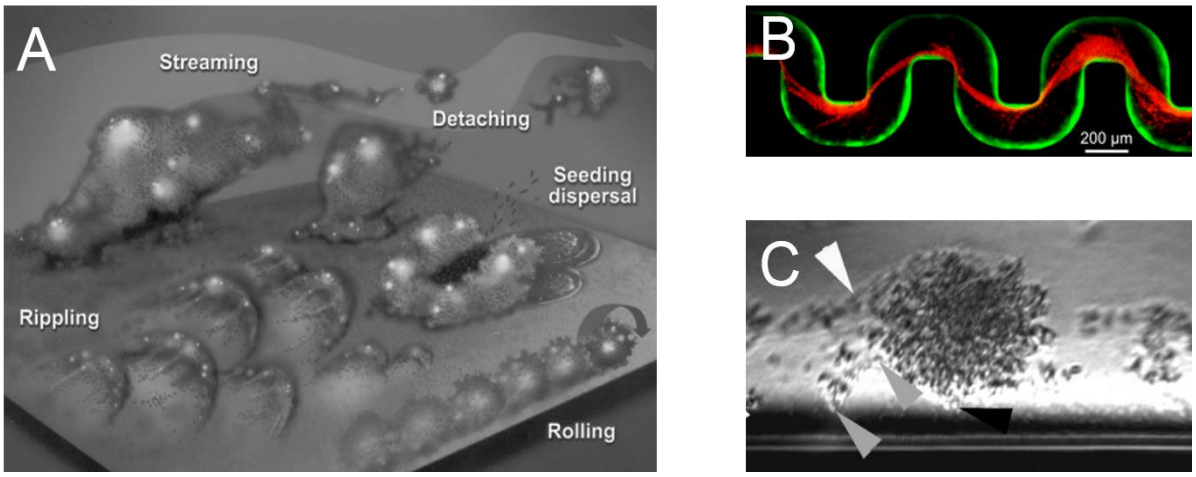

Figure 2-4: Biofilm mechanically induced detachment and deformation mechanisms (A) Overview of main deformation mechanisms, each mechanism is dependent upon the local environmental conditions, rippling, rolling and streaming generally occur under elevated levels of shear stress. Seeding dispersal is triggered via quorum sensing (P. Dirckx, Center for Biofilm Engineering, Montana State University, 2003) (B) *P. aeruginosa* can form streamers under elevated levels of shear stress microfluidic chambers, *P.* aeruginosa streamers show a high content of EPS substances and eDNA (Drescher et al., 2013) (C) Video images depict the rolling migration of a Staphlococcus. aureus biofilm, the tether of the structure is pointed out by the white arrow (Rupp et al., 2005).

erosion. Abrasion involves the collision of particles in the bulk flow with loosely adhered cells, which results in detachment (Rochex et al., 2009). Biofilm erosion occurs when fluid frictional forces detach weakly adhered cells which are not enmeshed within the EPS matrix (Klotz et al., 2019).

2.2 Biofilm EPS and microstructure

The production of extrapolymeric substance (EPS) is one of the signature features of the biofilm phenotype. After initial bacterial adhesion, EPS is produced through cellular metabolic activity signalled by changes to cell membrane stress which is a function the of adhesion force between the cell and the substrate (Busscher & van der Mei, 2012). The secretion of EPS modifies the substrate surface chemistry creating a surface conditioning layer reducing repulsive forces and creating more favourable hydrophobic conditions (Smith-Palmer et al., 2016). EPS is a biopolymer composite composed of carbohydrates, proteins, humic substances, lipids, nucleic acids, and uronic acids. The composition of EPS is highly varied and dependent upon a wide array of physicochemical and genotypic variables. The EPS matrix is structured in a series of channels and pores containing water. This keeps the biofilm hydrated and determines the diffusion rate and transport of nutrients and organic substances to the encapsulated bacteria (Sutherland, 2001; Wilking et al., 2013). The structure of these channel networks results in density heterogeneities and affects the overall viscoelastic properties of the biofilm aggregate (Flemming et al., 2007).

Nutrients diffuse through the matrix from the biofilm/ fluid boundary to the encapsulated cells fuelling growth. Thick densely populated biofilms experience oxygen and nutrient starvation (a vital component involved in the respiration of cells) for cells deep inside the biofilm away from the liquid interface, causing cell lysis in aerobic bacteria and creating anoxic microenviroments. The EPS structure can be digested by their own producer cells and other microorganisms when starved (Costa Oliveira et al., 2017; X. Zhang & Bishop, 2003). Other EPS molecules, such as phenol-soluble modulins, are influenced post secretion by the presence of eDNA, which causes a reduction in local pH resulting in an increased rate of amyloid polymerisation (Schwartz et al., 2016).

Due to heterogeneities in both composition and structure, EPS is amphiphilic. EPS substances, such as Bap (biofilm associated protein) in *Staphylococcus aureus* strains, have been shown to alter cell surface hydrophobicity to improve the favourability of adhesion and develop stronger bonds with the substrate over time

(Perera-Costa et al., 2014; Schiffer et al., 2019; Vadillo-Rodríguez et al., 2004). The hydrophobicity of *Pseudomonas* is affected by the secretion of Fap (Functional amyloid in *Pseudomonas*), which also influences stiffness (Zeng et al., 2015). In *Bacillus* strains, surface cell hydrophobicity controlled by the secretion of BslA (biofilm surface layer protein A), an amphiphilic protein which polymerizes into different conformations depending upon the air- water interfacial area (Kobayashi & Iwano, 2012).

Carbohydrates and proteins are key EPS components which control biofilm architecture and viscoelastic response. Carbohydrates are long chain polymers which increase mechanical rigidity of the microstructure through entanglements. The ratio of proteins to carbohydrates in multispecies biofilms is dependent on biofilm maturity (Frølund et al., 1996), hydrodynamic and nutrient conditions and exposure to chemical challenges (Fish et al., 2015). Within multispecies biofilms in drinking water distribution systems the protein to carbohydrate ratio in EPS increased by a factor of 6-13 x over a period of 3 months. Such a polymeric compositional change led to a 2-3 x increase in biofilm stiffness in response to disinfectant exposure (Yun Shen et al., 2016). The biofilm growth rate influences the EPS: bacteria ratio, in nutrient rich environments EPS: bacteria increases in comparison to nutrient poor conditions (Staudt et al., 2004). EPS production can be affected by mechanical stresses. For example, high shear stress can lead to increased polysaccharide production in *S. aureus* biofilms (Hou et al., 2018). The possibility of evolutionary adaptation of EPS composition to specific environments was recently postulated in the *P. aeruginosa* system. Clinical isolates of *P. aeruginosa* initially produce a high amount of alginate, a polysaccharide secreted during surface colonisation, before transitioning into secretion of architectural crosslinking polysaccharides Pel (pellicle) and Psl (polysaccharide synthesis locus) at later stages of growth (Kovach et al., 2017).

Perhaps the most widely acknowledged role of EPS is in providing shape and passive structure to biofilms, *Figure 2-5*. Our understanding of the organisation of structural polymers which confer biofilm mechanical stability is still in its infancy and the physical response of these polymers due to large forces is rarely investigated (Gordon et al., 2017). For model microbes, like *P. aeruginosa*, the polysaccharides Pel, Psl and alginate modulate the biofilm stiffness. Psl and Pel crosslink with additional matrix components such as e-DNA (extracellular DNA) and Cdr-A (cyclic diguanylate regulate TSP partner A) which increases biofilm stability and packing

density (Jennings et al., 2015; Reichhardt et al., 2018). In *E. coli* biofilms, cellulose is a major EPS component contributing to EPS elasticity and cohesion (Serra et al., 2013). Amyloid curli fibers have been demonstrated to produce a protective scaffolding network which protects against bacteriophage penetration (Vidakovic et al., 2018). In *Vibrio cholerae* biofilms VPS (Vibrio polysaccharide) is the major architectural polysaccharide, while a protein RbmA (Rugosity and biofilm structure modulator A) crosslinks cells, and two homologous proteins Bap (Biofilm associated protein) and RbmC (Rugosity and biofilm structure modulator C) support the functions of cell-surface adhesion and cross-linking with VPS (Jing Yan et al., 2018).

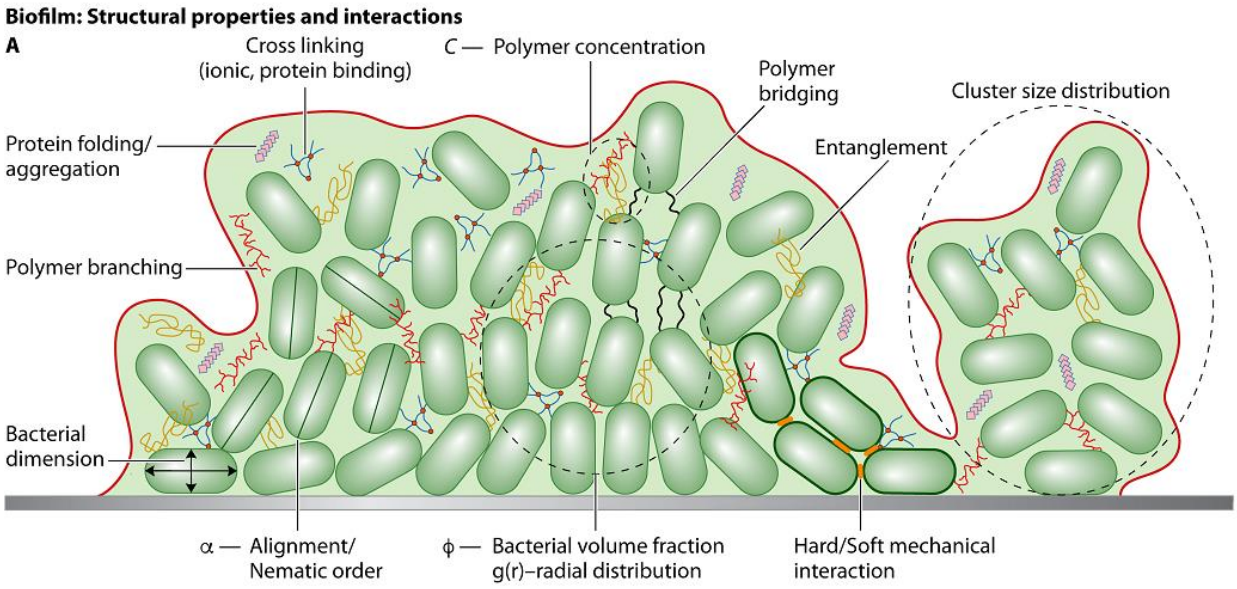

Figure 2-5: Schematic of a generic biofilm structure and parameters which are influence by EPS composition and specific EPS components. The resulting cellular arrangement and polymer interactions confluent to determine biofilm rheology and microstructure (Charlton et al., 2019).

Advances in single cell resolution microscopy have enabled improved characterisation of the biofilm microstructure from initial colonisation through to mature growth. Height dependence on viscoelasticity has also recently been exhibited in *S. aureus* biofilms where elasticity correlated with local packing and height (Hart et al., 2019). Studies upon the model *Vibrio cholerae* system offer an insight into the transitional stages which determine microstructural parameters and architectural evolution. Timelapse analysis and quantification of parameters, such as volume fraction, cell alignment and nematic order, appear to be segmented into 4 distinct phases. In the first phase cells are attached to the substratum as a monolayer, as adhesion to the substratum is stronger than intercellular bonds. The

second phase is entered as the number of cells increases above ~ 6, here alignment is locally disordered, and the colony retains a flat 2D structure. The third phase is entered as the colony size increases to 200 – 1000 cells. In this regime the 2D colonies buckle, causing growth to be directed away from the substratum and the formation of low cell density 3D colonies. In the fourth phase long range alignment and the 3D nematic order of the bacteria increase with cellular density. This results in a biofilm with highly aligned cells in the centre and alignment decreasing as a function of cell density away from the colony centre (Drescher et al., 2016).

2.3 Typical mechanical characterisation approaches

Owing to the multiscale nature of biofilms, there are many techniques which can be used to investigate the mechanical properties of biofilms, *Figure 2-6*. The characterisation of the material properties of biofilm are performed using a mixture of direct and indirect quantitative techniques using both *in situ* and *ex situ* growth conditions.

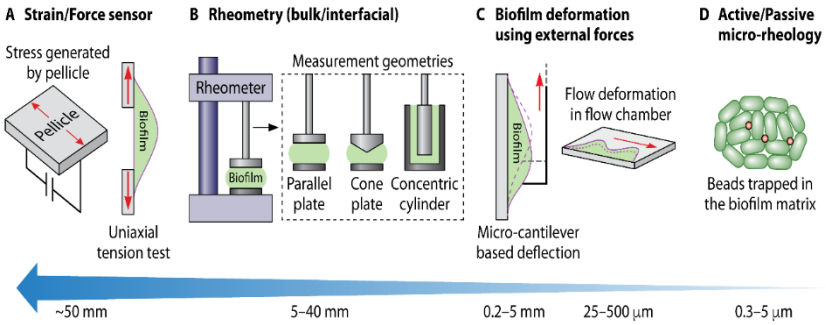

Figure 2-6: A variety of multiscale methods can be used to characterise biofilm rheology. (A) Strain and force sensors are used to measure the yield stress and moduli of liquid gas interface biofilms (pellicles). Uniaxial tension setups typically involve custom made growth cells which provide a platform to test agar grown biofilms. (B) Rheometers are the standard tool used to measure the bulk properties of agar grown and biofilms grown directly on the rheometer plates. These setups typically involve the use of parallel plate and cone plate geometries. Rheometers are also used to measure the interfacial rheology of pellicle biofilms. (C) Microscale microcantilever methods typically probe agar grown biofilms, this method calculates stress based upon knowing the spring constant of the cantilever. Cantilever methods allow increased control in determining the local region which is probed. Microfluidic chambers are platform to grow and probe submerged biofilms. Mechanical characterisation is performed using flow rate ramps and imaging the resulting biofilm deformation. (D) Microrheological techniques include both passive and active methods which enable highly localised measurements of biofilm rheology. Passive microrheology is performed using particle tracking, where moduli can be calculated based upon the mean squared displacement of beads trapped in the biofilm. Active microrheology includes techniques such as optical and magnetic tweezers which actively control the movement of embedded beads (Charlton et al., 2019).

2.3.1 Microscale mechanical characterisation techniques

Direct *in situ* visualisation of biofilm growth as well as mechanical characterisation is commonly performed using microfluidics flow cells in combination with high speed imaging techniques. Biofilm deformation in flow cells is a function of hydrodynamic shear. Images of biofilm deformation can be captured using a high-speed camera with conventional brightfield microscopes or at a slower speed using optical coherence tomography or confocal microscopy (Blauert et al., 2015; Paul Stoodley, John D. Boyle & Lappin-Scott, 1999; Picioreanu et al., 2018; Rupp et al., 2005). From these imaging datasets shear strain and shear stress can be calculated using image analysis, where biofilm deformation is tracked with time, enabling the calculation of elastic modulus (Mathias & Stoodley, 2009).

Biofilm flow cell experiments have revealed insights into biofilm structural deformation, biofilm ripple migration (Paul Stoodley, John D. Boyle & Lappin-Scott, 1999; Rupp et al., 2005), detachment (Stoodley et al., 2002; Walter et al., 2013) and streamer formation (Biswas et al., 2016). The controlled hydrodynamic conditions within flow cells enables testing of environmental parameters, such as nutrient concentration, temperature and pH. Flow cells have been used to study the effects of different chemicals (Eric et al., 2011; Kundukad et al., 2017), ionic concentration (Paquet-Mercier et al., 2016), turbulence (Teodósio et al., 2011), interactions between different species (W. Zhang et al., 2013) and the impact of nutrient and chemical gradients on biofilm morphology (J. L. Song et al., 2014; W. Zhang et al., 2011). Complex flow cell geometries can be manufactured to study the effects of hydrodynamics on matrix organisation, colonisation, competition (Aufrecht et al., 2019; Jing Yan et al., 2017) and have been used to study upstream twitching in *Pseudomonas aeruginosa* (Kyrylyuk et al., 2009; Yi Shen et al., 2012).

Microrheology is a commonly used in technique used in combination with microfluidic flow cells to measure biofilm mechanics and heterogeneity. Microrheological analysis in combination with confocal laser scanning microscopy enables the correlation of local mechanics to structural parameters such as the radial distribution function (Stewart et al., 2013). Microrheological methods are classified as either passive or active. Passive particle tracking micro-rheology is based upon the Brownian motion of micro-beads (typically 0.2 – 2 µm diameter). Using the generalised Stokes-Einstein equation the mean squared displacement of the tracer particles is used to calculate material compliance. Passive micro-rheology studies of biofilms have revealed how

elasticity varies with biofilm height and varies dependent upon morphological features, such as voids and clusters (H. Cao et al., 2016). Passive microrheology has also been used to evaluate how growth, shear rate, EPS composition, starvation and chemicals targeting different components in the EPS matrix modify biofilm viscoelasticity (Birjiniuk et al., 2014; Chew et al., 2014; Hart et al., 2019; S. S. Rogers et al., 2008). The predominant active micro-rheological technique applied to biofilms is magnetic tweezing, where paramagnetic beads are driven by a magnetic actuator. Magnetic tweezing has been used to assess the effect of shear stress on *E. coli* biofilm viscoelasticity during growth (Galy et al., 2012).

Cantilever methods of assessing biofilm mechanics can be performed at both the microscale and nanoscale. The setup is imaged using a microscope and the deformation of the cantilever is analysed using video analysis to calculate biofilm elastic modulus, toughness and failure strain (Aggarwal & Hozalski, 2010). To assess nanoscale variations in biofilm viscoelasticity and viscoelastic changes with morphology Atomic force microscopes (AFM) are commonly used. Two approaches are used with this method, the first involves growing the biofilm directly onto microbeads which are attached to AFM cantilever tips. The mechanics of the biofilm are then tested by compressing the biofilm on the surface of the microbead against a flat surface. This method has been used to measure biofilm elasticity and biofilm adhesion strength as a function of growth time, loading time, contact time and retraction velocity (Lau et al., 2009; Ziemba et al., 2016). An alternative method is to grow the biofilm in a flow chamber, then remove the chamber to allow access for the AFM cantilever tip or in culture dishes which can be transferred to the AFM stage (Mosier et al., 2012). This method has been used to measure the variations in elastic modulus as a function of micro-colony diameter and to evaluate the effect of oligosaccharides on biofilm elasticity (Kundukad et al., 2016; Powell et al., 2013). AFM studies have also measured environmental samples, such a drinking water distribution biofilm, to assess the effect of disinfectant on Young's modulus and wastewater biofilms (Safari et al., 2016; Yun Shen et al., 2016). In addition to mechanical nano-indentation tests, AFM also allows measurement of biofilm roughness, which has been used to assess the effect of specific EPS components in *B. subtilis* (Kesel et al., 2016).

2.3.2 Macroscale mechanical characterisation techniques

Macroscale biofilm mechanics can be measured using compression and tensile tests. Compression tests are generally performed on dynamic mechanical analyzers (DMA) (Körstgens et al., 2001). Recently however custom glass plunger setups and compression application using permeate flux have been used in combination with optical coherence tomography (OCT) devices to image biofilm compression and recovery (He et al., 2013; Hou et al., 2018). Compression tests are typically used to measure biofilm viscoelastic properties during creep or stress relaxation. The elastic and viscous constants can be determined using phenomenological spring dashpot models (Peterson et al., 2013). This quantitative approach has been used to assess the effects of nutrient composition and antimicrobial peptides on *P. aeruginosa* viscoelasticity and used to determine how polysaccharides, eDNA and water contributed to the viscoelastic response (Rozenbaum et al., 2019). Compression tests have also been used to assess the effects of osmotic pressure and sucrose concentration on the elasticity of *Streptococcus mutans* biofilms (Rmaile et al., 2013).

To investigate biofilm viscoelastic response to tensile strain, custom setups are primarily used. Each design shares fundamental similarities. Typically, the biofilm is grown on an agar surface which is poured directly into a mould attached to a load cell. The agar surface is positioned over a microscope setup to visualise deformation, where particle imaging velocimetry (PIV) can be used to track the deformation field. Tensile tests have been used to investigate biofilm growth induced compressive stresses, while PIV analysis enables the visualisation of non-affine deformations (Hollenbeck et al., 2016). Tensile tests have also revealed strain rate dependence and provide a suitable platform for assessing the effect of chemical treatment on tensile stress and rupture energy (Grumbein et al., 2016).

Rheometers are typically favoured for biofilm macroscale analysis. Rheometers enable direct measurement of viscoelastic material parameters through application of rotational oscillatory shear tests, stress relaxation and creep tests. (Houari et al., 2008; Pavlovsky et al., 2013; Vinogradov et al., 2004). The study of biofilm mechanics via rheometers is predominantly performed using three methods:

1) *In situ* interfacial rheology, where biofilm pellicles are grown at the liquid gas interface.

2) *In situ* grown biofilms, where a growth reactor is integrated onto a rheometer or biofilm is grown on filter paper on an agar pad and then transferred to a rheometer.
3) *Ex situ* growth on agar plates and transferred to the rheometer via scrapping.

The interfacial rheology method allows the growth conditions of the biofilm to be altered while simultaneously measuring the changes to elastic and viscous modulus of the biofilm surface. The effects of pH, nutrient concentration and surfactants on biofilm viscoelasticity have been investigated using this method (P A Rühs et al., 2014; Patrick A Rühs et al., 2013; Wu et al., 2012). More recently interfacial rheology was chosen to access the competition between cocultures of *Bacillus licheniformis* and *Pseudomonas fluorescens* over a period of 48 hrs (Abriat et al., 2019).

In situ biofilm reactors enable biofilm to be grown directly onto the rheometer geometries. Typically, agarose pads are directly attached to the bottom rheometer plate, with inlet and outlet tubing to provide nutrients or alter environmental parameters, such as pH. This method enables *in situ* biofilm growth in direct contact with rheometer plates where temperature is controlled using a Peltier plate. *In situ* reactors have been used to reveal the effect of temperature and salt concentration on the elastic stiffness of *S. epidermidis* biofilms (Pavlovsky et al., 2013, 2015) and to assess the effect of sucrose concentration on *S. mutans* (Waters et al., 2014). An unanswered element of these agarose pad experiments is the question of separating the viscoelastic contributions of the biofilm and agarose pad. However, generally there's a large difference between the stiffness of biofilm samples and agar. Another *in situ* approach, involved transfer of yeast biofilms grown on a removable disk, which could be attached to the bottom rheometer plate (Brugnoni et al., 2014).

The most used method for biofilm rheological characterisation using a rheometer is the *ex situ* growth and transfer method. Here biofilms are grown *ex situ* on agar plates or collected from the study specific environment to be tested *ex vivo*. This method is commonly used to assess environmental samples, such as wastewater biofilms, biofilms from cystic fibrosis patients or contaminant biofilms from food processing plants (Abbà et al., 2017; Kovach et al., 2017; Meera et al., 2009; Safari et al., 2014, 2016). For biofilms cultured on agar plates, osmotic pressure and nutrient composition can be modulated through agar concentration (Daalkhaijav et al., 2019; Jing Yan et al., 2018). This method has been used extensively to study the rheology of a wide range of biofilms, such as *P. aeruginosa*, *V. cholera* and *B. subtilis*

biofilms (Gloag et al., 2018; Huang et al., 2019; Kesel et al., 2016; Jing Yan et al., 2018).

As rheology is the primary technique adopted in this study, in the following section, I focus on rheological concepts which can be measured using a rheometer. It will cover creep and stress relaxation under shear using the rheometer using both small and large amplitude measurements.

2.4 Fundamental concepts of viscoelasticity

The recalcitrant nature of biofilm to mechanical removal treatments, such as washout and fluctuating levels of hydrodynamic shear, has been attributed to the viscoelastic behaviour of the biofilm matrix. Viscoelasticity is a combination of elastic and viscous behaviour. An elastic material deforms instantaneously to relieve stress and will reversibly return to its initial state when the force is removed; a viscous material relieves stress over time by continuous irreversible deformation. Viscoelastic materials thus exhibit a time dependent relationship between stress, σ and strain, ε, and can be characterised by two material relationships; stress relaxation and creep.

2.4.1 Stress relaxation

Stress relaxation describes the time dependent decrease of stress within a material when acted upon by a unit step strain ε_0 at time t_0. At t_0 the material is deformed by the unit step strain and stress increases until it reaches σ_0, the maximal stress. Stress then decays at a rate depending upon the viscoelastic materials stress relaxation properties until a limiting value (plateau) is reached. Relaxation is described using the relaxation modulus $G(t)$. A viscoelastic solid is defined as when the residual stress remaining within the material is nonzero ($G_\infty > 0$). A viscous fluid exhibits a residual stress decaying to zero ($G_\infty = 0$). A viscous fluid is able completely dissipate stress. While a viscoelastic solid may conserve stress.

The rate at which stress decays in a viscoelastic material can be described in terms of the relaxation time λ. Relaxation time is an estimation of the time taken for a material to fully relax. Materials with small relaxation times are fluid-like and dissipate stress quickly, whereas large relaxation times correspond to solid behaviour. The Deborah number is a dimensionless value used to describe the apparent fluidity of materials. The Deborah number describes the ratio of relaxation time λ to the observation time of an experiment λ_t,

$$De = \frac{\lambda}{\lambda_t} \quad [1]$$

The stress relaxation time is an important value to consider when performing oscillatory experimental work. If the period of observation is much shorter than the relaxation time, a material will display pure elastic behaviour which leads to unrepresentative results.

2.4.2 Creep

Creep is the time dependent increase in strain when a step stress is applied to a material. Creep tests are described using compliance $J(t)$, where $\varepsilon(t)$ is the strain, t is time and σ_0 is the step stress applied at t_0,

$$J(t) = \frac{\varepsilon(t)}{\sigma_0}. \quad . \qquad [2]$$

For a viscoelastic solid the strain will increase at first and then plateau at a non-zero equilibrium limiting value $\lim_{t \to \infty} J(t) = J_\infty$. For a viscoelastic fluid, the material strain will increase without any limit (Harvey Thomas Banks, 2010).

2.4.3 Representative mechanical models

In order to produce a constitutive law describing biofilm material properties, methods of modelling material deformation are required. Stress/ strain relationships in linear viscoelastic materials can be phenomenologically described using combinations of linear springs and linear dashpots. Elasticity is represented by a Hookean spring with spring constant G , *Figure 2-7*. While viscous behaviour is represented by a dashpot with viscosity η, *Figure 2-8*. Both elements can be configured in series and parallel, known respectively as the Kelvin-Voigt and Maxwell models. The Kelvin-Voigt and Maxwell models are the most simplistic models used to represent viscoelastic behaviour. For a linear spring, representing instantaneous elasticity and recovery,

$$\sigma = G\varepsilon. \qquad [3]$$

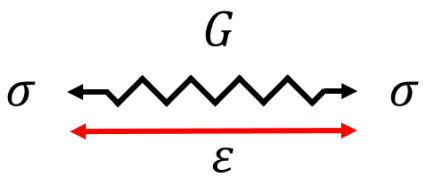

Figure 2-7: A linear elastic spring element, where σ is stress, ϵ is strain and G is the spring constant.

For the viscous dashpot element, the strain rate $\dot{\varepsilon}$ is proportional to stress σ. When a constant strain is applied, stress has an infinite value before quickly decaying to 0,

$$\sigma = \eta \frac{d\varepsilon}{dt}. \qquad [4]$$

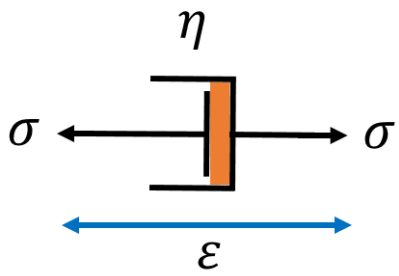

Figure 2-8: A viscous dashpot element, where σ is stress, ϵ is strain and η is viscosity.

The two element Maxwell model features a linear spring and linear dashpot in series *Figure 2-9*. Although simple, this model is important to represent unrecoverable strain in a material after a stress is removed, describing stress relaxation. The strain can be calculated in series as,

$$\varepsilon = \varepsilon_1 + \varepsilon_2, \quad [5]$$

which implies,

$$\varepsilon = \frac{\sigma_0}{G} + \frac{\sigma_0}{\eta} t. \quad [6]$$

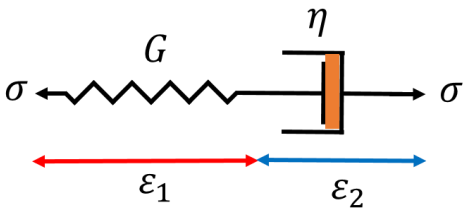

Figure 2-9: The Maxwell model is composed of a singular spring element with string constant G and singular dashpot element with viscosity η in series. The summation of the strain from the spring ϵ_1 and dashpot ϵ_2 equals the overall strain ϵ when a stress σ is applied.

The Kelvin Voigt model features a linear spring and linear dashpot in parallel, *Figure 2-10*. The Kelvin Voigt model represents delayed elasticity. Here stress from an applied strain is initially supported by the viscous element. As time increases the elastic spring slowly becomes more dominant in supporting stress, describing creep. The stress can be calculated as,

$$\sigma = \sigma_1 + \sigma_2, \quad [7]$$

which can be expressed as,

$$\sigma = G\varepsilon + \eta \frac{d\varepsilon}{dt}. \quad [8]$$

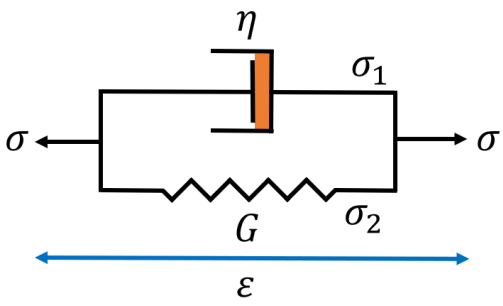

Figure 2-10: The Kelvin Voigt model is composed of a spring element with a spring constant G and a dashpot element of viscosity η in parallel. The summation of the stress from the spring σ_1 and dashpot σ_2 equals the total stress σ when a strain of ϵ is applied.

Due to the complex behaviour of biofilm, two element models are too simplistic to accurately model the time dependent stress/stain response to an imposed strain/stress. The most common material models used to describe a biofilm are the three element Jefferies model (Pavlovsky et al., 2013) and the four element Burger model (Towler et al., 2007), *Figure 2-11*. Creep tests have generally been used in biofilm literature in comparative studies focusing upon the effects of chemical treatment and temperature on biofilm mechanics. Creep models can also be applied to microscale step strain tests which can be performed with magnetic tweezers (Galy et al., 2012). The Burger model is the summation of a Kelvin Voigt element and a Maxwell element in a series configuration which results in a constitutive equation of the form,

$$\sigma + p_1\dot{\sigma} + p_2\ddot{\sigma} = q_1\dot{\varepsilon} + q_2\ddot{\sigma}, \quad [9]$$

where

$$p_1 = \frac{\eta_1}{G_1} + \frac{\eta_1}{G_2} + \frac{\eta_2}{G_2}, \quad [10]$$

$$p_2 = \frac{\eta_1\eta_2}{G_1G_2}, \quad [11]$$

$$q_1 = \eta_1, \quad [12]$$

and

$$q_2 = \frac{\eta_1\eta_2}{G_2}. \quad [13]$$

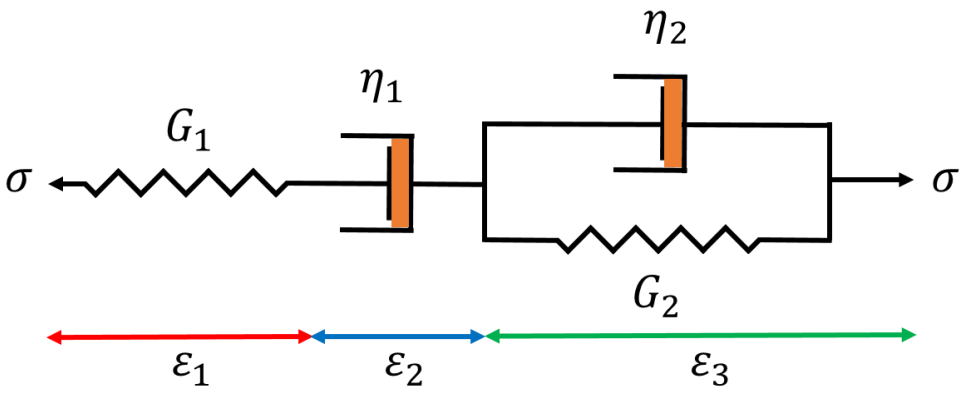

Figure 2-11: A four element Burgers model is composed of a Maxwell element and a Kelvin-Voigt element in series. Where G_1 and η_1 are the spring constant and viscosity of the Maxwell element and G_2 and η_1 are the spring constant and viscosity of the Kelvin Voigt element. The strain of each of these elements when under stress σ is represented by $\varepsilon_1, \varepsilon_2$ and ε_3.

At high frequencies, the burger model describes a material as a stiff elastic solid, with elastic modulus G_1, while at lower frequency the material acts viscoelastic with a much lower elastic modulus (William N. Findley, 1989). This model was used in tandem with experimental data from rheometer creep experiments with a data fitting algorithm to obtain the parameters featured within the model (Towler et al., 2003; Vinogradov et al., 2004). From the extraction of the Burger coefficients some groups have conducted computational experimentation on simple biofilm geometries within fluid solid interaction simulations, which have opened up the possibility of estimating the hydrodynamic forces through the bulk of a mature biofilm (Towler et al., 2007).

2.5 Principles of oscillatory shear rheology: data collection and analysis

Rheology focuses upon the flow properties of complex materials. A complex viscoelastic material displays neither ideal elastic behaviour, where deformation energy is completely recoverable, nor pure viscous behaviour where energy is completely dissipated. Due to the combination of elastic and viscous behaviours, viscoelastic materials don't display constant material values of elasticity or viscosity but are described through material functions. Material functions, such as the dynamic moduli G and the dynamic viscosity η, change as a function of imposed loading conditions, shear strain γ, shear strain rate $\dot{\gamma}$ and stress σ, and environmental parameters, such as the temperature T. Material functions are universally applicable regardless of the material class. Once acquired, material functions can be related to the structure of specific material classes, forming what is known as structure function relationships. The structure function relationships can then be used to explain how changes in material microstructure affects macroscale rheological function. One of

the most used pieces of equipment to characterise a material's macroscale rheology is the rheometer. Principally a rheometer consists of two plates, a lower loading plate, which is generally a temperature-controlled Peltier plate, and an upper plate, which is connected to a torque transducer. The material of interest is loaded on the lower plate and the upper plate is then brought into contact. The sample is then left to relax and equilibrate before being deformed with user defined shear stresses σ and shear strains γ. The measured parameters are then typically the torque τ, the displacement θ and the rotational velocity $\dot{\theta}$. Depending upon the type of material being tested, a number of different geometries can be selected, the most common of which are the parallel plate, the cone and plate and the bob and cup, otherwise known as a Couette cell, which is used to measure fluid viscosity. The parallel plate (PP) geometry consists of two flat plates and has a radially inhomogeneous flow field. The main advantage of the PP is the flexibility in selecting gap heights. This enables testing of a wide range of materials. The cone and plate (CP) geometry features a flat bottom plate and an upper plate with a cone angle α. In contrast to the PP, the CP geometry has a radially homogeneous flow field, however tests need to be performed at a predetermined gap size in order to produce a homogenous flow field. Equations for calculating torque and stress for both PP and CP can be seen in

Parameter	Parallel Plate	Cone and Plate
Torque	$\tau = \frac{\pi\dot{\theta}\eta R^4}{2h}$	$\tau = \frac{2\pi\dot{\theta}\eta R^3}{3\tan\theta}$
Stress	$\sigma = \frac{\tau}{2\pi R^3}\left[3 + \frac{dln\tau}{dln\dot{\gamma}_R}\right]$	$\sigma = \frac{3\tau}{2\pi R^3}$
Strain	$\theta\frac{R}{h}$	$\theta\frac{1}{\varphi}$

Table 2-1: Torque, stress and strain conversions for Parallel plate and Cone and plate rheometer geometries. The angular displacement is θ, $\dot{\theta}$ is the angular velocity, η is the viscosity, R is the geometry radius, h is the gap height, $\dot{\gamma}_R$ is the strain rate and φ is the cone angle.

The differences in measured torque between the PP and CP measurements are negligible within the linear viscoelastic region. However, within the non-linear LAOS range PP measurements tend to underestimate the measured stress. In order to fit

measured LAOS data from PP to equivalent CP geometries vertical and horizontal shift factors are used (H. Y. Song et al., 2017).

2.5.1 Rheometer nuisance factors

Several nuisance factors need to be taken into consideration during the operation of a rheometer in order to obtain reliable material functions (Ewoldt et al., 2015). The torque τ measured during a rheometer test is a function of material deformation, but also features inertial artefacts from the acceleration of the rheometer motor and geometry (Klemuk & Titze, 2009). Inertial artefacts are particularly important to consider when measuring soft biological materials with elastic moduli below 100 Pa and at high frequencies. Soft biological materials have a low material torque, so above a material specific frequency inertial effects can dominate over the stress response of the material, resulting in unrepresentative data. The magnitude of inertial effects is also influenced by a rheometer's operating design. Combined motor transducer (CMT) and Separate motor transducer (SMT) setups produce different magnitudes of inertial torque when measuring low elasticity fluids, *Figure 2-12*. SMT's produces an inertial torque which acts in the same direction as the sample torque. CMT's in contrast produce a comparatively higher inertial torque acting in the opposite direction to the sample torque (Genovese, 2012; Läuger & Stettin, 2016).

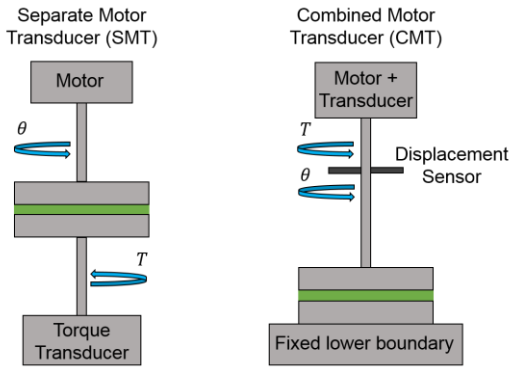

Figure 2-12: Illustrated is a representation of the separate motor transducer (SMT) and Combined motor transducer (CMT) rheometer configurations. The two featured rheometer configurations vary primarily by where torque is sensed and applied. In the SMT configuration the motor and torque transducer are separate, which enables separate control over each element. Whereas in the CMT system both motor and transducer are combined. The advantage of the SMT layout is that the effect of instrument inertia on the measured torque is reduced in comparison to CMT.

The impact of instrument inertia can become critical when testing a soft biomaterial at high frequencies or studying the gelling point in sol gel systems (Hudson et al.,

2017). Therefore, before performing oscillatory tests it is prudent to identify the frequency limit where inertial effects begin to dominate. An example of the instrument inertial effect at high frequencies is presented in *Figure 2-13*.

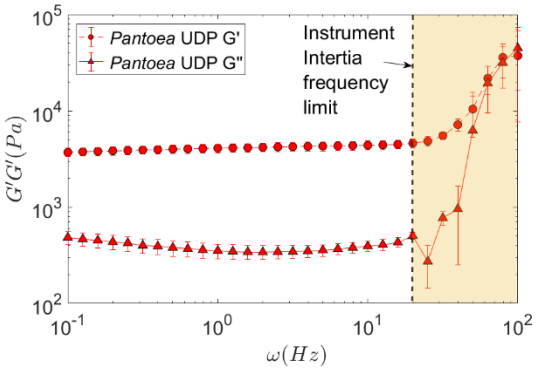

Figure 2-13: An example frequency sweep of a *Pantoea* sp. biofilm grown for 48 hr on an agar plate. The elasticity of the biofilm is represented by G', the storage modulus, whilst the viscous behaviour is represented by G'', the viscous modulus. The elastic and viscous moduli are in a plateau region until inertia effects begin to dominate the sample response. The dashed back line signifies the beginning of the region where instrument inertia torque dominates over sample torque. Within this region the apparent elastic and viscous moduli increase dramatically which is unrepresentative of the actual sample's response.

A key parameter associated with a rheometer test is the gap height h, the distance between the upper and lower geometries. The occurrence and magnitude of secondary flows are a key nuisance factor which are influenced by gap height. Secondary flows occur due to elastic shear wave propagation, viscous diffusion and when high shear rates are used due to fluid inertia (Yosick et al., 1998). The wave speed of secondary flows governs the wave propagation length l. If the gap height is 10 x lower than the wave propagation length, secondary flows will affect the measured rheology. The occurrence of secondary flows disturbs the uniform velocity gradient assumed during steady flow in an oscillatory test and cause unrepresentative increases to the measured viscosity. To avoid the presence of secondary flows the wave propagation length is calculated using,

$$l = \frac{1}{\cos\left(\frac{\delta}{2}\right)} \frac{|G^*|^{\frac{1}{2}}}{\rho} \frac{2\pi}{\omega}, \qquad [14]$$

where δ is the phase angle $G^*$is the complex modulus, ρ is the density and ω is the oscillation frequency (Schrag, 1977).

The presence of secondary flows is of importance when performing LAOS tests on biofilms, which exhibit shear thinning behaviour. For a shear thinning material as the shear strain amplitude increases, the complex modulus G^* decreases and the phase

angle δ increases, resulting in a reduction of the wave propagation length l. A reduction in l below the critical gap height results in non-representative nonlinear behaviour, leading to misinterpretation of LAOS data.

Rheometers typically function under the assumption of rotationally symmetric geometries; however this condition can be violated as a result of under/over filling, evaporation and poorly matched geometry alignment. Breaking of rotational symmetry or non-constant contact angle results in a surface tension torque which can be misinterpreted as a material response (Johnston & Ewoldt, 2013). To reduce or eliminate the effects of surface tension in rheology measurements, solvent traps can be used to eliminate sample evaporation. To ensure a constant contact line, a sample should be properly filled, *Figure 2-14*. Else significant errors in measured viscosity occur in both under and over filled scenarios (Hellström et al., 2014).

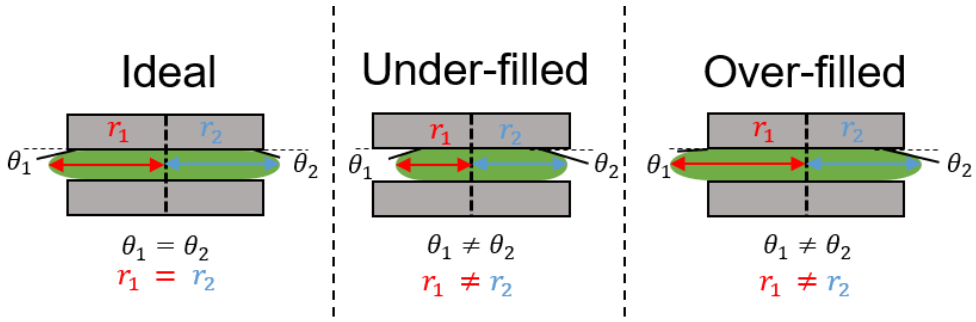

Figure 2-14: Schematic of the rheometer filling conditions. Ideally filled samples will have a contact line with constant contact angle θ and radius r. Under-filled and overfilled samples have a non-equal contact radius and non-equal contact angle. This leads to the occurrence of surface tension torques, which increase the measured torque, resulting in an overestimation elasticity and viscosity.

Rheological functions are calculated based on the assumption of a no slip boundary at the upper and lower geometries. However, this boundary condition can be violated by the occurrence of slip. Slip can cause significant artefacts at both low and high shear rates and strains (Ballesta et al., 2013). Presence of slip artefacts result in underestimation of yield stress and misinterpretation of non-linear behaviour in LAOS tests (Ozkan et al., 2012; Walls et al., 2003). To eliminate slip, roughened grit tape can be adhered to upper and lower geometries, geometries can be grit blasted, or adhesive bonding can be used to fix samples to each geometry. In some cases, custom geometries have been fabricated to alter material surface energy in order to combat hydrophobicity induced slip. Another factor which causes the violation of the no slip condition is shear banding. Shear banding occurs when strain is localised to a

narrow region within the sample height. This results in the sample being separated into two or more regions of differing flow velocity despite the same applied shear rate, resulting in large inhomogeneity to the flow field (Voigtmann, 2014).

2.5.2 Linear rheology theory

Creep and stress relaxation tests enable the characterisation of a viscoelastic material over extended periods of time. However, the response of a viscoelastic material to strain is also dependent upon strain rate. To fully describe the properties of a viscoelastic material on short time scales oscillatory tests are used. By imposing a continuous oscillatory stress/strain, multiple length and time scales can be probed enabling the quantification of elastic and viscous components. Oscillatory shear tests are performed by imposing a sinusoidal strain or stress. To probe the time dependency of a material, the frequency of the imposed wave is controlled, known as a frequency sweep. When yielding is of interest, strain/stress amplitude sweeps are performed, where the strain/stress amplitude of the sine wave is the controlling parameter. The oscillatory sin wave is described as,

$$\gamma(t) = \gamma_0 \sin(\omega t) \quad [15]$$

where the shear strain amplitude is denoted by γ_0 and the frequency by ω.

The stress response of a linear viscoelastic material to the imposed oscillation is a sine wave of the form:

$$\sigma(t) = \sigma_o \sin(wt + \delta). \quad [16]$$

For a purely elastic Hookean material the stress response is in phase with the loading strain, whereas for a purely viscous material the stress lags the strain by a phase angle of 90˚ . A viscoelastic material has elastic and viscous contributions to its stress response, so it exhibits a phase $0^\circ < \delta < 90^\circ$. Transforming [16] into its complex analogue we gain a relationship $\sigma^* = G^*\varepsilon^*$ in which G^* is defined as the complex dynamic modulus,

$$G^* = G' + iG''. \quad [17]$$

G^* is the summation of both the elastic and viscous behaviour, where G' is the storage modulus representing the stored energy and thus the recovered elastic energy per cycle in phase with the applied strain, and the loss modulus G'' describes the viscous behaviour of a material and thus the amount of energy dissipated due to viscous damping. The ratio of the storage modulus to the loss modulus gives the phase angle

and describes the amount of energy dissipated versus the amount of energy stored during a singular oscillatory cycle,

$$\delta = \tan^{-1}\frac{G''}{G'}. \qquad [18]$$

The linear regime of a viscoelastic material is defined as when the storage and loss moduli are independent of the imposed amplitude, *Figure 2-15*. This region is known as the linear viscoelastic regime (LVER). In the small amplitude oscillatory shear (SAOS) region the quiescent structure is probed, and negligible structural rearrangements occur. However, as the imposed strain increases the material elastic and viscous response become a function of strain amplitude. The region above SAOS is composed of the medium amplitude oscillatory shear (MAOS) and large amplitude oscillatory shear (LAOS) regions. In the MAOS and LAOS regimes the stress response function is no longer sinusoidal due to the presence of higher harmonics. The presence of these higher harmonics isn't considered within the linear viscoelasticity theoretical framework, so the storage and loss moduli fail to fully capture nonlinear viscoelastic behaviour.

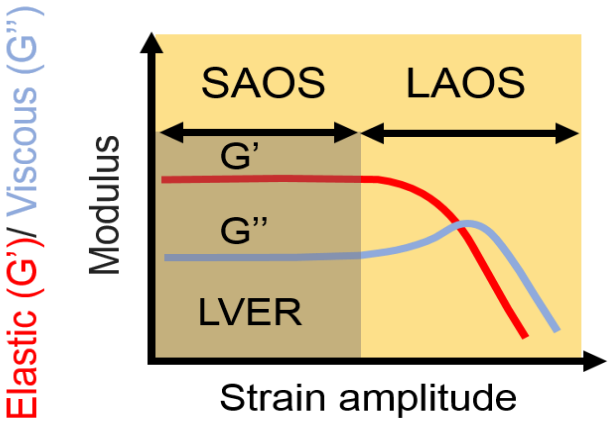

Figure 2-15: Generic schematic of an amplitude sweep plot. The red curve denotes the linear storage moduli G' and the blue line denotes the linear viscous moduli G'', in the small amplitude oscillatory shear (SAOS) region both moduli are independent of strain amplitude. When the linear viscoelastic regime is exceeded both G' and G'' become a function of strain amplitude which is defined as the large amplitude oscillatory shear (LAOS) region.

2.5.3 Origins of LAOS

The presence of higher harmonics within stress response in the non-linear regime have been acknowledged since the 1960's (Philippoff, 1966). However due to technological constraints, such as a low sampling rate and the presence of low to noise due to mechanical and electrical noise, investigators could only conduct

qualitative analysis using analogue stress response signals (Komatsu et al., 1973). However, the advent of analogue to digital converters (ADC) and increasingly sophisticated rheometers with lower noise enabled investigators to substantially increase the stress response sampling rate. The first quantitative approach to analysing LAOS data was Fourier transform rheology (FT-rheology) (Wilhelm, 2002). This methodology performed a Fourier transform on the stress response signal using,

$$\sigma(t) = \sum_{n=1,odd} \sigma_n \sin(n\omega_1 t + \delta_n). \quad [19]$$

Performing a Fourier transform over multiple periods resulted in a higher S/N ratio and enabled non-linear rheological analysis based on the Fourier harmonics (Hyun et al., 2003). Materials were analysed based upon the magnitude of Fourier harmonics to compliment qualitative analysis of the raw output stress waveforms, *Figure 2-16*.

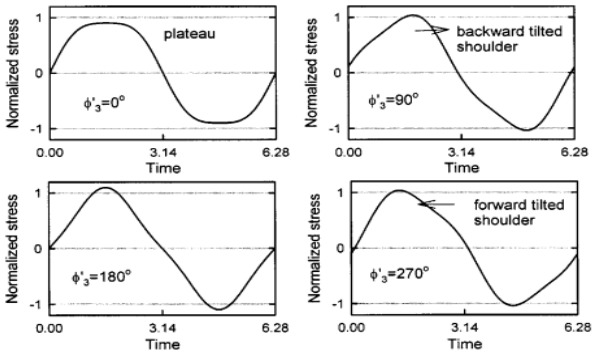

Figure 2-16: Different types of LAOS stress waveforms with their corresponding relative phase angle of the third Fourier harmonic for 4 different types of soft and hard polymer gels. The different waveform shapes correspond to different polymer microstructures. The plateau waveform was displayed for diblock copolymer gels. The backward tilted shoulder was displayed for soft gels. The forward tilted shoulder was displayed for polysaccharides xanthan gum and hyaluronic acid (Roth, 2012).

Non-linearity was quantified using the relative intensity of the third Fourier harmonic $I_{3/1}$,

$$I_{3/1} = \frac{I_3}{I_1} = \frac{\sigma_3}{\sigma_1} = \frac{\sqrt{(\sigma_3 \cos\ \delta_3)^2 + (\sigma_3 sin\delta_3)^2}}{\sqrt{(\sigma_1 \cos\ \delta_1)^2 + (\sigma_1 sin\delta_1)^2}}. \quad [20]$$

Within the medium amplitude oscillatory region $I_{3/1}$ behaviour is typically characterised through the exponent n which is calculated using,

$$\log\left(\frac{I_3}{I_1}\right) = a + n \log \gamma_0, \quad [21]$$

where a is an arbitrary constant and γ_0 is the strain amplitude. In early investigations using linear polymer solutions the exponent n was found to scale quadratically with strain. This relation had first been predicted using Doi- Edwards theory and has

subsequently been demonstrated using the pom pom model (Hyun et al., 2012; Pearson & Rochefort, 1982). However, the precise physical reason which causes this exponent value is still not understood. Subsequent experimental investigations have demonstrated that the gradient of $I_{3/1}$ varies with dependent upon polymer topology. The gradient of $I_{3/1}$ is known to be sensitive in detecting the amount of branching within polymer melts. For example, a highly branched high-density polyethylene melt has a $I_{3/1}$ gradient of $n \approx 1.6$ (Hyun et al., 2006, 2007).

2.5.4 Analysis of LAOS waveforms – theoretical background

This thesis focuses upon the nonlinear rheology of bacteria biofilms and uses a range of LAOS techniques to interpret rheometer data and understand the rheological signatures experimentally obtained. Therefore, I find it logical to spend some time introducing the foundational mathematical principles of each technique.

2.5.5 Stress symmetry

The total stress generated within a material is dependent upon the magnitude of strain (γ) and its derivative, strain rate ($\dot{\gamma}$). For a viscoelastic material the total stress (σ) is separated into an elastic response $G'(\omega)\gamma(\omega t)$, which is dependent upon the strain (γ), and the viscous response $G''(\omega)\frac{\dot{\gamma}(\omega t)}{\omega}$, which is dependent upon strain rate $\frac{\dot{\gamma}(\omega t)}{\omega}$. The three time dependent variables $\gamma, \dot{\gamma}/\omega \; and \; \sigma$ can be represented as vectors i, j, k within a $(\gamma, \frac{\dot{\gamma}}{\omega}, \sigma)$ coordinate system. These vectors map the path of a time dependent plane known as the stress surface, which represents the dynamic response of a material through an oscillatory cycle. The total stress response of a material is thus a function of frequency, strain and time which is assumed continuous and differentiable. By substituting $\gamma = x(t)$ and $\frac{\dot{\gamma}}{\omega} = y(t)$, the total stress can be represented as,

$$\sigma(\omega, \gamma_0, t) = \sigma(x, y), \qquad [22]$$

where γ_0 is the strain amplitude of the oscillation cycle. Inverting strain and strain rate produces a negative stress,

$$\sigma(-x, -y) = -\sigma(x, y), \qquad [23]$$

which makes stress σ an odd function as $f(-x) = -f(x)$. This property of stress is applicable to most soft materials (Kwang Soo et al., 2005). As both x and y are odd functions of their arguments, the total stress can be decomposed into

$$\sigma(x,y) = \frac{\sigma(x,y)-\sigma(-x,y)}{2} + \frac{\sigma(x,y)-\sigma(x,-y)}{2}, \quad [24]$$

since

$$\sigma(-x,y) = -\sigma(x,-y). \quad [25]$$

The first and second components of [24] represent an odd even and even odd contribution of total stress respectively,

$$\sigma_{OE} = \frac{\sigma(x,y)-\sigma(-x,y)}{2}, \quad [26]$$

$$\sigma_{EO} = \frac{\sigma(x,y)-\sigma(x,-y)}{2}. \quad [27]$$

Taking the contour integral over one period of oscillation [26] and [27] with respect to the odd component yields zero, a characteristic property of odd functions,

$$\oint \sigma_{OE} dx = 0, \quad [28]$$

$$\oint \sigma_{EO} dy = 0. \quad [29]$$

Which means that the total stress in the system is the contour integral of the even functions over one period of oscillation,

$$\oint \sigma dx = \oint \sigma_{EO} dx\,, \quad [30]$$

$$\oint \sigma dy = \oint \sigma_{OE} dy. \quad [31]$$

Proving that the decomposition of [24] is unique and satisfies [28] and [29] means that [26] and [27] are true and that total stress can be geometrically decomposed into elastic and viscous parts σ' and σ''. This decomposition is valid as in the linear viscoelastic region we can show that:

$$\sigma(x,y) = \sigma'(x,\gamma) + \sigma''(y,\gamma), \quad [32]$$

where

$$\sigma' = G'x(t) \quad [33]$$

and

$$\sigma'' = G''y(t). \quad [34]$$

where σ' is an odd function of x and σ'' is an odd function of y, meaning they are in the linear viscoelastic regime, so,

$$\oint \sigma' dx = 0, \quad [35]$$

$$\oint \sigma'' dy = 0, \quad [36]$$

And

$$\oint \sigma dx = \oint \sigma'' dx, \quad [37]$$

$$\oint \sigma dy = \oint \sigma' dy\,. \quad [38]$$

Which leads us to show the equivalency in decomposing LAOS stress into elastic and viscous components as with linear viscoelasticity,

$$\sigma' = \sigma_{OE,} \quad [39]$$

$$\sigma'' = \sigma_{EO,} \quad [40]$$

$$\sigma'(x,y) = \sigma'(x,\gamma), \quad [41]$$

$$\sigma''(x,y) = \sigma''(y,\gamma), \quad [42]$$

This then allows the interpretation of LAOS signal as an extension of the linear regime where Γ' and Γ'' are used as the dynamic moduli in the nonlinear region,

$$\sigma' = \Gamma'(x,\gamma)x, \quad [43]$$

$$\sigma'' = \Gamma''(y,\gamma), \quad [44]$$

which in the linear viscoelastic limit can also be used to represent the linear storage G' and loss modulus G'',

$$\lim_{\gamma\to 0}\Gamma'(x,\gamma) = G'(\omega), \quad [45]$$

$$\lim_{\gamma\to 0}\Gamma''(y,\gamma) = G''(\omega). \quad [46]$$

2.5.6 Fundamentals of Ewoldt Chebyshev method

Traditionally FT rheology involved the analysis of the stress response signal by performing a Fourier transform, from which the overall stress σ could be analysed in terms of the higher order shear moduli G_n' and G_n'' and the higher order viscosities η_n' and η_n'',

$$\sigma(t;\omega,\gamma_0) = \gamma_0 \sum_{n\,odd}\{G_n'(\omega,\gamma_0)\sin n\omega t + G_n''(\omega,\gamma_0)cosn\omega t\}, \quad [47]$$

$$\sigma(t;\omega,\gamma_0) = \dot{\gamma}_0 \sum_{n\,odd}\{\eta_n''(\omega,\gamma_0)\sin n\omega t + \eta_n'(\omega,\gamma_0)\cos n\omega t\}, \quad [48]$$

where γ_0 is the strain amplitude and $\dot{\gamma}_0$ is the strain rate amplitude.

However, this method suffers from a series of drawbacks:

1. The physical interpretation of higher harmonics is unclear.
2. Characterising non-linear behaviour using G_1' and G_1'' generally is not sensitive enough to provide an accurate representation of the non-linear behaviour.

To eliminate these weaknesses and construct a repeatable, consistent, physically interpretable framework, Ewoldt (Randy et al., 2008) took Cho's stress decomposition proof and argued that the Fourier transform of the total stress could be decomposed into elastic and viscous stresses:

$$\sigma' \equiv \frac{\sigma(\gamma,\dot{\gamma})-\sigma(-\gamma,\dot{\gamma})}{2} = \gamma_0 \sum_{n\,odd} G_n'(\omega,\gamma_0)\sin n\omega t\,, \quad [49]$$

$$\sigma'' \equiv \frac{\sigma(\gamma,\dot{\gamma})-\sigma(\gamma,-\dot{\gamma})}{2} = \gamma_0 \sum_{n\,odd} G_n''(\omega,\gamma_0)\cos n\omega t\,. \quad [50]$$

Plotting the Fourier transformed signal σ' and σ'' with respect to x and y results in a single valued curve.This approach captures the full Fourier transformed signal, including higher harmonics, which partially solves drawback 1. To characterise the curves Cho suggested using a polynomial regression analysis which is of the general form,

$$F = a_0 f_0(x) + a_1 f_1(x) + a_2 f_2(x) + \cdots + a_n f_n(x), \quad [51]$$

where a_n are the weighting coefficients on the fitting polynomials $f_n(x)$.However, polynomial analysis features an arbitrary user choice of the number of higher order terms used to represent each curve, which has a feedback effect in influencing the value of the lower order terms. To solve this issue Ewoldt proposed the adoption of Chebyshev polynomial basis functions, which determine the fitting points used during polynomial analysis. Chebyshev polynomials are suited towards describing LAOS due to their orthogonality in the domain [-1 1] which corresponds to $[-\gamma,\gamma]$ and are defined by,

$$\sigma'(x) = \gamma_0 \sum_{n:odd} e_n(\omega,\gamma_0)T_n(x), \quad [52]$$

$$\sigma''(y) = \dot{\gamma}_0 \sum_{n:odd} v_n(\omega,\gamma_0)T_n(y). \quad [53]$$

Here e_n is representative of the elastic Chebyshev harmonic and v_n is representative of the viscous Chebyshev harmonic. Only odd harmonic contributions are considered due to the flow symmetry assumption from FT rheology. The Chebyshev coefficients in the strain or strain rate domain are represented by,

$$e_n = G_n'(-1)^{\frac{n-1}{2}} \qquad n: odd, \tag{54}$$

$$v_n = \frac{G_n''}{\omega} = \eta_n' \qquad n: odd. \tag{55}$$

Both e_n and v_n can be physically interpreted by considering the phase angle δ_n of the complex modulus G_n^*,

$$\sigma = \gamma_0 \sum_{n:odd} |G_n^*| \sin(n\omega t + \delta_n). \tag{56}$$

For the third harmonic the magnitude of e_3 and v_3 can be related to a physical behaviour using the third order phase angle δ_n,

$$e_3 = -|G_3^*| \cos \delta_3 \begin{cases} > 0 \quad for \ \frac{\pi}{2} < \delta_3 < \frac{3\pi}{2}, & \text{Strain stiffening} \\ = 0 \quad for \ \delta_3 = \frac{\pi}{2}, \frac{3\pi}{2}, & \text{Linear elastic} \\ < 0 \quad for -\frac{\pi}{2} < \delta_3 < \frac{\pi}{2}, & \text{Strain softening} \end{cases} \tag{57}$$

$$v_3 = -\left|\frac{G_3^*}{\omega}\right| \sin \delta_3 \begin{cases} > 0 \quad for \quad 0 < \delta_3 < \pi, & \text{Strain thickening} \\ = 0 \quad for \quad \delta_3 = 0, \pi, & \text{Linear viscous} \\ < 0 \quad for \quad \pi < \delta_3 < 2\pi. & \text{Strain thinning} \end{cases} \tag{58}$$

Ewoldt also constructed geometrically derived moduli from the elastic and viscous Lissajous Bowditch plots, in order to capture the contribution of higher harmonics. In the elastic LB plots, local elastic response at zero strain is represented by the minimum strain modulus G_M' and at large strains by G_L', the large strain modulus. In the linear region G_M' and G_L' converge to G',

$$G_M' \equiv \left.\frac{d\sigma}{d\gamma}\right|_{\gamma=0} = \sum_{n\ odd} nG_n' = e_1 - 3e_3 + \cdots, \tag{59}$$

$$G_L' \equiv \left.\frac{\sigma}{\gamma}\right|_{\gamma=\pm\gamma_0} = \sum_{n\ odd} G_n'(-1)^{\frac{n-1}{2}} = e_1 + e_3 + \cdots. \tag{60}$$

From the viscous LB plots, local viscous response at zero strain is represented by the minimum viscosity modulus η_M' and at large strains by η_L' the large viscosity modulus. In the linear region η_M' and η_L' converge with G'',

$$\eta'_M \equiv \left.\frac{d\sigma}{d\dot{\gamma}}\right|_{\dot{\gamma}=0} = \frac{1}{\omega_n}\sum_{n\ odd} nG''_n(-1)^{\frac{n-1}{2}} = v_1 - 3v_3 + \cdots, \quad [61]$$

$$\eta'_L \equiv \left.\frac{\sigma}{\dot{\gamma}}\right|_{\dot{\gamma}=\pm\dot{\gamma}_0} = \frac{1}{\omega_n}\sum_{n\ odd} G''_n = v_1 + v_3 + \cdots. \quad [62]$$

The rate of change of the large viscosity modulus in comparison to the minimum viscosity modulus is indicative of the non-linear behaviours described in [59] and [60]. To represent these using the geometric measures the dimensionless numbers based on the strain, the stiffening ratio S and the shear thickening ratio T, are constructed. With a S value of zero, the gradients of the large elastic modulus and minimum elastic modulus are equivalent. This signifies a linear behaviour, in the limit where G'_M and G'_L converge to G'. A value of S > 0 corresponds to strain stiffening, which occurs when the gradient of G'_L is steeper than G'_M, signifying that at high strain the intercycle moduli of the material has increased. When S < 0 the material is exhibiting a strain softening response, and G'_M has a larger gradient than G'_L,

$$S \equiv \frac{G'_L - G'_M}{G'_L} = \frac{4e_3 + \cdots}{e_1 + e_3 + \cdots}. \quad [63]$$

The T ratio follows the same logic as the S ratio, with T = 0 signifying a linear response and T > 0 a shear thickening response and T< 0 a shear thinning response,

$$T \equiv \frac{\eta'_L - \eta'_M}{\eta'_L} = \frac{4v_3 + \cdots}{v_1 + v_3 + \cdots}. \quad [64]$$

2.5.7 Series of physical processes

Chebyshev analysis is a mathematically rigorous approach to analysing LAOS data using a static approach. However, the formulation of S and T ratios is inherently an intercycle averaged property. Since they are intercycle averaged metrics, S and T cannot fully describe the instantaneous response of a material, thus neglecting the transient material response to imposed strain. Additionally, the validity of stress symmetries which underlie the mathematics of the Chebyshev analysis cannot be experimentally guaranteed. Materials can exhibit even harmonics due to the occurrence of nuisance factors, such as secondary flows and slip. In order to circumvent these issues Rogers proposed a mathematical approach which relies upon differential geometry to characterise the trajectory of stress in the $(\gamma, \frac{\dot{\gamma}}{\omega}, \sigma)$ coordinate system (Donley et al., 2019; C.-W. Lee & Rogers, 2017; S. A. Rogers, 2017; S. A. Rogers & Lettinga, 2011). The series of physical processes (SPP) approach considers the change in material response in relation to a change in

instantaneous strain, as opposed to selecting the material moduli based upon total strain. This framework enables the interpretation of non-steady state oscillatory waves in addition to instantaneous material response and considers all data points sampled by a rheometer. In doing so a complete picture of the response of a material to strain and strain rate can be constructed, whereby the processes of extension, yielding, flow and deformation behaviour can be mapped through a singular oscillatory cycle.

As seen in the stress symmetry and Chebychev method derivation oscillatory strain γ and strain rate $\dot{\gamma}$ can be represented by,

$$\gamma(t) = \gamma_0 \sin \omega t, \quad [65]$$

and

$$\dot{\gamma}(t) = \gamma_0 \omega \cos \omega t, \quad [66]$$

and the stress is,

$$\sigma(t) = \gamma_0 (G'(\omega) \sin \omega t + G''(\omega) \cos \omega t). \quad [67]$$

SPP differs from static approaches, which use stress symmetry arguments, by showing that [65] can be rearranged to give,

$$G'(\omega)\gamma_0 sin\omega t + G''(\omega)\gamma_0 cos\omega t - \sigma(t) + 0 = 0, \quad [68]$$

which is reminiscent in structure of the general description of a plane,

$$ax + by + cz + d = 0. \quad [69]$$

As the material is driven externally by oscillations, the plane motion is set along a fixed path. To fully describe the trajectory of the plane the Frenet Serret TNB reference frame is used, *Figure 2-17*.

A continuous differentiable trajectory travelling through $\mathbb{R}^3$ space can be described by a series of coordinates A, with positions x, y, z,

$$A = \begin{bmatrix} A_x & A_y & A_z \end{bmatrix} = [x\ y\ z]. \quad [70]$$

The tangent T of the curve represents the unit vector travelling tangentially in the direction of motion, which is calculated using,

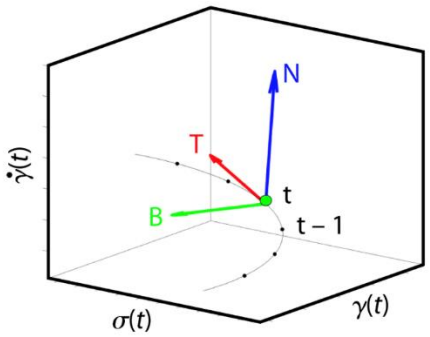

Figure 2-17: Schematic of the Fernet Serret TNB reference frame. The tangent (T), normal (N) and binormal (B) are unit vectors used to fully describe the trajectory of a path through strain γ, strain rate $\dot{\gamma}$ and stress σ coordinate space. The trajectory is formed of experimentally acquired discrete data points taken at time t in an oscillation period. The resolution of sampling is dependent upon the rheometer sampling frequency.

$$T = \frac{\dot{A}}{|\dot{A}|}, \qquad [71]$$

where $\dot{A}$ is the first order derivative of A and $|\dot{A}|$ is the magnitude of the first order derivative of A. From T the normal unit vector N of the curve can be calculated which is the derivative of the tangent vector,

$$N = \frac{\dot{T}}{|\dot{T}|} = \frac{\dot{A} \times (\ddot{A} \times \dot{A})}{|\dot{A}||\ddot{A} \times \dot{A}|}. \qquad [72]$$

Finally, B is the binormal unit vector which points perpendicularly to both T and N, and defines the orientation,

$$B = T \times N = \frac{\dot{A} \times \ddot{A}}{|\ddot{A} \times \dot{A}|}. \qquad [73]$$

By calculating the TNB unit vectors, trajectories through $(\gamma, \frac{\dot{\gamma}}{\omega}, \sigma)$ space can be fully described. By substituting the coordinate system $(\gamma, \frac{\dot{\gamma}}{\omega}, \sigma)$ into A we can show that a LAOS trajectory can be described by a series of points A,

$$A = [A_\gamma \;\; A_{\frac{\dot{\gamma}}{\omega}} \; A_\sigma] = [\gamma_0 sin\omega t \; \gamma_0 cos\omega t \; \sigma(t)] = [\, \gamma(t) \; \frac{\gamma(t)}{\omega} \dot{\sigma}(t)]. \qquad [74]$$

To describe the displacement of the stress plane in terms of the points within a trajectory and the associated binormal vector we use,

$$\sigma = G_t'(t)\gamma(t) + G_t''(t)\frac{\dot{\gamma}(t)}{\omega} + \frac{B_\gamma(t)}{B_\sigma(t)} A_\gamma(t) + \frac{B_{\frac{\dot{\gamma}}{\omega}}(t)}{B_\sigma(t)} A_{\frac{\gamma}{\omega}}(t) + A_\sigma(t), \qquad [75]$$

where B_γ is the binormal vector of strain and B_σ the binormal vector of stress and $B_{\frac{\dot{\gamma}}{\omega}}$ is the binormal vector of strain rate over frequency and $G_t'(t)$ and $G_t''(t)$ are the transient storage and transient loss moduli. Substituting [72] into [73] produces,

$$\sigma = G_t'\gamma + G_t''\frac{\gamma}{\omega} + \frac{B_\gamma}{B_\sigma}\gamma + \frac{\frac{B_{\dot{\gamma}}}{\omega}}{B_\sigma}\frac{\gamma}{\omega} + \sigma, \quad [76]$$

which can then be rearranged to yield,

$$\left[G_t' + \frac{B_\gamma}{B_\sigma}\right]\gamma + \left[G_t'' + \frac{\frac{B_{\dot{\gamma}}}{\omega}}{B_\sigma}\right]\frac{\dot{\gamma}}{\omega} = 0, \quad [77]$$

which can be solved by processing γ, $\dot{\gamma}$ and σ data through the TNB reference frame using [74]. Solving [77] results in the transient measures of viscoelasticity, the transient storage modulus,

$$G_t'(t) = -\frac{B_\gamma(t)}{B_\sigma(t)}, \quad [78]$$

and the transient loss modulus,

$$G_t''(t) = -\frac{\frac{B_{\dot{\gamma}}(t)}{\omega}}{B_\sigma(t)}. \quad [79]$$

2.5.8 Transient phase angle

In linear rheology the elastic and viscous components can be defined geometrically through the complex modulus G^* and the phase angle δ. The transient moduli can be described analogously in this way. This results in what is termed the complex transient modulus,

$$|G_t^*| = \sqrt{G_t'^2 + G_t''^2}, \quad [80]$$

and the transient phase angle,

$$\delta_t = \tan^{-1}\frac{G_t''}{G_t'}, \quad [81]$$

which describes the state of instantaneous yielding within a material.

2.6 Viscoelastic liquids, glasses and gels

The field of soft matter physics concerns the study of physical systems assembled through weak interactions which are easily deformed with thermal fluctuations or physical stresses (Likos, 2001). A spectrum of materials fall into this category including: foams, emulsions, gels, biological materials and colloids. These systems

are commonly heterogeneous and complex due to the transient nature of the material's microstructure and are classified as either passive or active. An active system is constantly out of equilibrium as constituents consume energy to convert into active mechanical processes, such as bacterial swimming or in mammalian systems where molecular protein motors drive spontaneous self-organisation of microtubule filaments (Lushi et al., 2014; Sanchez et al., 2012). A biofilm can be considered an active system whereby bacteria consume energy for cell division and EPS secretion. Within this field a primary aim is the formulation and dissection of structure – function relationships. Determining these relationships enables engineers to carefully design soft matter materials for practical applications. Soft matter systems exhibit self-organisation, where local interactions cause large scale ordering to emerge (Secor et al., 2015). The structure of these systems determines the materials mechanical properties.

The transitions between colloidal phases is a confluence of physical and chemical parameters, which can be simplified into two variables: packing fraction and interaction potential (V. J. Anderson & Lekkerkerker, 2002). The dynamics of each of these categories is driven by the diffusive motion of particle constituents, which range from fully diffusive in liquids to amorphous arrested states in glasses and gels. Packing fraction is simply the ratio of the solid particles volume to filler in the solution, while pairwise interaction potential describes the strength of particle – particle attraction. Varying each of these parameters results in different behaviours. In liquids packing fraction is low < 0.1, increasing the packing fraction results in increased elastic behaviour. As stiffer filler particles begin to interact with each other, the material becomes viscoelastic. Increasing the packing fraction further > 0.3 causes crowding and results in glassy and gel rheology (Laurati et al., 2011). The random packing limit (φ_{rpl}) of 0.64 for spheres results in complete dynamic arrest while φ_{rpl} in rod systems is dependent upon rod aspect ratio (Kyrylyuk et al., 2009). The interaction potentials differentiate glassy and gel dynamics.

Glasses are non-bonded systems whereas gels are bonded (Zaccarelli & Poon, 2009). In repulsive glassy system particle – particle interactions are weak/repulsive, less than a few kT. This non ergodic state structure is formed due to topological caging, constriction of movement by nearest neighbours driven by inter-particle repulsion. The transient nature of this non-crystalline structure is due to the stochastic Brownian diffusion of particles, in and out of cages. Gels and attractive glasses however, form percolated fractal network structures at low packing fractions, due to strong short-range attractive particle interactions (Tanaka et al., 2004). Such short-range forces include Van de Waals, attractive electrostatic interactions and depletion attraction. Gelation occurs when the packing fraction or interaction strength increases to a point where inter-particle clusters join to form a stress bearing space spanning network.

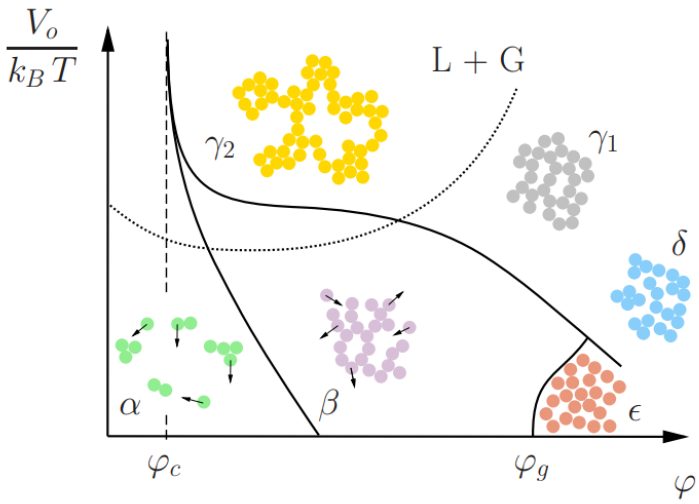

Figure 2-18: A phase diagram of colloidal phases against interaction potential ($\frac{V_0}{k_B T}$) and packing fraction (φ). At low packing fractions φ_c and interaction potential colloids freely move due to thermal brownian motion corresponding to disordered fluid behaviour (α). At an intermediate packing fraction, below the glass transition point φ_g particles are increasingly constricted, limiting free motion causing increases to viscosity (β). Belond the glass transition point particle motion is suppressed entirly which results in a frustrated state and formation of a glass. The mechanical properties of glasses are purely due to constriction of nearest neighbours, known phenomologically as cages and the rearrangment/relaxation of these cages underflow (ϵ). Increasing the interaction potential of the system results in the formation of bonded space spanning structures at low packing fractions. This state is known as gelation, where the attractive interparticle bonds determine the mechanical response of the system γ_2. The space spanning network morphology is influenced by interaction potential and packing faction. The density of the clusters and network connectivity reduces with lower interaction potential whilst particle crowding increases with an increasaing packing fractions (γ_1 and δ). The mechanical response of these conformations is a confluence of the interparticle bonding strength and the constriction of motion within the interparticle cages. Adapted from (Roth, 2012).

The transition between gel and glassy rheology is determined by the interplay between caging and bonding dynamics (Jia et al., 2018). As a consequence of the different length scales associated with bonding and caging, materials which feature both display different yielding dynamics, depicted in *Figure 2-18*.

2.7 Colloidal polymer gels

Colloidal polymer gel networks are self-supporting networks, composed of mixtures of colloids and polymers. The interactions which govern colloidal gel self-assembly are dependent upon the enthalpic interactions between polymers and colloidal (Zaccarelli, 2007). When enthalpic interaction is high enough this leads to permanent polymer absorption on the colloid surface. However, where enthalpic interaction isn't high enough this leads to a non-absorbing state, where the polymer isn't absorbed on the colloidal surface. In colloidal gels with a high non absorbing polymer concentration the entropic depletion attraction governs self-assembly (Eckert & Bartsch, 2002). Depletion attraction occurs when the non-absorbing polymer within the system is excluded from the surface at the colloid excluded volume layer. This leads to regions between proximate colloids where polymer is excluded, known as the overlap layer. The formation of the overlap layer induces an osmotic pressure and effective attractive force between the colloids, leading to contact aggregation (Marenduzzo et al., 2006). This type of attraction leads to an increase in the entropy of the colloidal polymer system. The magnitude of the depletion attraction is dependent upon the molecular weight of the polymer. Longer polymer chains result in a larger depletion layer, which causes an increase the effective attractive force and influences the structure of depletion induced aggregates (Burns et al., 2002).

For polymer colloids mixtures where polymer is absorbed onto a colloidal surface, two enthalpic interaction processes can occur. The thickness of the absorbed layer is determined by the solvent properties, such as ionic concentration and pH and the polymer chain length and concentration (Cohen Stuart et al., 1985). For instance, in solutes with high ionic strengths bridging flocculation is reduced as the polymer chains compress onto the colloidal surface. Regions on the colloid unsaturated with polymer may bond through polymer bridging (Swenson et al., 1998). Polymer bridging results in the formation of aggregated structures and can lead to gelation. The extent of aggregation is dependent upon the affinity of the polymer to the colloidal surface, for weakly adhesive polymers where interaction strength is below that of the system thermal energy bonding will be reversible (F. Yan et al., 2018). The

extent of bonding is also dependent upon the polymer weight, or chain length. Long chain polymers have been shown computationally to result in the formation of loops or double bonds (multiple colloidal polymer bonds on the same colloid), wasting potential bonds with neighboring colloids and increasing interstitial space (Howard et al., 2019). Polymer bridging interaction strength increases with polymer concentration, until a maximum bridging interaction point. Beyond this concentration point for thermodynamically stable bound polymer steric effects induce a repulsive interaction and excess polymer addition results in an increase in steric repulsion, and the emergence of steric stabilization, which prevents colloidal contact aggregation (Weeks et al., 2000). However colloidal/polymer mixtures can also display spectrums of these interaction behaviors. In mixtures where absorbed layers and a non-absorbed polymer a combination of short-range repulsion and long-range attraction is present, a behavior known as tele bridging (Hooper & Schweizer, 2005).

The structure of polymer colloidal gel mixtures can be decomposed into two networks, the colloidal network, which is mediated through the aforementioned entropic and enthalpic processes and the polymer network with forms between interacting polymer chains in the solvent phase. Polymer networks are mediated by a combination of physical, ionic and covalent interactions which vary as a function of the polymer chains properties. Physical interactions between long linear polymer chains are mediated through the polymer molecular weight and relaxation behavior. These characteristics are described using tube models such as the Doi Edward model (Linnes et al., 2013). In tube-based models polymer chain dynamics are described based upon the extent of topological constriction by neighboring polymer chains otherwise known as entanglement. In dense polymer solutions the thermal motion of the chains, known as reptation determines the relaxation behavior of the network. Increased constriction causes a reduction to chain relaxation time resulting in increased network strength. Ionic crosslinking between polymer chains is dependent upon the charge and protonated state of the polymer. Polymers can be cationic or anionic depending on the polymer chain chemistry and the pH of the bulk solvent. The extent of polymer ionic crosslinking is therefore dynamic and controllable, a trait which is harnessed in the production of responsive polymer materials with switchable mechanical properties such as ionically responsive elastomers (Miwa et al., 2018). The crosslinking of proteins and polysaccharides is primarily driven by electrostatic, hydrogen bonding and hydrophobic interactions and

enzymatic crosslinking (Gentile, 2020). Covalently crosslinked polymer networks are a function of the functional groups of the polymer and the concentration and valence of the related ionic moiety or ion. Alginate for example is a polymer network which requires the addition of calcium ions to form a gelated crosslinked structure (K. Y. Lee & Mooney, 2012). The interaction of ligands and ionic metals mediates crosslinking density and gelation through chelation, where cationic metals covalently bind with ligand polymer networks (Magami & Williams, 2019).

Combinations of different types of polymer network lead to the formation of interpenetrating polymer networks (Myung et al., 2008). Networks of this type have combined properties from the individual networks which results in a confluence of the mechanical attributes of each network, such in the construction of double network hydrogels (Sun et al., 2016). The formation of a double network hydrogel can result in enhanced hydrogel mechanical properties such as increased strength and emergence of seal healing properties (Lei et al., 2020). The collective interacts between colloidal and polymer networks are complex. Colloidal and matrix networks are generally bonded through weak intermolecular forces. When sheared colloidal motion induces hydrodynamic many body forces upon the polymer network structure, resulting in the emergence of complex mechanical behaviors. For example, inclusion of colloids into a polymer network can influence the stiffening and softening behavior by influencing the relaxation dynamics of the polymer network (van Oosten et al., 2019). One of the most well-known effects is the Payne or Fletcher-Gant effect which was first seen in particle filled rubber polymer networks. The effect emerges as the polymer particle filled material is sheared. The storage modulus of the material drops rapidly with increasing strain and at a material dependent strain the viscous modulus of the material increases, the magnitude of which is dependent upon the filler concentration (Drozdov & Dorfmann, 2002). The precise mechanism governing this effect is still debated however a number of possible mechanisms have been proposed such as; the breakdown/ reformation of the filler network, molecular disentanglement, agglomeration/deagglomeration of filler aggregates and desorption of the polymer chain bridges from the colloidal phase of the mixture (Heinrich & Klüppel, 2002).

2.8 Bacteria used within this thesis

In this thesis a variety of bacteria are used, this section provides background information of each strain and the motivation behind their selection for rheological analysis.

2.8.1 *Pseudomonas fluorescens*

Pseudomonas fluorescens is a rod-shaped, gram-negative bacterium commonly found in soil and water environments. In soils *P. fluorescens* has been shown to influence the mechanical properties of vermiculite and clays (Genovese, 2012). The EPS of *P. fluorescens* is known to be composed of functional amyloids which confer protection from desiccation and controls hydrophobicity and stiffness (Zeng et al., 2015). *P. fluorescens* biofilms have also been shown to have a high content of uronic acid, where uronic acid content in EPS was found to be between 32.8 – 39.3% when grown on glass and stainless steel (Kives et al., 2006). A major biofilm component of *P. fluorescens* is the adhesive protein LapA (large protein A), which is required for biofilm formation and cell surface localization. LapA is a large repeat surface protein and has an estimated molecular weight of ~520 kDa (Boyd et al., 2014). When knockout strains of LapA were compared to wild type, the cellular adhesive force was found to drop by a factor of 2 (Ivanov et al., 2012). The rheology of *P. fluorescens* has been studied using several different techniques. Interfacial rheology was used to characterise the time dependent mechanical properties of *P. fluorescens* pellicle (Patrick A Rühs et al., 2013), while CLSM microrheology was used to map local mechanical properties of statically grown *P. fluorescens*, revealing heterogeneities between the bacterial clusters and the void spaces (H. Cao et al., 2016). Recently *P. fluorescens* was used in a co-culture experiment with *Bacillus licheniformis* and the rheology of singular and mixed agar grown biofilms was compared. *P. fluorescens* was seen to dominate the co-culture population, and the resulting mechanical properties of the biofilm tended towards the properties of monoculture *P. fluorescens* (Abriat et al., 2019).

Pseudomonas fluorescens was selected as the model species for the experiments in chapter 1 due to the notable effect of chemical treatments on a bacterium found in the same genus *Pseudomonas aeruginosa*. *Pseudomonas fluorescens* was selected as a strain which was anticipated to respond to treatments with divalent cations and urea. I wanted to demonstrate the applicability of LAOS rheological techniques in characterising biofilm and detecting changes (in this case chemical composition) to

the biofilm microstructure. *Pseudomonas fluorescens* is also a soil dwelling strain which may encounter elevated concentrations of $CaCl_2$ and $FeCl_2$ and urea. However, the concentrations used within this chapter were increased beyond what would be expected to be found in nature. This was done to maximise the putative effect on the biofilm rheology. This is a commonly used method for chemical treatment studies on biofilm, as will be discussed in the chapter introduction.

2.8.2 *Pantoea sp.*

Pantoea sp. YR343 is a rod shaped, gram negative, motile bacterium, originally isolated from the rhiziosphere of *Populus deltoides* (Bible et al., 2016). *Pantoea* sp. YR343 is a nonpathogenic root and a plant leaf coloniser. It can promote plant growth through the biosynthesis of indole 3 acetic acid (IAA). IAA synthesis also results in the upregulation of EPS substances. When grown under flow, *Pantoea* sp. YR343 forms compact multicellular structures which can cause blockages in complex porous geometries (Aufrecht et al., 2019). *Pantoea* YR343 UDP is a deletion mutant of YR343 which is defective in EPS biosynthesis of amylovoran and stewartin, and forms linked cellular structures in flow (Aufrecht et al., 2019). Stewartin and amylovoran are both anionic polysaccharides; composed of glucose, galactose and gluconic acid (Bellemann et al., 1994). Functional divergence between the two is thought to have occurred at a protein level (Carlier et al., 2009). UDP is a gene that is also found in both *Pantoea stewartin* and *Pantoea amylovran*. *Pantoea stewartii* and *Erwinia amylovora* are known to agglomerate into structures known as symplasmata (Tecon & Leveau, 2016; Jing Yang et al., 2017)

Symplasmata clusters form from single cells and grow to contain several hundred densely aggregated cells, independent of the adhering surfaces, differentiating this phenotype from a biofilm (Cindy & Jean-Michel, 2003). This phenotype can be comparable to autoaggregation which occurs in a variety of different bacteria such as *Escherichia. coli* and *Staphylococcus aureus.* Autoaggregation is typically mediated by EPS surface molecules called autoagglutinins (Trunk et al., 2018). Autoagglutinins are a broad term encompassing surface proteins, eDNA and exopolysaachrides which promote aggregation and flocculation. Symplasmata formation has been postulated to be a protective mode of bacterial growth formed in response to environmental conditions, such as limited carbon sources and low pH. Typical characteristics of symplasmata clusters include dense cell-cell packing, a reduced

metabolic rate and oxygen level, and a reduction in transmembrane protein expression (Achouak et al., 1994; Feng et al., 2003; Yu et al., 2016). Various genes linked with uptake or degradation of carbon sources and phase variation have been linked to symplasmata (Duan et al., 2007; Jing Yang et al., 2017). In *P. agglomerans* symplasmata formation is linked to the LysR – type transcription regulator *lrhA*. The IrhA (*L*ysRhomologue A) protein controls flagella motility and has been linked to regulation of EPS production in *Pantoea alhagi*. Symplasmata formation has been shown to be dependent upon c-di-GMP in *Erwinia amylovora* (Edmunds et al., 2013; Jiang et al., 2015). An omnipresent feature of symplasmata is the production of extracellular capsular polysaccharides (CPS) commonly associated with adhesion, biofilm proliferation and virulence towards plants (Minogue et al., 2002).

Pantoea sp. YR343 was selected for experimentation to look into the effect of EPS secretion on biofilm rheology and microstructure due to the large difference in EPS production between the wild type and selected UDP mutant, which has a reduced production of amylovoran, a capsular polysaccharide (details of mutation found 4.2.1). *Pantoea* sp. YR343 is also a plant root colonizer which is a plant growth promoting rhizobacteria (PGPR). A comprehensive understanding the rheology of *Pantoea* sp. YR343 may help to inform understanding of how soil networks are affected by inclusion of *Pantoea* sp. YR343.

2.8.3 *Neisseria polysaccharea*

Neisseria polysaccharea is a diplococcus, gram negative bacterium closely related to *Neisseria meningitidis*, and was originally isolated from the throats of healthy children from Europe and Africa (J. Y. Riou et al., 1983). The EPS of *N. polysaccharea* is known to be composed of NpAS (*Neisseria polysaccharea* amylosucrase), which can synthesis an amylosucrose type polymer at high sucrose concentration (Daudé et al., 2013; Potocki de Montalk et al., 2000). This exopolysaccharide is produced in copious amounts in the presence of sucrose on agar plates and is composed of D-glucose (J.-Y. Riou et al., 1986). This bacterium was selected for comparison against *P. fluorescens*, *Streptococcus epidermidis* and *Comamonas denitrificans* due to its diplococcus shape and predominant polysaccharide EPS matrix.

2.8.4 *Staphylococcus epidermidis*

Staphylococcus epidermidis is a cocci, gram positive bacterium which is commonly found on the human skin and in infections associated with contaminated medical equipment, such as catheters (Otto & Silhavy, 2002). The EPS of *S. epidermidis* is

mainly comprised of PIA (Polysaccharide intercellular adhesion) a 210 kDa polysaccharide composed of repeating units of N- acetylglucosamine (chitosan) which is deposited on the cell wall surface (Cramton et al., 1999; M Ganesan et al., 2013). The network structure of PIA in *S. epidermidis* is thought to be predominantly structured through associative mechanisms of PIA, as opposed to entanglements (M Ganesan et al., 2013). The EPS of *S. epidermidis* also I known to be composed of a large repeat surface protein and surface adhesion protein Bap (Biofilm associated protein), which is a predominant component found in *S. epidermidis* biofilms isolated from human infections (Piessens et al., 2012). Certain strains of *S. epidermidis* are known to have large quantities of Embp (Extracellular matrix binding protein) a 1 MDa protein which promotes intercellular bonding and binds to the EPS matrix (Christner et al., 2010). The viscoelasticity of *S. epidermidis* has been shown to vary depending upon NaCl concentration; 86 and 135 mM NaCl results in increases to the elastic and viscous moduli, whereas at high concentrations of 770 mM the moduli decrease by an order of magnitude (Pavlovsky et al., 2013). The cause of this rheological change is possibly explained by a separate experiment on *S. epidermidis*, which used identical concentrations of NaCl, but focused upon microstructural changes. Here local number density was used to identify distinct density structural phenotypes. It was found that increasing NaCl resulted in lower packing fractions. Interestingly the presence of vancomycin also resulted in a lower packing fraction (Mahesh Ganesan et al., 2016; Stewart et al., 2015). *S. epidermidis* has been used to test the hypothesis that biofilms behave and self-assembly like a colloidal polymer gels. In this experiment *S. epidermidis* biofilms were compared with cultures of *S. epidermidis* mixed with isolated PIA and a colloids - PIA mixture. The resulting colloidal – PIA gel had a comparable microstructure and rheology to the *S. epidermidis* biofilm. The rate of self-assembly of the colloid - PIA and *S. epidermidis* biofilm was controlled by pH (Stewart et al., 2015).

S. epidermidis was selected for comparison against *P. fluorescens*, *Neisseria polysaccharea* and *Comamonas denitrificans* due to its commonality with *P. fluorescens* in having a major EPS component as a large repeat surface protein. Also since *S. epidermidis* is a cocci strain it would be a suitable analogue to a sphere colloidal gel system, which have an extensive literature regarding LAOS behavior. This characteristic would provide a way of accessing how the cocci shape influences breakdown in comparison to the rod-shaped strains. It was also selected due to the

known presence of intracellular adhesins within its EPS matrix, which were expected to contribute to short range bonding.

2.8.5 *Comamonas denitrificans*

Comamonas denitrificans is a rod shaped, gram negative bacterium originally isolated from activated sludge and commonly used as a biomarker for denitrification in wastewater treatment plates due to its efficient denitrifying activity (Andersson et al., 2008). *C. denitrificans* is a motile bacterium with a polar flagellum which forms filamentous chains in liquid culture (Gumaelius et al., 2001). The EPS of *C. denitrificans* is composed of proteins, polysaccharides and has a high content of eDNA. A thick layer of polysaccharide is produced around cell chains when grown in liquid, and the polysaccharide fraction is mainly composed of glucose and mannose (Andersson et al., 2009). *C. denitrificans* is also known to be a dominant exoelectrogenic bacterium (Xing et al., 2010) and have been detected as an anode populating bacterium in a constructed wetland microbial fuel cell system (F. Xu et al., 2019). This bacterium was selected for experimentation due to its filamentous growth, which I hypothesized would involve a short-range bonding. This contrasted with the other selected strains which were not filamentous. Additionally, it was selected due to its increasingly apparent industrial relevance in wastewater systems and application within microbial fuel cells.

Chapter 3 Rheology of *P. fluorescens* in different chemical environments

3.1 Introduction

Biofilms are a communal form of bacterial growth, which attach to and colonise aqueous surfaces (Flemming & Wingender, 2010). A defining feature of biofilm proliferation is the production of self-secreted extracellular polymeric substances (EPS), which confer the encapsulated bacteria protection from external challenges and determine biofilm architecture (Hobley et al., 2015). EPS is composed of polysaccharides, eDNA, lipids and a multitude of proteins. The EPS/bacterial composite material is a heterogeneous non equilibrium system, where structural properties evolve with time and in response to environmental conditions (Nadell et al., 2016). The dynamic combination of phenotypic responses and physicochemical interactions within the EPS results in large inter and intra species structural variability. The spatial organisation of biofilm contributes to specific biological functions, such as protection from bacteriophage attack and antibiotic challenges (Vidakovic et al., 2018). It has also been hypothesised that biofilms adapt the EPS composition to their local environment to improve mechanical resistance to removal (Kovach et al., 2017). It is therefore important to understand how EPS composition and the chemical environment influence the microstructure and mechanics of biofilms.

Biofilms characteristically exhibit viscoelastic mechanical behaviour, a time dependent response to applied stresses. Viscoelastic behaviour confers mechanical benefits to biofilm, such as resistance to erosion and the formation of complex structures, such as streamers (Kundukad et al., 2016). Due to the species - species variation in EPS matrix composition biofilms form a wide array of structures with different mechanical characteristics. These characteristics are also influenced by environmental physiochemical conditions. Microfluidic grown biofilms are highly hydrated, while biofilms grown at the liquid/air interface result in highly packed structures. Biofilms typically have viscoelastic properties akin to frustrated state materials like glasses or gels. Self- assembly of these frustrated states within a biofilm features numerous physicochemical interactions. EPS structure is determined by the secretion of species dependent polymers and physicochemical interactions between polymer chains, such as branching, crosslinking, protein aggregation and folding. While interparticle interactions are mediated by ionic concentration, hydrogen bonding, van de Waals forces and cell-cell mechanical interactions (Jing Yan et al., 2019).

Biofilms grow in diverse chemical environments. In natural environments, such as pipe systems, chemicals such as iron and calcium may be found in high concentrations. In environments where biofilm formation has damaging consequences, exogenous addition of metal salts can be used to disrupt the biofilm structure. Therefore, it is important to understand how metal salts modify biofilm rheology. Both Fe and Ca ions can be commonly found in the biofilms from different environments (Das et al., 2014). The presence of metal ions within polymer solutions can cause ionic crosslinking between the polymer chains within polymer networks resulting in altered mechanical properties (Mccoy & Muthukumar, 2010). In *B. subtilis* metal ions Fe^{2+} and Cu^{2+} have a fortification effect, due to effective crosslinking, resulting in increased elasticity (Grumbein et al., 2014). Typically, rheological studies investigating the effects of ion salts on biofilm viscoelasticity use higher molar concentrations than typically found in nature in order to maximise the putative effect on rheology. Studies applying chemical treatment using a 30-60 minutes soak in the selected metal ions have ranged between 50 mM up to 1 M in *B. subtilis* (Grumbein et al., 2016; Klotz et al., 2019). Metal ion studies on *P. aeruginosa* and *S. epidermidis* used a concentration of 0.2 M for a soak of 60 minutes (Jones et al., 2011), whilst a similar study on *P. aeruginosa* used concentrations ranging from 50 mM to 250 mM for a 60 minutes soak (Lieleg et al., 2011). A concentration of 0.25 M was used for various divalent cations for a 300 minutes soak of *Azotobacter vinelandii* (Kretschmer & Lieleg, 2020a).

Urea is an organic compound and known ‘chaotropic agent’ used in the treatment of biofilm and known to effect electrostatic interactions within polymer solutions through disruption of hydrogen bonds. Urea reduces the quality of water as a solvent reducing the solubility of polymer in water. *S. epidermidis* and *P. aeruginosa* biofilms have both been shown to weaken when treated with urea (Brindle et al., 2011). The treatment of flow cell grown *S. epidermidis* with 0.5 M urea was shown to cause swelling of 53% and an increase in compliance which coincided with significant biofilm removal. However, the effect of urea treatment on the rheology of *P. fluorescens* biofilm is presently unknown.

Viscoelastic behaviour can be decomposed into two regions, the linear viscoelastic region (LVER) and the non-linear region. Measurements in the linear region quantify the quiescent structure of a system, whilst in the nonlinear region the elastic and viscous properties of a material are a function of the applied strain. Typically, biofilms

are measured within the LVER however in the real-world biofilms experience large shear forces, in which a biofilm will deform within the nonlinear regime. Therefore, to understand this understudied rheological regime I propose to use large amplitude oscillatory shear (LAOS).

Large amplitude oscillatory shear (LAOS) tests investigate the non-linear viscoelastic behaviour of soft materials. Three main analytical techniques are used with LAOS data, each approach; Fourier transform rheology, Chebychev analysis and the series of physical processes (SPP) quantifies the nonlinear viscoelastic response at different temporal scales within an oscillatory cycle. These respective approaches can be categorised as; intercycle, intracycle and instantaneous methods of analysing oscillatory shear data recorded by a rheometer. LAOS tests have been performed on various colloidal, gel and polymer melt systems to investigate structure - property relationship. Experiments using model materials mediate viscoelastic response and material microstructure by varying physicochemical parameters such as ionic concentration and packing fraction (Juntae et al., 2014; Kim et al., 2014). Adopting a similar parametric approach for biofilms may help to improve the interpretation of biofilm rheological studies. This may enable researchers to answer questions regarding the range and strength of mechanical interactions within biofilms as well as introducing an improved technique over conventional methods to access how chemical treatments, polymer expression and environmental conditions effect biofilm nonlinear viscoelastic behaviour.

In this chapter I establish protocols designed to investigate the non-linear viscoelastic behaviour of biofilm using a model bacterium, *P. fluorescens*. I employed several LAOS analytical methods to explain how the non-linear rheology of *P. fluorescens* biofilms is affected by treatment with different chemical compounds. The chemical concentrations used in this chapter are typically greater than seen in nature. This was a conscious decision used to increase the putative effect of the chemical treatment on the biofilm rheology as a proof of concept of applicability of LAOS techniques.

3.2 Materials and Methods

3.2.1 Bacterial culture and sample collection

P. fluorescens (Migula 1895) was grown overnight in LB broth (Lennox, Sigma) from glycerol stocks at 24 ^{o}C with shaking (150 rpm). Overnight cultures of *P. fluorescens* (250 µL) was spread onto 1.5 % nutrient broth (24 g/L) agar plates with an L-shaped

spreader. The cultured agar plates were then incubated at 24 ^{o}C for 3 days. Before rheological characterisation, biofilms were incubated with 2 ml of 100 mM of $FeCl_2$, $CaCl_2$, urea or DDH_2O for 60 mins. A concentration of 100mM was selected to maximise the putative effect on biofilm rheology. The biofilm incubated with 2 ml DDH_2O was considered the control sample. After 60 mins the supernatant was discarded and the was biofilm left for 15 mins before testing. Biofilm was collected from the agar plates by scraping with a ground edge microscope slide. Biofilm was collected from 3 plates and transferred to the rheometer. Approximately 0.3 ml of biofilm was used for each test.

3.2.2 Linear rheological measurement

Rheological measurements were performed using a rheometer (Malvern Kinexus Pro+,UK) mounted on a passive isolation plate. The rheometer was operated in a strain-controlled mode. A 20 mm parallel plate geometry was used for all tests. To minimise slip between the biofilm and the parallel plates, 120 grade waterproof grit paper was attached to both the top and bottom plates. Biofilms were tested using a gap height of 0.8-1.2 mm. Each sample was trimmed using a razor blade and the gap height was adjusted to a normal force of 0.1 N. To prevent desiccation during measurements a solvent trap was used. The temperature of the biofilm was maintained at 25 ^{o}C using a Peltier plate which was built into the lower plate. Frequency sweeps were performed from 0.1 Hz to 50 Hz at a strain amplitude (γ) of 1 %.

3.2.3 Non-linear rheological measurement

Samples were transferred to the rheometer as previously described and left to relax for 5 minutes. Strain controlled LAOS measurements where performed for 24 strain γ amplitudes logarithmically spaced between 0.1 % and 250 %. All LAOS measurements were performed at 1 Hz. Raw data for the time, the angular displacement and the torque were sampled. For each strain 17 oscillatory cycles were sampled to ensure steady state oscillations.The raw data was processed using a custom matlab routine, found in appendix A. The Chebychev analysis was performed using a matlab routine MITlaos, kindly provided by Prof Randy Ewoldt. For each chemical treatment at least 3 biological replicate measurements were performed to ensure the trends sampled were reproducible.

3.2.4 CLSM of chemically treated *P. fluorescens* biofilm

After respective treatments, biofilm samples were stained *in situ* with 10 µM Syto63 (Sigma, UK), a cell permeable DNA stain and incubated for 30 minutes. After incubation biofilms were transferred from the agar surface to a 25 µL geneframe (Sigma, UK) via scraping. The geneframe was sealed with a #1.5 coverslip. Imaging was performed using a Leica SP8 confocal laser scanning microscopy (CLSM). Syto 63 was excited at a wavelength of 660 nm and an emission filter was set at 670-750 nm. A 100x oil immersion objective N/A 1.4 was used to image each biofilm. Random fields of view (FOV) were selected for each treatment with a window size 101 µm x101 µm. The pinhole was set at 1 airy units (AU). A total of n = 5 FOV were taken for each treatment. An Image J and MATlab code was written for image analysis, which are found in appendix B and C. Images were pre-processed by first applying a contrast limited adaptive histogram equalization (CLAHE) filter with a box size of 127 for denoising and contract enhancement. The image was then further smoothed using a Gaussian filter of radius 2. Then a Mexican hat filter of radius 3 was applied to each image and result was thresholded using an Otsu threshold. Mexican hat filtering, otherwise known as Laplacian of Gaussian filter (LoG), is a second derivative filter used to filter areas of rapid change (Sotak & Boyer, 1989). This method enables clear localisation of sharp edges and was the parameter with the highest sensitivity effecting the packing fraction. Mexican hat kernel sizes of pixel radius 2, 3 and 4 were compared. A radius of 4 resulted in an over estimation of packing fraction, as $\phi > 0.68$, above the random packing limit for rods with an aspect ratio over 3 (Kyrylyuk et al., 2009). The kernel size was set at 3, as this had substantially less noise than a kernel size of 2. To account for the cell membrane after thresholding was completed a dilation step was performed, which corresponded to an increase in cell width and cell length of 0.2 µm (Drescher et al., 2016). A comparison of the different imaging parameters tested can be found in appendix D. The packing fraction was then calculated as the ratio of cells to void space.

3.3 Results

3.3.1 Microstructure analysis

To compare the effects of DDH_2O, $CaCl_2$, $FeCl_2$ and Urea on the microstructure of *P. fluorescens,* CLSM images were taken of each biofilm after each respective chemical treatment as shown in *Figure 3-1*. To quantify the fraction of space filled by bacteria I calculated the packing fraction ϕ, *Figure 3-2*. The packing fraction of chemically treated *P. fluorescens* biofilms ranged between 0.46 - 0.63. Urea had the lowest packing fraction of 0.48 ± 0.03, its microstructure featured regions of void space which surrounded dense clusters of bacteria. DDH_2O had a packing fraction of 0.55 ± 0.03, its microstructure featured small regions of void space within a continuous mat of bacteria. $CaCl_2$ and $FeCl_2$ had respective packing fractions of 0.58 ± 0.03 and 0.61

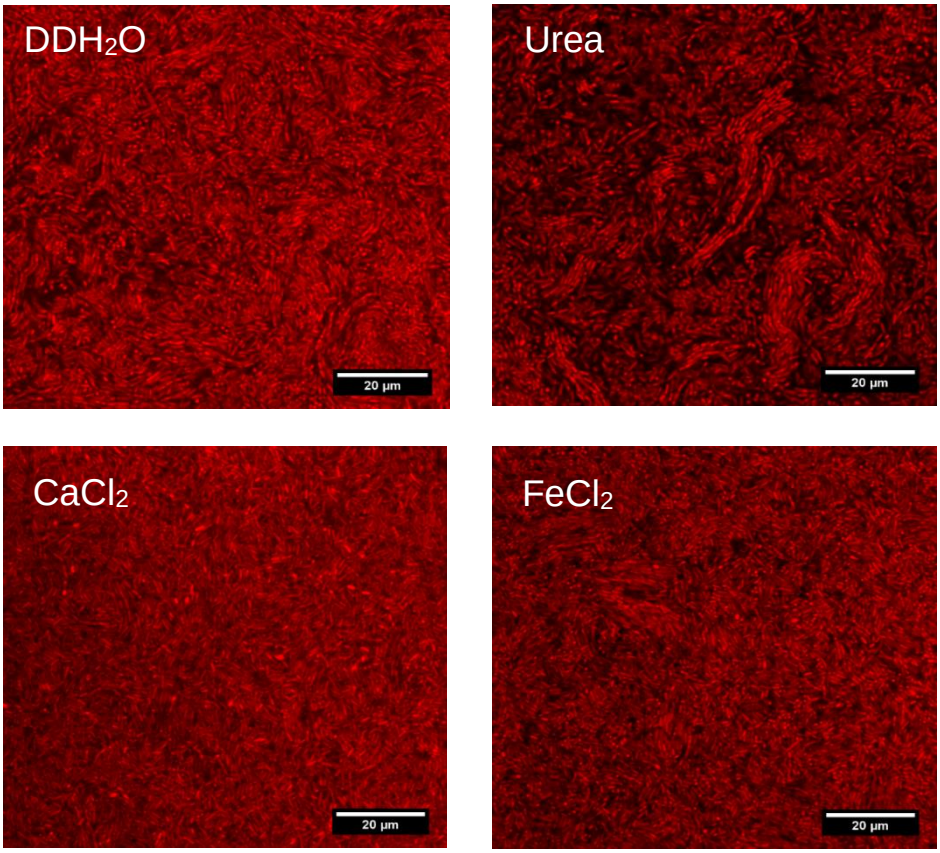

Figure 3-1: Representative CLSM images of a single slice of *P. fluorescens* after 60 mins chemical treatment. Slices were taken 10 μm above the coverslip. Urea treated *P. fluorescens* displayed a structure which appeared to exhibit increased void regions in comparison to $CaCl_2$ and $FeCl_2$. The differences between cation treatments $CaCl_2$ and $FeCl_2$ appeared minimal.

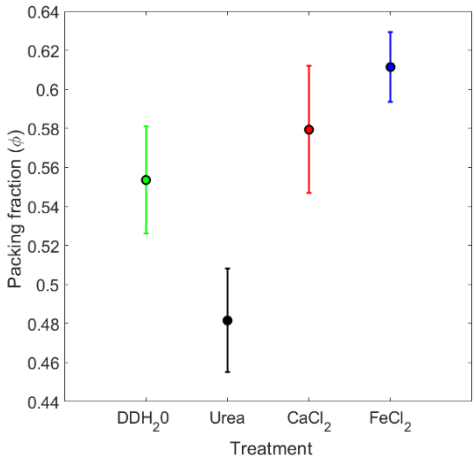

Figure 3-2: Packing fraction calculated from CLSM z slices for each chemically treated *P. fluorescens* biofilm, cells were stained with cell permeable DNA stain Syto 63. Error bars represent the standard deviation (n=3).

± 0.02. Both microstructures appeared absent of noticeable voids. The phase regime of colloidal rod packings depends on two main microstructural parameters, the packing fraction ϕ and the aspect ratio of *P. fluorescens* r. The average aspect ratio of *P. fluorescens* taken from CLSM images was r = 5.5± 0.4. Using a rod phase diagram constructed by Solomon the microstructure of each treated *P. fluorescens* can be categorised (Solomon & Spicer, 2010). Here the maximum packing limit for rods can be calculated using $\phi_{max} \approx \frac{5.4}{r}$ and the minimum percolation volume fraction for glasses is $\phi_{glass} = \frac{0.7}{r}$. This results in packing fraction bounds of $0.124 < \phi < 0.982$ for which *P. fluorescens* cellular packing can be considered in the rod glass regime. This relation provided by Soloman neglects the presence of an EPS matrix, however it provides context for the cellular packing regime. In a glassy regime each particle is constricted in its movement by its nearest neighbours', phenomenologically known as a cage. Energy is stored and dissipated through rearrangement of the phenomenological cages. High packing fractions ϕ reduce cage size leading to construction and reduced inner cage particle mobility. However, the presence of an interstitial EPS matrix between the *P. fluorescens* cells composed of major structural EPS components LapA and alginate increases the complexity of these cage interactions. In the presence of a polymeric matrix cage constriction will also be influenced by the EPS mediated intercellular bonding forces, which are mediated by the polymeric components.

3.3.2 Frequency sweeps of the chemically treated *P. fluorescens* biofilms

To measure the effect of each treatment on the viscoelastic properties of *P. fluorescens* biofilms linear and non-linear rheology measurements are performed. Each treatment will be compared to DDH_2O treated *P. fluorescens*, which will act as a control. To access the frequency dependence of each treated biofilm frequency sweeps are performed at a strain of 1%, *Figure 3-3*. The control treatment with DDH_2O had a G' equal to 582$\pm$ 54 Pa. Treatment with divalent cations $CaCl_2$ and $FeCl_2$ resulted in a strengthening effect with G' increasing to 1107$\pm$ 186 Pa and 1641$\pm$ 129 Pa respectively at ω = 0.1 Hz. The urea treatment resulted in softening effect, reducing G' to 248.2$\pm$ 48 Pa. For each treatment G' exhibited negligible frequency dependence, known as plateau behaviour. Plateau behaviour is indicative of an elastically dominant response ($G' > G''$) and is a typical characteristic of soft glassy gels and dense suspensions. However, for DDH_2O and urea treatments the viscous moduli G'' displayed a frequency dependence. For the control treatment G'' increased from 58$\pm$ 5 Pa to 90.96$\pm$ 8 Pa between ω = 10 – 50 Hz, while the urea treatment resulted in an increase from 34$\pm$ 4 Pa to 53.92$\pm$ 6 Pa. The increase in G'' at higher frequencies indicates the EPS network of DDH_2O and urea had longer time scale response in comparison to $FeCl_2$ and $CaCl_2$. Similar increased frequency dependence is known to occur in hydrogels with a reduced polymer crosslinking density (Gil & Hudson, 2007). This may lead to an increase in the equilibrium swelling point of the biofilm and explain the increased dissipation from the solvent phase at high frequencies (Parmar et al., 2013; van der Sman, 2015). This behaviour was

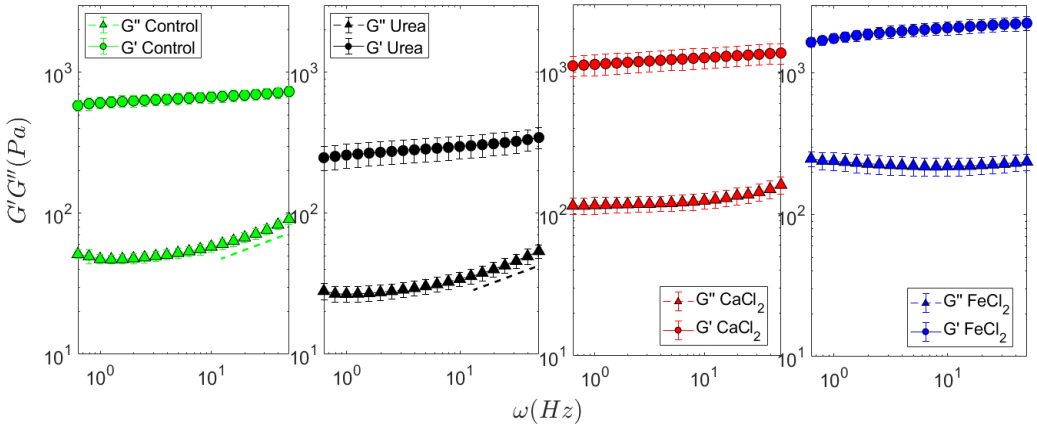

Figure 3-3: Frequency sweeps of chemically treated *P. fluorescens* biofilm. ω = 0.1 – 50 Hz and the strain γ =1 %. Circular symbols represent the elastic moduli G', triangle symbols represent the viscous moduli G''. The dashed lines signify the frequency dependence of the control and urea biofilms. The mean of three biological replicates $\pm$ standard deviation is shown.

absent for divalent cation treatment with FeCl2, which resulted in a G'' curve which exhibited a minimum at 6.28 Hz of 218$\pm$ 32 Pa. The presence of a G'' minimum is commonly seen in attractive glass/ gel systems suggesting that $FeCl_2$ addition strengthened the EPS network structure. The viscous modulus G'' minimum has been explained using mode coupling theory (MCT) for glassy colloidal systems near the glass transition point. The minimum emerges due to the transitioning of cage relaxation modes from α to β. β mode relaxation describes the diffusive motion of a particle within its surrounding cages and occurs over short times. α relaxation describes the particle escape from surrounding cages, which requires the coordination of several particle rearrangements, so occurs over longer times (Carrier & Petekidis, 2009). The results from these frequency sweeps suggest that urea treatment softens *P. fluorescens* biofilms by weakening the polymer EPS phase. The addition of $CaCl_2$ had a mild strengthening effect while $FeCl_2$ had a more noticeable strengthening effect. The minimum in G'' in $FeCl_2$ suggests the possibility that the strengthening effect of $FeCl_2$ originates from modification to the EPS structure, possible through ionic crosslinking with charged functional groups in the EPS matrix.

3.3.3 Chemically treated *P. fluorescens* biofilms display changes in yielding behaviour

To quantify the effect of each chemical treatment on the yielding behaviour of *P. fluorescens* biofilm amplitude sweeps were performed. An amplitude sweep measures the viscoelastic response to increasing strains and captures the yielding behaviour. Amplitude sweeps started in the LVER (γ < 1 %) through to the nonlinear

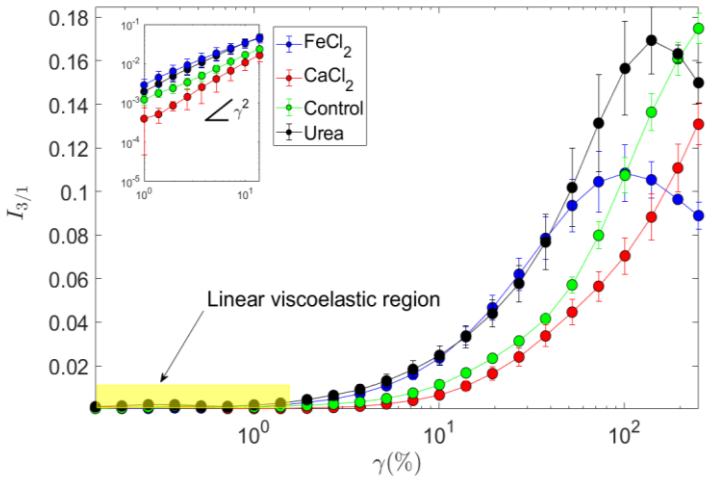

Figure 3-4: Nonlinear parameter ratio of third harmonic to the first. γ represents strain. The yellow box denotes the linear viscoelastic region. Inset, is a log-log plot showing the MAOS region which fell between γ =1 % and 10 %. The results shown are the mean $\pm$ standard deviation.

LAOS region (γ < 250 %). The nonlinear parameter $I_{\frac{3}{1}}$ is used as a quantitative method for identifying the transition from linear to non- linear behaviour, *Figure 3-4*. $I_{\frac{3}{1}}$ is used in combination with amplitude sweep measurements to determine the Linear viscoelastic region (LVER) and the medium amplitude oscillatory shear region (MAOS). The LVER probes the quiescent structure of each biofilm. In this region there is minimal structural rearrangement, and G' and G'' are independent of strain. A lack of structural rearrangement means the Fourier transform of the stress signal is dominated by the fundamental harmonic and $I_{\frac{3}{1}}$ is small. The MAOS region in ideal polymer melts is identified from $I_{\frac{3}{1}}$ plots by the near quadratic increase of $I_{\frac{3}{1}}$ with strain above the noise floor of the rheometer. The onset of nonlinearity begun at 0.5 %, 1.39 %, 1.92 % and 1.92 % for $FeCl_2$, DDH_2O, $CaCl_2$ and urea respectively. $I_{\frac{3}{1}}$ initially increased fastest in urea and $FeCl_2$ samples. $FeCl_2$ peaked at 0.11$\pm$ 0.01 at γ = 100% and urea peaked at 0.17$\pm$ 0.02 at γ = 140%. The drop after the peak in $I_{\frac{3}{1}}$ is due to the increase of harmonics higher than I_3. This can be attributed to fluidisation. At the point of fluidisation the non-linearities reduce as the stress response is dominated by liquidlike behaviour (Craciun et al., 2003). Amplitude sweeps enable the identification of the crossover strain γ_C ($G' = G''$). The cross over strain is the point where the biofilm viscoelasticity becomes viscously dominated. DDH_2O and urea biofilms had a γ_C of ~80 % and ~72 %, *Figure 3-5.* $FeCl_2$ and $CaCl_2$ had a γ_C of

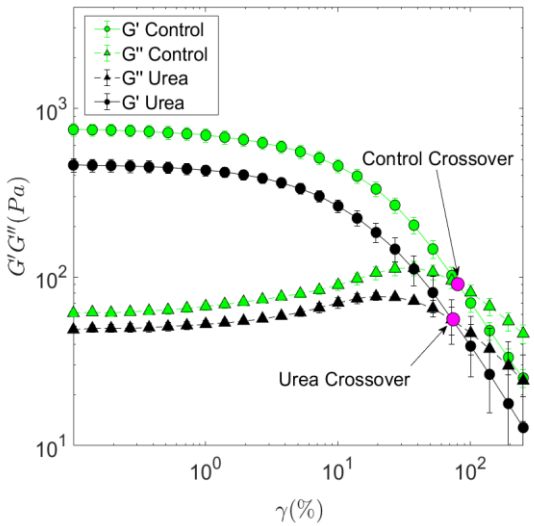

Figure 3-5: Amplitude sweeps of DDH2O and Urea treated *P. fluorescens* biofilm, ω = 1 Hz, γ = 0-250 %. The pink dots represent the yielding (crossover) point γ_C of the biofilm where $G' > G''$. Both the Control and Urea treated biofilms exhibit a viscous overshoot before the crossover point. The mean of three biological replicates $\pm$ standard deviation is shown.

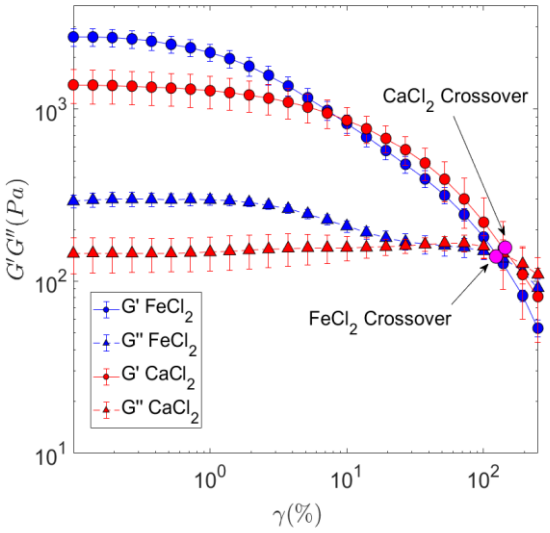

Figure 3-6: Amplitude sweeps of $FeCl_2$ and $CaCl_2$ treated *P. fluorescens* biofilm, ω = 1 Hz, γ = 0-250 %. The pink dots represent the yielding (crossover) point γ_C of the biofilm where $G' > G''$. The $CaCl_2$ treated biofilm didn't display an obvious stress overshoot before the crossover point. Treatment with $FeCl_2$ resulted in an increased strengthening effect in comparison to $CaCl_2$. The $FeCl_2$ treatment caused the viscous moduli to drop before the crossover point. The mean of three biological replicates $\pm$ standard deviation is shown.

~120 % and ~140 %, *Figure 3-6*. Each treatment exhibited the power law decrease after the cross over strain was exceeded, *Table 3-1*. The shear thinning response of the elastic and viscous modulus is theoretically known to exhibit a power law dependence on the strain of $G' \sim \gamma^{-2n}$ and $G'' \sim \gamma^{-n}$, where n is the power law gradient . This occurs with Maxwell type models and has also been seen

	n'	n''	$\frac{n'}{n''}$
DDH_2	-1.10$\pm$ 0.11	-0.63$\pm$ 0.02	1.75$\pm$ 0.08
Urea	-1.23$\pm$ 0.09	-0.73$\pm$ 0.11	1.68$\pm$ 0.22
$CaCl_2$	-1.10$\pm$ 0.02	-0.54$\pm$ 0.03	2.27$\pm$ 0.05
$FeCl_2$	-1.41$\pm$ 0.06	-0.64$\pm$ 0.04	2.28$\pm$ 0.09

Table 3-1: Power Law exponents for each chemically treated biofilm, n' is the elastic power law exponent and n' is the viscous power law exponent after the cross over strain γ_C. Measurements are presented as an average $\pm$ standard deviation from three biological replicates.

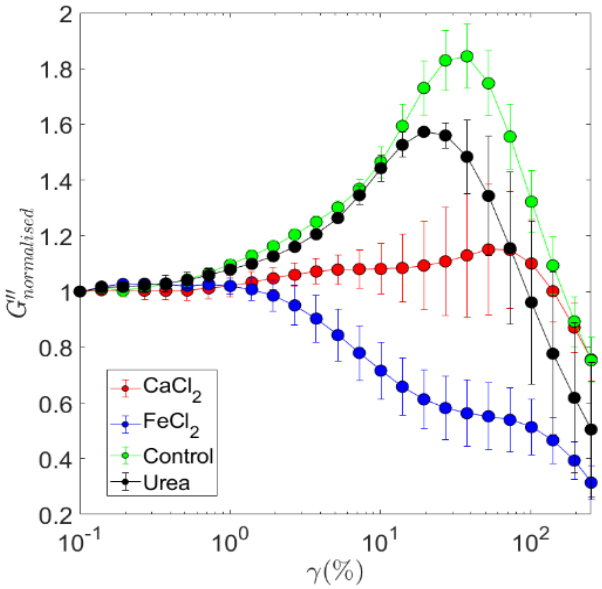

Figure 3-7: Plot of Viscous moduli G'' normalised by G'' from the linear viscoelastic region. Treatment with urea resulted in a reduced viscous overshoot in comparison to the control, the stress overshoot peak also occurred at a lower strain. Treatment with divalent cations eliminated the viscous stress overshoot behaviour. Treatment with $FeCl_2$ resulted in the appearance of a shouldered decrease in G''. $CaCl_2$ treated *P. fluorescens* biofilms exhibited behaviour intermediate to the control and $FeCl_2$ treatments. The mean of three biological replicates $\pm$ standard deviation is shown.

experimentally in a range of soft glassy materials (Hyun et al., 2003). DDH_2O and urea treatments resulted in an exponent ratio $\frac{n'}{n''}$ < 2. An exponent ratio below 2 has been demonstrated theoretically using Mode coupling theory (MCT) simulations (Poulos et al., 2013). Modifications to the dissipative behaviour of each treated biofilms were observed as the cross over strain was approached. Alterations in dissipative behaviour can be interpreted from shape of the viscous modulus G''. To clearly illustrate the alterations in G'' as a result of each treatment the viscous moduli G'' at each tested strain is normalized by the viscous moduli from the LVER G''_{LVER} to produce G''_{NORM} , *Figure 3-7*. Treatment with DDH_2O and urea resulted in similar dissipative behaviour, G''_{NORM} increased with strain and reached at peak of 1.84$\pm$ 0.11 and 1.57$\pm$ 0.02 at γ = 37.43 % and γ = 19.37 % respectively for DDH_2O and urea. This behaviour is characteristic of the type III class of viscoelastic material. Type III viscoelastic materials feature weak strain overshoots (Voigtmann, 2014), *Figure 3-8*. The increase in G''_{NORM} for this type of material occurs as the microstructure and polymeric network initially resists flow. At a critical strain the bonds within the polymeric matrix yield and the colloidal filler particles align with the

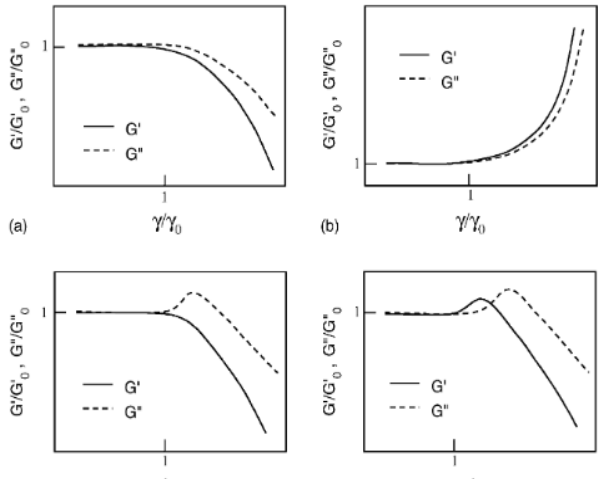

Figure 3-8: Four types of yielding featured in soft materials. (a) Type I - Strain thinning, (b) Type II - Strain hardening, (c) Type III - Weak strain overshoot, and (d) Type IV - strong strain overshoot. G' is the elastic moduli and G'' is the viscous moduli. G'_0 is the linear viscoelastic elastic moduli and G''_0 is the linear viscoelastic viscous moduli. $\frac{\gamma}{\gamma_0}$ is imposed strain γ normalised by the lowest imposed strain γ_0 in the strain sweep. This figure was adapted from (Hyun et al., 2002).

flow direction and resulting in thinning (Vaart et al., 2013). Type III behaviour is commonly seen in a multitude of repulsive glassy gel systems, such as hard sphere suspensions, colloidal polymer gels, polymer melts and hydrogels (Koumakis et al., 2012; J. D. Park et al., 2016; Zuidema et al., 2014). Type III yielding has been seen in several different biofilm species, such as rod-shaped *V. cholerae*, *B. subtilis* and *P. aeruginosa* (Huang et al., 2019; Kovach et al., 2017; Jing Yan et al., 2018). The difference in magnitude of G''_{NORM} between DDH_2O and urea is reflective of the reduced resistance to alignment in the flow of the urea treated biofilm structure in comparison to DDH_2O treatment. $FeCl_2$ treatment resulted in a structural modification distinct from urea and DDH_2O. G''_{NORM} exhibited a shoulder drop which begun at γ = 1 % and plateaued at γ = 37 % with a G''_{NORM} value of 0.56 ± 0.12, before decreasing again at γ = 72 %. This type of dissipative behaviour is reminiscent of an attractive gel/glass system (AG). Attractive glasses are materials which have microstructures mediated by short range interparticle interactions. AG materials characteristically exhibit two distinct yielding regimes, known as two step yielding. The characteristic curve of an attractive glass features a two-step decrease in G', and a shouldered decrease in G''. Phenomenologically the two-step yielding process is separated into two relaxation mechanisms. The first step is known as α relaxation and is attributed to a reduction in bond rigidity and breakup of the large structure into clusters. The second step is known as β relaxation, here the clusters formed in the first step begin to breakdown. Experimenters commonly induce two-step yielding in

colloidal glasses/gels by increasing the solvent ionic concentration to screen electrostatic repulsion. AG's have been studied experimentally using PMMA colloids, silica nanoparticles, deformable microgels and in surfactant suspension pastes (Ewoldt et al., 2010; Shukla et al., 2015; H. Zhang et al., 2016; Zhou et al., 2014). The G''_{NORM} curve for $CaCl_2$ displayed a reduced stress overshoot in comparison to DDH_2O and urea peaking at 1.15 ± 0.23. However, $CaCl_2$ didn't result in the distinct two step yielding seen due to addition of $FeCl_2$.

3.3.4 Chemical treatments cause a transition to both nonlinear thickening and softening behaviours

To visualise the transition from linear to non-linear behaviour, representative elastic (σ vs γ) and viscous (σ vs $\dot{\gamma}$) Lissajous – Bowditch plots (LB) are presented in *Figure 3-9*. Within the linear viscoelastic regime, the elastic LB curves are approximated by an ellipse. The ellipse shape indicates linear recoverable deformation. Here the LB plot reflects the fundamental harmonics G'_1 and G''_1 which are equivalent to the linear moduli G' and G'' in the LVER. As the imposed shear strain γ increases and enters the non-linear region the elastic LB plots deviate from an elliptical shape. The distortion from an ellipse is caused by the increased magnitude of higher Fourier harmonics. The enclosed area of the Lissajous loops increases with strain amplitude as the contribution of the higher energy storing harmonics increases. The enclosed Lissajous area represents the energy dissipation through each LAOS cycle (Kuczera et al., 2018). The shapes of the LB curves give a qualitative indication of the yield response of a material (Tao et al., 2019). Each of the chemically treated biofilms displayed elastic LB plots which became more rectangular at higher strains. The emergence of rectangular LB plots has been seeing in elastoplastic materials which have fully yielded (Ewoldt & McKinley, 2010). The viscous LB plots for DDH_2O and urea displayed self-intersections and secondary loops, *Figure 3-9d and Figure 3-9e*. Secondary loops occur due to stress overshoots, which can be described phenomenologically as when structural breakdown lags the instantaneous shear rate. Which is indicative of stress being dissipated at a faster rate than strain is accumulated (Armstrong et al., 2016). This results in simultaneous structural reformation and breakdown. The presence of secondary or "thixotrophic loops" are typically seen in materials exhibiting high nonlinearity. Secondary loops have been seen experimentally in thixotropic suspensions, food suspensions and micelles (Duvarci et al., 2017; Khandavalli et al., 2016; S. A. Rogers et al., 2011).

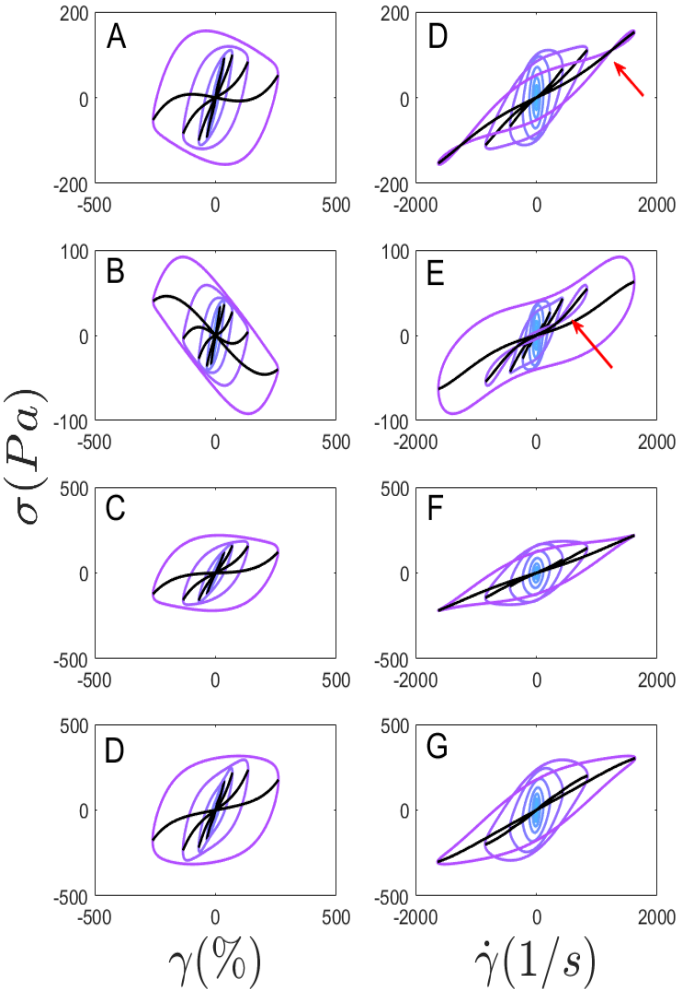

Figure 3-9: Lissajous Bowditch (LB) curves, showing strains from 0.1 to 250%.Left column: Elastic Lissajous curves, Right column viscous Lissajous curves. (A,D): Control, (B,E): urea, (C,F): $CaCl_2$, (D,G): $FeCl_2$. LB curves represent the strain, strain rate and stress behaviour of the chemically treated biofilms through a single period of oscillation. Colour from blue to purple represents low to high strain amplitude values. The shear strain values are represented by γ and the shear strain rate values are represented by $\dot{\gamma}$. Red arrows in D and E highlight the presence of secondary loops.

To obtain quantitative metrics from the LB plots the thickening ratio (T) [63] and the softening ratio (S) [62] are used. The thickening ratio represents viscous thickening/thinning and the stiffening ratio (S) represents elastic stiffening/softening. Within the LVER both T and S are expected to be zero, when $S > 0$ the material is strain softening. Each treatment exhibited strain rate softening behaviour which increased with increasing strain, *Figure 3-10*. Biofilms treated with DDH_2O and urea displayed rapid increases of S with DDH_2O biofilms peaking at $S = 2.95 \pm 1.25$ and urea treated biofilms peaking at $S = 3.7 \pm 1.9$. After the respective peaks, the S ratio for DDH_2O and urea both dropped below 0. The strain at which the S drop occurred

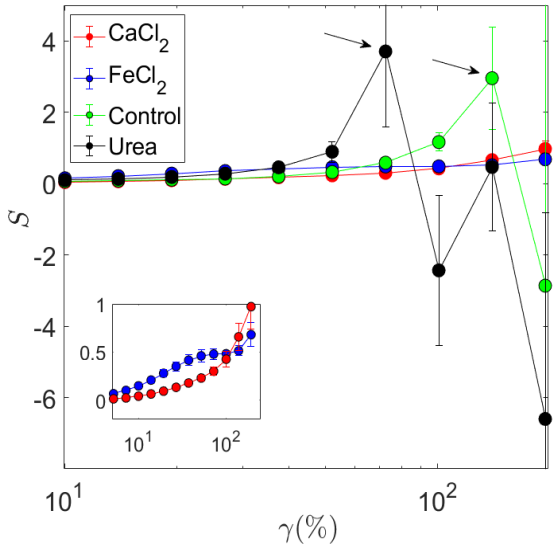

Figure 3-10: Stiffening ratio (S) for each chemically treated *P. fluorescens* biofilm. $S < 0$ denotes shear softening, $S > 0$ denotes shear stiffening. Inset plot focuses upon $CaCl_2$ and $FeCl_2$ stiffening. The black arrows represent the intracycle averaged yielding point of the urea treated and control biofilms. The mean of three biological replicates $\pm$ standard deviation is shown.

were 139 % and 72.5 % respectively which matched the strains at which LB secondary loops emerged. The drop in S could therefore be interpreted as the point of elastic stress overshoot for DDH_2O and urea biofilms. The S ratio for $CaCl_2$ and $FeCl_2$ treatments peaked at 0.97$\pm$ 0.23 and 0.68$\pm$ 0.12 respectively. The S ratio for $FeCl_2$ featured a plateau in S of 0.46$\pm$ 0.09, *Figure 3-10 inset*. This indicates that divalent treatment causes a reduction in strain softening within *P. fluorescens* biofilm. The T ratio is the ratio of the minimum strain-rate dynamic viscosity η_M and the large strain-rate dynamic viscosity η_L, *Figure 3-11*. DDH_2O and urea biofilms exhibited shear thickening ($T > 0$) which increased with strain. Both η_M and η_L increased, with η_L increasing at a faster rate, which is indicative of strain-rate thickening behaviour. η_L increased at a faster rate compared to η_M for urea treated biofilms in comparison to DDH_2O treated biofilms. This could be a result of faster breakdown of the urea structure and formation of clusters. This observation would agree with the reduced magnitude of the G'' overshoot in urea treated biofilms in comparison to DDH_2O. Faster breakdown of the urea treated biofilm structure would result in a lower G'' overshoot as the microstructure has a lower stress bearing capacity, so rearranges to align with the flow-field at a faster rate, reducing the peak averaged viscous moduli G''. For the $CaCl_2$ treated biofilm η_M and η_L increased at the same rate. This behaviour indicates that the structure thickened with an equal contribution from the

strain thickening and the strain-rate thickening. This could be representative of the increased elasticity within the microstructure due to the addition of $CaCl_2$. For $FeCl_2$ treated biofilms η_M and η_L initially increased at a similar rate. However at γ ~1 % η_L peaked at 27.84$\pm$ 1.97 Pa.s and began to drop. The drop in η_L represents a transitioning from strain rate thickening to strain rate thinning behaviour, thus the thinning of the $FeCl_2$ structure was predominantly driven by strain rate. Interestingly, η_L exhibited a plateau region between η_L = 21.20$\pm$ 2.05 Pa.s, which coincided with a peak in η_M of 29.15$\pm$ 1.20 Pa.s. This is representative of strain thickening where strain rate thinning remained constant. This could be attributed to a second breakdown mechanism in the $FeCl_2$ structure. After the plateau region both η_M and η_L declined, indicating both strain and strain-rate thinning. The behaviours of η_M and η_L are represented using the T ratio, found in *Figure 3-12*. Biofilms treated with urea peaked at T = 0.44$\pm$ 0.04 and DDH_2O treatment at T = 0.25$\pm$ 0.02. The T ratio of the $FeCl_2$ treated biofilm displayed a minimum of -0.39$\pm$ 0.08, after this point the ratio

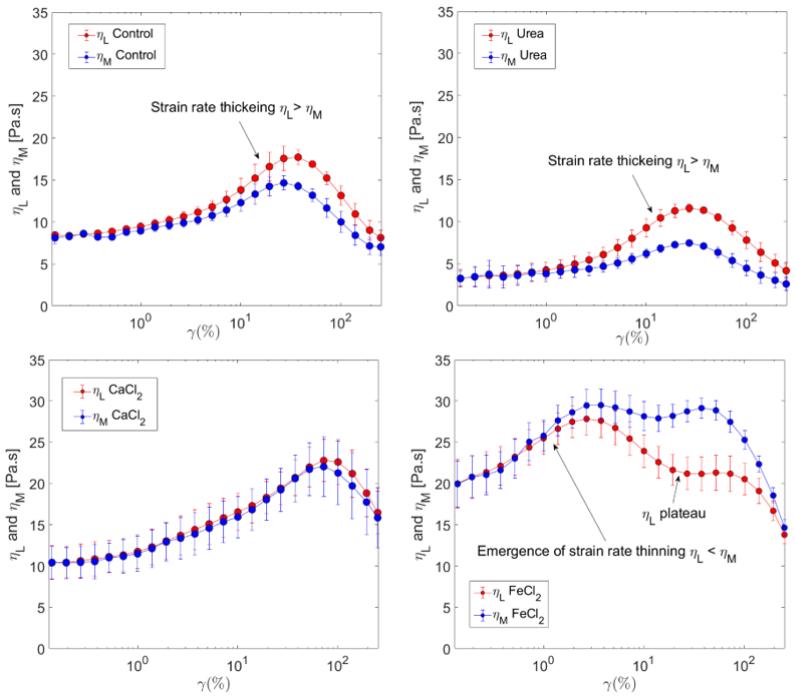

Figure 3-11: The minimum strain rate dynamic viscosity η_M (blue) and the large strain-rate viscosity η_L (red) are plotted against strain amplitude γ for each chemically treated biofilm. Strain rate thickening occurs when $\eta_L > \eta_M$, whilst strain rate thinning occurs when $\eta_L < \eta_M$. Addition of divalent cations $CaCl_2$ and $FeCl_2$ eliminated strain rate thickening behaviour which was exhibited in the control and urea biofilm. Treatment with $FeCl_2$ caused the emergence of strain rate thinning. The mean of three biological replicates $\pm$ standard deviation is shown.

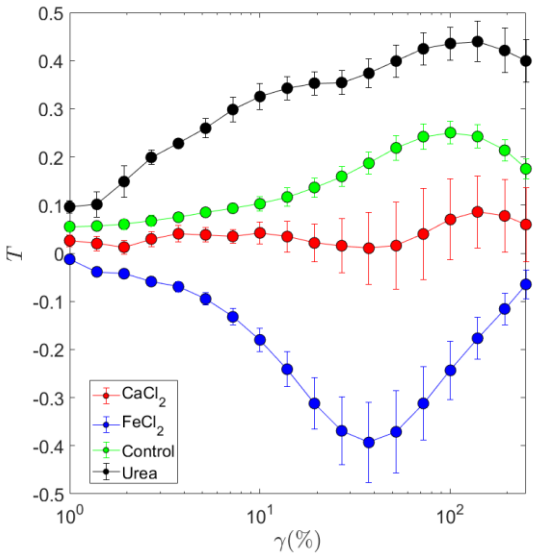

Figure 3-12: Thickening ratio (T) for each chemically treated *P. fluorescens* biofilm. T <0 denotes shear thinning, T >0 denotes shear thickening. Chemical treatment with $CaCl_2$ and Urea resulted in a respective decrease and increase in the thickening ratio in comparison to the control (DDH_2O). Treatment with $FeCl_2$ however resulted in the emergence of shear thinning behaviour. The mean of three biological replicates ± standard deviation are shown.

increased towards zero. As shown using η_M and η_L this thinning behaviour was due primarily to strain dependent thinning.

Using the Chebychev framework I have been able to illustrate the transitions in nonlinear behaviour of *P. fluorescens* biofilm in response to different chemical treatments. I have shown that treatment with divalent cations causes increases the prominence of strain thinning in comparison to DDH_2O and urea treated biofilms. The addition of $FeCl_2$ resulted in an earlier onset of strain thinning in comparison $CaCl_2$ and had a η_L plateau. Each treated biofilm displayed rheology consistent with glassy dynamics. To describe the breakdown in the EPS cell structure I move on to quantify the cage strength.

3.3.5 Sequence of physical processes analysis

To evaluate the stiffness of nearest neighbour cages in *P. fluorescens* biofilm the residual or cage modulus is used *Figure 3-13a*. The strength of the cage is determined by the components in a material system, in biofilm these components are the EPS network and cells. In this context the EPS matrix determines the intercellular bonding between cells and the long-range structure cells are embedded within. Whilst the packing of the bacteria determines the topological constraints of the cage. (Zaccarelli & Poon, 2009). The cage modulus is used to quantify the biofilm residual

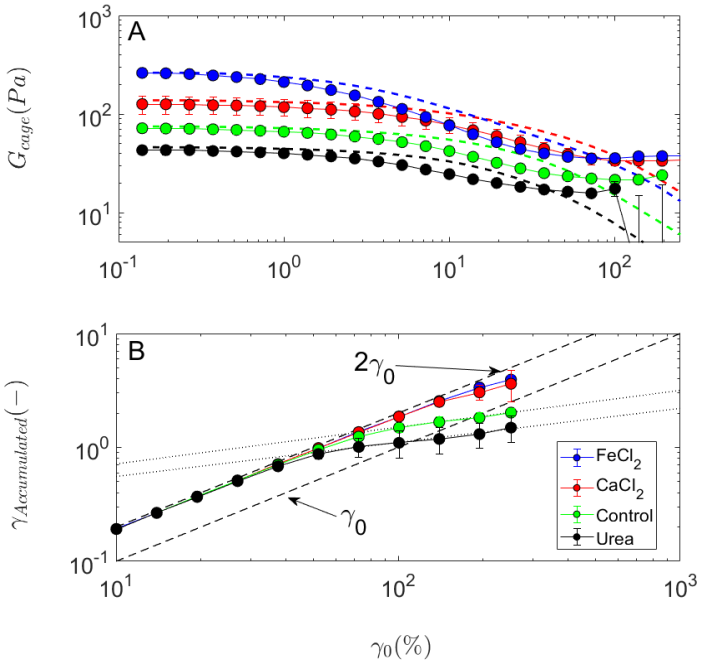

Figure 3-13: (A) Plot of G_{cage} against strain, dashed lines represent the respective elastic modulus values. (B) Plot of accumulated strain at the point of maximum stress, dashed lines represent ideal elastic and ideal viscous accumulated strain gradients. Dotted lines represent the gradient of control and urea accumulated strain ≈ 0.2. Strain amplitude is represented by $\gamma 0$, and the absolute strain accumulated at the point of maximum stress during an oscillation cycle is represented by $\gamma_{accumulated}$. For an elastically dominated system the maximum stress value is found at $2\gamma 0$, while for viscously dominated systems the maximum stress value is found at $\gamma 0$. Plotted is the mean$\pm$ standard deviation from 3- 5 biological replicates.

elasticity, $G_{cage} = \left.\frac{d\sigma}{d\gamma}\right|_{(\sigma = 0)}$. G_{cage} provides an indication of the EPS cell material strength after experiencing a complete oscillation of amplitude γ_0 (S. A. Rogers et al., 2011). For each chemical treatment G_{cage} and G' were equivalent in the LVER, this is expected as within the LVER no significant structural rearrangements occur. G_{cage} reduces with increasing strain for all treatments which is attributed to rearrangement of nearest neighbours and a reduction in the EPS strength as polysaccharide chains disentangle and protein bonds break. Rearrangements viscously dissipate energy altering the EPS bacteria structure and causing the reduction in G_{cage}. Each biofilm displayed a G_{cage} plateau at $\gamma\sim$ 75%. The similarities in G_{cage} plateau across each chemical treatment are reflective of the differences in residual cage strength. For typical hard sphere and soft sphere glassy systems G_{cage} decreases slightly and then stays reasonably constant at large strains e.g. 10-100 % as reported in (Vaart et al., 2013). However, the presence of an EPS matrix causes a larger respective drop in

G_{cage} in comparison to previous studies on model colloids which used spherical particles in the absence of a polymer matrix. This is due to the breakdown of the EPS polymer structure through each cycle. The difference in G_{cage} value between each treatment was consistent with the differences in LVER G' for each treatment. However, treatment with $FeCl_2$ resulted in G_{cage} converging with $CaCl_2$ treatments at γ= 10 %. The plateau values were 357$\pm$ 13 Pa and 336$\pm$ 32 Pa respectively. The convergence to similar plateau values can be explained in terms of the strain thinning behaviour of $FeCl_2$. $FeCl_2$ initially has stronger cages, however the cages are weakened at a faster rate than $CaCl_2$ due to strain thinning. $\gamma_{Accumulated}$ is the cumulative intercycle strain from the lower reversal point (the minimum point in a strain sin wave) to the point of maximum stress, *Figure 3-13b*. The gradient of the $\gamma_{Accumulated}$ curve is used to identify the dominant mode of stress accumulation. A material is deforming elastically when it has a gradient of $2\gamma_0$ and viscously flowing at a gradient of γ_0, with γ_0 being the strain amplitude. $\gamma_{Accumulated}$ is analogous to a yielding curve. Divalent cation treatments $FeCl_2$ and $CaCl_2$ displayed similar behaviour when transitioning from elastically to viscously dominated stress accumulation, an indication that the chemical mechanism resulting in the stiffening of *P. fluorescens* biofilm is similar. Both urea and DDH_2O treated biofilms displayed an increased viscous contribution to peak stress in comparison to $FeCl_2$ and $CaCl_2$. Our present observations have indicated that DDH_2O and Urea alter the rheological response of *P. fluorescens* through distinctly different mechanisms to chemical modification with divalent cations $FeCl_2$ and $CaCl_2$.

To build upon the intercyle averaged representation of non-linear behaviour and map the instantaneous yielding behaviour of the treated *P. fluorescens* biofilm, the transient moduli from the sequence of physical processes (SPP) is used, *Figure 3-134*. The SPP method calculates the time dependent elastic G_t' and viscous G_t'' moduli during a strain cycle of amplitude γ. To provide a more intuitive metric which describes the ratio of the elastic G_t' to viscous G_t'' contributions, the transient phase angle δ_t is presented, where $\delta_t = \frac{G'_t(t)}{G''_t(t)}$. The transient phase angel δ_t can be identified continuously at time t during each strain cycle of amplitude γ. The SPP plot of urea treatments resulted in a similar δ_t signature to the control. This signature featured two prominent yielding bands where $\delta_t > \frac{\pi}{4}$, which corresponds to viscously dominated incomplete yielding. These bands had a maximum value of $\delta_t \approx \frac{\pi}{2}$,

corresponding to a fully yielded viscously dominated response. These yielding bands were centred around $t = \frac{\pi}{2}$ and $t = \frac{3\pi}{2}$, where strain is at its largest. Therefore, yielding for the control and urea treatments was primarily strain dependent. The magnitude of δ_t was marginally higher at $\gamma \approx 25\%$ for the urea treatment, *Figure 3-134b*, indicating an earlier onset of yielding. The transition in yielding mechanism due to treatment with divalent cations $CaCl_2$ and $FeCl_2$ is illustrated in *Figure 3-134c and Figure 3-134d*. The transient phase angle plots of $CaCl_2$ and $FeCl_2$ show the emergence of a 1st yield zone between ≈ 2 – 100 %, where the 1st yielding step of $FeCl_2$ is highlighted by the red boxes. δ_t in this zone was higher in magnitude for $FeCl_2$ treatment than $CaCl_2$, this indicates the stronger effect of $FeCl_2$ on microstructural modification than $CaCl_2$. The first yielding zone for $FeCl_2$ occurred

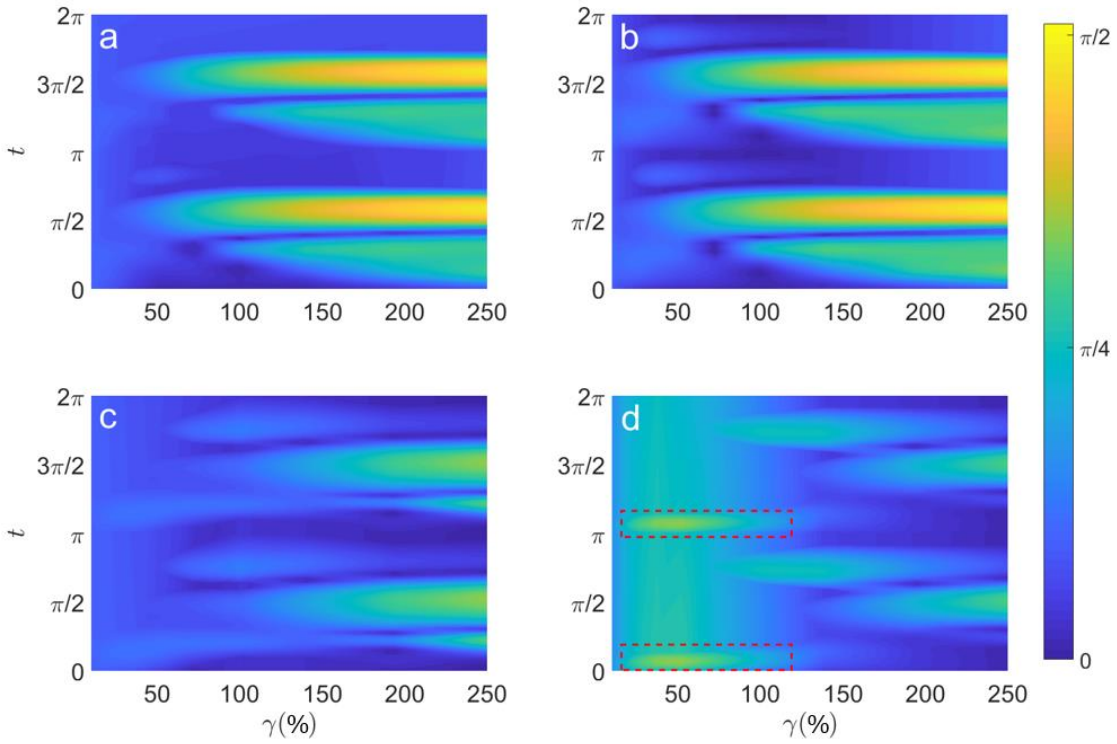

Figure 3-134: SPP transient phase angle plots for (A) Control, (B) urea, (C) $CaCl_2$ and (D) $FeCl_2$ where the red box denotes the 1st first yield step region. The colour bar is representative of the magnitude of the transient phase angle δ_t. The control (DDH2O) and urea treatments resulted in similar transient plot signatures. In both biofilms the dominant yielding mechanism was strain dependent. This is illustrated by the intense yellow bands centred around t = $\frac{\pi}{2}$ and t = $\frac{3\pi}{2}$, the point of maximum strain during a cycle of strain amplitude γ. When treated with divalent cations the presence of this yellow band reduced which is indicative of a more elastic response. This change is reflective of the increased elastic and viscous moduli of both $CaCl_2$ and $FeCl_2$. For $FeCl_2$ an additional region of yielding was prominent at low strains <100 %. This region is centred around t = 0 and t = π corresponding to where strain rate is at a maximum.

when t centred around 0 and π. These two regions are where strain rate is largest during the oscillation cycle. Therefore, the first yielding zone was predominantly strain rate dependent. The 2nd yield zone occurred at $t = \frac{\pi}{2}$ and $t = \frac{3\pi}{2}$ indicating the second yielding step in $FeCl_2$ treated biofilm was predominantly strain dependent, which was constant with where $CaCl_2$ also yielded. This behaviour agreed with Chebyshev intercycle analysis of η_M and η_L.

3.4 Discussion and Conclusions

In this chapter I adopted LAOS analysis techniques and applied them to quantitatively analyse the effects of chemical treatment, on the nonlinear viscoelastic response of *P. fluorescens* biofilms. Previous studies have investigated the effect of chemical treatment on biofilm viscoelasticity (Brindle et al., 2011). However, these studies used linear viscoelastic techniques which mainly enabled changes in stiffness to be quantified (Klotz et al., 2019; Kovach et al., 2017; Kretschmer & Lieleg, 2020b). These methods therefore neglect the non-linear regime. Analysing both the linear and nonlinear regimes therefore provides a more complete assessment of biofilm mechanical behaviour. The dynamics within the nonlinear regime lend themselves to phenomenological arguments which can be compared to analogous systems such as colloidal and polymer gels. Biofilms have been compared to double hydrogels, however arguments applied to the field of glassy colloidal gel rheology are rarely fully adopted to explain biofilm rheology (Jing Yan et al., 2018). In the following paragraph I will summarise the effect of each chemical treatment in the context of non-linear parameters.

P. fluorescens treated with urea displayed a reduction in packing fraction which correlated with a reduction in elastic and viscous modulus. Urea caused an elastic weakening of the microstructure as indicated by the increased magnitude of strain softening and strain-rate dependent thickening. The increase in non-linear thickening was reflected in the increase to of the *G''* overshoot. The EPS of *P. fluorescens* is known to have a high uronic acid content, a component found in xanthan gum, which also displays type III overshoot. Urea has been shown to cause swelling in several types of biofilms such as *S. epidermidis* (Jones et al., 2011) and weakening effects to *P. aeruginosa* (X. Chen & Stewart, 2002). Urea is a chaotropic compound which interferes with hydrogen bonding, reducing the stability of proteins. The presence of

urea as a co solute can lead to an effect termed “cononsolvency”. Cononsolvency has been demonstrated to occur in PNIPAm polymer colloidal gels when treated with water/urea (Sagle et al., 2009). The presence of the co solute urea causes the collapse of polymer chains, which then reswell at higher osmotic concentration. Swelling results due to a reduction in network crosslinking which changes in the equilibrium swelling point. This results in an increased solvent concentration which increases polymer chain mobility and mobility of filler particles. The cage strength is determined by the strength of the EPS matrix and the cellular network topology, which was quantified using the packing fraction ϕ. Within *P. fluorescens* this effect could cause a reduction in the cohesiveness of the EPS, the bonding strength of interparticle cages and reduced compaction of the bacterial topological network. This effect could occur in *P. fluorscens* by reducing hydrogen bonding of the uronic acid polysaccharide component. The cononsolvency effect may explain why the strain thickening ratio T was higher in urea than DDH_2O, as increased mobility within the polymer colloid system would result in higher energy dissipation due to the increased alignment of polymer chains and bacteria with the flow.

Treatment with $CaCl_2$ and $FeCl_2$ caused an increased ϕ for both treatments in comparison to DDH_2O. The packing fractions of $CaCl_2$ and $FeCl_2$ were equivalent. This indicated that the difference in linear and nonlinear behaviour of $CaCl_2$ and $FeCl_2$ was predominantly caused by $FeCl_2$ having a greater stiffening effect on EPS elasticity. The major adhesin protein of *P. fluorescens* is LapA, which is a part of a family of large repeat surface proteins known to bind calcium. The addition of $CaCl_2$ may have increased the crosslinking between LapA proteins or increased the stiffness of the protein (Boyd et al., 2014). The LapA polysaccharide is known to contain calcium binding motif on its C terminal region (Fuqua, 2010). A stiffer EPS structure through LapA crosslinking would result in stiffer interparticle cages. The difference in action between $CaCl_2$ and $FeCl_2$ could further be explained by the difference in the ionic radii of the two ions. This theory was recently posed after *Bacillus subtilis* B-1 and *Azotobacter vinelandii* where shown to respond with different degrees of stiffening to an array of metal ions (Kretschmer & Lieleg, 2020a). The differences in stiffening behaviour between the strains and metal ion treatments were postulated as being due to the differences in alginate conformation in the aforementioned bacteria. Alginate has been shown to be present in the EPS certain strains of *P. fluorescens*, however is known to be secreted only under certain

physiological conditions (Marshall et al., 2019). Non the less the probability of a stiffing effect increases with a reduction in ion size which corresponds with the increased stiffening effect, which is seen with $FeCl_2$, where the ionic radii of $FeCl_2$ is small than $CaCl_2$.

The rheology of $FeCl_2$ treated *P. fluorescens* biofilms displayed thinning behaviour which was mainly caused by strain-rate dependent thinning as indicated by the relative drop in η_L and coincided with the emergence of two step yielding. The presence of two step yielding was depicted using the SPP framework, through the emergence of an additional yielding band. The emergence of two yielding zones is a characteristic of attractive glassy/colloidal gel systems. Yielding in attractive glassy/colloidal gel systems occurs in two steps. The first step is densification which occurs when short range interparticle bonds within the nearest neighbour cages breakdown. The second step involves the breakdown of the topological constraints, in a biofilms, the bacteria/bacteria jamming and breakdown of the longer-range EPS matrix structure (Pham et al., 2006). The stiffening effect of $FeCl_2$ has been seen across several biofilm rheological studies (Grumbein et al., 2014; Klotz et al., 2019). Addition of $FeCl_2$ and $FeCl_3$ have been shown to increase the erosion stability of *B. subtilis* biofilms (Grumbein et al., 2014). These experiments test erosion detachment at a constant shear stress. The work presented here has demonstrated shear rate thinning behaviour in $FeCl_2$ and that shear rate is the predominant cause of yielding in $FeCl_2$ treated biofilms. This behaviour could be due to ionic crosslinking of $FeCl_2$ to the side branches of polyanionic EPS polysaccharides such as alginate. Ionic crosslinking would increase the elastic and viscous modulus in the linear regime but reduce viscous dissipation in the non-linear regime due to reduced polymer chain flexibility.

In this chapter I implemented a LAOS rheological framework towards the analysis of *P. fluorescens* biofilms treated with divalent metal cations and a chaotropic compound. By adopting LAOS techniques an in-depth characterisation of the nonlinear rheological effects of these chemicals on biofilm was achieved. The techniques applied provided increasingly sensitive measurements of the thickening/thinning and stiffening/softening dynamics within each biofilm. The intracycle (Chebychev method) and instantaneous (SPP) techniques enabled the strain and strain rate dependence of these nonlinear behaviours to be revealed. The improved sensitivity of these methods in comparison to solely using the elastic moduli

G' and viscous moduli G'' meant that subtle differences in shear thinning behaviour were detected between the divalent cation treatments. The difference in shear thinning behaviour between $CaCl_2$ and $FeCl_2$ was due to increased strain rate dependent thinning depicted by a relative change in η_L. The action of the chaotropic compound urea resulted in modification to the shear thickening behaviour of *P. fluorescens*. The main action of modification was reflected by the increase to the T ratio in comparison to the control. The increased thickening is suggestive of increased bacterial and EPS network rearrangement, which would result in increased energy dissipation. The increase to EPS network mobility is due to increased mobility of the polysaccharide chains and protein components such as alginate and LapA, which could be due to the cononsolvency effect.

Unravelling the polymeric interactions occurring within the EPS structure of biofilm which determine intercellular bonding strength and bacterial organisation requires the subtle detection of changes to rheology. This work provides a demonstration of an enhanced macroscale rheological characterisation platform for biofilms. The LAOS framework used here increases the resolution of biofilm rheological characterisation from cycle averaged properties to analysis using intercycle and instantaneous properties. This framework could be applied to improving rheological diagnostics of medically related biofilms such as CF sputum potentially providing a method of detecting specific protein/ polymer rheological signatures. For fundamental studies focused on accessing polysaccharide/ protein interactions the LAOS framework developed here could helpful in quantifying alterations in stiffening/softening, thickening/thinning behaviour assisting to improve interpretations of modified EPS network interactions.

Chapter 4 Effect of the production of polysaccharides amylovoran and stewartin on the microstructure and rheology of *Pantoea* sp. .

4.1 Introduction

In this chapter the rheological framework described in chapter 3 is applied to a plant growth promoting rhizo bacteria (PGPR) called *Pantoea sp. YR343*. The rationale behind this chapter is to demonstrate how the LAOS platform can be applied to access biofilm rheological phase transitions as a function of a change in EPS composition. In this case the EPS component which is modified is a capsular polysaccharide closely related to amylovoran and stewartin. The LAOS principles and framework are used to enhance the quantitative description of how polysaccharide

concentration impacts the phase behavior of this biofilm and the resulting rheology.

Plant growth promoting rhizo-bacteria (PGPR) are used as biocontrol agents and can increase resilience against pathogens in suboptimal soil conditions (Allison & Martiny, 2008). These biofilms act as facilitators of biocontrol within the plant root rhizosphere and an environment of elevated microbial density where bacterial ecology is actively influenced by plant root exudates (Beauregard et al., 2013; Sasse et al., 2018; Zhalnina et al., 2018). Root exudates drive symbiotic interactions between biofilm and roots, triggering biofilm formation and producing chemotactic secretions resulting in preferential, localised biofilm colonization (Y. Chen et al., 2012; Massalha et al., 2017; N. Zhang et al., 2014). EPS is a characteristic component of biofilm formation, excreted by bacterial cells and is composed of polysaccharides, proteins and DNA. The composition of EPS is phenotypically dependent and highly heterogeneous in mixed environments. The regulation of specific functional EPS components has been demonstrated to improve plant fitness in response to increases in salinity (Kasim et al., 2016), toxic soil contaminants (Mallick et al., 2018), plant - microbe adhesion (Zhao et al., 2015), species - species interaction (Z. Xu et al., 2013) and resistance to pathogenic attack (Molina-Santiago et al., 2019). Modulating specific EPS components can result in productivity fluctuations (Dragoš, Kiesewalter, et al., 2018) and changes to biofilm architecture (Hartmann et al., 2019).

In this chapter a combination of genetic modification, microscopy and rheometry is applied to understand the structural composition and rheology of an EPS defective strain *Pantoea* sp. YR343 UDP and an EPS producing strain *Pantoea* sp. YR343. Using a combination of confocal microscopy and fluorescent staining, changes in packing fraction and packing morphology caused by the deletion of amylovran and stewartin are investigated. Small and Large Amplitude Oscillatory shear rheometry is used to quantify the variations in the rheological characteristics of wild type and mutant *Pantoea sp.* YR343 biofilms. The study demonstrates that changes in the volume of secreted EPS has a drastic effect on the viscoelasticity and morphology of biofilms. It is demonstrated that cellular packing fraction and polysaccharide concentration can be controlled by varying the mixture ratio of *Pantoea* sp. YR343 and *Pantoea* sp. YR343 UDP, enabling the investigation of rheological phase transitions.

4.2 Materials and methods

4.2.1 Bacteria growth in liquid cultures and agar plates

Salt optimized broth plus glycerol (SOBG) medium was prepared by dissolving 20 g tryptone, 5 g yeast extract, 0.5 g NaCl, 2.4 g $MgSO_4$, 0.186 g KCl, 50 ml of 40% v/v glycerol (Sigma, UK) in 1 L of milli-Q water. SOBG agar had similar composition and in addition contained 15 g of agar. The *Pantoea* strains used within this experiment were kindly provided by the Oakridge national lab, Washington, USA. *Pantoea* sp. UDP is a mutant strain of *Pantoea* sp. YR343 with a transposon insertion in the gene PMI39_01848 which encodes UDP – galactose- lipid carrier transferase. This gene is the first gene in an operon that is responsible for synthesizing a type of EPS closely related to amylovoran and stewartin. This mutant has corresponding defects in biofilm formation, pellicle formation and root colonization (Aufrecht et al., 2019). *Pantoea* sp. YR 343 and the *Pantoea* sp. UDP mutant were grown overnight in SOBG medium at 24 °C with shaking (150 rpm). 150 µL of the overnight culture was pipetted on the sterile agar plates and was spread uniformly using a L shaped spreader. The bacteria were then allowed to grow for 24 hrs and subsequently scraped off from the surface of the agar using a glass slide.

4.2.2 Time lapse microscopy

Pantoea sp. YR343 and *Pantoea* sp. YR343 UDP were grown for 3 hrs in SOBG medium at 24 ^{o}C with shaking (150 rpm). 1.5 % agarose pads replete with M9 minimal media and 0.5 % glucose were prepared using 25 µL gene frames (Sigma, UK). Once the agarose had solidified, two strips were cut out to increase the air volume in the sealed frame. Timelapses were performed with monocultures of *Pantoea sp.* YR343 and *Pantoea sp.* YR343 UDP. For monocultures 1 µL of culture adjusted to OD = 0.2 was pipetted onto the agarose pad. Dual cultures were performed at a ratio of 10:1, *Pantoea sp.* YR343: *Pantoea sp.* YR343 UDP. Overnight cultures were independently corrected to an OD = 0.2 before being combined, 1 µL of dual culture was then pipetted onto the agarose pad. A #1.5 coverslip (Sigma, UK) was used to seal the Gene frame. A razor blade was used to seal the coverslip being careful to press outside the perimeter of the Gene frame so to avoid excessive pressure on the agarose. Time lapse imaging was performed using a Nikon Eclipse Ti-S microscope (Nikon, Japan) fitted with a CoolLED pE-4000 light source (CoolLED, UK). A perfect focus system (Nikon Perfect Focus System (PFS)) was used to minimize Z drift. The microscope was used in phase contrast mode. The

temperature was controlled using an environmental chamber which surrounded the microscope and was set at 24 ^{o}C. Images (1024 x 1024) were taken with a 63x objective oil immersion lens and acquired every 10 mins for 12 hrs. Fields of view (FOV) were selected at random. For each condition timelapses were repeated 3 times.

4.2.3 Rheometry

A 20 mm plate-plate geometry and a Kinexus Pro+ rheometer as described in the previous chapter were used for rheometric measurements. Circular adhesive backed 120 grit paper were adhered to both the plates to reduce the instances of slip. Biofilm was scraped from agar plates using a ground edged microscope slides and (1 plate per run) were placed onto the grit paper. The top plate was moved into contact with the biofilm to ensure a uniformly loaded configuration. The plate gap was set at 1 mm and samples were trimmed with a razor blade. A solvent trap was used to prevent desiccation. Strain controlled frequency sweeps were performed at a strain of γ = 1% and a frequency range of ω = 0.1 – 15 Hz was used for both the wild type and the mutant. For large amplitude oscillatory shear (LAOS) experiments the rheometer was operated in a strain-controlled mode and amplitude sweeps were performed from γ = 1 – 1000%. LAOS tests were performed at constant frequencies (0.15, 0.375, 0.5, 0.75, 1 Hz). A decimator setting of 5 was used for the UDP mutant and a decimator setting of 30 was used for the WT. The decimator is an internal PID controller in the Malvern Kinexus which can be adjusted to obtain distortion free sinusoidal input strain waveforms. Internal details of the decimator haven't been provided by Malvern.

Creep measurements were performed using the aforementioned rheometer with 20 mm grit paper and a plate-plate geometry at $\sigma = 30$ Pa for 300 seconds. Creep curves were then fitted with the Burger model using a curve fitting code in MATlab. Least squares regression was used for curve fitting. Creep curves were averaged from n= 3 measurements.

4.2.4 Packing fraction calculation

The packing fraction for the WT, UDP and the respective mixture ratios was calculated using the same method as chapter 1 with one modification. The dilation step was eliminated as the cell membranes were stained with 1µg/ml of FM 1-43, a lipophilic styryl compound which targets the plasma membrane of a cell. FM 1-43 has an excitation wavelength of 488 nm (Thermofisher, UK) was used at a concentration

of 1 µM. The stain was incubated for 15 mins prior to addition of Syto 63, a nucleic acid stain. FM 1-43 was excited at 488 nm an excitation separation distance of 172 nm from Syto 63 to ensure blead through was negligible. Syto 63 and FM 1-43 were acquired in separate channels with emission filters of 498 – 630 nm for FM 1-43 and 670-750 nm for Syto 63. Images were then preprocessed using the protocol from chapter 3 (without the dilation step). The Syto 63 and FM 1-43 channels were combined resulting in a micrograph representing both intercellular DNA and the bacterial membrane. Packing fraction was calculated based upon the ratio of cells/membrane signal to void space.

4.3 Results

4.3.1 *Pantoea* sp. macrostructure is drastically different to *Pantoea* sp. UDP

To compare the macrostructure of *Pantoea* sp. and *Pantoea* sp. UDP, each strain was cultured on SOBG agar plates. Stark differences in colony morphology after 72 hr were seen, *Pantoea* sp. produced large colonies with a diameter of 21.5 mm, while UDP colonies were smaller, with a diameter of 8.05 mm, *Figure 4-1*. The structure of the *Pantoea* sp. appeared to be significantly less viscous than the *Pantoea* sp. UDP when scraped with a glass slide after 72 hrs.

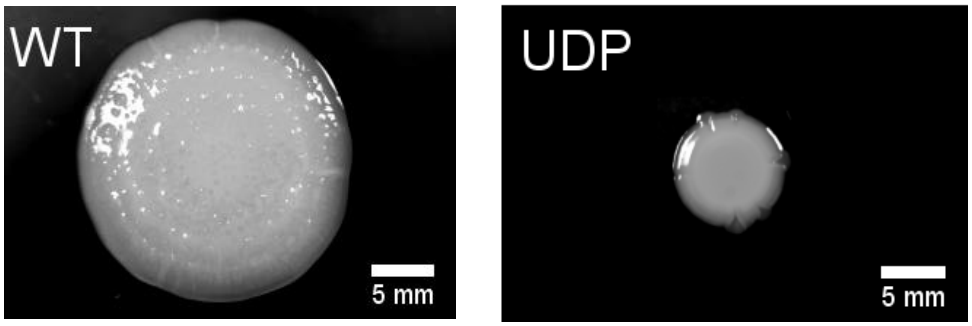

Figure 4-1: Representative growth of *Pantoea* sp. WT and UDP mutants on SOBG agar. The morphology of the wild type stain is swelled in comparison to the UDP mutant strain, which appears compact. The morphological difference is suggestive that reduced production of the hydrophilic polysaccharide amylovoran alters the equilibrium swelling point of the mutant strain.

4.3.2 Agarose pad timelapses reveal different packing structures in *Pantoea* sp. and *Pantoea* sp. UDP

To visualize the differences in colony morphology on a single cell level *Pantoea* sp. YR343 wild type (WT) was grown on M9 agarose pads, *Figure 4-2*. Early stage colonies (< 240 mins) grew with a compact structure, with daughter cell positioning dependent upon cell shoving. At a time t ranging from 300 - 370 mins WT continued

to secrete EPS. Secretion of EPS resulted in a reduction of the local packing fraction and increased cell- cell distances. For *Pantoea* sp. YR343 UDP (UDP) colony topology remained tightly packed, with colony geometry determined through bacteria - bacteria shoving. After visualizing the stark differences in the packing of the WT and UDP strains I sort to access the topology of mixtures of the EPS secreting sparsely packed WT and tightly packed UDP. As with pure WT and UDP cultures, the mixtures exhibited a similar packing structure until t = 240 mins. At t = 240 mins the WT strain began secreting amylovran from within tightly packed clusters. The EPS secretion resulted in a reduction to the packing at the center of the WT/UDP cluster at t = 300-370 mins and dramatically reorganized the colony topology. After the EPS secretion event, the cluster shrank in size as UDP grew into the secreted amylovoran.

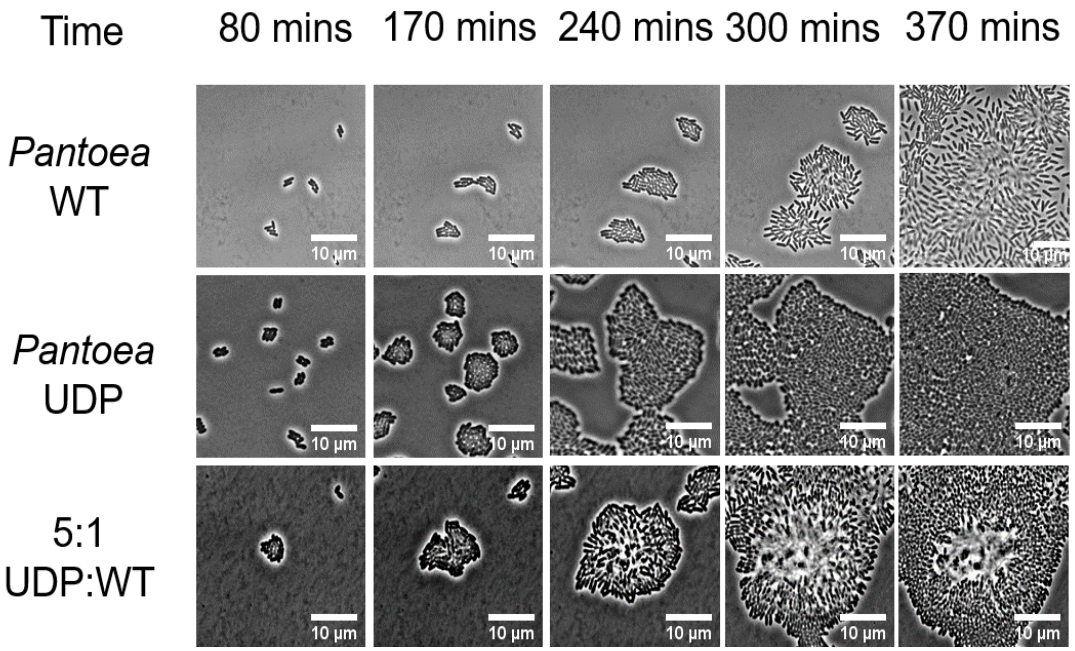

Figure 4-2: Representative bright-field time lapses of *Pantoea* WT, *Pantoea* UDP and mixtures of *Pantoea* UDP and WT at a ratio of 5:1. Time starts at 0 mins and increases in *Pantoea* WT initially grows in tight clusters and at around 300 mins into the experiment amylovoran EPS is secreted causing an increase in EPS volume surrounding each bacteria and a global reduction in packing fraction. UDP remains tightly packed throughout the experiment. 5:1 Mixtures of WT: UDP result in tightly packed clusters which have regions of low packing fraction due to the expression of amylovoran from the WT strain.

4.3.3 Packing fraction of *Pantoea* sp. can be controlled by mixing different ratios of *Pantoea* sp. and *Pantoea* sp. UDP

To access the effect of modulation of the packing fraction of *Pantoea* sp. YR343 on rheology, 4 different mixture ratios were selected UDP:WT; 10:1, 50:1, 100:1 and

250:1. CLSM was used to image each mixture, this enables thin Z slice imaging by removing out of plane structures and quantitative imaging at different depths in the biofilm structure, *Figure 4-3*. Each imaging slice was then used to compute the packing fraction ϕ of each mixture, *Figure 4-4*. As expected, there was a noticeable contrast in packing between WT and UDP, the packing fraction of WT averaged ϕ= 0.16$\pm$ 0.04. Increasing the ratio of UDP caused increases to the packing fraction. UDP biofilms had a packing fraction of ϕ= 0.64$\pm$ 0.08 close to the random packing limit for rods. The morphology of WT was defined by the presence of dispersed bacterial clusters. As the concentration of UDP increased, the size of the bacterial clusters increased, resembling the morphology of polymer-colloid depletion gels. In polymer-colloid systems, aggregation of clusters is dependent upon polymer concentration. High concentrations of non-absorbing polymer can cause depletion attraction, a short-range attractive force, causes phase separation of the polymer and filler particles, resulting in cluster formation (Dibble et al., 2006). The morphology of 250:1 appeared to feature fewer voids and was increasingly packed with bacteria confined by nearest neighbors. This morphology is reminiscent of glasses where

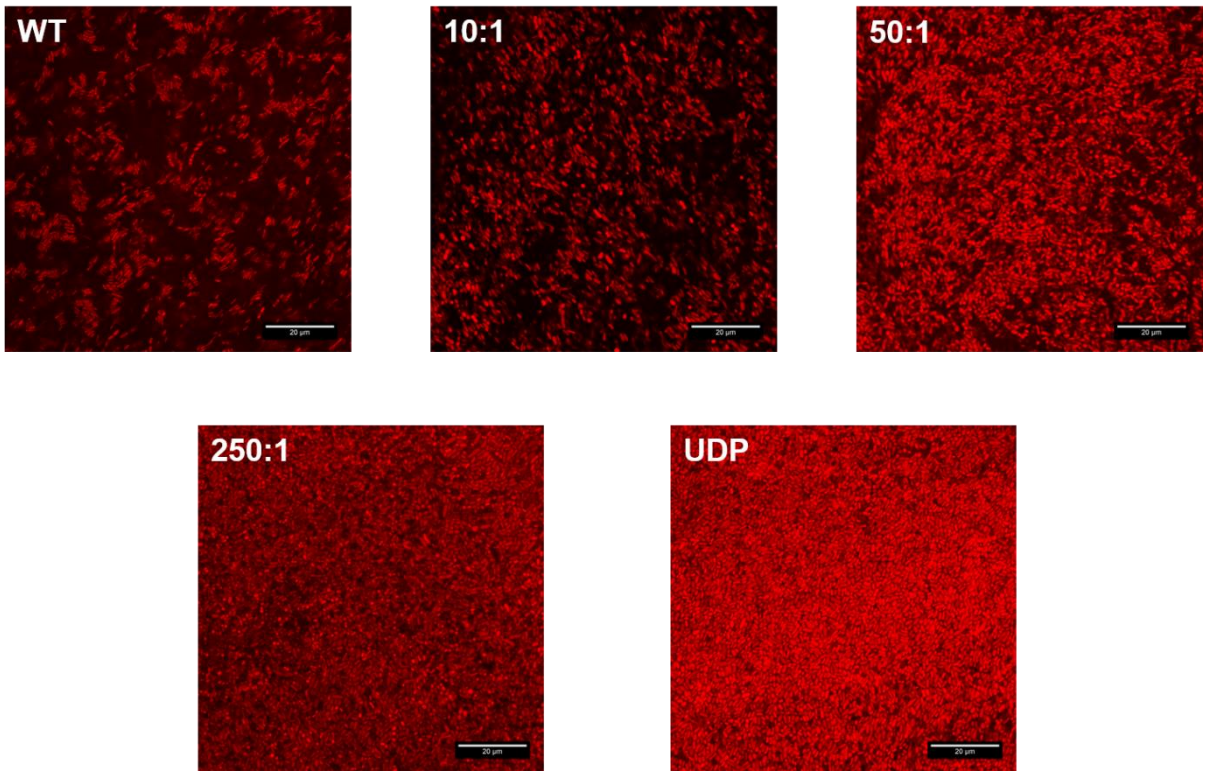

Figure 4-3: Representative CLSM of *Panteoa* WT, 50:1 UDP:WT mixtures, 250:1 UDP:WT mixtures and UDP mixtures. Cells were stained using Syto63 and FM-64 to stain the cell cytoplasm and cellular membrane. Images were taken 15 µm above the coverslip. Increase in the ratio of UDP resulted in an increase to the biofilm packing fraction. The WT displayed many smaller clusters, as UDP concentration increased, the EPS between the clusters reduced and cell density increased. The scale bar is 20 µm.

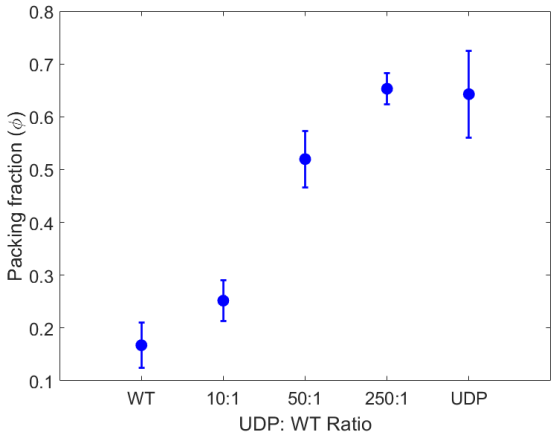

Figure 4-4: Plot of packing fraction against *Pantoea* WT and UDP and UDP:WT mixtures. The packing fraction is calculated from CLSM images of *Pantoea* WT, *Pantoea* mixtures 10:1, 50:1, 250:1 and *Pantoea* UDP. Presented is the mean± standard deviation from 8 fields of view per sample.

UDP structures were uniformly jammed with an absence of noticeable voids.

4.3.4 *Pantoea* sp. WT displays different rheological behaviour to *Pantoea* sp. UDP

Amplitude sweeps were performed on each pure culture shown in *Figure 4-5*. *Pantoea* WT exhibited an average linear elastic modulus of 58± 5 Pa, while G' for UDP was 4450± 550 Pa, ~2 orders higher than WT. The viscous modulus G'' of WT was 12.7± 1.5 Pa whereas UDP was 360± 55 Pa, ~1.25 orders higher in viscosity then WT. The linear viscoelastic limit for WT was significantly larger than UDP, at 37.1 % while UDP was 3.7 %, indicating structural rearrangement at lower strains for

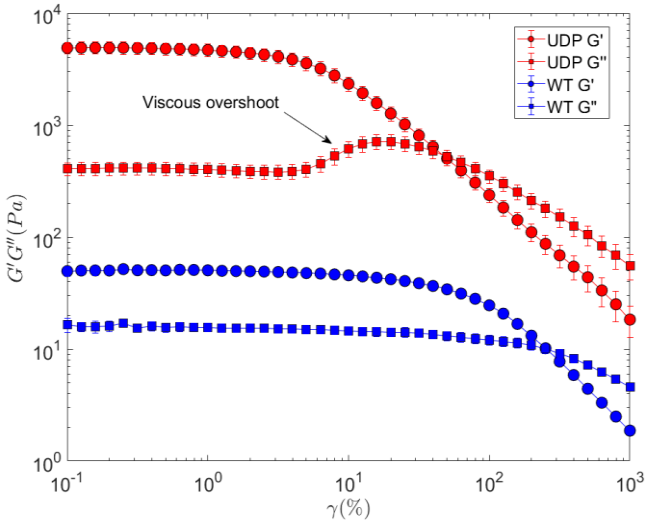

Figure 4-5: Amplitude sweep of *Pantoea* WT and *Pantoea* UDP at ω = 0.5 Hz and γ = 0.1 % - 1000 %. *Pantoea* UDP features a prominent viscous moduli overshoot after exceeding the linear viscoelastic region. *Pantoea* WT features no such overshoots. Presented is the mean± standard deviation (n=5).

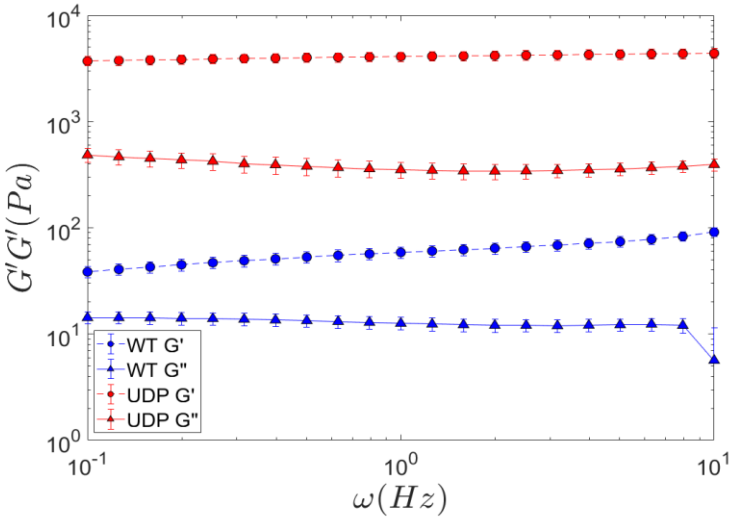

Figure 4-6: Frequency sweeps of *Pantoea* WT and *Pantoea* UDP, performed at 0.1 % strain probing a frequency range of ω = 0.1 - 12.5 Hz. Plotted is the mean $\pm$ standard deviation from biological replicates (n = 5).

UDP. UDP exhibited a single well-defined hump in G'' which began to increase at 3.7 % and peaked at a G'' value of 708$\pm$ 107 Pa. The presence of this hump is commonly found in glasses and emulsions when colloid packing fraction is near or above the random close packing limit. The hump has been termed type III yielding and signifies the occurrence of weak strain overshoots (Hyun et al., 2011). WT featured a dissipation mechanism comparable to viscoelastic liquids. Viscoelastic liquids are characteristically absent of viscous overshoots in G''. Reptating polymer networks display this type of behavior. Reptation polymer networks form through the overlapping and entanglements of high molecular weight long chain linear polysaccharides, like amylovoran and stewartin. The reptation network dynamics depend on the polymer molecular weights and chain relaxation time, where topological constriction be neighboring polymer chains restrict the chain motion. Amylovoran is notably large with a molecular mass of 1 MDa (Nimtz et al., 1996). This is also a feature of colloidal gels with packing fractions below the random packing limit. Frequency sweeps for WT revealed a mild increase in G' and G'' with increasing frequency, *Figure 4-6*. This compared to UDP which exhibited frequency independence over the range of frequencies probed. The mild frequency dependence of WT indicates that the solvent/polymer network contribution was more notable in the WT microstructure than UDP. This behavior could be caused by a high concentration of amylovoran which is hydrophilic. This would result in increased solvent absorption due to the higher equilibrium swelling point in comparison to UDP. Similar swelling behavior like this occurs in hydrogels when hydrophilic functional

groups are added to polysaccharide chains (Kuang et al., 2011). This could explain the swelled structure seen in the agar image of *Pantoea* WT. The contribution of water to biofilm mechanics at short time scales has also been quantified using stress relaxation experiments (He et al., 2013). The absence of viscous overshoots in the amplitude sweep of *Pantoea* WT support the classification of WT as a viscoelastic liquid. The presence of the type III hump and plateau behavior of the UDP frequency sweep agree with characteristic repulsive glassy material. As the difference between the mutant strain UDP and WT is the expression of amylovoran and stewartin, the transition from viscoelastic liquid to glassy behavior could be dependent on the volume of secreted EPS.

4.3.5 Mixtures of *Pantoea* WT:UDP enable investigation of the transition between viscoelastic liquid and viscoelastic glass behavior

In order to evaluate the effect of differing packing fractions and morphological features on the rheological behavior of *Pantoea* sp. biofilm, a series of oscillatory and step strain experiments were performed adopting LAOS techniques to evaluate nonlinear viscoelastic behavior. Amplitude sweeps are presented in *Figure 4-7* and *Figure 4-8*. For clarity the elastic moduli G', *Figure 4-7* and the viscous moduli G'', *Figure 4-8* are represented separately. *Figure 4-7* depicts the storage modulus of 10:1, 50:1, 100:1 and 250:1 mixture. As the ratio of *Pantoea* sp. UDP is increased, the elastic moduli increased, 10:1 had a G' value of 83$\pm$ 13 Pa and a G'' value of

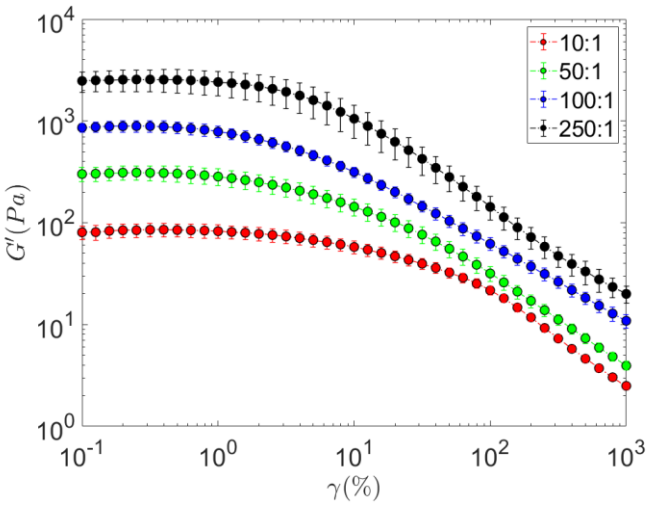

Figure 4-7: Amplitude sweeps depicting the elastic modulus of *Pantoea* UDP: WT mixtures from 10:1 to 250:1. The amplitude sweeps were performed at a frequency = 0.5 Hz through a strain range of 0.1-1000 %. Points plotted are the mean$\pm$ standard deviation (n=5) from biological replicates.

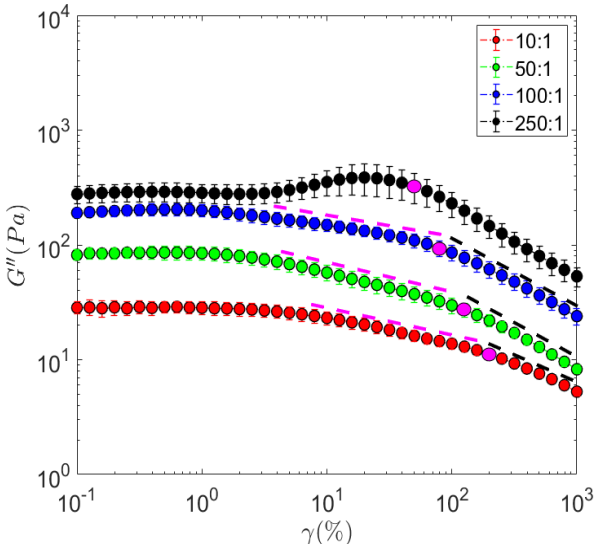

Figure 4-8: Plotted is the viscous modulus of *Pantoea* UDP: WT mixtures from a series of amplitude sweep performed at frequency = 0.5 Hz from strain 0.1-1000%. The cross over point γ_c for each ratio is represented by a pink dot. The pink dashed line represents the intermediate power law gradient before the yield stress. The black dashed line represents power law behaviour after the yield strain. The exponents values can be found in Table 4-1. Points plotted are the mean$\pm$ standard deviation (n=5) from biological replicates.

28$\pm$ 4 Pa, a 43 % increase in comparison to the WT. The 50:1 and 100:1 ratio exhibited G' values of 300$\pm$ 47 Pa and 882$\pm$ 104 Pa respectively. 250:1 had an elastic modulus of 2572$\pm$ 585 Pa which remained constant (within <10 %) during the LVER range. Increased concentration of UDP resulted in increased viscous moduli for each ratio and resulted in changes to the shape of the viscous modulus curve in the MAOS and LAOS region. At ratios of 10:1, 50:1 and 100:1, G'' exhibited two power law gradients, $G''_{MAOS} \sim {\gamma_0}^{-\frac{1}{2}\upsilon}$ and $G''_{LAOS} \sim {\gamma_0}^{-\upsilon}$, the first found in the medium amplitude oscillatory shear (MAOS) region (γ = 8 - 100%) and the second in the LAOS region γ = 100 -1000%. G'' gradients in the MAOS region were approximately half the gradient of G'' in the LAOS region, *Table 4-1*. The emergence of power law behavior in the MAOS region is particularly interesting, as this signifies the presence of multiple relaxation times, a characteristic frequently seen in complex biological materials like cells and a property of polymeric gels with multiple relaxation times (de Sousa et al., 2020). The behavior of G'' transitioned towards type III weak strain overshoot yielding, which was previously seen in the pure UDP strains. It is evident that the secretion of amylovoran and stewartin influences the packing fraction and cluster morphology of UDP: WT ratios causing a transition in behavior from viscoelastic liquid (WT) to glassy behavior (UDP). Reducing the relative

concentration of amylovoran and stewartin results in a change to the dissipative behavior of *Pantoea.* sp as reflected in the viscous moduli G'', which is seen in the 10:1, 50:1 and 100:1 mixture. The transition point between MAOS and LAOS regions is marked by the cross over strain $\gamma_c = (G' = G'')$. The cross over strain is defined as the strain at which viscous dissipative behavior of the material becomes equal to the elastic stiffness. The cross over strain was seen to vary between mixture ratios. For 10:1 mixture $\gamma_c =$ 199.55 %, for 50:1 γ_c =125.88 %, 100:1 γ_c = 79.42 % and 250:1 γ_c = 50.11 %. Therefore, it's apparent that γ_c reduced with increased elastic and viscous moduli, increased packing fraction and reduced EPS concentration. The decrease in crossover strain with increased packing fraction and emergence of the hump at 250:1 is known as the Payne effect (Cassagnau, 2003). This effect was discovered in rubber compounds where the cross over strain of rubber decreases with increased filler volume. Presently there isn't a singular proven theory which explains the cause behind this phenomenon, there are two main hypotheses which may explain this effect. The first is linked to agglomeration and de-agglomeration as the filler network breaks down with increasing strain (Meera et al., 2009). The second theory concerns the disentanglement of polymer chains (H. Xu et al., 2020).

Ratio	Gradient (MAOS)	Gradient (LAOS)
10:1	-0.40± 0.02 (7.94 - 158 %)	-0.99± 0.03 (199 - 1000 %)
50:1	-0.43± 0.03 (2 - 100 %)	-0.91± 0.04 (125 - 1000 %)
100:1	-0.46± 0.03 (1.25 - 100 %)	-0.93± 0.04 (125- 1000 %)

Table 4-1: Table of the MAOS and LAOS power law gradients for different ratios of *Pantoea* sp. (UDP:WT) . The values in brackets represent the strain range the power law gradient correspond to. Presented is the mean± standard deviation from 5 biological replicates.

4.3.6 Stress strain and creep response of *Pantoea.* sp mixtures

To gain insight into the stress response to imposed oscillatory strain, the total stress at each strain amplitude was plotted on a stress strain plot, *Figure 4-9a.* At low strain values, within the LVER, stress is proportional to strain and therefore has a linear gradient. A deviation from the linear gradient signifies nonlinear material yielding and structural breakdown.

From stress strain curves, a stress of 30 Pa was selected for step strain creep experiments of *Pantoea* UDP: WT mixtures. A constant stress of 30 Pa was applied to each mixture for a period of 300 seconds, over which time the creep behavior of the material was measured, *Figure 4-9b*. The creep curves for each mixture were then fitted to the 4-element burger model, a phenological model composed of Maxwell and Kelvin Voigt elements in series. The Maxwell and Kelvin Voigt spring and dashpot coefficients for each *Pantoea* mixture are found in *Table 4-2*. The creep tests enable longer time scale characterization of each UDP: WT mixture behavior under constant stress in comparison to the SAOS frequency sweeps. The creep behavior of each mixture is dependent upon the elastic and viscous properties of each biofilm. For 250:1 mixture, and lesser for 100:1 and 50:1, creep ringing was evident at start up. Creep ringing occurs due to the inertia of the rheometer motor/ geometry and an underdamped oscillatory response. Ringing was less apparent in 10:1 sample, suggesting a reduction in the biofilm elasticity and viscosity reduced biofilm damping resulting in reduced creep ringing oscillations. Creep ringing can in principle be used to determine viscoelastic properties of a biofilm (Goudoulas & Germann, 2016; Hubert & Ali, 2014; McKinley, 2007). The creep curve of 10:1 showed an initial stress bearing capacity until ~10 seconds into the test. Here the

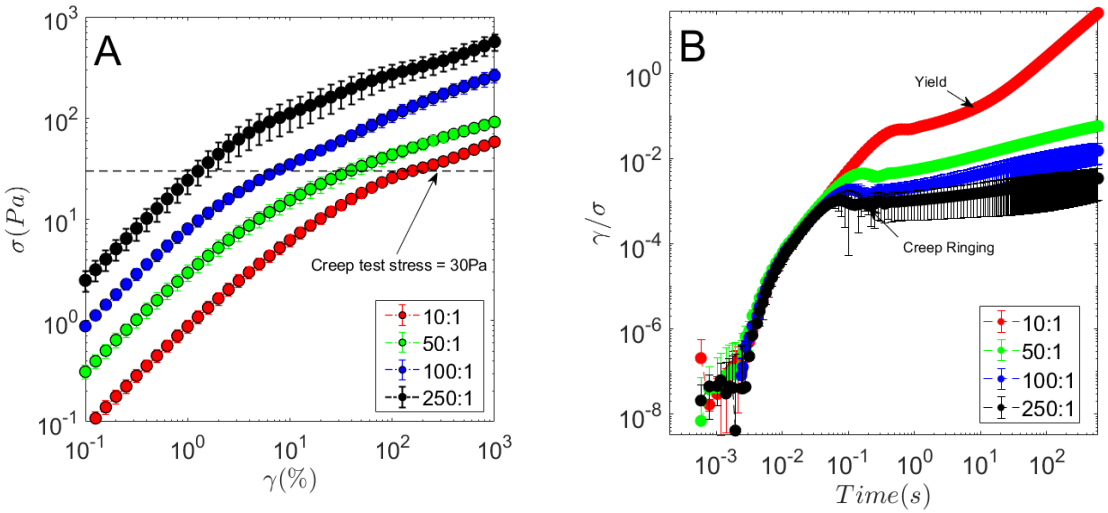

Figure 4-9: (a) Stress strain plots of *Pantoea* mixtures UDP: WT, dashed line represents the stress selected for subsequent creep tests. Plotted is the mean ± standard deviation (n=5) biological replicates. The legend represents the UDP: WT ratio. (b) Creep plots of *Pantoea* Mixtures. Creep curves were performed at a stress of 30 Pa. 10:1 exhibits yielding, which can be seen by the increase in gradient after an initial plateau. Plotted is the mean ± standard deviation (n=5) biological replicates.

structure began to yield as indicated by the increased gradient of $\frac{\gamma}{\sigma}$ beyond ~10 seconds. This result demonstrated that 30 Pa was outside the LVER for 10:1. Ratios of 50:1, 100:1 and 250:1 were tested in the linear region and fitted to the Burgers model. At short time periods the viscosity η_1 of each mixture was comparable with 50:1 having a viscous coefficient η_1 of 53.10$\pm$ 4.21 kPa.s, 100:1 a η_1 of 58.47$\pm$ 6.32 kPa.s and 250:1 a η_1 of 59.68$\pm$ 10.43 kPa.s. The differences into short term behavior were reflected within the elastic term G_1. Increasing the UDP ratio effectively decreases the amylorvan concentration and resulted in G_1 increasing from 4.58$\pm$ 0.57 kPa at 50:1 to 11.89$\pm$ 2.48 kPa at 100:1 and 32.12$\pm$ 7.35 kPa at 250:1. Longer time behavior is represented by G_2 and η_2. Increasing UDP concentration from 50:1 to 100:1 to 250:1 resulted in an increase to the long-term elasticity $G_2$from 0.69$\pm$ 0.28 kPa to 2.37$\pm$ 0.83 kPa and 12.01$\pm$ 5.82 kPa respectively. This result indicates that as the concentration of amylovoran reduces *Pantoea* biofilms are increasingly elastic over short and long-time scales. However, the short time scale viscosity η_1 was comparatively insensitive to a reduction in polysaccharide concentration, while the long-term viscosity η_2 increased with decreasing amylovoran.

Mixture	G_1 (kPa)	G_2 (kPa)	η_1 (kPa.s)	η_2(kPa.s)
50:1	4.58$\pm$ 0.57	0.69$\pm$ 0.28	53.10$\pm$ 4.21	47.69$\pm$ 5.73
100:1	11.89$\pm$ 2.48	2.37$\pm$ 0.83	58.47$\pm$ 6.32	141.44$\pm$ 24.57
250:1	32.12$\pm$ 7.35	12.01$\pm$ 5.82	59.68$\pm$ 10.43	215.34$\pm$ 50.25

Table 4-2: Calculated Burger coefficients from the 4 element Burger model for *Pantoea* Mixtures (UDP:WT). G_1 and $\eta_1$are the initial short time response elasticity and viscosity, respectively. G_2 and η_2 are the long time elastic and viscous responses, respectively. Presented is the mean $\pm$ standard deviation (n=5) biological replicates.

4.3.7 Increases in UDP concentration reduce the $\frac{I_3}{1}$ gradient

To quantify the degree of non-linearity within each mixture, the ratio of the 3rd Fourier harmonic to the fundamental harmonic from each stress waveform was calculated, *Figure 4-10*. In the linear region the magnitude of the 3rd harmonic is negligible and below the floor level of noise in the rheometer system. When linearity is violated the stress sinusoidal response distorts. The magnitude of the distortion can be quantified

by measuring the magnitude of higher harmonics. The 3rd harmonic is typically used from the Fourier transformed stress signal and increases with strain when the LVER is exceeded. The region where linearity is initially violated until the cross over strain γ_C is known as the medium amplitude oscillatory shear (MAOS) region and has recently been used to test an array of polymer melts. MAOS test protocols have an advantage over LAOS tests in that samples aren't tested to destruction, allowing repeat measurements of expensive/small volume samples. The gradient of the Fourier ratio in the MAOS region as a function of strain has been used to interpret the crosslinking density and the degree of connectivity in polymer structures. Here the ratio of the third to first harmonic is used to characterize the rate of accumulation of non-linearity (a proxy for structural rearrangement) in the mixture samples. At low concentrations of UDP, the $I_{3/1}$ gradient is appreciably higher than at higher UDP concentrations. The $I_{3/1}$ gradient for the 10:1 mixture was 1.49$\pm$ 0.02. The $I_{3/1}$ gradient reduced with increasing concentration of UDP, 50:1 was 1.12$\pm$ 0.06 and 100:1 was 0.74$\pm$ 0.04 until a gradient at 250:1 of 0.64$\pm$ 0.03. Noticeably the initial magnitude of $I_{3/1}$is higher for more concentrated UDP mixtures, suggesting that a higher packing fraction biofilm rearrange at lower strains, in accordance with the Payne Effect. In the 50:1 and 100:1 UDP: WT mixtures $I_{3/1}$ displayed two distinct

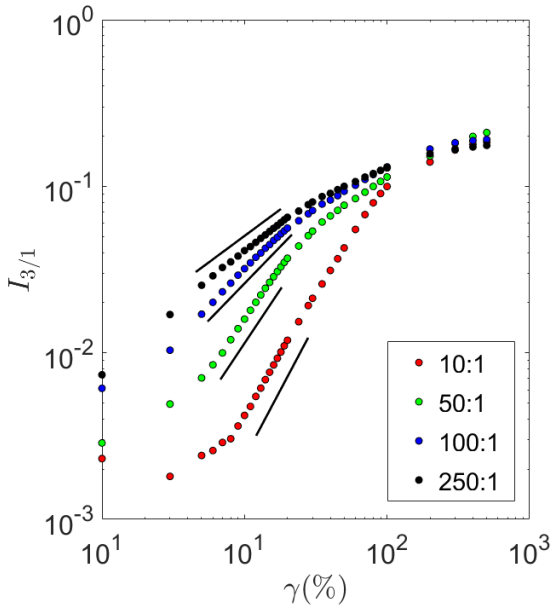

Figure 4-10: Intrinsic non- linear parameter plot of the ratio of the third Fourier harmonic to the first Fourier harmonic as a function of strain for *Pantoea* mixtures (UDP: WT). Black lines denote the MAOS gradients. MAOS gradients are taken from when $I_{3/1}$ initially begins to increase.

gradients. This differed from 10:1 and 250:1 mixture which featured less distinct changes in gradient as the strain approached the LAOS transition points.

4.3.8 Intercycle Chebychev method reveals a transition in non-linear thickening behavior

To explain the results from cycle averaged amplitude sweeps, $I_{\frac{3}{1}}$ measures and detect the nonlinear behavior contributing to the intermediate power law rheology for the 50:1 and 100:1 samples, the intercycle Chebychev method from Ewoldt was adopted. Nonlinear thickening and thinning behavior is represented using the T ratio plot, *Figure 4-11*. The *Pantoea* WT exhibited thickening $(T > 0)$ between γ = 177 %-501 % ranging between T = 0.24± 0.01 – 0.29± 0.03. Adding UDP to WT resulted in a transition from nonlinear viscoelastic thickening to thinning $(T < 0)$. Increasing the UPD concentration from 50:1 to 100:1 caused the emergence of thinning behavior to reduce from γ = 89.1 % to γ = 31.6 % a result agreeing with our earlier observation linked to the Payne effect. However, as the UDP ratio increased from 100:1 to 250:1, the onset of thinning shifted back to γ = 89.1 %. In addition, thickening was also observed which peaked at 0.11± 0.05 at γ = 8 % before the onset of thinning. The change in rheological behavior coincides with the transition from a clustered microstructure seen in the 50:1 mixtures to the homogeneously packed structure type

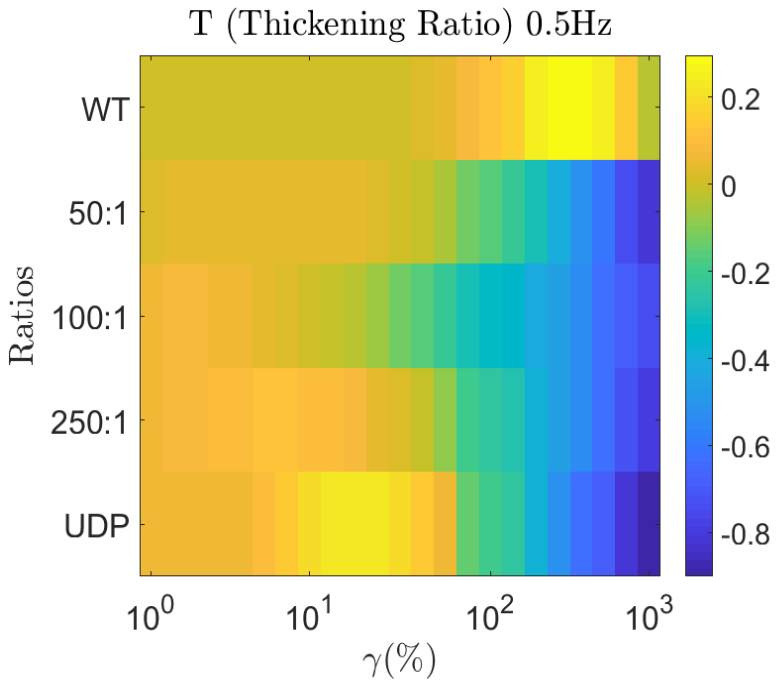

Figure 4-11: Thickening fingerprint for *Pantoea* mixtures (UDP:WT). Measurements were performed at a frequency of 0.5 Hz and at strains γ = 0.1 -1000%. The colour bar represents the magnitude of the thickening ratio T. WT represents pure *Pantoea* WT biofilms and UDP represents pure *Pantoea* UDP biofilms.

of 250:1. In UDP monoculture biofilms thickening occurred between γ = 5.6 %- 44.7 % peaking at a value of 0.23$\pm$ 0.04, this was followed by a transition to a thinning regime.

Next, the intercycle stiffening behavior (S) of each mixture is compared. *Pantoea* WT displayed a drop in S from 1.71$\pm$ 0.48 to -6.07$\pm$ 1.50 at γ = 354.8 -501.2 %, symptomatic of bulk fluidization, also known as the unjamming point (Perge et al., 2014). In the 50:1 biofilm the strain value for bulk fluidization increased to γ = 707.9 %. The UDP mutant and the 250:1 mixture had comparable stiffening values through the strain range, both peaking γ = 1000 %, where S = 0.67$\pm$ 0.05 for UDP and S = 0.65$\pm$ 0.06 for the 250:1 mixture. This indicates elastic similarity between these samples which agrees with the cycle averaged data presented in the previous amplitude sweep. The Lissajous bowditch plots for each tested frequency and at 7 selected strains γ are found in the appendix F.

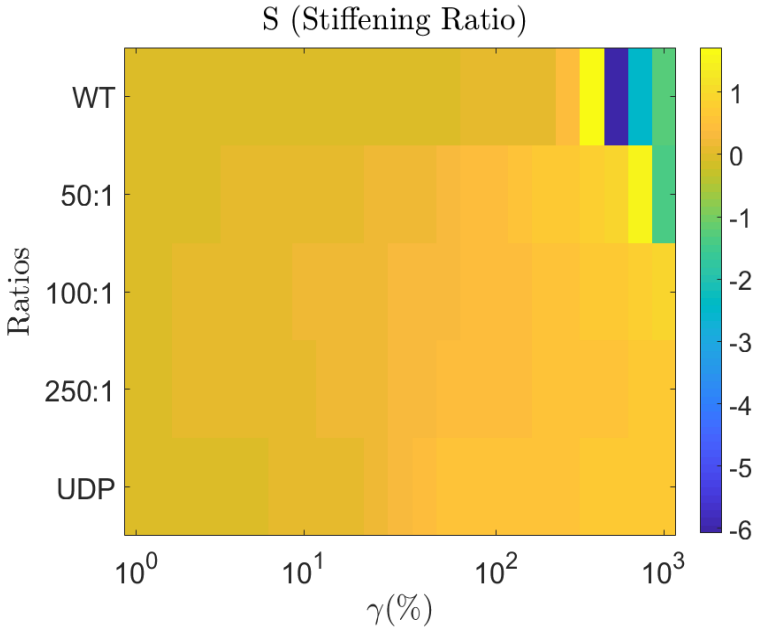

Figure 4-12: The stiffening ratio for *Pantoea* mixtures (UDP:WT), the measurements were performed at a frequency of 0.5 Hz from a strain of 0.1 – 1000 %. The colour bar represents the magnitude of the stiffening ratio S. Displayed are the mean values from 5 biological replicates.

4.3.9 Sequence of physical processes analysis

In order to measure the changes in instantaneous viscoelastic response caused by varying the ratio of *Pantoea* sp. YR343 to *Pantoea* sp. YR343 UDP the sequence of physical processes (SPP) is used. Plots of transient phase angle δ_t were constructed from averaged transient loss $G''_t(t)$ and transient storage moduli $G'_t(t)$ as defined in chapter 2. The SPP method is used to detect the type of deformation behavior for

each *Pantoea* sp. mixture occurring during an oscillatory cycle of amplitude γ. Deformation events can be elastically dominated, dependent upon strain, or viscously dominated, dependent upon strain rate. The balance between elastic and viscous behavior is represented using δ_t. For $\delta_t < \frac{\pi}{4}$ the material's response is dominated by elastic deformation whereas for $\delta_t > \frac{\pi}{4}$ viscous dissipation dominates the material response. Due to the mathematical construction of the SPP analysis, the balance between elastic and viscous contributions (δ_t) can be tracked through a complete sinusoidal oscillation, $0 < t < 2\pi$. The maximum strain γ is therefore found at $t = \frac{\pi}{2}$ and $t = \frac{3\pi}{2}$ while maximum strain rate is found at $t = 0$ and $t = \pi$.

The pure *Pantoea* WT biofilm was dominated by reversible elastic deformation at strains γ < 50 %, signified by δ_t being lower than $\frac{\pi}{4}$, *Figure 4-13*. This behavior corresponds to the large LVER of the WT biofilm. Between γ = 50 - 100 % the transient phase angle δ_t increased to around $\frac{\pi}{4}$, but remained independent of t. This behavior indicates a parity in recoverable elastic deformation and unrecoverable viscous dissipation across the amplitude cycle. Between γ = 100- 150 % the transient phase angle increased to $\delta_t \approx \frac{\pi}{2}$, *Figure 4-13 dashed boxes*. The broad region of $\delta_t \approx \frac{\pi}{2}$ is representative of the *Pantoea* WT biofilm deformation being viscously dominated and unrecoverable, indicative of significant microstructural rearrangement. This region occupied much of the biofilm response through t, and only reduced in value when t centred around $\frac{\pi}{2}$ and $\frac{3\pi}{2}$. This indicates that *Pantoea* WT yielding and rearrangement was strain rate driven and dominated by the viscous component of the biofilm network. When strain γ increased above 150 % the *Pantoea* WT biofilm completely yielded, as indicated by regions where $\delta_t > \frac{\pi}{2}$. This behavior corresponds to complete fluidization and microstructural breakdown. The region occurred over a broad range of the oscillatory cycle, however featured a sub region where δ_t peaked, *Figure 4-13 dotted boxes*.

As previously shown, mixing EPS deficient UDP with WT causes a transition in the viscoelastic phase behaviour from viscoelastic liquid to glassy behaviour. The SPP analysis enables the visualisation of this phase transition as a function of time. Mixing UDP with WT resulted in the appearance of a yielding spike through the strain range centred around $t = \pi$ in the oscillatory cycle for each of the UDP: WT mixture, *Figure*

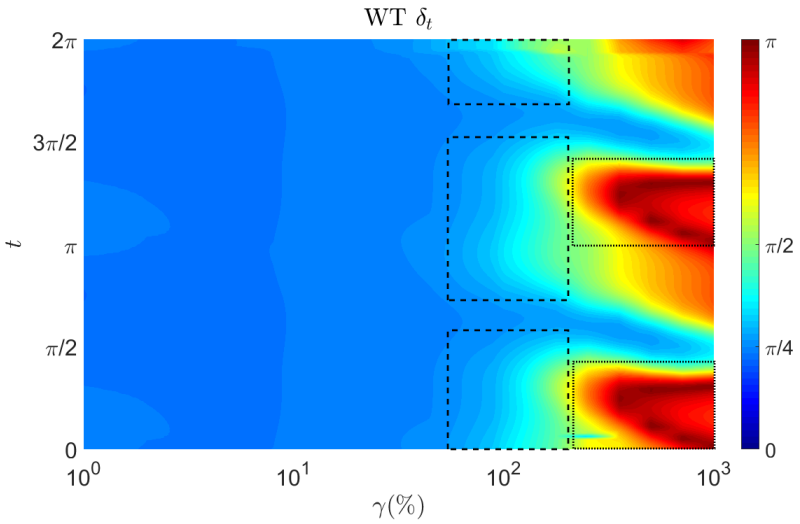

Figure 4-13: Transient Phase angle plot of *Pantoea WT* performed at 0.5 Hz. In this plot the time point during a complete oscillation cycle between 0 and 2π where the transient phase angle δ_t is measured at t. The strain amplitude of each oscillatory cycle is represented by γ. The colourbar represents the transient phase angle δ_t. The transient phase angle is measured from 0 to π. A δ_t of 0 represents a fully elastic Hookean response, a δ_t of π represents a fully viscous response and complete structural yielding. The dashed boxes highlight the regions where the biofilm begins to exhibit yielding. The solid boxes represent regions where the biofilm is nearing a completely fluidised state within a strain cycle.

4-14 dashed boxes. The emergence of this yielding region signifies an increase in viscous rearrangement events (as strain rate is at a maximum through t = 0 and t = π), which are absent in the pure WT biofilm. The mixtures had an increased dependence of δ_t on t at small strains. This indicates the mixture structures are more responsive to the strain wave than the WT, *Figure 4-14 dot-dash box*. Compared to the WT biofilm in the 50:1 mixtures the sub regions of complete yielding $\delta_t > \frac{\pi}{2}$ becomes narrower in t, *Figure 4-14a dotted box.* This trend continues with the 100:1 mixture. From 50:1 to 100:1 the yielding spike increases, occurring at higher magnitude at lower strains *Figure 4-14b dashed box* while for the rest of t, deformation is increasingly elastically dominated *Figure 4-14b dot dash box*. The change in low strain behavior is also accompanied by a change to the high strain behavior. The subregion of complete yielding $\delta_t > \frac{\pi}{2}$ shifts and extends to lower strain regions, *Figure 4-14b solid box*. When the UDP ratio is increased from 100:1 to 250:1, the yielding spike reduces. This represents a decrease in strain rate dependent yielding in the low strain region. This behavior is accompanied by a

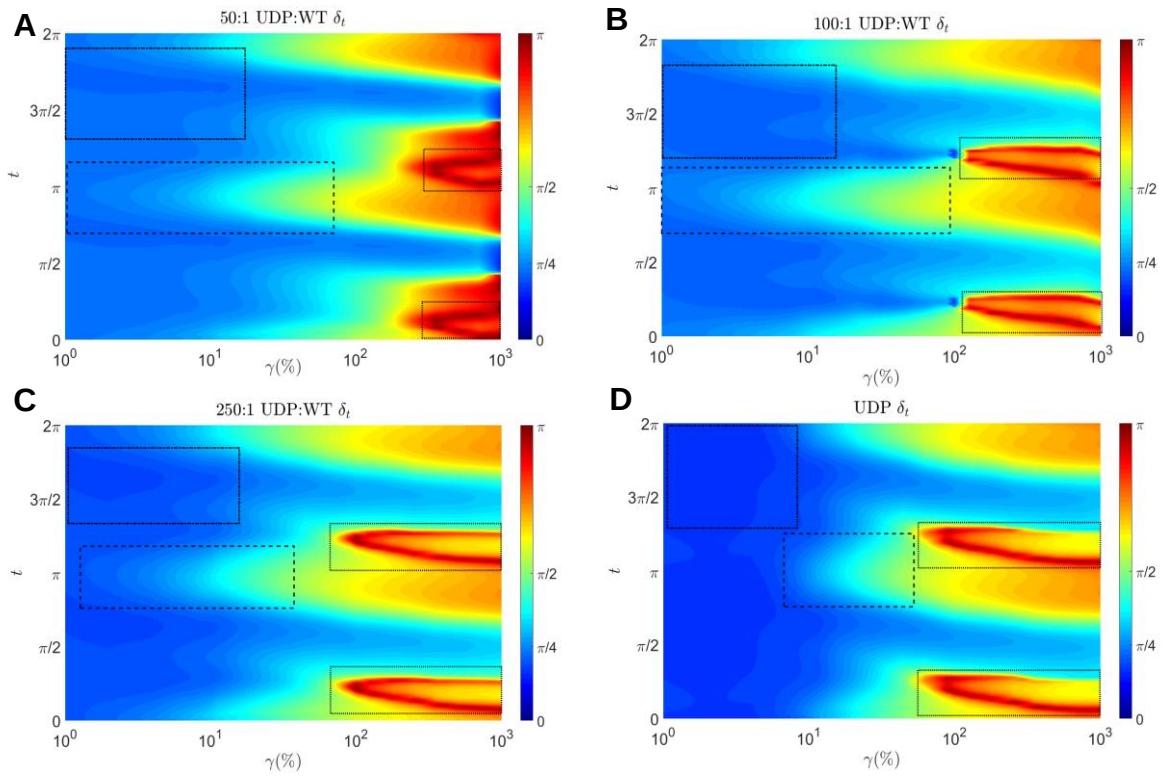

Figure 4-14: Transient Phase angle plot of *Pantoea.*sp at increasing UDP: WT ratios. In this plot the thick dash line boxes in the top left of each plot represent the region where strain γ for the respective strain amplitude is largest during an oscillation cycle. This region for each biofilm is elastically dominated. By reducing the amylovoran quantity in the biofilm this region grew increasingly elastically dominated. The dash box in each plot represents the region where strain rate was highest during the respective oscillation cycle. This region reduced in prominence as amylovoran concentration was reduced, signifying an increase in elasticity. The solid line box's represent the region during an oscillation cycle at the respective strains where the material was completely yielded. With a reduction in amylovan this region grew to occur at lower strains. At high amylovoran concentration 50:1 the region of complete yielding grew to occur over a larger proportion of the oscillation.

reduction in δ_t for the rest of t through the oscillation cycle, *Figure 4-14c dashdot dash box*. Compared to the 100:1 mixture the subregion of complete yielding for 250:1 occurred at lower strains, *Figure 4-14c dotted box*. The trend of a reducing yield peak at small strains continued when the packing fraction was increased from 250:1 to the monoculture of UDP, *Figure 4-14d dashed box*. The small strain behavior of UDP also was increasingly elastic in response of the oscillation cycle, *Figure 4-14d dashdot box,* whist the region of complete yielding remained comparable to the 250:1 mixture, *Figure 4-14d solid*.

4.4 Discussion and conclusions

In this chapter I have shown how the rheology of a bacterial biofilm is influenced by the secretion of EPS. The EPS composition of *Pantoea* sp. was manipulated through

genetic modification by deleting the UDP operon which controls the secretion of amylovoran, a capsular acidic polysaccharide. The WT *Pantoea* sp. had a macrostructure which was swelled and had a corresponding microstructure with a low packing of ϕ= 0.16$\pm$ 0.04. This could be due to the high concentrations of amylovoran, a hydrophilic exopolysaachride, which would increase the equilibrium swelling point of the biofilm. The bacteria within the microstructure were separated into small clusters. These microstructural characteristics are like other strains which are known to have amylovoran as an EPS component such as *Pantoea stewartii* and *Erwinia pyrifoliae* (Tecon & Leveau, 2016).

Pantoea WT was characteristic of a viscoelastic liquid and reptation polymer network by displaying a constant viscous modulus G'' until yielding and then shear thinning. Repatating entangled polymer networks form in concentrated polymer solutions through the constriction of polymer motion by topological constraints by neighboring chains. The relaxation time of this network is influenced by polymer molecular weight and chain relaxation. The molecular weight of amylovoran is between 1- 5 MDa depending upon the culture conditions. When produced from agar plate culture conditions amylovroan is known to have a molecular size of 5 MDa (Schollmeyer et al., 2012). As the polysaccharide network is sheared entanglements break and reform. When the strain rate is above the rate of entanglement formation the material shear thins. If the rate of entanglement formation between different regions of the chain is above the shear rate the viscosity of the solution remains constant.

Deletion of UDP which controls amylovoran production resulted in a microstructure which tightly packed ϕ= 0.64$\pm$ 0.08. The rheological behavior of the UDP deletion biofilm was typical of glasses and weak gels, exhibiting a prominent vicious overshoot. In repulsive glassy systems, weak bonding interactions and physical jamming and caging are primarily responsible for the stress bearing capacity of the structure.

The difference in amylovoran production between WT and UDP meant that by culturing mixtures of these two strains the amylovoran concentration and packing fraction could be varied in a controlled manner. This framework enabled the study of the phase transition between the viscoelastic liquid behavior of WT and glassy rheology of the UDP mutant, analogous to the methodology used to study colloidal gel phase transitions. In these studies, the control variables are colloid packing

fraction and colloidal bonding strength, which can be controlled using polymer concentration, ionic concentration and pH (Mendoza et al., 2018).

The concentration of amylovoran was inversely linked to the packing fraction and bacterial cluster size. Bacteria have been shown to aggregate due to various mechanisms such as, interactions depletion attraction (Dorken et al., 2012) and through autoagglutinins such as Ag43 in *E. coli* and PIA in *S. aureus* (Ageorges et al., 2019; Haaber et al., 2012). Amylovoran is a cell surface bound capsular exopolysaccharide, analogous to an absorbing polymer on a colloidal surface. The timelapse images of the WT showed cell – cell repulsion with increasing polymer concentration. Increased EPS secretion resulted in increased bacterial separation. Computational studies of polymer bound colloidal mixtures have demonstrated that colloidal packing density is reduced with an increase in polymer molecular weight and concentration (Howard et al., 2019). However, the precise clustering mechanism of *Pantoea* sp. warrants further study.

When the ratio of UDP in the mixture was increased thus decreasing amylovoran concentration the elastic G' and viscous moduli G'' increased. The increase in G' and G'' coincided with an increase to the packing fraction. This is a commonly found characteristic of colloidal gel systems, as the relative proportion of stiff (in comparison to the polymer chains) colloids increases. In the case of a biofilm, the colloids being the bacteria and the polymer chains being the EPS. It was also recently shown that gel elasticity is a function of the concentration of interconnected clusters (Whitaker et al., 2019). The yield strain of the *Pantoea* sp. mixtures reduced with increasing concentrations of UDP, a phenomenon known as the Payne effect. The dynamics of the Payne effect within the *Pantoea* sp. biofilm was revealed using the intercycle T ratio. The T ratio revealed a mild thickening behavior in the pure WT biofilm. The magnitude of thickening reduced and the emergence of thinning ($T < 0$) occurred at lower strains at intermediate packing fractions (50:1 and 100:1 ratios). This effect has been seen in a variety of particle filled polymer networks and has been attributed to the increasing hydrodynamics effect of the particles on the polymer network whereby the associated effect amplifies the local strain of the polymer matrix (Y. Song & Zheng, 2016). When the packing fraction transitions from intermediate to high (250:1 or pure UDP) the onset of thinning ($T < 0$) increases to higher strains. Preempting the onset of thinning behavior is the emergence of a thickening region ($T < 0$). The transition in

T behavior from low, intermediate to high ratios of UDP could potentially be explained by the considering the relative contribution of the EPS network against the bacteria network at each ratio. The balance between these two networks could be noticed in the viscous moduli G'' curve of the 10:1, 50:1 and 100:1 mixture. These curves exhibited two distinct regions of power law behavior. The first in the MAOS region $G''_{MAOS} \sim {\gamma_0}^{-\frac{1}{2}\upsilon}$ and the second in the LAOS region $G''_{LAOS} \sim {\gamma_0}^{-\upsilon}$ where υ is the exponent for the power law behavior after the cross over point in the LAOS region for ratios. The double power law gradient found in G'' is symptomatic of a system with two distinct processes which each are a confluence of multiple relaxation times. Reptating polymer networks feature a spectrum of relaxation times due to the variety of entanglement configurations present. The presence of two power law gradients may relate to the presence of these two dominant networks within the biofilm. The EPS network being predominantly structured through polysaccharide entanglements and the second being the bacteria/bacteria jamming interactions.

The intercellular bonding strength within *Pantoea* sp. biofilms appears to be low due to the repulsive glassy behavior of the UDP pure strain and viscoelastic liquid state of the WT specimen. Thus a collision incident between clusters is likely to cause cluster breakup, which is reflected through the reduced strain at which thinning behavior is exhibited as the concentration of UDP is increased from 50:1 to 100:1. When the ratio is increased to 250:1 the rheology becomes dominated by glassy jamming. This is reflected by the emergence of the type III hump and an increased strain before the crossover point and the onset of thinning. In this phase, thinning is preceded by thickening (type III) which is caused by the increased energy required to rearrange the jammed rod state.

This chapter demonstrated how the ratio of EPS to bacteria is a main determinant of the biofilm rheological response in biofilms which feature an EPS with hydrophilic capsular polysaccharides. The *Pantoea* sp. WT produced large quantities of EPS containing amylovoran. The high concentrations of EPS and large molecular weight of amylovoran appeared to form an entangled EPS network which dominated the rheological response. This resulted in a viscoelastic liquid behavior akin to a reptating gel network with a low strength (low G' in the LVER) and a high yield strain. The rheological response of *Pantoea* sp. UDP: WT mixtures displayed a two-stage power law behavior which was attributed to the interplay between the EPS network and the

bacteria network, akin to a double network hydrogel (Jia Yang et al., 2018). The balance between which of the two networks dominated the rheological response was controlled by the EPS concentration of the biofilm. Reducing the polymer concentration coincided with an increased packing fraction and shift in the T behavior of the biofilm. This shift was related to the Payne effect and hydrodynamic interactions between the bacteria and EPS which amplified local strain of the polymer matrix. The reduced polymer concentration resulted in an increase to nonlinear strain thinning at intermediate packing fractions, which was depicted in the SPP analysis. The thinning behavior was then suppressed at lower EPS concentration as bacteria/bacteria constriction through increased topological caging increased in prominence.

In this chapter I demonstrated how the secretion of a hydrophilic capsular exopolysaccharide influences the microstructural and rheological phases behavior in a PGPR bacterial strain. I showed that by controlling EPS through mixing a wild type EPS producer with an EPS deficient mutant the controlled study of biofilm phase transitions could be performed. The nonlinear techniques of LAOS provided detailed information into to the thinning and thickening associated with the rheological phase behavior which could be interpreted with reference to EPS network properties and the constriction of the bacteria network.

The framework used here therefore could be relevant towards studying how EPS components interact within the EPS network and used to access how changes in entanglements and crosslinking between components alters biofilm behavior in high shear environments. This frame work could be used to study EPS network modified due to polymer/protein interactions, such as LecB and Psl in *P. aeruginosa* and the impact of alginate on phase behavior and large strain deformation (Kovach et al., 2017; Passos da Silva et al., 2019). The framework may also be relevant for investigating how biofilm EPS concentration alters porous media hydrodynamics, such as soil, where biofilm fluid interactions can substantially influence flow fields (Aufrecht et al., 2018, 2019; Carrel et al., 2018). Conversely the concepts of LAOS may have application in tailoring the rheological properties of synthetically modified PGPR specifically for a target plant species and specific soil properties.

Chapter 5 Results: Multiplicity of yielding in bacterial biofilms

5.1 Introduction

Over the previous two chapters it has been demonstrated how LAOS provides insights into the yielding dynamics of chemically treated biofilms, where attraction and packing influence macroscale rheology, and shown how EPS secretion influences phase transitions in *Pantoea* sp. YR343 resulting in transitions between viscoelastic liquid and glassy behavior. In this chapter I compared the rheology of 4 bacterial strains which exhibit contrasting rheology. I investigated 2 rod-shaped bacteria: *Comamonas denitrificans* and *Pseudomonas fluorescens*, a cocci bacterium, *Staphylococcus epidermidis* and a diplococcus bacterium, *Neisseria polysaccharea*.

Biofilms display rheological behavior similar to colloidal glasses and gels. Depending upon the culture method, air-solid interface, interfacial liquid-air or submerged liquid flow, biofilms exhibit properties ranging from viscoelastic liquid to gel (Pavlovsky et al., 2013; P A Rühs et al., 2014). The rheological behavior of a biofilm varies with the physicochemical environment and the phenotypic expression of proteins and polysaccharides. In corresponding soft matter systems, the rheology is mediated by the colloidal packing fraction and the interaction strength. The magnitude of colloid /colloid interaction strength and packing fraction determines the viscoelastic response of soft matter systems which can be categorised into 3 distinct phases; liquid, glass or gel (Y. Xu et al., 2018). These phases are widely studied in well characterised colloidal systems where the packing fraction, electrolyte concentration, pH and temperature are modulated to control interparticle interaction strength (Y. Xu et al., 2018). As the packing density of a structure is increased, the interaction strength between the particles becomes of increasing importance (Solomon & Spicer, 2010). Gels and glasses can be subcategorized as attractive or repulsive (Zaccarelli & Poon, 2009). Glassy rheology is primarily driven by the self-confinement of particles by their nearest neighbors and this structure is termed a cage. In an unperturbed structure, particles remain within their cages, but as the material is sheared particles hop and migrate in and out of the cages, resulting in structural rearrangement and yielding. Glassy systems are primarily formed by repulsive long-range interactions (Voigtmann, 2014). Gel systems have comparatively high particle interaction strength, which results in the self-assembly of networked structures at low packing fractions. Depending upon the strength of interaction, the gel is categorised

as either repulsive or attractive. In a repulsive system the attraction between particles is weak, and systems display a single yielding process (Shao et al., 2013; Zhi et al., 2015). With increasing interaction strength an additional yielding process occurs, resulting in two step yielding. To fully capture the rich dynamics which occur in each viscoelastic phase and construct structure property relationships, both linear and nonlinear rheology need to be quantified. The type of rearrangement dynamics which cause the transitioning from elastic to viscous dominant behavior can be captured using Large amplitude oscillatory shear (LAOS). The LAOS techniques used here enable us to quantitatively characterize emergent non-linear behavior, providing a platform to compare gel/glassy rearrangement processes.

5.2 Materials and methods

5.2.1 Bacterial strain and growth

P. fluorescens Migula 1895 and *Comamonas denitrificans* 123 ATCC 700936 were purchased from the ATCC and *Staphylococcus epidermidis* 096R was kindly provided as a gift from Prof. Grant Burgess, Newcastle University, UK. *Neisseria polysaccharea* 31001 was provided as a gift from Dr. Nick Jakubovics, Newcastle University, UK. *P. fluorescens* Migula, *Comamonas denitrificans* 123 and *Staphylococcus epidermidis* 096R were cultured overnight in Tryptic soy broth (TSB). Cultures were adjusted to an OD of 0.2. 150 µl of culture was distributed over the surface of 1 % TSA plates using an L-shaped spreader. *P. fluorescens* and *C. denitrificans* were incubated at 24 ^{o}C for 48 hours. *S. epidermidis* was incubated at 37 ^{o}C for 48 hours. *Neisseria polysaccharea* 31001 was cultured in BHI broth overnight anaerobically at 37 ^{o}C in candle jars and distributed over chocolate agar plates in an anaerobic chamber for 48 hr at 37 ^{o}C.TSB agar (per 1 L) contained 30 g tryptic soy broth (Sigma) and agar concentration dependent upon experiment (ranging from 0.5 % - 1.5 %). Blood agar contained 37 g/L brain heart infusion (Oxoid), 5 g/L yeast extract (Merck) and 15 g/L agar (Merck). After sterilization, 5 % (v/v) defibrinated horse blood (TCS Biosciences) was added. Chocolate agar was prepared using the same recipe except that, after the addition of horse blood, the medium was heated to 70 °C for 10 min.

5.2.2 Non-linear rheology - LAOS

A strain-controlled rheometer (Malvern Kinexus Pro+) was mounted on a passive isolation plate with a 20 mm parallel plate geometry. 120 grit paper was adhered to the top and bottom geometries to prevent slip. The temperature was controlled at 25

ºC using a Peltier plate and a solvent trap was used to prevent desiccation. Biofilm samples were collected from the agar surface using a ground microscope slide. Tests were performed at a gap height of 1 mm. Amplitude sweeps were taken at ω= 0.5 Hz at a strain γ = 0.1 – 1000 %. Samples were pre-sheared at 0.5 Hz for 120 seconds, then left for 600 seconds to stabilise before performing amplitude sweeps. Raw data was preprocessed using custom MATlab scripts and boxcar averaged with a window size of 50. MITlaos, a MATlab based GUI was used to perform Chebychev analysis. SPP analysis was performed using the MATlab routine SPP_v1, kindly provided by Dr Simon Rogers.

5.2.3 CLSM

48 hr biofilm samples were imaged *ex situ*. Briefly samples were stained with 0.25 ml of 10µM Syto 63, a cell permeable DNA stain in for 30 mins. Biofilms were then stained for 30 mins with 1µg/ml FM 1-43, a lipophilic styryl compound which targets the plasma membrane of cells (Thermofisher,UK). 25 µL of sample was then collected using a ground microscope slide and transferred to a 25 µL geneframe. A #1.5 coverslip was used to seal the frame. Imaging was performed using a Leica SP8 stimulated emission depletion (STED) confocal microscope with 100 x 1.4 N/A oil immersion lens. Biofilms were imaged at a depth of 10 µm from the zero position. FM 1-43 was excited at 488 nm and Syto 63 at 640nm. This corresponds to an excitation separation distance of 172 nm to ensure blead through between channels was negligible. Syto 63 and FM 1-43 were acquired in separate channels with emission filters of 498 – 630 nm for FM 1-43 and 670-750 nm for Syto 63.

5.2.4 Image analysis

Images were processed using ImageJ and custom MATlab scripts. Briefly, images were bandpass filtered, Mexican hat filtered then median filtered before an Otsu BW threshold was applied. The packing fraction was calculated using equation,

$$\phi_{pack} = \frac{Npixel=1}{N_{total\ pixels}}, \qquad [80]$$

using the same method as was applied in chapter 4.

5.2.5 *C. denitrificans* flocculation protocol

C. denitrificans was cultured in TSB for 48 hr at 24 ºC with shaking until an OD of 2, measured at 595 nm using a photospectrometer (Cary 100 Bio). 4 ml of culture was centrifuged for 90 seconds at 1000 g and 3 ml of culture media was discarded. The culture was then pipette up and down 10 times with a 1000 µL pipette and vortex

mixed for 10 seconds to re-suspend. Cells were stained with 10 µM Syto 9 (Thermofisher, UK), a cell permeable DNA strain. The stained culture was covered with tinfoil to block light and left for 30 mins. After 30 mins the culture was then pipette up and down 10 times with a 50 µL pipette and vortex mixed for 10 seconds before transfer to a 50 µL geneframe slide which was produced by layering 2 x 25 µL (10 mm x 10 mm x 0.25 mm) Geneframes (Thermofisher,UK) and sealed with a no 1.5 coverslip. Time lapses images of gelation were performed 15 µm above the coverslip surface at 40 x to enable imaging of the resultant structure and avoid counting bacteria which had sedimented to the coverslip surface. Timelapses were performed for 15 mins with imaging every 10 seconds on a fixed field of view (FOV). Experiments were repeated with 3 different samples. After the timelapse experiment, a Z stack of the structure was acquired from the coverslip (z = 0 µm) to z = 40 µm in steps of 0.5 µm using a 40 x objective. Finally, a tilescan of 5 x 5 (n = 25) images was taken 15 µm above the coverslip at 40 x.

5.3 Results

5.3.1 *Comamonas denitrificans* displays attractive glass/gel rheology

To compare the short- and long-range attractions of each of the selected strains, the rheological signatures were first determined. *Comamonas denitrificans* exhibited a linear elastic modulus of 10000± 500 Pa and a viscous moduli of 3000± 150 Pa, *Figure 5-1* which corresponded to a phase angle of 16 °± 2 °. G' begun to decrease above strain values of 0.1 % which coincided with the decrease of the viscous moduli at a strain of 0.25 %. Between 37 -100 % strain the elastic moduli G' displayed a plateau shoulder region. Within the same strain range the viscous moduli G'' crossovers with G'($G' = G''$) and G'' increases from 131± 37 Pa to 218± 52 Pa. The σ vs γ curve had two distinct regions; the initial linear gradient transitioned into a region of slow stress accumulation between 0.37 -13 %. Between 19 -139 % the stress strain gradient increased until a second reduction in stress strain gradient event at 139 %, signified by the dashed arrow in *Figure 5-1*. Similar amplitude sweeps have been seen for mixtures of positively and negatively charged combinations of colloidal particles with radius 210 nm at a packing fraction of 0.52. Here the dominating attractive interactions between particles was electrostatic with a strength ~5 kT. The electrostatic strength in this system was controlled by NaCl

concentration (Zong et al., 2013). Therefore, it appears that *C. denitrificans* exhibits rheology like an attractive glass/gel, a novel finding in biofilms.

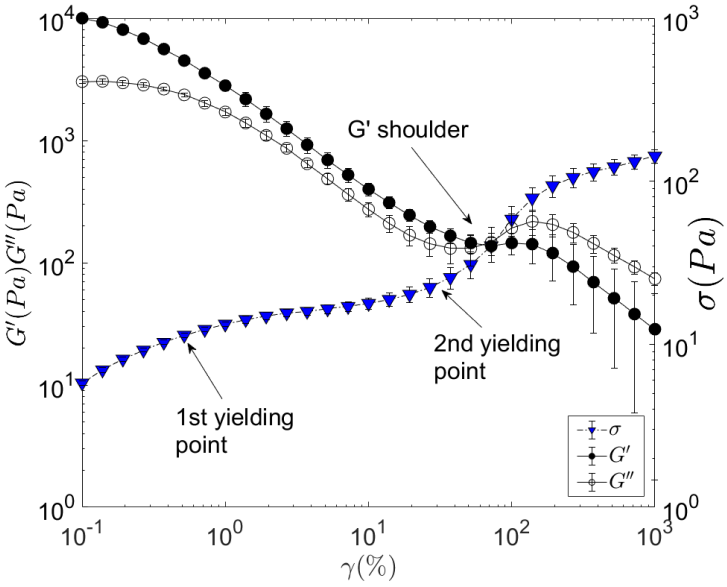

Figure 5-1: Amplitude Sweep of *Comamonas denitrificans* biofilm grown for 48 hr, the amplitude sweep is performed at a frequency of 0.5 Hz. The elastic modulus G' exhibits a shoulder as the viscous stress overshoot begins, this characteristic has been seen in attractive colloidal gels. Presented is the mean and standard deviation from n = 3 biological replicates.

5.3.2 *Pseudomonas fluorescens* displays repulsive glassy rheology

P. fluorescens exhibited a storage modulus of 1250± 175 Pa with a viscous modulus of 100± 17 Pa, corresponding to a phase angle 5 °± 1 °. The LVER extended until a strain of 19.8 % and a cross over ($G' = G''$) occurred at a strain of 26.8 %, *Figure 5-2*. As with chapter 1, *P. fluorescens* exhibited a type III hump within the MAOS region before a yield strain was reached.

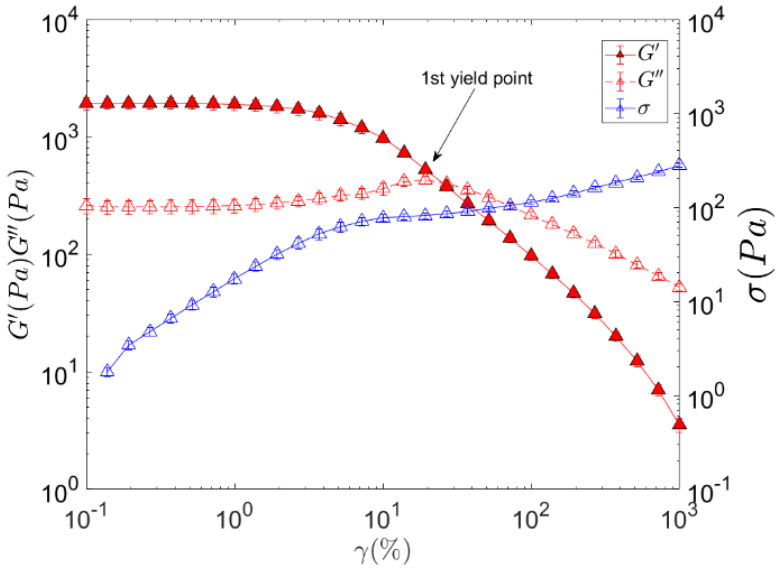

Figure 5-2: Amplitude Sweep of *Pseudomonas fluorescens* biofilm grown for 48 hr, the amplitude sweep is performed at a frequency of 0.5 Hz. Presented is the mean and standard deviation from n = 5 biological replicates.

5.3.2 Rheology of diplococcus and coccus bacteria

The elastic moduli of the diplococcus strain *N. polysaccharea* were measured to be 275± 21 Pa with a viscous moduli of 45± 6 Pa, *Figure 5-3,* corresponding to a phase angle of 10 º± 2º. The LVER extended until 26.8 %, and the cross over (G' = G'') occurred at a strain of 71.94 %. The yielding behaviour of *N. polysaccharea* was absence of a stress overshoots, characteristic behaviour of a viscoelastic liquid and reptation polymer networks. In addition, a reduction from G'' = 43± 5 Pa to 36± 4 Pa

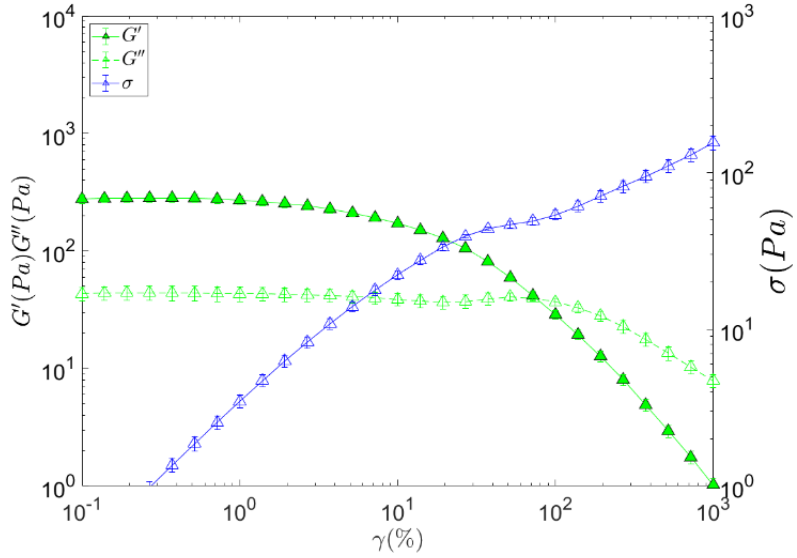

Figure 5-3: Amplitude Sweep of *Neisseria polysaccharea* biofilm grown for 48 hr, the amplitude sweep is performed at a frequency of 0.5 Hz. Presented is the mean and standard deviation from n = 5 biological replicates

before the crossover point (G' = G'') was noticed. This feature will be discussed in more detail using the more sensitive Chebychev analysis approach.

S. epidermidis exhibited an elastic moduli of 1100± 591 Pa with a viscous modulus of 80± 39 Pa, *Figure 5-4*, corresponding to a phase angle of 5 °± 3 °. The LVER of *S. epidermidis* was exceeded at 1 % and cross over (G' = G'') at a strain of 37.2 %. These values are an order of magnitude higher than previously measured rheometer values which is attributed to the agar plate grown method used in this study in comparison to submerged in-situ grown examples (di Stefano et al., 2009; Pavlovsky et al., 2013). *S. epidermidis* exhibited two noticeable peaks in its viscous moduli, the first occurring at 1.9 % and the second at 37 %. The nature the G'' curve for *S. epidermidis* is suggestive of two step yielding. In combination with *C. denitrificans* this first time that this two-step yielding has been observed in biofilm. *S. epidermidis* displayed yielding curves reminiscent of rheology from a multitude of attractive colloidal gel studies conducted at intermediate to high packing fractions (Koumakis & Petekidis, 2011; Shao et al., 2013) and pickering emulsions (Hermes & Clegg, 2013). For clarity the values of elastic modulus G', viscous modulus G'', LVER limit and cross over point for each biofilm are presented in Table 5-1.

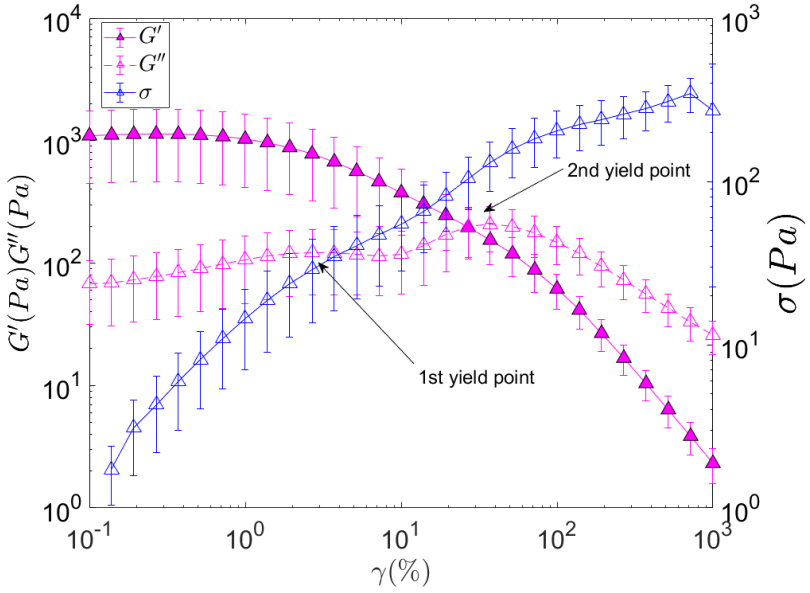

Figure 5-4: Amplitude Sweep of *Staphylococcus epidermidis* biofilm grown for 48 hr, the amplitude sweep is performed at a frequency of 0.5 Hz. Presented is the mean and standard deviation from n = 3 biological replicates

Strain	G' (Pa)	G'' (Pa)	γ_c ($G' = G''$)	LVER
C. denitrificans	10000± 501	3030± 15	71.94%	0.013%
P. fluorescens	1277± 179	101± 18	26.8%	7.2%
S. epidermidis	1098± 591	68± 39	26.8%	1.3%
N. polysaccharea	276± 22	43± 6	71.94%	26.8 %

Table 5-1: Linear elastic and viscous modulus values, crossover strain and Linear viscoelastic limit values for each tested biofilm. Presented are mean and standard deviation from n=3-5 biological replicates

5.3.3 *C. denitrificans* and *S. epidermidis* exhibit two step yielding

The elastic stress $\gamma G'$ to strain plot is shown in *Figure 5-5a* . $\gamma G'$ is used instead of σ to decompose the elastic stress from the viscous stress contribution to illustrate when elastic failure (yielding) occurs in each biofilm. Deviation from a linear $\gamma G'$ vs γ gradient signifies yielding. *C. denitrificans* and *S. epidermidis* exhibit two stages of yielding, *C. denitrificans* yields at 18.43± 7.71 Pa and 124.6± 28.92 Pa whilst *S. epidermidis* yields at 20.97± 12.29 Pa and 63.40± 21.93 Pa. The most notable difference between the $\gamma G'$ vs γ behaviour of *C. denitrificans* and *S. epidermidis* is between the first and second yielding points. After the first yield point in *C. denitrificans* the elastic stress $\gamma G'$ plateaus until 40.65± 17.46 Pa after which the stress gradient increases rapidly to the second yielding point at 124.6± 28.92 Pa. For *S. epidermidis* biofilms this plateau is absent, instead a second linear gradient is

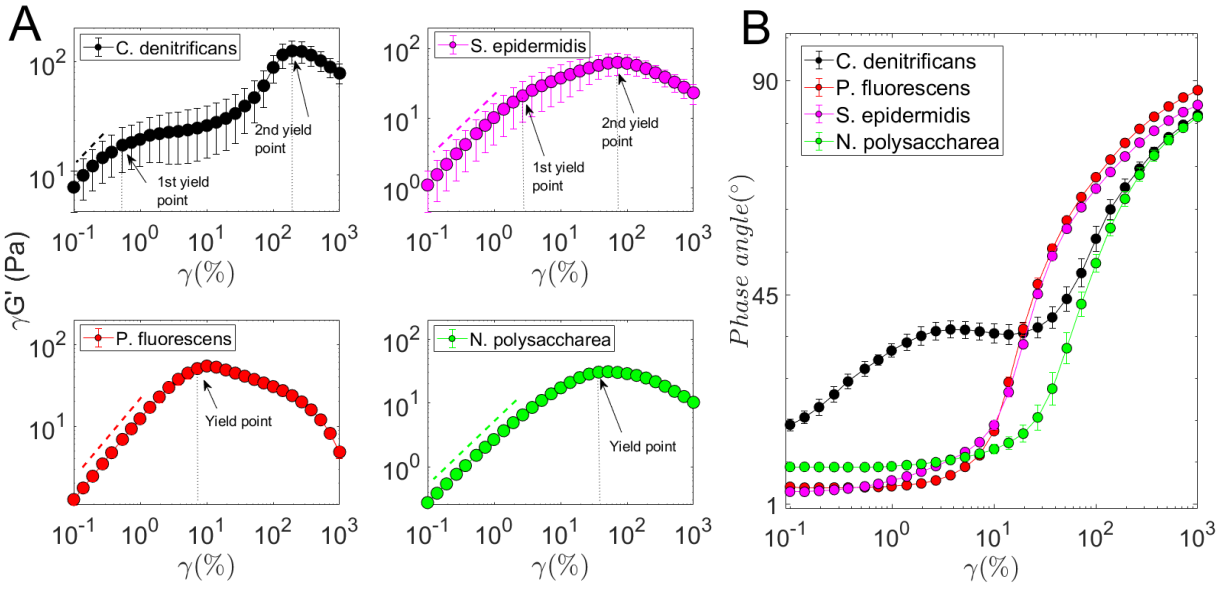

Figure 5-5: (A) Elastic stress vs strain curves for *Comamonas denitrificans*, *Pseudomonas fluorescens*, *Staphylococcus epidermidis* and *Neisseria polysaccharea*. The black labelled arrows denote the yielding points of each biofilm. (B) Plot of the corresponding phase angles for each biofilm with increasing strain. *C. denitrificans* displays a plateau region at intermediate strains.

present until the second yielding point at 63.40± 21.93 Pa. After the second yield point $G'\gamma$ declines linearly, demonstrating both biofilm species follow the Herchel Buckley shear thinning relation when fluidised. The elastic stress strain behaviour of *P. fluorescens* exhibited a single yield point material at 50.77± 6.52 Pa. *N. polysaccharea* displayed a yield point at 30.37± 1.10 Pa which outwardly appeared like *P. fluorescens*. However the rate of change in gradient of $G'\gamma$ (%) after the first yield point in comparison to the rate of change of $G'\gamma$ (%) after the second yield points of *C. denitrificans* and *S. epidermidis* and the singular yield point of *P. fluorescens* is more gradual. Plots of the phase angle for each bacterial strain are found in *Figure 5-5b*. *C. denitrificans* exhibited the highest initial phase angle 17.68 °±1.26 °, signifying that *C. denitrificans* had a larger viscous component to its total viscoelastic response than the other bacterial strains. The phase angle increased at low strains before a plateau at approximately 37.35 °±1.88 °, signifying that increases in strain in this region resulted in an equal reduction in elastic and viscous moduli. Interestingly the phase angle behaviour of *P. fluorescens* and *S. epidermidis* was highly comparable across the tested strain range. The initial phase angle of *P. fluorescens* was 4.64 °± 0.31 ° and *S. epidermidis* was 3.62 °± 0.19 °. *N. polysaccharea* had a slightly higher phase angle of 8.83 °± 0.81 °.

5.3.4 Two step yielding mechanism depends on the range of EPS network bonding and bacterium topology

To investigate the apparent differences in yielding behaviour within each biofilm the nonlinear intracycle thickening ratio (T) was accessed, *Figure 5-6*. *C. denitrificans* exhibited rheology akin to an attractive gel/glass structure with short range bonding. Interestingly T was neutral (≈ 0) before the first yielding point, this behaviour was despite an evidential reduction in elastic and viscous moduli between γ = 0.1 - 1 % in the cycled averaged data. This suggests that short length scale rearrangements/bond breaking are causing the simultaneous drops in G' and G''. *C. denitrificans* exhibits two yielding points, as was shown in *Figure 5-5.* After the first yielding point which corresponded to $\gamma = 2.6$ %, thinning occurred. This is signified in the (T) ratio plot by the dashed back arrow, *Figure 5-6* . The first step in two step yielding has been attributed to breakdown in short range bonds. This would occur within a biofilm due to the breakdown of intercellular EPS bonds. The second yielding point for *C. denitrificans* is preceded by a T minima of -0.30± 0.02, this behaviour is like the behaviour exhibited by $FeCl_2$ treated *P. fluorescens* in chapter 1. After the minimum T increased to -0.09± 0.01, indicating the contribution of a minor thickening

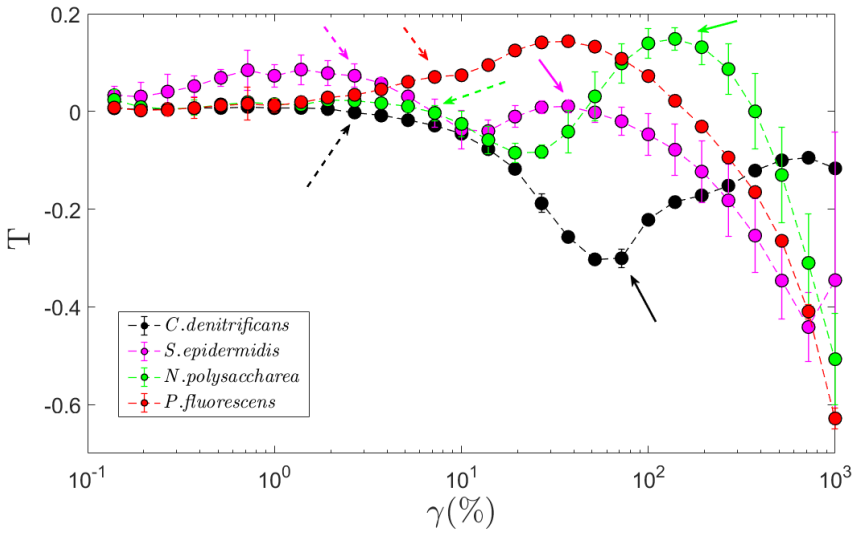

Figure 5-6: Thickening ratio (T) for tested 48hr grown biofilms. Black arrows represent yielding points from stress strain curve for *C. denitrificans*, pink arrows, *S. epidermidis*, green arrows, *N. polysaacharea* and red arrows, *P. fluorescens*. Dashed lines signify the first yielding point and solid lines represent the second yielding point. Presented is the mean± standard deviation from n= 3- 6 biological replicates.

mechanism after the second yield point. *S. epidermidis* exhibited an increase in T to 0.08± 0.04 before the first yielding point at $\gamma = 2.6$ % after which T begins to fall to -0.04± 0.02 signifying a breakup of biofilm into clusters. The cycle averaged moduli G' and G'' of *N. polysaccharea* displayed were characteristic to a viscoelastic liquid, however the T ratio revealed the presence of two step nonlinear thickening. The two-step process occurred at a first yielding point of $\gamma = 7.2$ % and the second at $\gamma = 139$ %. The minima of T after the first yielding point was -0.08± 0.02 and maxima of the second yielding point was 0.15± 0.02. Both *S. epidermidis* and *N. polysaccharea* had T curves with a peak – trough – peak shape. However, the difference between the minima and maxima of the trough and peak for greater for *N. polysaccharea.* The similarity in curve shape between these two strains maybe due to morphology. Both strains have low aspect ratios which were comparable. *S. epidermidis* is a cocci shaped bacterium and had an aspect ratio of 1.03± 0.06. The morphology of *N. polysaccharea* is slightly different due to its diploccous shape, however had a comparable aspect ratio of 1.13± 0.08. The packing fractions were also comparable, *S. epidermidis* ϕ = 0.48± 0.02 vs *N. polysaccharea* ϕ = 0.47± 0.04. The similarities in packing fraction and bacterium aspect ratio suggests that differences in EPS network composition and structure are likely responsible for the differences between T peak and trough values and the strains they occurred at. However, the similarities in the shape of the T curve are more than likely due to similar topology. The

representative LB plots of each of the tested bacteria are found in the appendix G. The first step in two-step yielding in attractive colloidal glass and microgels systems has been attributed to in cage nearest neighbour motion, a process of colloids constricted by nearest neighbours locally yielding and the breakdown short range interparticle bonds. The second step has been attributed to the breakdown of the stress bearing topological constrains of nearest neighbour cages (Genovese, 2012). In a biofilm system the first yielding process would be analogous to short range intercellular bonds breaking down locally between nearest neighbour cells at small strains. The second process would then be due to breakdown of the longer-range EPS polymer components which bind the together macrostructure of the nearest neighbour cages. The macrostructural breakdown of the longer-range EPS network would cause unjamming of the nearest neighbour cages, resulting in flow alignment and shear thinning (Zong et al., 2013).

To compare the breakdown of cage strength the G_{cage} moduli is used. The cage modulus of each biofilm is seen in *Figure 5-7*. For *C. denitrificans*, G_{cage} reduces rapidly from 10590$\pm$ 540 Pa at γ = 0.15 % to a minimum of 317$\pm$ 8 Pa at γ = 37.33 %. After this point the cage moduli increases from the minimum to a stable value centred around 639$\pm$ 11 Pa. As with the T ratio *S. epidermidis* and *N. polysaccharea* display similar trends in G_{cage} behaviour. The curves are shifted, reflecting the higher

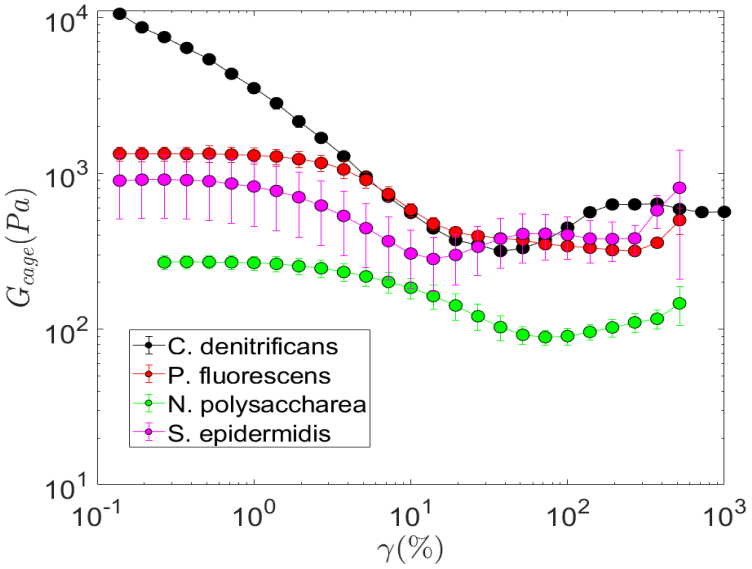

Figure 5-7: G_{cage} plot for each biofilm, *C. denitrificans* displays a significant drop as strain increases and converges around the plateau values of *S. epidermidis* and *P. fluorescens*. Shown are the mean$\pm$ standard deviation from 3- 5 biological repeats.

strength of *S. epidermidis* 912± 398 Pa compared to 270± 26 Pa and both feature a linear portion at low strains γ < 1 %. Both curves then decrease in value towards a minimum of 282± 108 Pa and 88± 10 Pa before recovering to 382± 80 Pa and 117± 16 Pa respectively. Interestingly the respective ratio between the starting strength and G_{cage} minimum of the cocci/ diplococcus strains was lower than for the rod bacterium strain. *S. epidermidis* and *N. polysaccharea* had a reduction ratio of 3.46± 0.31 and 3.08± 0.15, which compared to 4.37± 0.41 and 33.47± 1.79 for *P. fluorescens* and *C. denitrificans*. This observation suggests that biofilms with rod bacterium lose an increased proportion of their residual strength in comparison to cocci/diplococcus bacterium. This is likely due an interplay between the reorientation and alignment of the rod geometry under flow. This effect would cause the breakdown of topological constrains and bacterial jamming, resulting in a more exaggerated reduction in cage strength in comparison to cocci and diplococci bacterium. For *P. fluorescens* biofilms a singular well-defined drop in G_{cage} was present, this suggesting a singular yielding mechanism. The convergence of G_{cage} values between *C. denitrificans*, *S. epidermidis* and *P. fluorescens* at high strains is suggestive of comparable cage strength. This convergence occured when the short-range components in the EPS matrix's of *C. denitrificans* and *S. epidermidis* broke down.

As with chapter 1 and 2 each biofilm species was fingerprinted using the SPP method. This method is used to build phase maps which can fully describe the occurrence of yielding events. Depending upon where yield occurs, we can make assumptions as to the range of attraction controlling the rheology of each tested bacterium. The phase plot of *C. denitrificans* highlights how yielding predominantly occurs at low strain values *Figure 5-8a* red and cyan boxes. These two distinct bands are present during each half cycle and the first centred around $t = \frac{\pi}{2}, \frac{3\pi}{2}$ where strain is largest and between $t = 0$ and $t = \pi$ and $t = \frac{3\pi}{2}$ and 2π denoting the occurrence of both strain dependent (red boxes) and strain/strain rate dependent (cyan boxes) yielding events. The magnitude of yielding in the cyan region was higher than the strain dependent yielding events. These two yielding regions were out of phase with each other, suggesting that the first yielding point in *C. denitrificans* could be a confluence of two separate breakdown processes, one strain dependent, the other strain/strain-rate dependent. It is possible the strain dependent mechanism (red box)

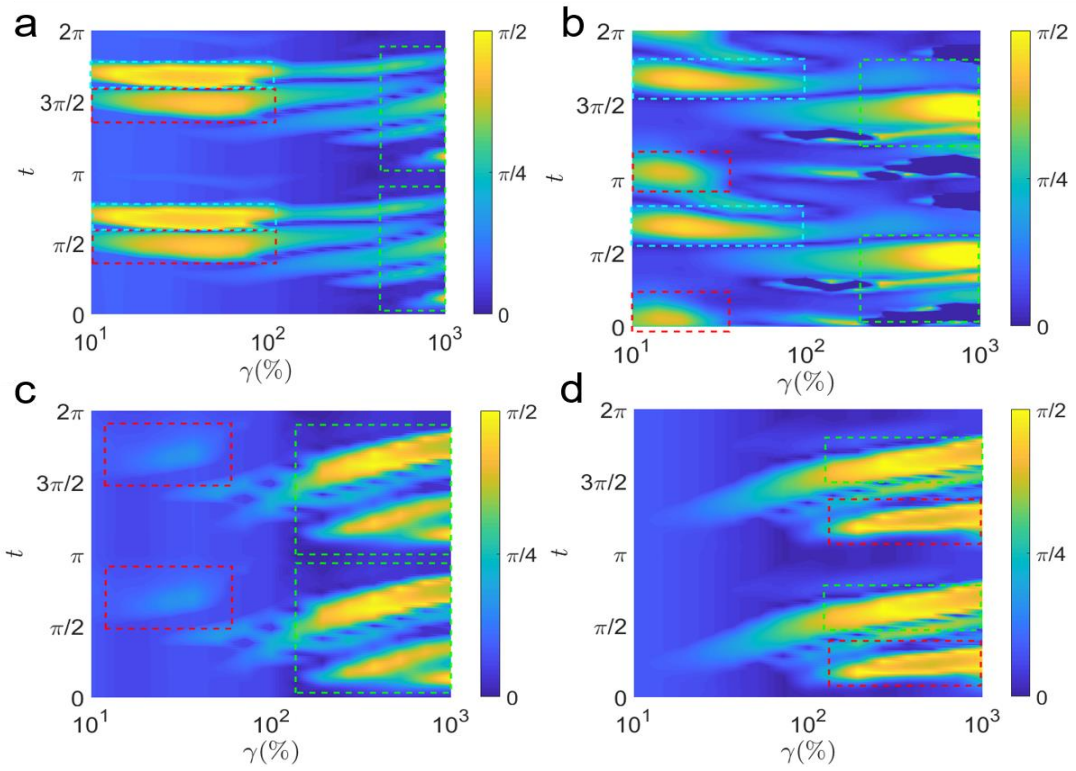

Figure 5-8: Transient phase angle plots from amplitude sweeps performed at 0.5 Hz at strain amplitudes ranging from γ of 0.1 % to 1000%. The instantaneous phase angle δ_t was continuously measured throughout each amplitude cycle at time t (a) *C. denitrificians,* the red dashed boxes denote a strain dependent 1st stage yielding process whilst the cyan boxes denote a strain/strain rate dependent 1st stage yielding process. The green boxes denote 2nd stage yielding processes (b) *S. epidermidis,* the red dashed boxes denote a strain rate dependent 1st stage yielding process whilst the cyan boxes denote a strain/strain rate dependent 1st stage yielding process. The green boxes denote a 2nd stage yielding process (c) *N. polysaccharea,* the red boxes denote the faint emergence of a 1st stage yielding behaviour. The green boxes denote strain/strain rate dependent yielding. (d) *P. fluorescens,* the green boxes and red boxes denote strain/strain rate dependent yielding.

relates to the breakdown of short-range intercellular bonds, and the second (cyan box) relates to the reorientation of bacteria. The second stage yielding bands (green boxes) for *C. denitrificans* are significantly less prominent that the first yield zone and comparatively against to the other species. This suggesting that the 1st yielding stage in *C. denitrificans* is responsible for most of the microstructural modification and is suggestive of an EPS network which is short ranged with a much weak long-range structure. For *S. epidermidis* the SPP phase diagrams clearly shows two separate regions of yielding, an initial yielding stage followed by a second stage of yielding, *Figure 5-8b*. The second stage of yielding in *S. epidermidis* had a higher δ_t than *C. denitrificans*. This suggests that at low strains the macrostructure of *S. epidermidis* is preserved to a greater extent than *C. denitrificans*, as an increased proportion of structural breakdown occurs in the second yielding region. In *N. polysaccharea* a

small region of partial yielding was apparent at low strains, *Figure 5-8c*. This reinforces the observation from the *T* plot that a mild form of two step yielding is present, supporting a classification of *N. polysaccharea* as a weakly attractive glass (red boxes). The second yielding phase in *N. polysaccharea* at higher strains is more prominent (green boxes). The phase plot for *P. fluorescens* as expected from chapter 1 features a singular dominant region of yielding extending unbroken from strains of ~ 60 %, *Figure 5-8d*.

5.3.5 Microstructural analysis of each biofilm

To assess the differences in microstructure between each rheologically characterised strain CLSM was used to image each of 48 hr grown biofilms, *Figure 5-9*. *P. fluorescens* had a packing fraction of 0.62± 0.03. The cells were tightly packed, with small regions of axially aligned cells. The structure of *S. epidermidis* had a packing fraction of 0.55± 0.02 with an absence of voids, the average diameter of each cell was 0.68± 0.05 µm. The structure of *N. polysaccharea* had a packing fraction of 0.58± 0.04, however the diplicoccus individual cells have an aspect ratio slightly

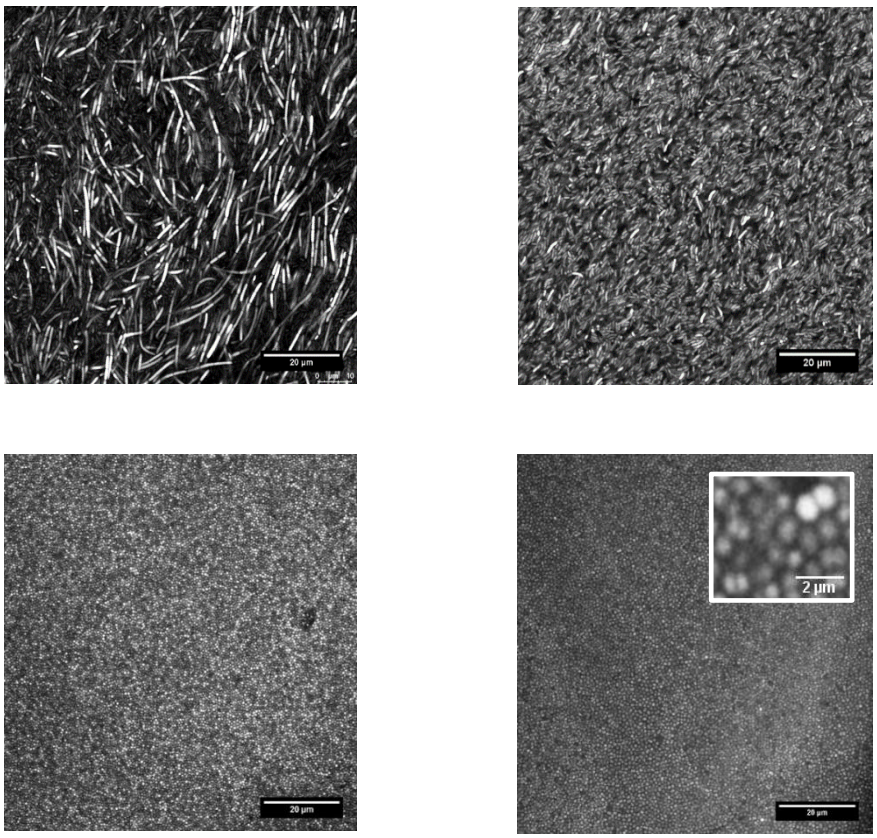

Figure 5-9: Representative CLSM images of 48 hr agar plate grown biofilms (A) *C. denitrificans* a morphology of interwoven filamentous networks with an apparent nematic ordering and alignment (B) *P. fluorescens* (C) *S. epidermidis* (D) *N. polysaccharea,* inset depicts the diplococcus shape.

higher than 1 at 1.13± 0.08 with a major axis of 0.73± 0.05 µm. From the similarity in packing fractions between each of the tested strains, *Figure 5-10* it can be concluded that the rheology differences between the strains was the result of differences in EPS composition and cell morphology. For spherical colloid glasses/gels the range of bonding length can be compared by estimating the localization length r_L, using

$$G' \approx \frac{\phi}{r_L^2}, \qquad [82]$$

where G' is the storage modulus and ϕ is the packing fraction. This relation was predicted using naïve mode coupling theory (NMCT) and has been applied experimentally to compare bonding and caging dynamics within binary mixtures of colloids (Douglas & Kenneth, 2008; Jia et al., 2015). The localization length r_L is used to compare spherical shaped *S. epidermidis* and *N. polysaccharea*. *S. epidermidis* had a r_L =0.032D and *N. polysaccharea* had a r_L =0.056D, where D is the average cell diameter. The higher value of r_L indicates an increased amount of caging in comparison to bonding within *N. polysaccharea.*

C. denitrificans *had a packing fraction of 0.65± 0.02 and a microstructure which was composed of aligned filaments of cells. The filaments intertwine and coil in the axial direction resulting in alignment. Two types of junction zones can be seen, the axially adjacent aligning filaments looked in proximate, which suggests the possibility of bonding between aligned filaments. Overlapping filaments were also seen, these two types of networks have been theorised to occur in supramolecular assembly of gels*

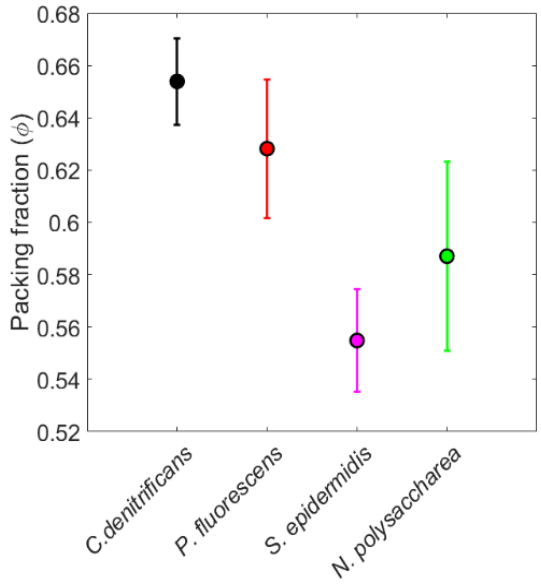

Figure 5-10: Calculated packing fraction of each bacterial biofilm. The packing fraction of the biofilms were broadly comparable. Presented is the mean ± standard deviation from 8 FOV.

(Raghavan & Douglas, 2012). The occurrence of filamentous growth in C. denitrificans *has been observed in liquid culture. Filamentous growth is known to occur due to several mechanisms. Filaments can form due to physical connection preventing disconnection of daughter cells, this can be caused by proteinaceous complexes. Additionally, an inability to separate from daughter cells can also be due to cells with defects in cell division (Claessen et al., 2014). The averaged dimensions and aspect ratio of each strain is summarised in*

Table 5-2.

Bacteria	Length (µm)	Width (µm)	Aspect Ratio (r)
C. denitrificans	2.79± 0.21	0.64± 0.08	4.38± 0.35
P. fluorescens	2.27± 0.19	0.43± 0.04	5.22± 0.17
S. epidermidis	0.68± 0.05	0.65± 0.04	1.03± 0.06
N. polysaccharea	0.73± 0.05	0.65± 0.06	1.13± 0.08

Table 5-2: Summary of the length, width and aspect ratio of individual bacteria taken from 13 replicate CLSM images. Presented is the mean± standard deviation.

5.3.6 *C. denitrificans* forms gel like aggregates in culture

The striking similarities between the rheology of mixtures of oppositely charged colloids with strong short-range attraction and attractive colloidal gels and the LAOS behavior of *C. denitrificans* led me to hypothesis that cell-cell bonding and the filamentous growth mode of *C. denitrificans* was a major contributing mechanism. Since *C. denitrificans* exhibited attractive glassy/gel behaviour I hypothesised that the short-range interactions between bacteria would be large in comparison to similarly rod-shaped *P. fluorescens*. Colloidal gels with a high attractive strength form gelated space spanning structures at low packing fractions, to test if *C. denitrificans* behaved as an attractive colloidal gel the aggregation dynamics of concentrated cultures of *C. denitrificans* and *P. fluorescens* (OD = 2 concentrated 3 x) were compared. To test for the presence of network formation a series of microscopy experiments to visualise aggregation were performed. *Figure 5-11* shows representative images of a time-lapse experiment comparing *C. denitrificans* and *P. fluorescens* aggregation. *P. fluorescens* showed a homogeneous distribution of bacteria from T = 0 mins to T = 15 mins. *C. denitrificans* had a high initial presence of clusters interspersed with single bacteria, after 7.5 mins a space spanning network had developed in length and number of junctions (cell-cell attachment). The network densified and formation plateaued after 15 mins. Junction formation in *C. denitrificans* was consistently higher than *P. fluorescens.* After 15 mins tile scan imaging were performed which showed

the self-similar fractal like network structure of *C. denitrificans*. The network was structured with cellular clusters jointed by “floppy bridges”, a morphology typically seen in colloidal gels (Tsurusawa et al., 2019).

The range of interaction between neighbouring cells will be a function of the EPS surface and exopolymers. From the CLSM gelation experiments and the rheological signature it appears that *C. denitrificans* is mainly structured by short range intercellular bonding which results in the filamentous morphology as seen in *Figure 5-9*a. *C. denitificans* is known to grow in long filamentous chains encased within a thick polysaccharide capsule (Andersson et al., 2009). The cell- cell attraction is evidently short ranged as can be seen from the CLSM gelation experiment. The short-ranged behaviour is seen in SPP data where yielding mainly occurs at low strains. The short-range attraction could be the result of proteinaceous bridges or autoagglutinins between mother and daughter cells. Aggregation of *C. denitrificans* may also be due to secretion of hydrophobic polysaccharides and the formation of a cell capsule as recently seen in *Bacillus licheniformis* (Z. Wang et al., 2017). Based

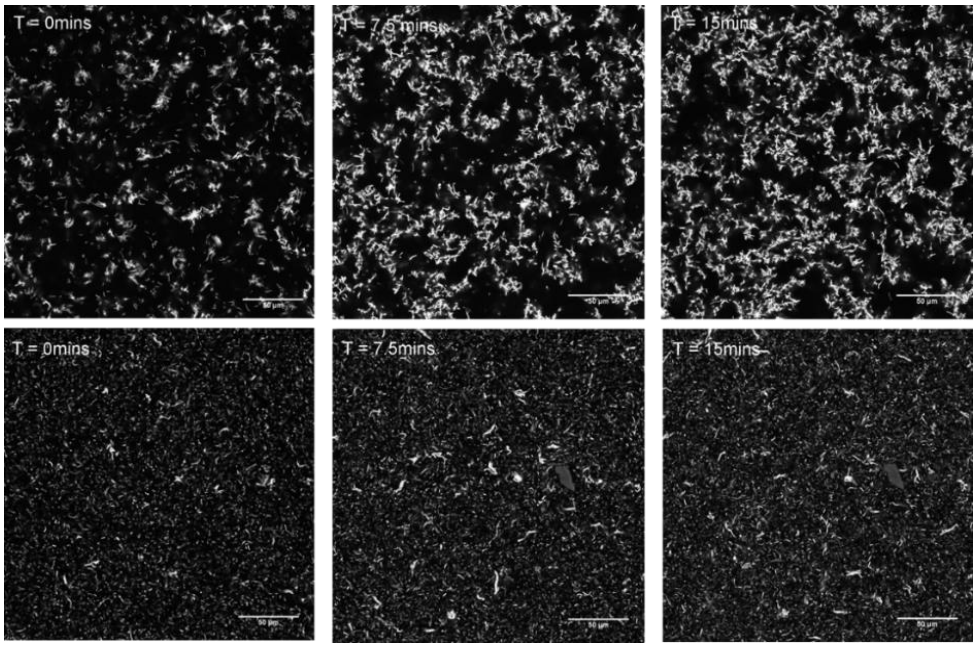

Figure 5-11: (Top row) Micrographs display a 15 mins timelapse of a concentrated *C. denitrificans* culture (OD = 2, 3x concentrated) autoaggregating. After 15 mins a space spanning network is formed which is composed of clusters connected by floppy bridges. (Bottom row) A liquid culture of *P. fluorescens* (OD = 2, 3x concentrated) does not display autoaggregative behaviour. After 15 mins no space spanning network is formed, and the cells are homogeneously distributed within the FOV.

upon the apparent short-range filamentous behaviour of *C. denitrificans* it is probable that the mechanism responsible for the low yield strain and first yielding step is due

to the breakdown of bacterial filaments as strain is increased. An additional contributing factor behind the strong shear thinning behaviour of *C. denitrificans* is the highly aligned structure of the filaments. Strong alignment in the orientation fields of many rod colloidal and disk mixtures results in increased shear thinning (Philippe et al., 2013). *C. denitrificans* begins with a native structure with has high orientation order which may explain its shear thinning behaviour at low strains. At low strains the rotation and movement of bacterial filaments which lead to structural rearrangement and viscous dissipation is minimal. The lack of viscous dissipation was reflected in the low in the thickening ratio T from γ = 0.1 - 10 %, which had a maximum at 10% of 0.05$\pm$ 0.01. The breaking of the short range bacterial filaments bonds causes a corresponding reduction in G' from 10000$\pm$ 502 Pa to 400$\pm$ 47 Pa and G'' from 3000$\pm$ 110 Pa to 131$\pm$ 38 Pa in the γ = 0.1 - 10 % region. The elastic modulus initially reducing at a higher rate than viscous moduli up until a strain of 2 %, as see in the initial increase in phase angle. Here the phase angle reaches a plateau value of 37°. Similar behaviour of a low linear viscoelastic region (γ < 0.4%) with simultaneous declines in viscous and elastic modulus have been seen in systems of oppositely charged colloidal particles (Yiwu et al., 2013). Here it was noted that for binary mixtures, maintaining a stable cage is challenging due to geometric selection where particles can only form bonds with oppositely charged particles when in a specific orientation (Meakin & Djordjevic, 1986). *C. denitrificans* also exhibited weak caging behaviour, as was shown in *Figure 5-7*, which could be due to geometric selection of “sticky” regions on the bacterial surface. At low strains short range broken bonds would accumulate, causing a reduction in elastic modulus G'. The low strain values in this region preserving the long-range microstructure restricting particle rotational mobility. As strain increases the number of bond breaking events increases, reducing both G' and G''. The plateaued phase angle behaviour could be due to the simultaneous occurrence of increased bacterial alignment with flow and short-range bond breaking. At strains above the phase angle plateau the interaction distance for short range bonding is exceeded, causing a rapid decline in G' . The increased alignment with flow causes intercycle thinning as the networked structure of filament chains is destroyed, this is seen in the aforementioned T plot. At this point phase angle increases from the plateau, with a corresponding reduction in thinning behaviour from T = -0.30$\pm$ 0.02 to 0.09$\pm$ 0.01 and increase in G_{cage} from a minimum of 317$\pm$ 8 Pa to 632$\pm$ 6 Pa. This signifies an increase in viscous dissipation and

rearrangement of the macrostructure. At this point in accordance with other two step yielding phenological concepts the macrostructure will be composed of interspersed clusters, with intercluster bacteria bound by short range bonds. The viscous overshoot from G'' = 131$\pm$ 33 Pa to 218$\pm$ 52 Pa could be attributed to the increased mobility of clusters. Rearrangement and breakdown of filamentous microstructure into clusters would increase dissipation though hydrodynamic interactions causing an increase in viscous dissipation and thickening behaviour, seen in the shoulder of G' and reduction in thinning ratio (T). The simultaneous increase in G_{cage} could then be attributed to cluster aggregation mediated by the depth of intercellular interaction potential and sticking probability, which is a function of the depth of the potential well and the kinetic energy of cluster – particle and cluster/cluster collisions (Linnes et al., 2013; Veshchunov, 2015).

5.4 Discussions and Conclusions

In this chapter it was shown how EPS bonding range and cell morphology drive the rheology of 4 different bacterial strains. The packing fraction for each of the biofilms were comparable. The nonlinear rheology and mechanisms of stress relief of each biofilm displayed geometry dependent characteristics, which was mainly noticeable in the T ratio. This can be explained by taking into consideration the degrees of freedom of the spherical and rod morphologies, and how they orientate under flow. The EPS matrix in biofilms suppresses Brownian diffusion by restricting translational and rotational degrees of freedom (Drescher et al., 2016). A spheroid particle has both rotational and translational degrees of freedom when constraint by nearest neighbour cages. As the particle is spheroid stress is relieved through translational movement. For the case of *S. epidermidis* and *N. polysaccharea* two main mechanisms of stress rearrangement are seen. This manifests as two step yielding. This type of yielding for spherical particles has been seen in several colloidal rheology studies, but not until now within biofilm systems (Kramb & Zukoski, 2011). *N. polysaccharea* exhibited nonlinear thickening behaviour similar *S. epidermidis* which can be classified as an attractive glassy system. *N. polysaccharea* had an aspect ratio of 1.13 which falls into the glass region as calculated by Zhang who performed NMCT simulations comparing degrees of freedom in a glassy system against particle aspect ratio and packing fraction (R. Zhang & Schweizer, 2009). Further, the nonlinear thickening behaviour of *N. polysaccharea* appeared similar in

behaviour to *S. epidermidis*, but was shifted, which is attributed to a higher intercellular bonding strength of the *S. epidermidis* biofilm. Rod shaped bacteria *C. denitrificans* and *P. fluorescens* displayed different yielding behaviour in comparison to spherical bacteria, this can be related to the increased aspect ratio, which was 4.38 ± 0.35 and 5.22 ± 0.17 respectively. Aspect ratios of this size in systems with packing fractions $\phi \sim 0.6$ correspond to double glassy systems. In this regime the bacterial cages are localized both rotationally and in translation. However, *C. denitrificans* and *P. fluorescens* have distinct differences between the EPS polymer networks and consequently has distinctly different non-linear behaviour. *P. fluorescens* displayed behaviour of a typical repulsive glassy system characterised by a singular well-defined hump in viscous modulus before the yield point. The singular hump is a consequence of both the breakdown of the EPS network supporting the bacterial cages and the rotational and translational breakdown of the bacterial cages. The yielding dynamics and similarities to other model repulsive glassy materials leads us to believe that EPS network in *P. fluorescens* is long ranged and evenly distributed around the perimeter of each cell, like a colloidal filled polymer composite (Genovese, 2012). From this it is assumed that the EPS matrix of *P. fluorescens* may not feature a particularly dominant autoagglutinin and the stress bearing mechanism is mediated by polymer interactions within the EPS matrix. On the other hand, *C. denitrificans* appears to have strong short-range intercellular bonding, this behaviour was evident from SPP phase plot and in the aggregation experiments. The combination of aggregation into a space spanning network at low volume fractions and presence of two step yield lead us to classify *C. denitrificans* as an attractive gel system. In comparison to *P. fluorescens* it seems that the stress bearing structure of *C. denitrificans* is due to surface bound polymers, which controls polymer bridging between bacteria. The surface bound polymer maybe linked to the polysaccharide *C. denitrificans* is encapsulated within when grown in liquid cultures and on agarose pads (Andersson et al., 2009).

The occurrence of two step yielding in *S. epidermidis* also indicated short range intercellular bonding. The EPS matrix of *S. epidermidis* is known to feature two autoagglutinins; PIA an exopolysaccharide encoded through the *icaADBC* (intercellular adhesion) operon, Aap (accumulation associated protein) a 220 kDa microbial surface components recognising adhesive matrix molecule (MSCRAMM) (Rohde et al., 2005). Secretion of Aap has been shown to increase biofilm formation

under dynamic flow conditions and produce a more structured biofilm. Aap is predominantly localised to the cell surface, causing direct nearest neighbour cell bonding, whereas PIA forms longer string like attachments between multiple bacteria (Schommer et al., 2011). Since PIA and Aap both contribute to short-range intercellular bonding they could be the biofilm components which yield during the first step of the two-step yield process. The second step yielding process of *S. epidermidis* was more prominent than *C. denitrificans*, which could be seen in the SPP phase plot. This indicates that *S. epidermidis* had an EPS network also with longer ranged stress bearing components. A possible candidate component is Embp, a 1 MDa protein which binds to the extracellular matrix, however, is secreted in low volumes unless induced environmental factors such as osmotic stress (Linnes et al., 2013). The long string like attachment of PIA to multiple cells may also be responsible for the second longer range yielding step.

The work performed within this chapter demonstrated the application of LAOS towards the quantification and characterisation of short- and long-range EPS bonding. The nonlinear signatures of these biofilms were also used to compare the effects of bacteria shape. In colloidal gels the colloid geometry is known to influence yielding and breakdown of the macrostructure, the main difference being an increase flow alignment effect and nematic ordering in rod systems. This work demonstrated the application of the SPP method, where it was applied to detect differences in short- and long-range bonding interactions within the EPS matrix of each bacterial strain. From the SPP fingerprints it was easily noticeable that *C. denitrificans* had strong short-range interactions, this resulted in a biofilm with a very high strength (G' = 10000 $\pm$ 501 Pa) but extensive yielding behaviour at low strain values. The short-range behaviour of *C. denitrificans* was reflected by the autoaggregation behaviour in liquid culture and the formation of space spanning networks (gelation). SPP analysis also revealed that *S. epidermidis* displayed short range bonding. *S. epidermidis* is also known to autoaggregate in liquid culture through the EPS autoagglutins PIA and Aap. Thus, from this work we have shown that SPP analysis maybe a promising method to detect the autoaggregation potential of bacterial strains. SPP analysis could be used as a macroscale probe for deciphering between short range and longer-range EPS network strength. This could be a promising technique to link macroscale rheological behaviour to microscale aggregation dynamics.

Chapter 6 Conclusions and future work

6.1 Conclusions

In this work I performed a series of rheological studies, using several different bacteria each with distinct properties. In addition to performing standard linear rheological protocols, I have applied analytical techniques of LAOS to quantify the nonlinear behaviour of each biofilm. I was able to relate changes in EPS network composition and bacterial arrangement to the yielding behaviour of each biofilm. These behaviours where then explained using concepts from model polymer gels and colloidal gel studies. I have assessed the effect of bacteria morphology and strength and locality of EPS networks on biofilm mechanics and demonstrated how biofilm rheology can be explained using analogies to well characterised colloidal soft matter systems. In doing so, I have begun to demonstrate an agreement between the principles which govern both biofilm and well characterised colloidal soft matter systems.

This thesis has demonstrated that biofilms have a wide spectrum of rheological responses characteristic of several different phases. The first bacterium experimented upon was *P. fluorescens,* a rod-shaped bacterium with an EPS matrix known to be composed of alginate and LapA. This bacterium demonstrated behaviour akin to a soft glass or a filled polymer network. This was characterised by the viscous overshoot behaviour the biofilm exhibited in its viscous modulus as the cross over strain was approached. The presence of the viscous modulus overshoot upon approaching the cross over strain was also seen in the similarity rod shaped *Pantoea* sp. YR343 UDP mutant strain. This bacterium had a mutation to the UDP operon, which resulted in the suppression of the production of a major EPS polysaccharide component, amylovoran. The emergence of the viscous overshoot is commonly seen in repulsive glass systems, where interparticle bonding strength is weak. The commonality of nonlinear thickening behaviour of both these strains suggest that these two bacteria are absent of EPS components with strong intercellular bonding functionalities. This point can be supported when the bacterium *C. denitrificans* is considered. *C. denitrificans*, like *P. fluorescens* and *Pantoea* sp. is a rod-shaped bacterium, with a comparable aspect ratio to *P. fluorescens,* 4.38$\pm$ 0.35 vs 5.22$\pm$ 0.17 respectively. However, *C. denitrificans* displayed two-step yielding behaviour, the first yielding point was at very low strains < 1%, then the

second yielding point was at 139 %. This transition in behaviour, from a single yielding point with a viscous overshoot, to a two-step yielding behaviour is commonly seen in colloidal glasses and gels, when interparticle bonding strength is increased. Therefore, it was suspected that *C. denitrificans* featured an EPS component which produced strong short-range intercellular bonds. This hypothesis was supported by its rapid autoaggregation dynamics in liquid culture, which resulted in fractal like space spanning networks. The presence of autoaggregation suggested that the short-ranged EPS component could be a possible autoagglutinin, contributing to the attractive glass/gel behaviour. The range and prominence of the single or two step yielding processes were precisely mapped using the series of physical processes (SPP) method. This analysis technique produced distinct phase maps which clearly showed the regions where the “soft repulsive glass” and “soft attractive glass” biofilms yielded. The difference between the soft repulsive glass and attractive glass/gel therefore appears to due be the range of bonding due to the EPS matrix, as the relative packing fractions of *Pantoea* sp. UDP (ϕ = 0.64$\pm$ 0.08), *P. fluorescens* (ϕ = 0.62$\pm$ 0.03), and *C. denitrificans* (ϕ = 0.65$\pm$ 0.02) are comparable. The range of bonding in the EPS matrix was studied in chapter 3 through treatment with two different types of chemical compounds: divalent cations and a chaotropic agent to *P. fluorescens*. The divalent cations $CaCl_2$ and $FeCl_2$ produced a stiffening effect. The stiffening effect was likely due to ionic crosslinking with negatively charged EPS components. However, the two divalent cation compounds increased stiffness to different degrees. $FeCl_2$ had a larger stiffening effect. The increase in stiffness was accompanied by the presence of strain rate thinning in the nonlinear region and the emergence of two-step yielding. The two-step yielding in the $FeCl_2$ treated *P. fluorescens* shared similar nonlinear thinning behaviour with the two-step yielding of *C. denitrificans*. Both biofilms displayed a T ratio which featured a drop to a thinning minimum and then increased back to neutrality. The T minimum of *C. denitrificans* was slightly smaller, -0.30$\pm$ 0.02 in comparison to $FeCl_2$ treated *P. fluorescens*, -0.39$\pm$ 0.08. However, the dependency of the thinning behaviour on strain and strain rate are different. The SPP plots for *C. denitrificans* show that the first yielding process for *C. denitrificans* is centred around $t = \frac{\pi}{2}, \frac{3\pi}{2}$, where strain is highest. Whereas the first yielding process for $FeCl_2$ treated *P. fluorescens* was centred around $t = 0, \pi$, where strain rate is highest. The differences between the first yielding point between these two biofilms could be due to the way in which the

respective EPS networks structure the biofilm. *C. denitrificans* appears to be dominantly structured through intercellular bonding between neighbouring bacteria. A polymer network like this would have a small interaction range, meaning that lower length scales are required to breakdown the network (Pham et al., 2006). This form of structural breakdown would be strain dependent, as when the structure is sheared beyond the interaction range, structural breakdown occurs. On the other hand the stiffening effect on *P. fluorescens* treated with $FeCl_2$ is likely dominated by ionic crosslinking of the EPS network which supports the cells, instead of intercellular bonding.

This thesis has also shown that biofilms can transition between viscoelastic liquid and viscoelastic glassy phases by mediating the production of specific EPS molecules. This was demonstrated using mixtures of *Pantoea* sp. YR343 and *Pantoea* sp. YR343 UDP, a mutant deficient in production of the capsular acidic polysaccharide amylovoran. Biofilm polysaccharide concentration was varied by mixing different ratios of wild type and mutant strains. This provided a system in which the phase transitions from viscoelastic liquid to soft repulsive glassy rheology could be rheologically investigated. This platform was able to highlight the transition from a polymer network dominated rheological response to a glassy response which was increasingly dominated by bacteria/bacteria jamming. Using the chebychev method and the SPP method I was able to reveal in detail how the nonlinear thinning and thickening behaviour evolved during the phase transition. This phase transition also exhibited behaviour akin to the Payne effect, where the onset of a reduction in elasticity occurs at lower strains with increasing packing fraction. The exact mechanism behind this yielding mode is still debated. However, the chebychev and SPP method revealed the nonlinear dynamics which accompanied this effect. These two methods were able to provide extra information, used to decipher the double power law behaviour which was detected in the G'' curve. This double power law behaviour was attributed to the interplay between the polymer network and the bacteria network at low, intermediate and high packing fractions. The evolution in the nonlinear thickening behaviour was described using the T ratio and depicted in the phase behaviour plots from the SPP method. These results suggested that the transition, from a polymer network dominated response was increasingly dominated by the restriction in motion of the bacterial network, as packing fraction increased towards the random packing limit.

The methodology used throughout this thesis has a series of limitations which need to be considered. The biofilms throughout this thesis were cultured *ex situ* on agar plates. They were then transferred to the rheometer via mechanical scrapping. Scrapping was carefully performed with ground edge microscope slides to avoid cutting and accidently collecting the agar. The action of perturbing the native structure of each biofilm may have altered the biofilm mechanical properties. However, this is a commonly used method when studying biofilm macroscale rheology (Gloag et al., 2018; Kretschmer & Lieleg, 2020a). It is also expected that biofilms grown using the agar culture method at the solid gas interface may vary in EPS composition and component molecular mass in comparison biofilms grown on solid- liquid interfaces (Schollmeyer et al., 2012). This change of environment may alter bacteria gene expression, resulting in a change to polymer network composition and bacterial arrangement within the biofilm microstructure. The difference between being grown on a solid gas interface and solid liquid interface would also be expected to result in differences in solvent concentration within the EPS network (Jing Yan et al., 2018). Biofilms grown at the solid liquid interface would have an increased solvent concentration, which may explain why biofilms grown at solid gas interfaces exhibit elasticity and viscosity, values sometimes several magnitudes higher. Biofilms throughout this thesis were imaged using CLSM in order to calculate packing fraction. In chapter 3 the cytoplasm of the bacteria was stained, this was compensated for by applying a dilation step in the image processing pipeline to account for the cell membrane. Therefore, there remains a possibility that the packing fraction was underestimated. However, the packing fractions in this chapter were used to compare the effect of treatment with divalent cations and a chaotropic compound. In chapters 4 and 5 a cell membrane stain, FM 1-43 was used in addition to Syto 63, a cell permeable DNA stain. These two channels were then combined, which provided a more representative estimation of the biofilm packing fractions.

The approach outlined in this thesis centred around improving our understanding of biofilm rheological behaviour by using nonlinear high-fidelity methods. This approach enabled rheological fingerprinting, which captured the range and strength of bonding within the EPS matrix. This approach has potential applications for both fundamental investigations of how matrix components interact to determine structure and as an initial characterisation step for environmental isolates. However, the concept of mechanically fingerprinting biofilms also has potential applications within medical

diagnostics. For instance, biofilms isolated from cystic fibrosis patients show a highly variable rheological properties (Kovach et al., 2017). The mechanical properties of these biofilms is known to influence the cough clearance index of patients (Gloag et al., 2018). The application of the techniques used within this thesis may have relevance in fingerprinting these types of biofilms over time, to access how treatments effect the range and strength of the EPS matrix. On the other hand, the LAOS techniques applied here could also have industrial relevance. For instance, rheological fingerprinting be used as a characterisation stage in the tailoring of biofilm genetic mutants for use in the 3D printing of functional biofilm materials (Balasubramanian et al., 2019).

6.2 Future work

To build upon the approach and findings of this thesis and develop our understanding of biofilm rheology several future tasks and avenues could be explored.

1. Apply rheo-optical methods to visualise the yielding mechanisms of *C. denitrificians* and *S. epidermidis*. Performing simultaneous characterisation of structure and viscoelastic response. This experiment would assist in understanding how structural properties such as radial distribution function, packing, cluster size and porosity correlate with biofilm viscoelastic response. Imaging the microstructural behaviour of these biofilms in parallel the non-linear methods would provide a deeper understanding of two step yielding, and the process by which these biofilms breakdown. It would be particularly interesting to use EPS deletion mutants of *S. epidermidis*, as the major polymeric components are well characterised and this biofilm displayed two-step yielding. A catalogue of mutants deficient in PIA, Aap, Embp or Bap would provide a set of strains with varying interaction strengths and ranges. The fingerprints and microstructural breakdown of these biofilms could then be used to understand the bonding range of each EPS component. This knowledge could then be applied towards understanding if *S. epidermidis* adapts its matrix composition in response to its mechanical environmental.
2. Identify the polysaccharide/protein secreted by *C. denitrificans* which results in short range polar attraction and flocculation behaviour. By identifying this EPS molecule genetic variants with inducible expression could be constructed. An inducible mutant would allow regulation of the intercellular bonding strength of *C. denitrificans*. This mutant could then be used as an analogous rod shaped patchy colloidal particle with a controllable pairwise interaction potential. The

system of *C. denitrificans* can be used to investigate the emergence of elasticity within colloidal gel networks. The two main questions this system could assist in answering would be related to why viscoelastic materials yield in a brittle mode and why others yield like a viscoelastic liquid. Using the aforementioned mutant would enable the investigation into the effect of short-range bonding on yielding mode. The second fundamental question which could be investigated using *C. denitrificans* is how the influence of local hydrodynamics influences gelation and microstructure of the space spanning structure. This is an important fundamental question in understanding how active particles influence the mechanical properties of gels and has industrial and fundamental importance. This could be studied by tracking the motion of *C. denitrificans* during the formation of the space spanning structure and mapping the flow fields using PIV. This data could then be used to investigate how fluid structure interactions influence the network microstructure and parameters such as nematic order, pairwise correlation function and co-ordination number.

3. Perform co- culture experiments with *C. denitrificans* which is dominated by short range interactions and *P. fluorescens* which is dominated by long range interactions. It would be interesting to evaluate the competition between these two strains which display contrasting ranges in interaction. Does the short-range nature of *C. denitrificans* which has a slower growth rate than *P. fluorescens* confer survival advantages? How would the long-range *P. fluorescens* microstructure interact with *C. denitrificans*? Would mixing these two species at different ratios result in a system in which I can controllably shift between two step and one step yielding? If so this system could be evaluated using rheo- optical methods mentioned in point 1.
4. Access the feasibility of using *C. denitrificans* as a bio- ink for 3D printing functional denitrifying wastewater treatment filters and pre seeding filter systems. Over the past few years, a couple of groups have experimented with using genetically engineered biofilm forming strains such as *Pseudomonas putida, Acetobacter slinum* and *E. coli* as bio inks within 3d printing systems (Balasubramanian et al., 2019; Huang et al., 2019; Schaffner et al., 2017). There are two main concepts used to produce these printed functional living materials. The first is to mix concentrated bacterial cultures with a synthetic hydrogel, where the bacteria produce the functionality, and the hydrogel

provides the supporting polymer network (Schaffner et al., 2017). The printability of the material is therefore mainly determined by the viscoelastic properties of the hydrogel. The second method negates the addition of a supporting synthetic hydrogel polymer network and directly prints biofilms which have been collected from agar plates (Huang et al., 2019). Printable biofilms therefore need to viscously flow during the printing process and have enough stiffness to maintain the desired morphology. This technique was attempted using various genetic mutants of *B. subtilis*, where genetic manipulation of EPS composition was used to control viscoelasticity and subsequent printability. As shown in this thesis *C. denitrificans* has a very high stiffness $G' \sim 10000$ Pa, which is approximately an order of magnitude higher than the *B. subtilis* biofilms used in the aforementioned study. However as demonstrated with *B. subtilis*, the printability of biofilms improves with a reduced stiffness. I hypothesise that the first step yield point of *C. denitrificans* at very low strains < 1 % and resulting shear thinning properties would mitigate the increased stiffness of *C. denitrificans* biofilm during printing. This rheological characteristic could mean that its feasible to print *C. denitrificans* structures which have a stiffness up to an order of magnitude higher than contemporary studies. This could yield benefits in the manufacture of 3d printed denitrification filters and microbial fuel cells.

5. Investigate the applicability of the Flory- Rehner model to calculate the crosslinking density within biofilms (van der Sman, 2015). This model is applied by calculating the weight difference between a saturated network and the network after it has been dried out. The Flory Rehner model is typically applied to the swelling of rubber networks. However, I believe this thesis has shown that polymer rheology theory for rubber and colloidal systems can be closely related to the rheological responses of bacterial biofilms. If I can show that the Flory – Rehner model is applicable to biofilms this may be a simple way of calculating cross linking and EPS component cross linker affinities in biofilm. For example, this theory could be used to investigate the affinity of protein – polysaccharide crosslinkers which are already known to interact, but quantitative evidence of their affinities is less well known.

References

Abbà, A., Collivignarelli, M. C., Manenti, S., Pedrazzani, R., Todeschini, S., & Bertanza, G. (2017). Rheology and Microbiology of Sludge from a Thermophilic Aerobic Membrane Reactor. *Journal of Chemistry*, *2017*, 8764510. https://doi.org/10.1155/2017/8764510

Abriat, C., Virgilio, N., Heuzey, M.-C., & Daigle, F. (2019). Microbiological and real-time mechanical analysis of Bacillus licheniformis and Pseudomonas fluorescens dual-species biofilm. *Microbiology*, *165*(7), 747–756. https://doi.org/10.1099/mic.0.000819

Achouak, W., Heulin, T., Villemin, G., & Balandreau, J. (1994). Root colonization by symplasmata-forming Enterobacter agglomerans. *FEMS Microbiology Ecology*, *13*(4), 287–294. https://doi.org/10.1111/j.1574-6941.1994.tb00075.x

Ageorges, V., Schiavone, M., Jubelin, G., Caccia, N., Ruiz, P., Chafsey, I., Bailly, X., Dague, E., Leroy, S., Paxman, J., Heras, B., Chaucheyras-Durand, F., Rossiter, A. E., Henderson, I. R., & Desvaux, M. (2019). Differential homotypic and heterotypic interactions of antigen 43 (Ag43) variants in autotransporter-mediated bacterial autoaggregation. *Scientific Reports*, *9*(1), 11100. https://doi.org/10.1038/s41598-019-47608-4

Aggarwal, S., & Hozalski, R. M. (2010). Determination of biofilm mechanical properties from tensile tests performed using a micro-cantilever method. *Biofouling*, *26*(4), 479–486. https://doi.org/10.1080/08927011003793080

Allison, S. D., & Martiny, J. B. H. (2008). Resistance, resilience, and redundancy in microbial communities. *Proceedings of the National Academy of Sciences*, *105*(Supplement 1), 11512–11519. https://doi.org/10.1073/pnas.0801925105

Anderson, B. N., Ding, A. M., Nilsson, L. M., Kusuma, K., Tchesnokova, V., Vogel, V., Sokurenko, E. v, & Thomas, W. E. (2007). Weak rolling adhesion enhances bacterial surface colonization. *Journal of Bacteriology*, *189*(5), 1794–1802. https://doi.org/10.1128/JB.00899-06

Anderson, V. J., & Lekkerkerker, H. N. W. (2002). Insights into phase transition kinetics from colloid science. *Nature*, *416*(6883), 811–815. https://doi.org/10.1038/416811a

Andersson, S., Dalhammar, G., Land, C. J., & Kuttuva Rajarao, G. (2009). Characterization of extracellular polymeric substances from denitrifying organism Comamonas denitrificans. *Applied Microbiology and Biotechnology*, *82*(3), 535. https://doi.org/10.1007/s00253-008-1817-3

Andersson, S., Kuttuva Rajarao, G., Land, C. J., & Dalhammar, G. (2008). Biofilm formation and interactions of bacterial strains found in wastewater treatment systems. *FEMS Microbiology Letters*, *283*(1), 83–90. https://doi.org/10.1111/j.1574-6968.2008.01149.x

Angelaalincy, M. J., Navanietha Krishnaraj, R., Shakambari, G., Ashokkumar, B., Kathiresan, S., & Varalakshmi, P. (2018). Biofilm Engineering Approaches for Improving the Performance of Microbial Fuel Cells and Bioelectrochemical Systems. *Frontiers in Energy Research*, *6*, 63. https://doi.org/10.3389/fenrg.2018.00063

Armstrong, M. J., Beris, A. N., Rogers, S. A., & Wagner, N. J. (2016). Dynamic shear rheology of a thixotropic suspension: Comparison of an improved structure-based model with large amplitude oscillatory shear experiments. *Journal of Rheology*, *60*(3), 433–450. https://doi.org/10.1122/1.4943986

Aufrecht, J. A., Fowlkes, J. D., Bible, A. N., Morrell-Falvey, J., Doktycz, M. J., & Retterer, S. T. (2019). Pore-scale hydrodynamics influence the spatial evolution of bacterial biofilms in a microfluidic porous network. *PLoS ONE*, *14*(6), e0218316. https://doi.org/10.1371/journal.pone.0218316

Aufrecht, J. A., Timm, C. M., Bible, A., Morrell-Falvey, J. L., Pelletier, D. A., Doktycz, M. J., & Retterer, S. T. (2018). Quantifying the Spatiotemporal Dynamics of Plant Root Colonization by Beneficial Bacteria in a Microfluidic Habitat. *Advanced Biosystems*, *2*(6), 1800048. https://doi.org/doi:10.1002/adbi.201800048

Balasubramanian, S., Aubin-Tam, M.-E., & Meyer, A. S. (2019). 3D Printing for the Fabrication of Biofilm-Based Functional Living Materials. *ACS Synthetic Biology*, *8*(7), 1564–1567. https://doi.org/10.1021/acssynbio.9b00192

Ballesta, P., Koumakis, N., Besseling, R., Poon, W. C. K., & Petekidis, G. (2013). Slip of gels in colloid–polymer mixtures under shear. *Soft Matter*, *9*(12), 3237–3245. https://doi.org/10.1039/C3SM27626K

Beauregard, P. B., Chai, Y., Vlamakis, H., Losick, R., & Kolter, R. (2013). Bacillus subtilis biofilm induction by plant polysaccharides. *Proceedings of the National Academy of Sciences*, *110*(17), E1621. https://doi.org/10.1073/pnas.1218984110

Beenken, K. E., Spencer, H., Griffin, L. M., & Smeltzer, M. S. (2012). Impact of extracellular nuclease production on the biofilm phenotype of Staphylococcus aureus under in vitro and in vivo conditions. *Infection and Immunity*, *80*(5), 1634–1638. https://doi.org/10.1128/IAI.06134-11

Belas, R. (2014). Biofilms, flagella, and mechanosensing of surfaces by bacteria. *Trends in Microbiology*, *22*(9), 517–527. https://doi.org/https://doi.org/10.1016/j.tim.2014.05.002

Bellemann, P., Bereswill, S., Berger, S., & Geider, K. (1994). Visualization of capsule formation by Erwinia amylovora and assays to determine amylovoran synthesis. *International Journal of Biological Macromolecules*, *16*(6), 290–296. https://doi.org/https://doi.org/10.1016/0141-8130(94)90058-2

Beroz, F., Yan, J., Meir, Y., Sabass, B., Stone, H. A., Bassler, B. L., & Wingreen, N. S. (2018). Verticalization of bacterial biofilms. *Nature Physics*, *14*(9), 954–960. https://doi.org/10.1038/s41567-018-0170-4

Bible, A. N., Fletcher, S. J., Pelletier, D. A., Schadt, C. W., Jawdy, S. S., Weston, D. J., Engle, N. L., Tschaplinski, T., Masyuko, R., Polisetti, S., Bohn, P. W., Coutinho, T. A., Doktycz, M. J., & Morrell-Falvey, J. L. (2016). A Carotenoid-Deficient Mutant in Pantoea sp. YR343, a Bacteria Isolated from the Rhizosphere of Populus deltoides, Is Defective in Root Colonization. *Frontiers in Microbiology*, *7*, 491. https://doi.org/10.3389/fmicb.2016.00491

Birjiniuk, A., Billings, N., Nance, E., Hanes, J., Ribbeck, K., & Doyle, P. S. (2014). Single particle tracking reveals spatial and dynamic organization of the Escherichia coli biofilm matrix. *New Journal of Physics*, *16*(8), 85014. https://doi.org/10.1088/1367-2630/16/8/085014

Biswas, I., Ghosh, R., Sadrzadeh, M., & Kumar, A. (2016). Nonlinear deformation and localized failure of bacterial streamers in creeping flows. *Scientific Reports*, *6*(1), 32204. https://doi.org/10.1038/srep32204

Blauert, F., Horn, H., & Wagner, M. (2015). Time-resolved biofilm deformation measurements using optical coherence tomography. *Biotechnology and Bioengineering*, *112*(9), 1893–1905. https://doi.org/10.1002/bit.25590

Boyd, C. D., Smith, T. J., El-Kirat-Chatel, S., Newell, P. D., Dufrêne, Y. F., & O'Toole, G. A. (2014). Structural Features of the Pseudomonas fluorescens; Biofilm Adhesin LapA Required for LapG-Dependent Cleavage, Biofilm Formation, and Cell Surface Localization. *Journal of Bacteriology*, *196*(15), 2775. https://doi.org/10.1128/JB.01629-14

Brindle, E. R., Miller, D. A., & Stewart, P. S. (2011). Hydrodynamic deformation and removal of Staphylococcus epidermidis biofilms treated with urea, chlorhexidine, iron chloride, or DispersinB. *Biotechnology and Bioengineering*, *108*(12), 2968–2977. https://doi.org/10.1002/bit.23245

Brugnoni, L. I., Tarifa, M. C., Lozano, J. E., & Genovese, D. (2014). In situ rheology of yeast biofilms. *Biofouling*, *30*(10), 1269–1279. https://doi.org/10.1080/08927014.2014.981165

Burns, J. L., Yan, Y., Jameson, G. J., & Biggs, S. (2002). The Effect of Molecular Weight of Nonadsorbing Polymer on the Structure of Depletion-Induced Flocs. *Journal of Colloid and Interface Science*, *247*(1), 24–32. https://doi.org/https://doi.org/10.1006/jcis.2001.8115

Burrows, L. L. (2012). Pseudomonas aeruginosa Twitching Motility: Type IV Pili in Action. *Annual Review of Microbiology*, *66*(1), 493–520. https://doi.org/10.1146/annurev-micro-092611-150055

Busscher, H. J., & van der Mei, H. C. (2012). How do bacteria know they are on a surface and regulate their response to an adhering state? *PLoS Pathogens*, *8*(1), e1002440–e1002440. https://doi.org/10.1371/journal.ppat.1002440

Cao, H., Habimana, O., Safari, A., Heffernan, R., Dai, Y., & Casey, E. (2016). Revealing region-specific biofilm viscoelastic properties by means of a micro-rheological approach. *Npj Biofilms And Microbiomes*, *2*, 5. https://doi.org/10.1038/s41522-016-0005-y

Cao, M., & Goodrich-Blair, H. (2017). Ready or Not: Microbial Adaptive Responses in Dynamic Symbiosis Environments. *Journal of Bacteriology*, *199*(15), e00883-16. https://doi.org/10.1128/jb.00883-16

Carlier, A., Burbank, L., & von Bodman, S. B. (2009). Identification and characterization of three novel EsaI/EsaR quorum-sensing controlled stewartan exopolysaccharide biosynthetic genes in Pantoea stewartii ssp. stewartii. *Molecular Microbiology*, *74*(4), 903–913. https://doi.org/doi:10.1111/j.1365-2958.2009.06906.x

Carrel, M., Morales, V. L., Beltran, M. A., Derlon, N., Kaufmann, R., Morgenroth, E., & Holzner, M. (2018). Biofilms in 3D porous media: Delineating the influence of the pore network geometry, flow and mass transfer on biofilm development. *Water Research*. https://doi.org/10.1016/j.watres.2018.01.059

Carrier, V., & Petekidis, G. (2009). Nonlinear rheology of colloidal glasses of soft thermosensitive microgel particles. *Journal of Rheology*, *53*(2), 245–273. https://doi.org/10.1122/1.3045803

Cassagnau, P. (2003). Payne effect and shear elasticity of silica-filled polymers in concentrated solutions and in molten state. *Polymer*, *44*(8), 2455–2462. https://doi.org/https://doi.org/10.1016/S0032-3861(03)00094-6

Charlton, S. G. v, White, M. A., Jana, S., Eland, L. E., Jayathilake, P. G., Burgess, J. G., Chen, J., Wipat, A., & Curtis, T. P. (2019). Regulating, measuring and modelling the viscoelasticity of bacterial biofilms. *Journal of Bacteriology*, JB.00101-19. https://doi.org/10.1128/JB.00101-19

Chen, X., & Stewart, P. S. (2002). Role of electrostatic interactions in cohesion of bacterial biofilms. *Applied Microbiology and Biotechnology*, *59*(6), 718–720. https://doi.org/10.1007/s00253-002-1044-2

Chen, Y., Cao, S., Chai, Y., Clardy, J., Kolter, R., Guo, J., & Losick, R. (2012). A Bacillus subtilis sensor kinase involved in triggering biofilm formation on the roots of tomato plants. *Molecular Microbiology*, *85*(3), 418–430. https://doi.org/10.1111/j.1365-2958.2012.08109.x

Chew, S. C., Kundukad, B., Seviour, T., van der Maarel, J. R. C., Yang, L., Rice, S. A., Doyle, P., & Kjelleberg, S. (2014). Dynamic Remodeling of Microbial Biofilms by Functionally Distinct Exopolysaccharides. *MBio*, *5*(4). https://doi.org/10.1128/mBio.01536-14

Christner, M., Franke, G. C., Schommer, N. N., Wendt, U., Wegert, K., Pehle, P., Kroll, G., Schulze, C., Buck, F., Mack, D., Aepfelbacher, M., & Rohde, H. (2010).

The giant extracellular matrix-binding protein of Staphylococcus epidermidis mediates biofilm accumulation and attachment to fibronectin. *Molecular Microbiology*, *75*(1), 187–207. https://doi.org/10.1111/j.1365-2958.2009.06981.x

Cindy, E. M., & Jean-Michel, M. (2003). The Ecological Significance of Biofilm Formation by Plant-Associated Bacteria. *Annual Review of Phytopathology*, *41*(1), 429–453. https://doi.org/10.1146/annurev.phyto.41.022103.134521

Claessen, D., Rozen, D. E., Kuipers, O. P., Søgaard-Andersen, L., & van Wezel, G. P. (2014). Bacterial solutions to multicellularity: a tale of biofilms, filaments and fruiting bodies. *Nature Reviews Microbiology*, *12*, 115. https://doi.org/10.1038/nrmicro3178

Cohen Stuart, M. A., Cosgrove, T., & Vincent, B. (1985). Experimental aspects of polymer adsorption at solid/solution interfaces. *Advances in Colloid and Interface Science*, *24*, 143–239. https://doi.org/https://doi.org/10.1016/0001-8686(85)80030-0

Costa Oliveira, B. E., Cury, J. A., & Ricomini Filho, A. P. (2017). Biofilm extracellular polysaccharides degradation during starvation and enamel demineralization. *PLoS ONE*, *12*(7), e0181168–e0181168. https://doi.org/10.1371/journal.pone.0181168

Craciun, L., Carreau, P. J., Heuzey, M.-C., van de Ven, T. G. M., & Moan, M. (2003). Rheological properties of concentrated latex suspensions of poly(styrene-butadiene). *Rheologica Acta*, *42*(5), 410–420. https://doi.org/10.1007/s00397-003-0295-x

Cramton, S. E., Gerke, C., Schnell, N. F., Nichols, W. W., & Götz, F. (1999). The Intercellular Adhesion (ica) Locus Is Present in Staphylococcus aureus; and Is Required for Biofilm Formation. *Infection and Immunity*, *67*(10), 5427. https://doi.org/10.1128/IAI.67.10.5427-5433.1999

Cucarella, C., Solano, C., Valle, J., Amorena, B., Lasa, I., & Penadés, J. R. (2001). Bap, a Staphylococcus aureus surface protein involved in biofilm formation. *Journal of Bacteriology*, *183*(9), 2888–2896. https://doi.org/10.1128/JB.183.9.2888-2896.2001

Daalkhaijav, U., Sriramulu, T. W. W., & ED1 - Dinesh. (2019). Effects of Medium Components on the Bulk Rheology and on the Formation of Ferning Patterns for

Biofilm of Pseudomonas aeruginosa. In A. L. Dunham (Ed.), *Pseudomonas Aeruginosa - An Armoury Within* (p. Ch. 2). IntechOpen. https://doi.org/10.5772/intechopen.85240

Das, T., Sehar, S., Koop, L., Wong, Y. K., Ahmed, S., Siddiqui, K. S., & Manefield, M. (2014). Influence of Calcium in Extracellular DNA Mediated Bacterial Aggregation and Biofilm Formation. *PLoS ONE*, *9*(3), e91935. https://doi.org/10.1371/journal.pone.0091935

Daudé, D., Champion, E., Morel, S., Guieysse, D., Remaud-Siméon, M., & André, I. (2013). Probing Substrate Promiscuity of Amylosucrase from Neisseria polysaccharea. *ChemCatChem*, *5*(8), 2288–2295. https://doi.org/10.1002/cctc.201300012

de Sousa, J. S., Freire, R. S., Sousa, F. D., Radmacher, M., Silva, A. F. B., Ramos, M. v, Monteiro-Moreira, A. C. O., Mesquita, F. P., Moraes, M. E. A., Montenegro, R. C., & Oliveira, C. L. N. (2020). Double power-law viscoelastic relaxation of living cells encodes motility trends. *Scientific Reports*, *10*(1), 4749. https://doi.org/10.1038/s41598-020-61631-w

di Stefano, A., D'Aurizio, E., Trubiani, O., Grande, R., di Campli, E., di Giulio, M., di Bartolomeo, S., Sozio, P., Iannitelli, A., Nostro, A., & Cellini, L. (2009). Viscoelastic properties of Staphylococcus aureus and Staphylococcus epidermidis mono-microbial biofilms. *Microbial Biotechnology*, *2*(6), 634–641. https://doi.org/10.1111/j.1751-7915.2009.00120.x

Dibble, C. J., Kogan, M., & Solomon, M. J. (2006). Structure and dynamics of colloidal depletion gels: Coincidence of transitions and heterogeneity. *Physical Review E*, *74*(4), 41403. https://doi.org/10.1103/PhysRevE.74.041403

Donlan, R. M. (2002). Biofilms: microbial life on surfaces. *Emerging Infectious Diseases*, *8*(9), 881–890. https://doi.org/10.3201/eid0809.020063

Donley, G. J., de Bruyn, J. R., McKinley, G. H., & Rogers, S. A. (2019). Time-resolved dynamics of the yielding transition in soft materials. *Journal of Non-Newtonian Fluid Mechanics*, *264*, 117–134. https://doi.org/https://doi.org/10.1016/j.jnnfm.2018.10.003

Dorken, G., Ferguson, G. P., French, C. E., & Poon, W. C. K. (2012). Aggregation by depletion attraction in cultures of bacteria producing exopolysaccharide. *Journal*

of The Royal Society Interface, *9*(77), 3490–3502. https://doi.org/10.1098/rsif.2012.0498

Douglas, C. V., & Kenneth, S. S. (2008). Theory of gelation, vitrification, and activated barrier hopping in mixtures of hard and sticky spheres. *The Journal of Chemical Physics*, *128*(8), 84509. https://doi.org/10.1063/1.2837295

Dragoš, A., Kiesewalter, H., Martin, M., Hsu, C.-Y., Hartmann, R., Wechsler, T., Eriksen, C., Brix, S., Drescher, K., Stanley-Wall, N., Kümmerli, R., & Kovács, Á. T. (2018). Division of Labor during Biofilm Matrix Production. *Current Biology*, *28*(12), 1903-1913.e5. https://doi.org/https://doi.org/10.1016/j.cub.2018.04.046

Dragoš, A., Martin, M., Garcia, C. F., Kricks, L., Pausch, P., Heimerl, T., Bálint, B., Maróti, G., Bange, G., López, D., Lieleg, O., & Kovács, Á. T. (2018). Collapse of genetic division of labour and evolution of autonomy in pellicle biofilms. *Nature Microbiology*. https://doi.org/10.1038/s41564-018-0263-y

Drescher, K., Dunkel, J., Nadell, C. D., van Teeffelen, S., Grnja, I., Wingreen, N. S., Stone, H. A., & Bassler, B. L. (2016). Architectural transitions in Vibrio cholerae biofilms at single-cell resolution. *Proceedings of the National Academy of Sciences*, *113*(14), E2066. https://doi.org/10.1073/pnas.1601702113

Drescher, K., Shen, Y., Bassler, B. L., & Stone, H. A. (2013). Biofilm streamers cause catastrophic disruption of flow with consequences for environmental and medical systems. *Proceedings of the National Academy of Sciences*, *110*(11), 4345. https://doi.org/10.1073/pnas.1300321110

Drozdov, A. D., & Dorfmann, A. (2002). The payne effect for particle-reinforced elastomers. *Polymer Engineering & Science*, *42*(3), 591–604. https://doi.org/10.1002/pen.10974

Duan, J., Yi, T., Lu, Z., Shen, D., & Feng, Y. (2007). Rice endophyte Pantoea agglomerans YS19 forms multicellular symplasmata via cell aggregation. *FEMS Microbiology Letters*, *270*(2), 220–226. https://doi.org/10.1111/j.1574-6968.2007.00677.x

Duvarci, O. C., Yazar, G., & Kokini, J. L. (2017). The SAOS, MAOS and LAOS behavior of a concentrated suspension of tomato paste and its prediction using the Bird-Carreau (SAOS) and Giesekus models (MAOS-LAOS). *Journal of Food Engineering*, *208*, 77–88. https://doi.org/10.1016/j.jfoodeng.2017.02.027

Eckert, T., & Bartsch, E. (2002). Re-entrant Glass Transition in a Colloid-Polymer Mixture with Depletion Attractions. *Physical Review Letters*, *89*(12), 125701. https://doi.org/10.1103/PhysRevLett.89.125701

Edmunds, A. C., Castiblanco, L. F., Sundin, G. W., & Waters, C. M. (2013). Cyclic Di-GMP modulates the disease progression of Erwinia amylovora. *Journal of Bacteriology*, *195*(10), 2155–2165. https://doi.org/10.1128/JB.02068-12

Ellison, C. K., Kan, J., Dillard, R. S., Kysela, D. T., Ducret, A., Berne, C., Hampton, C. M., Ke, Z., Wright, E. R., Biais, N., Dalia, A. B., & Brun, Y. v. (2017). Obstruction of pilus retraction stimulates bacterial surface sensing. *Science*, *358*(6362), 535. https://doi.org/10.1126/science.aan5706

Eric, R. B., David, A. M., & Philip, S. S. (2011). Hydrodynamic deformation and removal of Staphylococcus epidermidis biofilms treated with urea, chlorhexidine, iron chloride, or DispersinB. *Biotechnology and Bioengineering*, *108*(12), 2968–2977. https://doi.org/doi:10.1002/bit.23245

Ewoldt, R. H., Johnston, M. T., & Caretta, L. M. (2015). Experimental Challenges of Shear Rheology: How to Avoid Bad Data. In S. E. Spagnolie (Ed.), *Complex Fluids in Biological Systems: Experiment, Theory, and Computation* (pp. 207–241). Springer New York. https://doi.org/10.1007/978-1-4939-2065-5_6

Ewoldt, R. H., & McKinley, G. H. (2010). On secondary loops in LAOS via self-intersection of Lissajous–Bowditch curves. *Rheologica Acta*, *49*(2), 213–219. https://doi.org/10.1007/s00397-009-0408-2

Ewoldt, R. H., Winter, P., Maxey, J., & McKinley, G. H. (2010). Large amplitude oscillatory shear of pseudoplastic and elastoviscoplastic materials. *Rheologica Acta*, *49*(2), 191–212. https://doi.org/10.1007/s00397-009-0403-7

Feng, Y., Shen, D., Dong, X., & Song, W. (2003). In vitro symplasmata formation in the rice diazotrophic endophyte Pantoea agglomerans YS19. *Plant and Soil*, *255*(2), 435–444. https://doi.org/10.1023/a:1026079203474

Fish, K. E., Collins, R., Green, N. H., Sharpe, R. L., Douterelo, I., Osborn, A. M., & Boxall, J. B. (2015). Characterisation of the physical composition and microbial community structure of biofilms within a model full-scale drinking water distribution system. *PloS One*, *10*(2), e0115824–e0115824. https://doi.org/10.1371/journal.pone.0115824

Fleming, D., Chahin, L., & Rumbaugh, K. (2017). Glycoside Hydrolases Degrade Polymicrobial Bacterial Biofilms in Wounds. *Antimicrobial Agents and Chemotherapy*, *61*(2), e01998-16. https://doi.org/10.1128/AAC.01998-16

Flemming, H.-C. (2011). The perfect slime. *Colloids and Surfaces B: Biointerfaces*, *86*(2), 251–259. https://doi.org/http://dx.doi.org/10.1016/j.colsurfb.2011.04.025

Flemming, H.-C., Neu, T. R., & Wozniak, D. J. (2007). The EPS matrix: the "house of biofilm cells." *Journal of Bacteriology*, *189*(22), 7945–7947. https://doi.org/10.1128/JB.00858-07

Flemming, H.-C., & Wingender, J. (2010). The biofilm matrix. *Nature Reviews Microbiology*, *8*(9), 623–633. https://doi.org/10.1038/nrmicro2415

Flemming, H.-C., & Wuertz, S. (2019). Bacteria and archaea on Earth and their abundance in biofilms. *Nature Reviews Microbiology*, *17*(4), 247–260. https://doi.org/10.1038/s41579-019-0158-9

Frølund, B., Palmgren, R., Keiding, K., & Nielsen, P. H. (1996). Extraction of extracellular polymers from activated sludge using a cation exchange resin. *Water Research*, *30*(8), 1749–1758. https://doi.org/http://dx.doi.org/10.1016/0043-1354(95)00323-1

Fuqua, C. (2010). Passing the baton between laps: adhesion and cohesion in Pseudomonas putida biofilms. *Molecular Microbiology*, *77*(3), 533–536. https://doi.org/10.1111/j.1365-2958.2010.07250.x

Galy, O., Latour-Lambert, P., Zrelli, K., Ghigo, J.-M., Beloin, C., & Henry, N. (2012). Mapping of bacterial biofilm local mechanics by magnetic microparticle actuation. *Biophysical Journal*, *103*(6), 1400–1408. https://doi.org/10.1016/j.bpj.2012.07.001

Ganesan, M, Stewart, E. J., Szafranski, J., Satorius, A. E., Younger, J. G., & Solomon, M. J. (2013). Molar mass, entanglement, and associations of the biofilm polysaccharide of Staphylococcus epidermidis. *Biomacromolecules*, *14*(5), 1474–1481. https://doi.org/10.1021/bm400149a

Ganesan, Mahesh, Knier, S., Younger, J. G., & Solomon, M. J. (2016). Associative and Entanglement Contributions to the Solution Rheology of a Bacterial

Polysaccharide. *Macromolecules*, *49*(21), 8313–8321. https://doi.org/10.1021/acs.macromol.6b01598

Genovese, D. B. (2012). Shear rheology of hard-sphere, dispersed, and aggregated suspensions, and filler-matrix composites. In *Advances in Colloid and Interface Science*. https://doi.org/10.1016/j.cis.2011.12.005

Gentile, L. (2020). Protein–polysaccharide interactions and aggregates in food formulations. *Current Opinion in Colloid & Interface Science*, *48*, 18–27. https://doi.org/https://doi.org/10.1016/j.cocis.2020.03.002

Ghosh, P., Mondal, J., Ben-Jacob, E., & Levine, H. (2015). Mechanically-driven phase separation in a growing bacterial colony. *Proceedings of the National Academy of Sciences*, *112*(17), E2166. https://doi.org/10.1073/pnas.1504948112

Gil, E. S., & Hudson, S. M. (2007). Effect of Silk Fibroin Interpenetrating Networks on Swelling/Deswelling Kinetics and Rheological Properties of Poly(N-isopropylacrylamide) Hydrogels. *Biomacromolecules*, *8*(1), 258–264. https://doi.org/10.1021/bm060543m

Gjermansen, M., Nilsson, M., Yang, L., & Tolker-Nielsen, T. (2010). Characterization of starvation-induced dispersion in Pseudomonas putida biofilms: genetic elements and molecular mechanisms. *Molecular Microbiology*, *75*(4), 815–826. https://doi.org/10.1111/j.1365-2958.2009.06793.x

Gloag, E. S., German, G. K., Stoodley, P., & Wozniak, D. J. (2018). Viscoelastic properties of Pseudomonas aeruginosa variant biofilms. *Scientific Reports*, *8*(1), 9691. https://doi.org/10.1038/s41598-018-28009-5

Gordon, V. D., Davis-Fields, M., Kovach, K., & Rodesney, C. A. (2017). Biofilms and mechanics: a review of experimental techniques and findings. *Journal of Physics D: Applied Physics*, *50*(22), 223002. https://doi.org/10.1088/1361-6463/aa6b83

Goudoulas, T. B., & Germann, N. (2016). Viscoelastic properties of polyacrylamide solutions from creep ringing data. *Journal of Rheology*, *60*(3), 491–502. https://doi.org/10.1122/1.4945819

Grumbein, S., Opitz, M., & Lieleg, O. (2014). Selected metal ions protect Bacillus subtilis biofilms from erosion. *Metallomics*, *6*(8), 1441–1450. https://doi.org/10.1039/C4MT00049H

Grumbein, S., Werb, M., Opitz, M., & Lieleg, O. (2016). Elongational rheology of bacterial biofilms in situ. *Journal of Rheology*, *60*(6), 1085–1094. https://doi.org/10.1122/1.4958667

Guilhen, C., Charbonnel, N., Parisot, N., Gueguen, N., Iltis, A., Forestier, C., & Balestrino, D. (2016). Transcriptional profiling of Klebsiella pneumoniae defines signatures for planktonic, sessile and biofilm-dispersed cells. *BMC Genomics*, *17*(1), 237. https://doi.org/10.1186/s12864-016-2557-x

Gumaelius, L., Magnusson, G., Pettersson, B., & Dalhammar, G. (2001). Comamonas denitrificans sp. nov., an efficient denitrifying bacterium isolated from activated sludge. *International Journal of Systematic and Evolutionary Microbiology*, *51*(3), 999–1006. https://doi.org/doi:10.1099/00207713-51-3-999

Ha, D.-G., & O'Toole, G. A. (2015). c-di-GMP and its Effects on Biofilm Formation and Dispersion: a Pseudomonas Aeruginosa Review. *Microbiology Spectrum*, *3*(2), 10.1128/microbiolspec.MB-0003-2014–2014. https://doi.org/10.1128/microbiolspec.MB-0003-2014

Haaber, J., Cohn, M. T., Frees, D., Andersen, T. J., & Ingmer, H. (2012). Planktonic aggregates of Staphylococcus aureus protect against common antibiotics. *PloS One*, *7*(7), e41075–e41075. https://doi.org/10.1371/journal.pone.0041075

Hart, J. W., Waigh, T. A., Lu, J. R., & Roberts, I. S. (2019). Microrheology and Spatial Heterogeneity of Staphylococcus aureus Biofilms Modulated by Hydrodynamic Shear and Biofilm-Degrading Enzymes. *Langmuir*, *35*(9), 3553–3561. https://doi.org/10.1021/acs.langmuir.8b04252

Hartmann, R., Singh, P. K., Pearce, P., Mok, R., Song, B., Díaz-Pascual, F., Dunkel, J., & Drescher, K. (2019). Emergence of three-dimensional order and structure in growing biofilms. *Nature Physics*, *15*(3), 251–256. https://doi.org/10.1038/s41567-018-0356-9

Harvey Thomas Banks, S. H. and Z. R. K. (2010). A Brief Review of Elasticity and Viscoelasticity for Solids. *Advances in Applied Mathematics and Mechanics*, *Vol. 3*(No. 1), 1–51.

He, Y., Peterson, B. W., Jongsma, M. A., Ren, Y., Sharma, P. K., Busscher, H. J., & van der Mei, H. C. (2013). Stress relaxation analysis facilitates a quantitative approach towards antimicrobial penetration into biofilms. *PLoS ONE*, *8*(5), e63750–e63750. https://doi.org/10.1371/journal.pone.0063750

Heinrich, G., & Klüppel, M. (2002). Recent Advances in the Theory of Filler Networking in Elastomers. In *Filled Elastomers Drug Delivery Systems* (pp. 1–44). Springer Berlin Heidelberg. https://doi.org/10.1007/3-540-45362-8_1

Hellström, L. H. O., Samaha, M. A., Wang, K. M., Smits, A. J., & Hultmark, M. (2014). Errors in parallel-plate and cone-plate rheometer measurements due to sample underfill. *Measurement Science and Technology*, *26*(1), 15301. https://doi.org/10.1088/0957-0233/26/1/015301

Hengge, R. (2009). Principles of c-di-GMP signalling in bacteria. *Nature Reviews Microbiology*, *7*(4), 263–273. https://doi.org/10.1038/nrmicro2109

Hermes, M., & Clegg, P. S. (2013). Yielding and flow of concentrated Pickering emulsions. *Soft Matter*, *9*(31), 7568–7575. https://doi.org/10.1039/C3SM50889G

Hobley, L., Harkins, C., MacPhee, C. E., & Stanley-Wall, N. R. (2015). Giving structure to the biofilm matrix: an overview of individual strategies and emerging common themes. *FEMS Microbiology Reviews*, *39*(5), 649–669. https://doi.org/10.1093/femsre/fuv015

Hofer, U. (2018). New diversity in the sulfur cycle. *Nature Reviews Microbiology*, *16*, 260. https://doi.org/10.1038/nrmicro.2018.32

Høiby, N., Bjarnsholt, T., Givskov, M., Molin, S., & Ciofu, O. (2010). Antibiotic resistance of bacterial biofilms. *International Journal of Antimicrobial Agents*, *35*(4), 322–332. https://doi.org/https://doi.org/10.1016/j.ijantimicag.2009.12.011

Hollenbeck, E. C., Douarche, C., Allain, J.-M., Roger, P., Regeard, C., Cegelski, L., Fuller, G. G., & Raspaud, E. (2016). Mechanical Behavior of a Bacillus subtilis Pellicle. *The Journal of Physical Chemistry B*, *120*(26), 6080–6088. https://doi.org/10.1021/acs.jpcb.6b02074

Hooper, J. B., & Schweizer, K. S. (2005). Contact Aggregation, Bridging, and Steric Stabilization in Dense Polymer−Particle Mixtures. *Macromolecules*, *38*(21), 8858–8869. https://doi.org/10.1021/ma051318k

Hou, J., Veeregowda, D. H., van de Belt-Gritter, B., Busscher, H. J., & van der Mei, H. C. (2018). Extracellular Polymeric Matrix Production and Relaxation under Fluid Shear and Mechanical Pressure in Staphylococcus aureus Biofilms. *Applied and Environmental Microbiology*, *84*(1), e01516-17. https://doi.org/10.1128/AEM.01516-17

Houari, A., Picard, J., Habarou, H., Galas, L., Vaudry, H., Heim, V., & di Martino, P. (2008). Rheology of biofilms formed at the surface of NF membranes in a drinking water production unit. *Biofouling*, *24*(4), 235–240. https://doi.org/10.1080/08927010802023764

Howard, M. P., Jadrich, R. B., Lindquist, B. A., Khabaz, F., Bonnecaze, R. T., Milliron, D. J., & Truskett, T. M. (2019). Structure and phase behavior of polymer-linked colloidal gels. *The Journal of Chemical Physics*, *151*(12), 124901. https://doi.org/10.1063/1.5119359

Huang, J., Liu, S., Zhang, C., Wang, X., Pu, J., Ba, F., Xue, S., Ye, H., Zhao, T., Li, K., Wang, Y., Zhang, J., Wang, L., Fan, C., Lu, T. K., & Zhong, C. (2019). Programmable and printable Bacillus subtilis biofilms as engineered living materials. *Nature Chemical Biology*, *15*(1), 34–41. https://doi.org/10.1038/s41589-018-0169-2

Hubert, K. C., & Ali, M. (2014). An instrument design concept to minimize creep ringing during step-stress experiments with viscoelastic materials. *Applied Physics Letters*, *105*(3), 34102. https://doi.org/10.1063/1.4890739

Hudson, R. E., Holder, A. J., Hawkins, K. M., Williams, P. R., & Curtis, D. J. (2017). An enhanced rheometer inertia correction procedure (ERIC) for the study of gelling systems using combined motor-transducer rheometers. *Physics of Fluids*, *29*(12), 121602. https://doi.org/10.1063/1.4993308

Hug, L. A., Baker, B. J., Anantharaman, K., Brown, C. T., Probst, A. J., Castelle, C. J., Butterfield, C. N., Hernsdorf, A. W., Amano, Y., Ise, K., Suzuki, Y., Dudek, N., Relman, D. A., Finstad, K. M., Amundson, R., Thomas, B. C., & Banfield, J. F. (2016). A new view of the tree of life. *Nature Microbiology*, *1*(5), 16048. https://doi.org/10.1038/nmicrobiol.2016.48

Humphries, J., Xiong, L., Liu, J., Prindle, A., Yuan, F., Arjes, H. A., Tsimring, L., & Suel, G. M. (2017). Species-Independent Attraction to Biofilms through Electrical Signaling. *Cell*, *168*(1–2), 200-209 e12. https://doi.org/10.1016/j.cell.2016.12.014

Hyun, K., Ahn, K. H., Lee, S. J., Sugimoto, M., & Koyama, K. (2006). Degree of branching of polypropylene measured from Fourier-transform rheology. *Rheologica Acta*, *46*(1), 123–129. https://doi.org/10.1007/s00397-006-0098-y

Hyun, K., Baik, E. S., Ahn, K. H., Lee, S. J., Sugimoto, M., & Koyama, K. (2007). Fourier-transform rheology under medium amplitude oscillatory shear for linear and branched polymer melts. *Journal of Rheology*, *51*(6), 1319–1342. https://doi.org/10.1122/1.2790072

Hyun, K., G. Nam, J., Wilhelm, M., H Ahn, K., & J Lee, S. (2003). Nonlinear response of complex fluids under LAOS (large amplitude oscillatory shear) flow. *Korea-Australia Rheology Journal, 15(2), 97-105.* http://hdl.handle.net/11858/00-001M-0000-000F-6307-F

Hyun, K., Kim, W., Joon Park, S., & Wilhelm, M. (2012). Numerical simulation results of the nonlinear coefficient Q from FT-Rheology using a single mode pom-pom model. *Journal of Rheology*, *57*(1), 1–25. https://doi.org/10.1122/1.4754444

Hyun, K., Wilhelm, M., Klein, C. O., Cho, K. S., Nam, J. G., Ahn, K. H., Lee, S. J., Ewoldt, R. H., & McKinley, G. H. (2011). A review of nonlinear oscillatory shear tests: Analysis and application of large amplitude oscillatory shear (LAOS). *Progress in Polymer Science*, *36*(12), 1697–1753. https://doi.org/https://doi.org/10.1016/j.progpolymsci.2011.02.002

Ivanov, I. E., Boyd, C. D., Newell, P. D., Schwartz, M. E., Turnbull, L., Johnson, M. S., Whitchurch, C. B., O'Toole, G. A., & Camesano, T. A. (2012). Atomic force and super-resolution microscopy support a role for LapA as a cell-surface biofilm adhesin of Pseudomonas fluorescens. *Research in Microbiology*. https://doi.org/10.1016/j.resmic.2012.10.001

Jayathilake, P. G., Gupta, P., Li, B., Madsen, C., Oyebamiji, O., González-Cabaleiro, R., Rushton, S., Bridgens, B., Swailes, D., Allen, B., McGough, A. S., Zuliani, P., Ofiteru, I. D., Wilkinson, D., Chen, J., & Curtis, T. (2017). A mechanistic Individual-based Model of microbial communities. *PLoS ONE*, *12*(8), e0181965. https://doi.org/10.1371/journal.pone.0181965

Jennings, L. K., Storek, K. M., Ledvina, H. E., Coulon, C., Marmont, L. S., Sadovskaya, I., Secor, P. R., Tseng, B. S., Scian, M., Filloux, A., Wozniak, D. J., Howell, P. L., & Parsek, M. R. (2015). Pel is a cationic exopolysaccharide that cross-links extracellular DNA in the Pseudomonas aeruginosa biofilm matrix. *Proceedings of the National Academy of Sciences*, *112*(36), 11353. https://doi.org/10.1073/pnas.1503058112

Jia, D., Cheng, H., & Han, C. C. (2018). Interplay between Caging and Bonding in Binary Concentrated Colloidal Suspensions. *Langmuir*, *34*(9), 3021–3029. https://doi.org/10.1021/acs.langmuir.7b03965

Jia, D., Hollingsworth, J. v, Zhou, Z., Cheng, H., & Han, C. C. (2015). Coupling of gelation and glass transition in a biphasic colloidal mixture—from gel-to-defective gel-to-glass. *Soft Matter*, *11*(45), 8818–8826. https://doi.org/10.1039/C5SM01531F

Jiang, J., Wu, S., Wang, J., & Feng, Y. (2015). AHL-type quorum sensing and its regulation on symplasmata formation in Pantoea agglomerans YS19. *Journal of Basic Microbiology*, *55*(5), 607–616. https://doi.org/10.1002/jobm.201400472

Johnston, M. T., & Ewoldt, R. H. (2013). Precision rheometry: Surface tension effects on low-torque measurements in rotational rheometers. *Journal of Rheology*, *57*(6), 1515–1532. https://doi.org/10.1122/1.4819914

Jones, W. L., Sutton, M. P., McKittrick, L., & Stewart, P. S. (2011). Chemical and antimicrobial treatments change the viscoelastic properties of bacterial biofilms. *Biofouling*, *27*(2), 207–215. https://doi.org/10.1080/08927014.2011.554977

Juntae, K., Dimitri, M., Manfred, W., & Matthew, E. H. (2014). Microstructure and nonlinear signatures of yielding in a heterogeneous colloidal gel under large amplitude oscillatory shear. *Journal of Rheology*, *58*(5), 1359–1390. https://doi.org/10.1122/1.4882019

Kallmeyer, J., Pockalny, R., Adhikari, R. R., Smith, D. C., & D'Hondt, S. (2012). Global distribution of microbial abundance and biomass in subseafloor sediment. *Proceedings of the National Academy of Sciences*, *109*(40), 16213–16216. https://doi.org/10.1073/pnas.1203849109

Kasim, W. A., Gaafar, R. M., Abou-Ali, R. M., Omar, M. N., & Hewait, H. M. (2016). Effect of biofilm forming plant growth promoting rhizobacteria on salinity

tolerance in barley. *Annals of Agricultural Sciences*, *61*(2), 217–227. https://doi.org/https://doi.org/10.1016/j.aoas.2016.07.003

Kesel, S., Grumbein, S., Gümperlein, I., Tallawi, M., Marel, A.-K., Lieleg, O., & Opitz, M. (2016). Direct Comparison of Physical Properties of Bacillus subtilis NCIB 3610 and B-1 Biofilms. *Applied and Environmental Microbiology*, *82*(8), 2424–2432. https://doi.org/10.1128/aem.03957-15

Kevin Kim, M., Drescher, K., Shun Pak, O., Bassler, B. L., & Stone, H. A. (2014). Filaments in curved streamlines: rapid formation ofStaphylococcus aureusbiofilm streamers. *New Journal of Physics*, *16*(6), 65024. https://doi.org/10.1088/1367-2630/16/6/065024

Khandavalli, S., Hendricks, J., Clasen, C., & Rothstein, J. P. (2016). A comparison of linear and branched wormlike micelles using large amplitude oscillatory shear and orthogonal superposition rheology. *Journal of Rheology*, *60*(6), 1331–1346. https://doi.org/10.1122/1.4965435

Kim, J., Merger, D., Wilhelm, M., & Helgeson, M. E. (2014). Microstructure and nonlinear signatures of yielding in a heterogeneous colloidal gel under large amplitude oscillatory shear. *Journal of Rheology*, *58*(5), 1359–1390. https://doi.org/10.1122/1.4882019

Kives, J., Orgaz, B., & SanJosé, C. (2006). Polysaccharide differences between planktonic and biofilm-associated EPS from Pseudomonas fluorescens B52. *Colloids and Surfaces B: Biointerfaces*. https://doi.org/10.1016/j.colsurfb.2006.04.018

Klemuk, S. A., & Titze, I. R. (2009). Determining motor inertia of a stress-controlled rheometer. *Journal of Rheology*, *53*(4), 765–780. https://doi.org/10.1122/1.3119056

Klotz, M., Kretschmer, M., Goetz, A., Ezendam, S., Lieleg, O., & Opitz, M. (2019). Importance of the biofilm matrix for the erosion stability of Bacillus subtilis NCIB 3610 biofilms. *RSC Advances*, *9*(20), 11521–11529. https://doi.org/10.1039/C9RA01955C

Kobayashi, K., & Iwano, M. (2012). BslA(YuaB) forms a hydrophobic layer on the surface of Bacillus subtilis biofilms. *Molecular Microbiology*, *85*(1), 51–66. https://doi.org/10.1111/j.1365-2958.2012.08094.x

Komatsu, H., Mitsui, T., & Onogi, S. (1973). Nonlinear Viscoelastic Properties of Semisolid Emulsions. *Transactions of the Society of Rheology*, *17*(2), 351–364. https://doi.org/10.1122/1.549285

Körstgens, V., Flemming, H.-C., Wingender, J., & Borchard, W. (2001). Uniaxial compression measurement device for investigation of the mechanical stability of biofilms. *Journal of Microbiological Methods*, *46*(1), 9–17. https://doi.org/https://doi.org/10.1016/S0167-7012(01)00248-2

Koumakis, N., Pamvouxoglou, A., Poulos, A. S., & Petekidis, G. (2012). Direct comparison of the rheology of model hard and soft particle glasses. *Soft Matter*, *8*(15), 4271–4284. https://doi.org/10.1039/C2SM07113D

Koumakis, N., & Petekidis, G. (2011). Two step yielding in attractive colloids: transition from gels to attractive glasses. *Soft Matter*, *7*(6), 2456–2470. https://doi.org/10.1039/C0SM00957A

Kovach, K., Davis-Fields, M., Irie, Y., Jain, K., Doorwar, S., Vuong, K., Dhamani, N., Mohanty, K., Touhami, A., & Gordon, V. D. (2017). Evolutionary adaptations of biofilms infecting cystic fibrosis lungs promote mechanical toughness by adjusting polysaccharide production. *Npj Biofilms And Microbiomes*, *3*(1), 1. https://doi.org/10.1038/s41522-016-0007-9

Kramb, R. C., & Zukoski, C. F. (2011). Exploration of the volume fraction above which suspensions of spherical and weakly anisotropic colloid particles cannot flow. *Journal of Rheology*, *55*(5), 1085–1101. https://doi.org/10.1122/1.3613983

Kretschmer, M., & Lieleg, O. (2020a). Chelate chemistry governs ion-specific stiffening of Bacillus subtilis B-1 and Azotobacter vinelandii biofilms. *Biomaterials Science*. https://doi.org/10.1039/C9BM01763A

Kretschmer, M., & Lieleg, O. (2020b). Chelate chemistry governs ion-specific stiffening of Bacillus subtilis B-1 and Azotobacter vinelandii biofilms. *Biomaterials Science*. https://doi.org/10.1039/C9BM01763A

Kuang, J., Yuk, K. Y., & Huh, K. M. (2011). Polysaccharide-based superporous hydrogels with fast swelling and superabsorbent properties. *Carbohydrate Polymers*, *83*(1), 284–290. https://doi.org/https://doi.org/10.1016/j.carbpol.2010.07.052

Kuczera, S., Gentile, L., Brox, T. I., Olsson, U., Schmidt, C., & Galvosas, P. (2018). Multilamellar Vesicle Formation Probed by Rheo-NMR and Rheo-SALS under Large Amplitude Oscillatory Shear. *Langmuir*, *34*(28), 8314–8325. https://doi.org/10.1021/acs.langmuir.8b01510

Kundukad, B., Schussman, M., Yang, K., Seviour, T., Yang, L., Rice, S. A., Kjelleberg, S., & Doyle, P. S. (2017). Mechanistic action of weak acid drugs on biofilms. *Scientific Reports*, *7*(1), 4783. https://doi.org/10.1038/s41598-017-05178-3

Kundukad, B., Seviour, T., Liang, Y., Rice, S. A., Kjelleberg, S., & Doyle, P. S. (2016). Mechanical properties of the superficial biofilm layer determine the architecture of biofilms. *Soft Matter*, *12*(26), 5718–5726. https://doi.org/10.1039/C6SM00687F

Kuypers, M. M. M., Marchant, H. K., & Kartal, B. (2018). The microbial nitrogen-cycling network. *Nature Reviews Microbiology*, *16*(5), 263–276. https://doi.org/10.1038/nrmicro.2018.9

Kwang Soo, C., Kyu, H., Kyung Hyun, A., & Seung Jong, L. (2005). A geometrical interpretation of large amplitude oscillatory shear response. *Journal of Rheology*, *49*(3), 747–758. https://doi.org/10.1122/1.1895801

Kyrylyuk, A. v, Wouterse, A., & Philipse, A. P. (2009). Random Packings Of Rod-Sphere Mixtures Simulated By Mechanical Contraction. *AIP Conference Proceedings*, *1145*(1), 211–214. https://doi.org/10.1063/1.3179895

Lau, P. C. Y., Dutcher, J. R., Beveridge, T. J., & Lam, J. S. (2009). Absolute quantitation of bacterial biofilm adhesion and viscoelasticity by microbead force spectroscopy. *Biophysical Journal*, *96*(7), 2935–2948. https://doi.org/10.1016/j.bpj.2008.12.3943

Läuger, J., & Stettin, H. (2016). Effects of instrument and fluid inertia in oscillatory shear in rotational rheometers. *Journal of Rheology*, *60*(3), 393–406. https://doi.org/10.1122/1.4944512

Laurati, M., Egelhaaf, S. U., & Petekidis, G. (2011). Nonlinear rheology of colloidal gels with intermediate volume fraction. *Journal of Rheology*, *55*(3), 673–706. https://doi.org/10.1122/1.3571554

Lee, C. K., de Anda, J., Baker, A. E., Bennett, R. R., Luo, Y., Lee, E. Y., Keefe, J. A., Helali, J. S., Ma, J., Zhao, K., Golestanian, R., O'Toole, G. A., & Wong, G. C. L. (2018). Multigenerational memory and adaptive adhesion in early bacterial biofilm communities. *Proc Natl Acad Sci U S A*, *115*(17), 4471–4476. https://doi.org/10.1073/pnas.1720071115

Lee, C.-W., & Rogers, S. A. (2017). A sequence of physical processes quantified in LAOS by continuous local measures. *Korea-Australia Rheology Journal*, *29*(4), 269–279. https://doi.org/10.1007/s13367-017-0027-x

Lee, K. Y., & Mooney, D. J. (2012). Alginate: properties and biomedical applications. *Progress in Polymer Science*, *37*(1), 106–126. https://doi.org/10.1016/j.progpolymsci.2011.06.003

Lei, K., Li, Z., Zhu, D., Sun, C., Sun, Y., Yang, C., Zheng, Z., & Wang, X. (2020). Polysaccharide-based recoverable double-network hydrogel with high strength and self-healing properties. *Journal of Materials Chemistry B*, *8*(4), 794–802. https://doi.org/10.1039/C9TB01679A

Lieleg, O., Caldara, M., Baumgärtel, R., & Ribbeck, K. (2011). Mechanical robustness of Pseudomonas aeruginosa biofilms. *Soft Matter*, *7*(7), 3307–3314. https://doi.org/10.1039/c0sm01467b

Likos, C. N. (2001). Effective interactions in soft condensed matter physics. *Physics Reports*, *348*(4), 267–439. https://doi.org/https://doi.org/10.1016/S0370-1573(00)00141-1

Linnes, J. C., Ma, H., & Bryers, J. D. (2013). Giant Extracellular Matrix Binding Protein Expression in Staphylococcus epidermidis is Regulated by Biofilm Formation and Osmotic Pressure. *Current Microbiology*, *66*(6), 627–633. https://doi.org/10.1007/s00284-013-0316-7

Lushi, E., Wioland, H., & Goldstein, R. E. (2014). Fluid flows created by swimming bacteria drive self-organization in confined suspensions. *Proceedings of the National Academy of Sciences*, *111*(27), 9733. https://doi.org/10.1073/pnas.1405698111

Maddah, H., & Chogle, A. (2017). Biofouling in reverse osmosis: phenomena, monitoring, controlling and remediation. *Applied Water Science*, *7*(6), 2637–2651. https://doi.org/10.1007/s13201-016-0493-1

Madsen, J. S., Burmølle, M., Hansen, L. H., & Sørensen, S. J. (2012). The interconnection between biofilm formation and horizontal gene transfer. *FEMS Immunology & Medical Microbiology*, *65*(2), 183–195. https://doi.org/10.1111/j.1574-695X.2012.00960.x

Magami, S. M., & Williams, R. L. (2019). Gelation via cationic chelation/crosslinking of acrylic-acid-based polymers. *Polymer International*, *68*(12), 1980–1991. https://doi.org/10.1002/pi.5910

Mallick, I., Bhattacharyya, C., Mukherji, S., Dey, D., Sarkar, S. C., Mukhopadhyay, U. K., & Ghosh, A. (2018). Effective rhizoinoculation and biofilm formation by arsenic immobilizing halophilic plant growth promoting bacteria (PGPB) isolated from mangrove rhizosphere: A step towards arsenic rhizoremediation. *Science of The Total Environment*, *610–611*, 1239–1250. https://doi.org/https://doi.org/10.1016/j.scitotenv.2017.07.234

Marenduzzo, D., Finan, K., & Cook, P. R. (2006). The depletion attraction: an underappreciated force driving cellular organization. *Journal of Cell Biology*, *175*(5), 681–686. https://doi.org/10.1083/jcb.200609066

Marshall, D. C., Arruda, B. E., & Silby, M. W. (2019). Alginate genes are required for optimal soil colonization and persistence by Pseudomonas fluorescens Pf0-1. *Access Microbiology*, *1*(3), e000021. https://doi.org/10.1099/acmi.0.000021

Martinez-Corral, R., Liu, J., Süel, G. M., & Garcia-Ojalvo, J. (2018). Bistable emergence of oscillations in growing Bacillus subtilis biofilms. *Proceedings of the National Academy of Sciences*, *115*(36), E8333. https://doi.org/10.1073/pnas.1805004115

Massalha, H., Korenblum, E., Malitsky, S., Shapiro, O. H., & Aharoni, A. (2017). Live imaging of root–bacteria interactions in a microfluidics setup. *Proceedings of the National Academy of Sciences*, *114*(17), 4549–4554. https://doi.org/10.1073/pnas.1618584114

Mathias, J. D., & Stoodley, P. (2009). Applying the digital image correlation method to estimate the mechanical properties of bacterial biofilms subjected to a wall shear stress. *Biofouling*, *25*(8), 695–703. https://doi.org/10.1080/08927010903104984

Mccoy, J. L., & Muthukumar, M. (2010). Dynamic light scattering studies of ionic and nonionic polymer gels with continuous and discontinuous volume transitions. *Journal of Polymer Science Part B: Polymer Physics*, *48*(21), 2193–2206. https://doi.org/10.1002/polb.22101

McKinley, R. H. E. and G. H. (2007). Creep Ringing in Rheometry or How to Deal with Oft-discarded Data in Step Stress Tests! *Rheology Bulletin*, *76*(1) 4-6.

Meakin, P., & Djordjevic, Z. B. (1986). Cluster-cluster aggregation in two-monomer systems. *Journal of Physics A: Mathematical and General*, *19*(11), 2137–2153. https://doi.org/10.1088/0305-4470/19/11/023

Meera, A. P., Said, S., Grohens, Y., & Thomas, S. (2009). Nonlinear Viscoelastic Behavior of Silica-Filled Natural Rubber Nanocomposites. *The Journal of Physical Chemistry C*, *113*(42), 17997–18002. https://doi.org/10.1021/jp9020118

Mendoza, L., Batchelor, W., Tabor, R. F., & Garnier, G. (2018). Gelation mechanism of cellulose nanofibre gels: A colloids and interfacial perspective. *Journal of Colloid and Interface Science*, *509*, 39–46. https://doi.org/https://doi.org/10.1016/j.jcis.2017.08.101

Miller, M. B., Skorupski, K., Lenz, D. H., Taylor, R. K., & Bassler, B. L. (2002). Parallel Quorum Sensing Systems Converge to Regulate Virulence in Vibrio cholerae. *Cell*, *110*(3), 303–314. https://doi.org/https://doi.org/10.1016/S0092-8674(02)00829-2

Minogue, T. D., Trebra, M. W., Bernhard, F., & Bodman, S. B. von. (2002). The autoregulatory role of EsaR, a quorum-sensing regulator in Pantoea stewartii ssp. stewartii: evidence for a repressor function. *Molecular Microbiology*, *44*(6), 1625–1635. https://doi.org/10.1046/j.1365-2958.2002.02987.x

Mitrofanova, O., Mardanova, A., Evtugyn, V., Bogomolnaya, L., & Sharipova, M. (2017). Effects of Bacillus Serine Proteases on the Bacterial Biofilms. *BioMed Research International*, *2017*, 8525912. https://doi.org/10.1155/2017/8525912

Miwa, Y., Kurachi, J., Kohbara, Y., & Kutsumizu, S. (2018). Dynamic ionic crosslinks enable high strength and ultrastretchability in a single elastomer. *Communications Chemistry*, *1*(1), 5. https://doi.org/10.1038/s42004-017-0004-9

Molina-Santiago, C., Pearson, J. R., Navarro, Y., Berlanga-Clavero, M. V., Caraballo-Rodriguez, A. M., Petras, D., García-Martín, M. L., Lamon, G., Haberstein, B., Cazorla, F. M., de Vicente, A., Loquet, A., Dorrestein, P. C., & Romero, D. (2019). The extracellular matrix protects Bacillus subtilis colonies from Pseudomonas invasion and modulates plant co-colonization. *Nature Communications*, *10*(1), 1919. https://doi.org/10.1038/s41467-019-09944-x

Mosier, A. P., Kaloyeros, A. E., & Cady, N. C. (2012). A novel microfluidic device for the in situ optical and mechanical analysis of bacterial biofilms. *Journal of Microbiological Methods*, *91*(1), 198–204. https://doi.org/http://dx.doi.org/10.1016/j.mimet.2012.07.006

Myung, D., Waters, D., Wiseman, M., Duhamel, P.-E., Noolandi, J., Ta, C. N., & Frank, C. W. (2008). Progress in the development of interpenetrating polymer network hydrogels. *Polymers for Advanced Technologies*, *19*(6), 647–657. https://doi.org/10.1002/pat.1134

Nadell, C. D., Drescher, K., & Foster, K. R. (2016). Spatial structure, cooperation and competition in biofilms. *Nature Reviews Microbiology*, *14*(9), 589–600. https://doi.org/10.1038/nrmicro.2016.84

Ni, L., Yang, S., Zhang, R., Jin, Z., Chen, H., Conrad, J. C., & Jin, F. (2016). Bacteria differently deploy type-IV pili on surfaces to adapt to nutrient availability. *Npj Biofilms And Microbiomes*, *2*, 15029. https://doi.org/10.1038/npjbiofilms.2015.29 https://www.nature.com/articles/npjbiofilms201529#supplementary-information

Nimtz, M., Mort, A., Domke, T., Wray, V., Zhang, Y., Qui, F., Coplin, D., & Geider, K. (1996). Structure of amylovoran, the capsular exopolysaccharide from the fire blight pathogen Erwinia amylovora. *Carbohydrate Research*. https://doi.org/10.1016/0008-6215(96)00070-5

Orazi, G., & O'Toole, G. A. (2017). Pseudomonas aeruginosa Alters Staphylococcus aureus Sensitivity to Vancomycin in a Biofilm Model of Cystic Fibrosis Infection. *MBio*, *8*(4), e00873-17. https://doi.org/10.1128/mBio.00873-17

Otto, K., & Silhavy, T. J. (2002). Surface Sensing and Adhesion of Escherichia coli Controlled by the Cpx-Signaling Pathway. *Proceedings of the National Academy of Sciences of the United States of America*, *99*(4), 2287–2292. http://www.jstor.org/stable/3057957

Ozkan, S., Gillece, T. W., Senak, L., & Moore, D. J. (2012). Characterization of yield stress and slip behaviour of skin/hair care gels using steady flow and LAOS measurements and their correlation with sensorial attributes. *International Journal of Cosmetic Science*, *34*(2), 193–201. https://doi.org/10.1111/j.1468-2494.2012.00702.x

Pakkulnan, R., Anutrakunchai, C., Kanthawong, S., Taweechaisupapong, S., Chareonsudjai, P., & Chareonsudjai, S. (2019). Extracellular DNA facilitates bacterial adhesion during Burkholderia pseudomallei biofilm formation. *PLoS ONE*, *14*(3), e0213288. https://doi.org/10.1371/journal.pone.0213288

Paquet-Mercier, F., Parvinzadeh Gashti, M., Bellavance, J., Taghavi, S. M., & Greener, J. (2016). Effect of NaCl on Pseudomonas biofilm viscosity by continuous, non-intrusive microfluidic-based approach. *ArXiv E-Prints*.

Park, A., Jeong, H.-H., Lee, J., Kim, K. P., & Lee, C.-S. (2011). Effect of shear stress on the formation of bacterial biofilm in a microfluidic channel. *BioChip Journal*, *5*(3), 236. https://doi.org/10.1007/s13206-011-5307-9

Park, J. D., Ahn, K. H., & Wagner, N. J. (2016). Structure-rheology relationship for a homogeneous colloidal gel under shear startup. *Journal of Rheology*, *61*(1), 117–137. https://doi.org/10.1122/1.4971993

Parmar, A. S., Hill, S., Vidyasagar, A., Bello, C., Toomey, R., & Muschol, M. (2013). Frequency and temperature dependence of poly(N-isopropylacrylamide) gel rheology. *Journal of Applied Polymer Science*, *127*(3), 1527–1537. https://doi.org/10.1002/app.37561

Passos da Silva, D., Matwichuk, M. L., Townsend, D. O., Reichhardt, C., Lamba, D., Wozniak, D. J., & Parsek, M. R. (2019). The Pseudomonas aeruginosa lectin LecB binds to the exopolysaccharide Psl and stabilizes the biofilm matrix. *Nature Communications*, *10*(1), 2183. https://doi.org/10.1038/s41467-019-10201-4

Paul Stoodley, John D. Boyle, Z. L., & Lappin-Scott, H. M. (1999). Structural Deformation of Bacterial Biofilms Caused by Short-Term Fluctuations in Fluid Shear: An In Situ Investigation of Biofilm Rheology. *Biotechnology and Bioengineering*, *65*, 83–92. https://doi.org/10.1002/(SICI)1097-0290(19991005)65:1<83::AID-BIT10>3.0.CO;2-B

Pavlovsky, L., Sturtevant, R. A., Younger, J. G., & Solomon, M. J. (2015). Effects of Temperature on the Morphological, Polymeric, and Mechanical Properties of Staphylococcus epidermidis Bacterial Biofilms. *Langmuir*, *31*(6), 2036–2042. https://doi.org/10.1021/la5044156

Pavlovsky, L., Younger, J. G., & Solomon, M. J. (2013). In situ rheology of Staphylococcus epidermidis bacterial biofilms. *Soft Matter*, *9*(1), 122–131. https://doi.org/10.1039/C2SM27005F

Pearson, D. S., & Rochefort, W. E. (1982). Behavior of concentrated polystyrene solutions in large-amplitude oscillating shear fields. *Journal of Polymer Science: Polymer Physics Edition*, *20*(1), 83–98. https://doi.org/10.1002/pol.1982.180200107

Perera-Costa, D., Bruque, J. M., González-Martín, M. L., Gómez-García, A. C., & Vadillo-Rodríguez, V. (2014). Studying the Influence of Surface Topography on Bacterial Adhesion using Spatially Organized Microtopographic Surface Patterns. *Langmuir*, *30*(16), 4633–4641. https://doi.org/10.1021/la5001057

Perge, C., Taberlet, N., Gibaud, T., & Manneville, S. (2014). Time dependence in large amplitude oscillatory shear: A rheo-ultrasonic study of fatigue dynamics in a colloidal gel. *Journal of Rheology*, *58*(5), 1331–1357. https://doi.org/10.1122/1.4887081

Peterson, B. W., van der Mei, H. C., Sjollema, J., Busscher, H. J., & Sharma, P. K. (2013). A Distinguishable Role of eDNA in the Viscoelastic Relaxation of Biofilms. *MBio*, *4*(5). https://doi.org/10.1128/mBio.00497-13

Pham, K. N., Petekidis, G., Vlassopoulos, D., Egelhaaf, S. U., Pusey, P. N., & Poon, W. C. K. (2006). Yielding of colloidal glasses. *Europhysics Letters (EPL)*, *75*(4), 624–630. https://doi.org/10.1209/epl/i2006-10156-y

Philippe, A. M., Baravian, C., Bezuglyy, V., Angilella, J. R., Meneau, F., Bihannic, I., & Michot, L. J. (2013). Rheological Study of Two-Dimensional Very Anisometric Colloidal Particle Suspensions: From Shear-Induced Orientation to Viscous Dissipation. *Langmuir*, *29*(17), 5315–5324. https://doi.org/10.1021/la400111w

Philippoff, W. (1966). Vibrational Measurements with Large Amplitudes. *Transactions of the Society of Rheology*, *10*(1), 317–334. https://doi.org/10.1122/1.549049

Picioreanu, C., Blauert, F., Horn, H., & Wagner, M. (2018). Determination of mechanical properties of biofilms by modelling the deformation measured using optical coherence tomography. *Water Research*, *145*, 588–598. https://doi.org/https://doi.org/10.1016/j.watres.2018.08.070

Piessens, V., de Vliegher, S., Verbist, B., Braem, G., van Nuffel, A., de Vuyst, L., Heyndrickx, M., & van Coillie, E. (2012). Intra-species diversity and epidemiology varies among coagulase-negative Staphylococcus species causing bovine intramammary infections. *Veterinary Microbiology*, *155*(1), 62–71. https://doi.org/https://doi.org/10.1016/j.vetmic.2011.08.005

Potocki de Montalk, G., Remaud-Simeon, M., Willemot, R.-M., Sarçabal, P., Planchot, V., & Monsan, P. (2000). Amylosucrase from Neisseria polysaccharea: novel catalytic properties. *FEBS Letters*, *471*(2–3), 219–223. https://doi.org/10.1016/S0014-5793(00)01406-X

Poulos, A. S., Stellbrink, J., & Petekidis, G. (2013). Flow of concentrated solutions of starlike micelles under large-amplitude oscillatory shear. *Rheologica Acta*, *52*(8), 785–800. https://doi.org/10.1007/s00397-013-0703-9

Powell, L. C., Sowedan, A., Khan, S., Wright, C. J., Hawkins, K., Onsøyen, E., Myrvold, R., Hill, K. E., & Thomas, D. W. (2013). The effect of alginate oligosaccharides on the mechanical properties of Gram-negative biofilms. *Biofouling*, *29*(4), 413–421. https://doi.org/10.1080/08927014.2013.777954

Raghavan, S. R., & Douglas, J. F. (2012). The conundrum of gel formation by molecular nanofibers, wormlike micelles, and filamentous proteins: gelation without cross-links? *Soft Matter*, *8*(33), 8539–8546. https://doi.org/10.1039/C2SM25107H

Randy, H. E., Hosoi, A. E., & Gareth, H. M. (2008). New measures for characterizing nonlinear viscoelasticity in large amplitude oscillatory shear. *Journal of Rheology*, *52*(6), 1427–1458. https://doi.org/10.1122/1.2970095

Reichhardt, C., Wong, C., Passos da Silva, D., Wozniak, D. J., & Parsek, M. R. (2018). CdrA Interactions within the Pseudomonas aeruginosa Biofilm Matrix Safeguard It from Proteolysis and Promote Cellular Packing. *MBio*, *9*(5), e01376-18. https://doi.org/10.1128/mBio.01376-18

Riou, J. Y., Guibourdenche, M., & Popoff, M. Y. (1983). A new taxon in the genus Neisseria. *Annales de l'Institut Pasteur / Microbiologie*, *134*(2, Supplement B), 257–267. https://doi.org/https://doi.org/10.1016/S0769-2609(83)80038-6

Riou, J.-Y., Guibourdenche, M., Perry, M. B., MacLan, L. L., & Griffith, D. W. (1986). Structure of the exocellular D-glucan produced by Neisseria polysaccharea. *Canadian Journal of Microbiology*, *32*(12), 909–911. https://doi.org/10.1139/m86-167

Rmaile, A., Carugo, D., Capretto, L., Zhang, X., Wharton, J. A., Thurner, P. J., Aspiras, M., Ward, M., & Stoodley, P. (2013). Microbial tribology and disruption of dental plaque bacterial biofilms. *Wear*, *306*(1), 276–284. https://doi.org/https://doi.org/10.1016/j.wear.2013.02.010

Rochex, A., Massé, A., Escudié, R., Godon, J.-J., & Bernet, N. (2009). Influence of abrasion on biofilm detachment: evidence for stratification of the biofilm. *Journal of Industrial Microbiology & Biotechnology*, *36*(3), 467–470. https://doi.org/10.1007/s10295-009-0543-x

Rogers, S. A. (2017). In search of physical meaning: defining transient parameters for nonlinear viscoelasticity. *Rheologica Acta*, *56*(5), 501–525. https://doi.org/10.1007/s00397-017-1008-1

Rogers, S. A., Erwin, B. M., Vlassopoulos, D., & Cloitre, M. (2011). A sequence of physical processes determined and quantified in LAOS: Application to a yield stress fluid. *Journal of Rheology*, *55*(2), 435–458. https://doi.org/10.1122/1.3544591

Rogers, S. A., & Lettinga, M. P. (2011). A sequence of physical processes determined and quantified in large-amplitude oscillatory shear (LAOS): Application to theoretical nonlinear models. *Journal of Rheology*, *56*(1), 1–25. https://doi.org/10.1122/1.3662962

Rogers, S. S., van der Walle, C., & Waigh, T. A. (2008). Microrheology of Bacterial Biofilms In Vitro: Staphylococcus aureus and Pseudomonas aeruginosa. *Langmuir*, *24*(23), 13549–13555. https://doi.org/10.1021/la802442d

Rohde, H., Burdelski, C., Bartscht, K., Hussain, M., Buck, F., Horstkotte, M. A., Knobloch, J. K.-M., Heilmann, C., Herrmann, M., & Mack, D. (2005). Induction of Staphylococcus epidermidis biofilm formation via proteolytic processing of the

accumulation-associated protein by staphylococcal and host proteases. *Molecular Microbiology*, *55*(6), 1883–1895. https://doi.org/10.1111/j.1365-2958.2005.04515.x

Roth, M. (2012). *Rheology of arrested colloids: a parameter study using novel experimental methods.* http://ubm.opus.hbz-nrw.de/volltexte/2012/3009/pdf/doc.pdf.

Rozenbaum, R. T., van der Mei, H. C., Woudstra, W., de Jong, E. D., Busscher, H. J., & Sharma, P. K. (2019). Role of Viscoelasticity in Bacterial Killing by Antimicrobials in Differently Grown Pseudomonas aeruginosa Biofilms. *Antimicrobial Agents and Chemotherapy*, *63*(4), e01972-18. https://doi.org/10.1128/AAC.01972-18

Rühs, P A, Böcker, L., Inglis, R. F., & Fischer, P. (2014). Studying bacterial hydrophobicity and biofilm formation at liquid–liquid interfaces through interfacial rheology and pendant drop tensiometry. *Colloids and Surfaces B: Biointerfaces*, *117*, 174–184. https://doi.org/https://doi.org/10.1016/j.colsurfb.2014.02.023

Rühs, Patrick A, Böni, L., Fuller, G. G., Inglis, R. F., & Fischer, P. (2013). In-Situ Quantification of the Interfacial Rheological Response of Bacterial Biofilms to Environmental Stimuli. *PLoS ONE*, *8*(11), e78524. https://doi.org/10.1371/journal.pone.0078524

Rupp, C. J., Fux, C. A., & Stoodley, P. (2005). Viscoelasticity of Staphylococcus aureus Biofilms in Response to Fluid Shear Allows Resistance to Detachment and Facilitates Rolling Migration. *Applied and Environmental Microbiology*, *71*(4), 2175–2178. https://doi.org/10.1128/aem.71.4.2175-2178.2005

Rusconi, R., Lecuyer, S., Autrusson, N., Guglielmini, L., & Stone, H. A. (2011). Secondary Flow as a Mechanism for the Formation of Biofilm Streamers. *Biophysical Journal*, *100*(6), 1392–1399. https://doi.org/https://doi.org/10.1016/j.bpj.2011.01.065

Rutherford, S. T., & Bassler, B. L. (2012). Bacterial quorum sensing: its role in virulence and possibilities for its control. *Cold Spring Harbor Perspectives in Medicine*, *2*(11), a012427. https://doi.org/10.1101/cshperspect.a012427

Safari, A., Habimana, O., Allen, A., & Casey, E. (2014). The significance of calcium ions on Pseudomonas fluorescens biofilms – a structural and mechanical study. *Biofouling*, *30*(7), 859–869. https://doi.org/10.1080/08927014.2014.938648

Safari, A., Tukovic, Z., Cardiff, P., Walter, M., Casey, E., & Ivankovic, A. (2016). Interfacial separation of a mature biofilm from a glass surface – A combined experimental and cohesive zone modelling approach. *Journal of the Mechanical Behavior of Biomedical Materials*, *54*, 205–218. https://doi.org/http://dx.doi.org/10.1016/j.jmbbm.2015.09.013

Sagle, L. B., Zhang, Y., Litosh, V. A., Chen, X., Cho, Y., & Cremer, P. S. (2009). Investigating the Hydrogen-Bonding Model of Urea Denaturation. *Journal of the American Chemical Society*, *131*(26), 9304–9310. https://doi.org/10.1021/ja9016057

Sanchez, T., Chen, D. T. N., DeCamp, S. J., Heymann, M., & Dogic, Z. (2012). Spontaneous motion in hierarchically assembled active matter. *Nature*, *491*(7424), 431–434. https://doi.org/10.1038/nature11591

Sasse, J., Martinoia, E., & Northen, T. (2018). Feed Your Friends: Do Plant Exudates Shape the Root Microbiome? *Trends in Plant Science*, *23*(1), 25–41. https://doi.org/https://doi.org/10.1016/j.tplants.2017.09.003

Sauer, K., Cullen, M. C., Rickard, A. H., Zeef, L. A. H., Davies, D. G., & Gilbert, P. (2004). Characterization of nutrient-induced dispersion in Pseudomonas aeruginosa PAO1 biofilm. *Journal of Bacteriology*, *186*(21), 7312–7326. https://doi.org/10.1128/JB.186.21.7312-7326.2004

Schaffner, M., Rühs, P. A., Coulter, F., Kilcher, S., & Studart, A. R. (2017). 3D printing of bacteria into functional complex materials. *Science Advances*, *3*(12), eaao6804. https://doi.org/10.1126/sciadv.aao6804

Schiffer, C., Hilgarth, M., Ehrmann, M., & Vogel, R. F. (2019). Bap and Cell Surface Hydrophobicity Are Important Factors in Staphylococcus xylosus Biofilm Formation. *Frontiers in Microbiology*, *10*(1387). https://doi.org/10.3389/fmicb.2019.01387

Schollmeyer, M., Langlotz, C., Huber, A., Coplin, D. L., & Geider, K. (2012). Variations in the molecular masses of the capsular exopolysaccharides

amylovoran, pyrifolan and stewartan. *International Journal of Biological Macromolecules*. https://doi.org/10.1016/j.ijbiomac.2012.01.003

Schommer, N. N., Christner, M., Hentschke, M., Ruckdeschel, K., Aepfelbacher, M., & Rohde, H. (2011). Staphylococcus epidermidis uses distinct mechanisms of biofilm formation to interfere with phagocytosis and activation of mouse macrophage-like cells 774A.1. *Infection and Immunity*, *79*(6), 2267–2276. https://doi.org/10.1128/IAI.01142-10

Schrag, J. L. (1977). Deviation of Velocity Gradient Profiles from the “Gap Loading” and “Surface Loading” Limits in Dynamic Simple Shear Experiments. *Transactions of the Society of Rheology*, *21*(3), 399–413. https://doi.org/10.1122/1.549445

Schultz, M. P., Bendick, J. A., Holm, E. R., & Hertel, W. M. (2011). Economic impact of biofouling on a naval surface ship. *Biofouling*, *27*(1), 87–98. https://doi.org/10.1080/08927014.2010.542809

Schwartz, K., Ganesan, M., Payne, D. E., Solomon, M. J., & Boles, B. R. (2016). Extracellular DNA facilitates the formation of functional amyloids in Staphylococcus aureus biofilms. *Molecular Microbiology*, *99*(1), 123–134. https://doi.org/10.1111/mmi.13219

Secor, P. R., Sweere, J. M., Michaels, L. A., Malkovskiy, A. V., Lazzareschi, D., Katznelson, E., Rajadas, J., Birnbaum, M. E., Arrigoni, A., Braun, K. R., Evanko, S. P., Stevens, D. A., Kaminsky, W., Singh, P. K., Parks, W. C., & Bollyky, P. L. (2015). Filamentous Bacteriophage Promote Biofilm Assembly and Function. *Cell Host & Microbe*, *18*(5), 549–559. https://doi.org/https://doi.org/10.1016/j.chom.2015.10.013

Serra, D. O., Richter, A. M., & Hengge, R. (2013). Cellulose as an Architectural Element in Spatially Structured Escherichia coli Biofilms. *Journal of Bacteriology*, *195*(24), 5540. https://doi.org/10.1128/JB.00946-13

Shao, Z., Negi, A. S., & Osuji, C. O. (2013). Role of interparticle attraction in the yielding response of microgel suspensions. *Soft Matter*, *9*(22), 5492–5500. https://doi.org/10.1039/C3SM50209K

Shen, Yi, Siryaporn, A., Lecuyer, S., Gitai, Z., & Stone, H. A. (2012). Flow directs surface-attached bacteria to twitch upstream. *Biophysical Journal*, *103*(1), 146–151. https://doi.org/10.1016/j.bpj.2012.05.045

Shen, Yun, Huang, C., Monroy, G. L., Janjaroen, D., Derlon, N., Lin, J., Espinosa-Marzal, R., Morgenroth, E., Boppart, S. A., Ashbolt, N. J., Liu, W.-T., & Nguyen, T. H. (2016). Response of Simulated Drinking Water Biofilm Mechanical and Structural Properties to Long-Term Disinfectant Exposure. *Environmental Science & Technology*, *50*(4), 1779–1787. https://doi.org/10.1021/acs.est.5b04653

Sherman, E., Bayles, K., Moormeier, D., Endres, J., & Wei, T. (2019). Observations of Shear Stress Effects on Staphylococcus aureus Biofilm Formation. *MSphere*, *4*(4), e00372-19. https://doi.org/10.1128/mSphere.00372-19

Shukla, A., Arnipally, S., Dagaonkar, M., & Joshi, Y. M. (2015). Two-step yielding in surfactant suspension pastes. *Rheologica Acta*, *54*(5), 353–364. https://doi.org/10.1007/s00397-015-0845-z

Smith, W. P. J., Davit, Y., Osborne, J. M., Kim, W., Foster, K. R., & Pitt-Francis, J. M. (2017). Cell morphology drives spatial patterning in microbial communities. *Proceedings of the National Academy of Sciences*, *114*(3), E280. https://doi.org/10.1073/pnas.1613007114

Smith-Palmer, T., Lin, S., Oguejiofor, I., Leng, T., Pustam, A., Yang, J., Graham, L. L., Wyeth, R. C., Bishop, C. D., DeMont, M. E., & Pink, D. (2016). In Situ Confocal Raman Microscopy of Hydrated Early Stages of Bacterial Biofilm Formation on Various Surfaces in a Flow Cell. *Applied Spectroscopy*, *70*(2), 289–301. https://doi.org/10.1177/0003702815620539

Solomon, M. J., & Spicer, P. T. (2010). Microstructural regimes of colloidal rod suspensions, gels, and glasses. *Soft Matter*, *6*(7), 1391–1400. https://doi.org/10.1039/B918281K

Song, H. Y., Salehiyan, R., Li, X., Lee, S. H., & Hyun, K. (2017). A comparative study of the effects of cone-plate and parallel-plate geometries on rheological properties under oscillatory shear flow. *Korea-Australia Rheology Journal*, *29*(4), 281–294. https://doi.org/10.1007/s13367-017-0028-9

Song, J. L., Au, K. H., Huynh, K. T., & Packman, A. I. (2014). Biofilm responses to smooth flow fields and chemical gradients in novel microfluidic flow cells. *Biotechnology and Bioengineering*, *111*(3), 597–607. https://doi.org/10.1002/bit.25107

Song, Y., & Zheng, Q. (2016). A Guide for Hydrodynamic Reinforcement Effect in Nanoparticle-filled Polymers. *Critical Reviews in Solid State and Materials Sciences*, *41*(4), 318–346. https://doi.org/10.1080/10408436.2015.1135415

Sotak, G. E., & Boyer, K. L. (1989). The laplacian-of-gaussian kernel: A formal analysis and design procedure for fast, accurate convolution and full-frame output. *Computer Vision, Graphics, and Image Processing*, *48*(2), 147–189. https://doi.org/https://doi.org/10.1016/S0734-189X(89)80036-2

Staudt, C., Horn, H., Hempel, D. C., & Neu, T. R. (2004). Volumetric measurements of bacterial cells and extracellular polymeric substance glycoconjugates in biofilms. *Biotechnology and Bioengineering*, *88*(5), 585–592. https://doi.org/10.1002/bit.20241

Stewart, E. J., Ganesan, M., Younger, J. G., & Solomon, M. J. (2015). Artificial biofilms establish the role of matrix interactions in staphylococcal biofilm assembly and disassembly. *Scientific Reports*, *5*, 13081. https://doi.org/10.1038/srep13081

Stewart, E. J., Satorius, A. E., Younger, J. G., & Solomon, M. J. (2013). Role of Environmental and Antibiotic Stress on Staphylococcus epidermidis Biofilm Microstructure. *Langmuir*, *29*(23), 7017–7024. https://doi.org/10.1021/la401322k

Stoodley, P., Cargo, R., Rupp, C. J., Wilson, S., & Klapper, I. (2002). Biofilm material properties as related to shear-induced deformation and detachment phenomena. *Journal of Industrial Microbiology and Biotechnology*, *29*(6), 361–367. https://doi.org/10.1038/sj.jim.7000282

Sun, W., Xue, B., Li, Y., Qin, M., Wu, J., Lu, K., Wu, J., Cao, Y., Jiang, Q., & Wang, W. (2016). Polymer-Supramolecular Polymer Double-Network Hydrogel. *Advanced Functional Materials*, *26*(48), 9044–9052. https://doi.org/10.1002/adfm.201603512

Sutherland, I. W. (2001). Biofilm exopolysaccharides: a strong and sticky framework. *Microbiology*, *147*(1), 3–9. https://doi.org/10.1099/00221287-147-1-3

Swenson, J., Smalley, M. v, & Hatharasinghe, H. L. M. (1998). Mechanism and Strength of Polymer Bridging Flocculation. *Physical Review Letters*, *81*(26), 5840–5843. https://doi.org/10.1103/PhysRevLett.81.5840

Tanaka, H., Meunier, J., & Bonn, D. (2004). Nonergodic states of charged colloidal suspensions: Repulsive and attractive glasses and gels. *Physical Review E*, *69*(3), 31404. https://doi.org/10.1103/PhysRevE.69.031404

Tanner, R. I. (2000). *Engineering rheology* (2nd ed..). New York : Oxford University Press.

Tao, R., Rice, K. D., Djakeu, A. S., Mrozek, R. A., Cole, S. T., Freeney, R. M., & Forster, A. M. (2019). Rheological Characterization of Next-Generation Ballistic Witness Materials for Body Armor Testing. *Polymers*, *11*(3). https://doi.org/10.3390/polym11030447

Tasaki, S., Nakayama, M., & Shoji, W. (2017). Self-organization of bacterial communities against environmental pH variation: Controlled chemotactic motility arranges cell population structures in biofilms. *PLoS ONE*, *12*(3), e0173195. https://doi.org/10.1371/journal.pone.0173195

Tecon, R., & Leveau, J. H. J. (2016). Symplasmata are a clonal, conditional, and reversible type of bacterial multicellularity. *Scientific Reports*, *6*, 31914. https://doi.org/10.1038/srep31914

Teodósio, J. S., Simões, M., Melo, L. F., & Mergulhão, F. J. (2011). Flow cell hydrodynamics and their effects on E. coli biofilm formation under different nutrient conditions and turbulent flow. *Biofouling*, *27*(1), 1–11. https://doi.org/10.1080/08927014.2010.535206

Towler, B. W., Cunningham, A., Stoodley, P., & McKittrick, L. (2007). A model of fluid–biofilm interaction using a Burger material law. *Biotechnology and Bioengineering*, *96*(2), 259–271. https://doi.org/10.1002/bit.21098

Towler, B. W., Rupp, C. J., Cunningham, A. L. B., & Stoodley, P. (2003). Viscoelastic Properties of a Mixed Culture Biofilm from Rheometer Creep Analysis. *Biofouling*, *19*(5), 279–285. https://doi.org/10.1080/0892701031000152470

Trunk, T., Khalil, H. S., & Leo, J. C. (2018). Bacterial autoaggregation. *AIMS Microbiology*, *4*(1), 140–164. https://doi.org/10.3934/microbiol.2018.1.140

Tsurusawa, H., Leocmach, M., Russo, J., & Tanaka, H. (2019). Direct link between mechanical stability in gels and percolation of isostatic particles. *Science Advances*, *5*(5), eaav6090. https://doi.org/10.1126/sciadv.aav6090

Vaart, K. van der, Yasser, R., Rojman, Z., Zhibing, H., Daniel, B., & Peter, S. (2013). Rheology of concentrated soft and hard-sphere suspensions. *Journal of Rheology*, *57*(4), 1195–1209. https://doi.org/10.1122/1.4808054

Vadillo-Rodríguez, V., Busscher, H. J., Norde, W., de Vries, J., & van der Mei, H. C. (2004). Atomic force microscopic corroboration of bond aging for adhesion of Streptococcus thermophilus to solid substrata. *Journal of Colloid and Interface Science*, *278*(1), 251–254. https://doi.org/https://doi.org/10.1016/j.jcis.2004.05.045

Valiei, A., Kumar, A., Mukherjee, P. P., Liu, Y., & Thundat, T. (2012). A web of streamers: biofilm formation in a porous microfluidic device. *Lab Chip*, *12*(24), 5133–5137. https://doi.org/10.1039/C2LC40815E

van der Sman, R. G. M. (2015). Biopolymer gel swelling analysed with scaling laws and Flory–Rehner theory. *Food Hydrocolloids*, *48*, 94–101. https://doi.org/https://doi.org/10.1016/j.foodhyd.2015.01.025

van Oosten, A. S. G., Chen, X., Chin, L., Cruz, K., Patteson, A. E., Pogoda, K., Shenoy, V. B., & Janmey, P. A. (2019). Emergence of tissue-like mechanics from fibrous networks confined by close-packed cells. *Nature*, *573*(7772), 96–101. https://doi.org/10.1038/s41586-019-1516-5

Veshchunov, M. S. (2015). Extension of the new kinetic approach to slow Brownian coagulation with finite sticking probability. *Journal of Engineering Thermophysics*, *24*(1), 1–11. https://doi.org/10.1134/S1810232815010014

Vidakovic, L., Singh, P. K., Hartmann, R., Nadell, C. D., & Drescher, K. (2018). Dynamic biofilm architecture confers individual and collective mechanisms of viral protection. *Nature Microbiology*, *3*(1), 26–31. https://doi.org/10.1038/s41564-017-0050-1

Vinogradov, A. M., Winston, M., Rupp, C. J., & Stoodley, P. (2004). Rheology of biofilms formed from the dental plaque pathogen Streptococcus mutans. *Biofilms*, *1*(01), 49–56. https://doi.org/doi:10.1017/S1479050503001078

Voigtmann, T. (2014). Nonlinear glassy rheology. *Current Opinion in Colloid & Interface Science*, *19*(6), 549–560. https://doi.org/https://doi.org/10.1016/j.cocis.2014.11.001

Walls, H. J., Caines, S. B., Sanchez, A. M., & Khan, S. A. (2003). Yield stress and wall slip phenomena in colloidal silica gels. *Journal of Rheology*, *47*(4), 847–868. https://doi.org/10.1122/1.1574023

Walter, M., Safari, A., Ivankovic, A., & Casey, E. (2013). Detachment characteristics of a mixed culture biofilm using particle size analysis. *Chemical Engineering Journal*, *228*, 1140–1147. https://doi.org/https://doi.org/10.1016/j.cej.2013.05.071

Wang, X., Hao, M., Du, X., Wang, G., & Matsushita, J.-I. (2016). The Mechanical Analysis of the Biofilm Streamer Nucleation and Geometry Characterization in Microfluidic Channels. *Computational and Mathematical Methods in Medicine*, *2016*, 7819403. https://doi.org/10.1155/2016/7819403

Wang, Z., Chen, Z., Yang, L., Tan, F., Wang, Y., Li, Q., Chang, Y.-I., Zhong, C.-J., & He, N. (2017). Effect of surface physicochemical properties on the flocculation behavior of Bacillus licheniformis. *RSC Advances*, *7*(26), 16049–16056. https://doi.org/10.1039/C6RA28057A

Waters, M. S., Kundu, S., Lin, N. J., & Lin-Gibson, S. (2014). Microstructure and Mechanical Properties of In Situ Streptococcus mutans Biofilms. *ACS Applied Materials & Interfaces*, *6*(1), 327–332. https://doi.org/10.1021/am404344h

Weeks, J. R., Duijneveldt, J. S. van, & Vincent, B. (2000). Formation and collapse of gels of sterically stabilized colloidal particles. *Journal of Physics: Condensed Matter*, *12*(46), 9599–9606. https://doi.org/10.1088/0953-8984/12/46/307

Whitaker, K. A., Varga, Z., Hsiao, L. C., Solomon, M. J., Swan, J. W., & Furst, E. M. (2019). Colloidal gel elasticity arises from the packing of locally glassy clusters. *Nature Communications*, *10*(1), 2237. https://doi.org/10.1038/s41467-019-10039-w

Wilhelm, M. (2002). Fourier-Transform Rheology. *Macromolecular Materials and Engineering*, *287*(2), 83–105. https://doi.org/10.1002/1439-2054(20020201)287:2<83::AID-MAME83>3.0.CO;2-B

Wilking, J. N., Zaburdaev, V., de Volder, M., Losick, R., Brenner, M. P., & Weitz, D. A. (2013). Liquid transport facilitated by channels in Bacillus subtilis biofilms. *Proceedings of the National Academy of Sciences of the United States of America*, *110*(3), 848–852. https://doi.org/10.1073/pnas.1216376110

William N. Findley, J. S. L. and K. O. (1989). *Creep and relaxation of nonlinear viscoelastic materials*. *Dover publications*.

Wu, C., Lim, J. Y., Fuller, G. G., & Cegelski, L. (2012). Quantitative Analysis of Amyloid-Integrated Biofilms Formed by Uropathogenic Escherichia coli at the Air-Liquid Interface. *Biophysical Journal*, *103*(3), 464–471. https://doi.org/10.1016/j.bpj.2012.06.049

Xiao, J., Hara, A. T., Kim, D., Zero, D. T., Koo, H., & Hwang, G. (2017). Biofilm three-dimensional architecture influences in situ pH distribution pattern on the human enamel surface. *International Journal of Oral Science*, *9*(2), 74–79. https://doi.org/10.1038/ijos.2017.8

Xing, D., Cheng, S., Logan, B. E., & Regan, J. M. (2010). Isolation of the exoelectrogenic denitrifying bacterium Comamonas denitrificans based on dilution to extinction. *Applied Microbiology and Biotechnology*, *85*(5), 1575–1587. https://doi.org/10.1007/s00253-009-2240-0

Xu, F., Ouyang, D., Rene, E. R., Ng, H. Y., Guo, L., Zhu, Y., Zhou, L., Yuan, Q., Miao, M., Wang, Q., & Kong, Q. (2019). Electricity production enhancement in a constructed wetland-microbial fuel cell system for treating saline wastewater. *Bioresource Technology*, *288*, 121462. https://doi.org/10.1016/J.BIORTECH.2019.121462

Xu, H., Fan, X., Song, Y., & Zheng, Q. (2020). Reinforcement and Payne effect of hydrophobic silica filled natural rubber nanocomposites. *Composites Science and Technology*, *187*, 107943. https://doi.org/https://doi.org/10.1016/j.compscitech.2019.107943

Xu, Y., Atrens, A. D., & Stokes, J. R. (2018). “Liquid, gel and soft glass” phase transitions and rheology of nanocrystalline cellulose suspensions as a function of concentration and salinity. *Soft Matter*, *14*(10), 1953–1963. https://doi.org/10.1039/C7SM02470C

Xu, Z., Shao, J., Li, B., Yan, X., Shen, Q., & Zhang, R. (2013). Contribution of bacillomycin D in Bacillus amyloliquefaciens SQR9 to antifungal activity and biofilm formation. *Applied and Environmental Microbiology*, *79*(3), 808–815. https://doi.org/10.1128/AEM.02645-12

Yan, F., Zhu, Z., Dong, X., Wang, C., Meng, X., Xie, Y., Zhang, G., & Qiu, D. (2018). Kinetics of Polymer Desorption from Colloids Probed by Aggregation-Induced Emission Fluorophore. *Langmuir*, *34*(24), 7006–7010. https://doi.org/10.1021/acs.langmuir.7b04215

Yan, J, Sharo, A. G., Stone, H. A., Wingreen, N. S., & Bassler, B. L. (2016). Vibrio cholerae biofilm growth program and architecture revealed by single-cell live imaging. *Proc Natl Acad Sci U S A*, *113*(36), E5337-43. https://doi.org/10.1073/pnas.1611494113

Yan, Jing, Fei, C., Mao, S., Moreau, A., Wingreen, N. S., Košmrlj, A., Stone, H. A., & Bassler, B. L. (2019). Mechanical instability and interfacial energy drive biofilm morphogenesis. *ELife*, *8*, e43920. https://doi.org/10.7554/eLife.43920

Yan, Jing, Moreau, A., Khodaparast, S., Perazzo, A., Feng, J., Fei, C., Mao, S., Mukherjee, S., Košmrlj, A., Wingreen, N. S., Bassler, B. L., & Stone, H. A. (2018). Bacterial Biofilm Material Properties Enable Removal and Transfer by Capillary Peeling. *Advanced Materials*, *30*(46), 1804153. https://doi.org/doi:10.1002/adma.201804153

Yan, Jing, Nadell, C. D., Stone, H. A., Wingreen, N. S., & Bassler, B. L. (2017). Extracellular-matrix-mediated osmotic pressure drives Vibrio cholerae biofilm expansion and cheater exclusion. *Nature Communications*, *8*(1), 327. https://doi.org/10.1038/s41467-017-00401-1

Yang, Jia, Li, Y., Zhu, L., Qin, G., & Chen, Q. (2018). Double network hydrogels with controlled shape deformation: A mini review. *Journal of Polymer Science Part B: Polymer Physics*, *56*(19), 1351–1362. https://doi.org/10.1002/polb.24735

Yang, Jing, Yu, J., Jiang, J., Liang, C., & Feng, Y. (2017). D-tyrosine affects aggregation behavior of Pantoea agglomerans. *Journal of Basic Microbiology*, *57*(2), 184–189. https://doi.org/10.1002/jobm.201600455

Yiwu, Z., Guangcui, Y., Chuanzhuang, Z., & Charles, C. H. (2013). Differentiating bonding and caging in a charged colloid system through rheological

measurements. *The Journal of Chemical Physics*, *138*(18), 184902. https://doi.org/10.1063/1.4803857

Yosick, J. A., Giacomin, J. A., Stewart, W. E., & Ding, F. (1998). Fluid inertia in large amplitude oscillatory shear. *Rheologica Acta*, *37*(4), 365–373. https://doi.org/10.1007/s003970050123

Yu, X., Jiang, J., Liang, C., Zhang, X., Wang, J., Shen, D., & Feng, Y. (2016). Indole affects the formation of multicellular aggregate structures in Pantoea agglomerans YS19. *The Journal of General and Applied Microbiology*, *62*(1), 31–37. https://doi.org/10.2323/jgam.62.31

Zaccarelli, E. (2007). Colloidal gels: equilibrium and non-equilibrium routes. *Journal of Physics: Condensed Matter*, *19*(32), 323101. https://doi.org/10.1088/0953-8984/19/32/323101

Zaccarelli, E., & Poon, W. C. K. (2009). Colloidal glasses and gels: The interplay of bonding and caging. *Proceedings of the National Academy of Sciences*, *106*(36), 15203. https://doi.org/10.1073/pnas.0902294106

Zeng, G., Vad, B. S., Dueholm, M. S., Christiansen, G., Nilsson, M., Tolker-Nielsen, T., Nielsen, P. H., Meyer, R. L., & Otzen, D. E. (2015). Functional bacterial amyloid increases Pseudomonas biofilm hydrophobicity and stiffness. *Frontiers in Microbiology*, *6*, 1099. https://doi.org/10.3389/fmicb.2015.01099

Zhalnina, K., Louie, K. B., Hao, Z., Mansoori, N., da Rocha, U. N., Shi, S., Cho, H., Karaoz, U., Loqué, D., Bowen, B. P., Firestone, M. K., Northen, T. R., & Brodie, E. L. (2018). Dynamic root exudate chemistry and microbial substrate preferences drive patterns in rhizosphere microbial community assembly. *Nature Microbiology*, *3*(4), 470–480. https://doi.org/10.1038/s41564-018-0129-3

Zhang, C., Huang, J., Zhang, J., Liu, S., Cui, M., An, B., Wang, X., Pu, J., Zhao, T., Fan, C., Lu, T. K., & Zhong, C. (2019). Engineered Bacillus subtilis biofilms as living glues. *Materials Today*. https://doi.org/https://doi.org/10.1016/j.mattod.2018.12.039

Zhang, H., Yu, K., Cayre, O. J., & Harbottle, D. (2016). Interfacial Particle Dynamics: One and Two Step Yielding in Colloidal Glass. *Langmuir*, *32*(50), 13472–13481. https://doi.org/10.1021/acs.langmuir.6b03586

Zhang, N., Wang, D., Liu, Y., Li, S., Shen, Q., & Zhang, R. (2014). Effects of different plant root exudates and their organic acid components on chemotaxis, biofilm formation and colonization by beneficial rhizosphere-associated bacterial strains. *Plant and Soil*, *374*(1), 689–700. https://doi.org/10.1007/s11104-013-1915-6

Zhang, R., & Schweizer, K. S. (2009). Theory of coupled translational-rotational glassy dynamics in dense fluids of uniaxial particles. *Physical Review E*, *80*(1), 11502. https://doi.org/10.1103/PhysRevE.80.011502

Zhang, W., Sileika, T., & Packman, A. I. (2013). Effects of fluid flow conditions on interactions between species in biofilms. *FEMS Microbiology Ecology*, *84*(2), 344–354. https://doi.org/10.1111/1574-6941.12066

Zhang, W., Sileika, T. S., Chen, C., Liu, Y., Lee, J., & Packman, A. I. (2011). A novel planar flow cell for studies of biofilm heterogeneity and flow-biofilm interactions. *Biotechnology and Bioengineering*, *108*(11), 2571–2582. https://doi.org/10.1002/bit.23234

Zhang, X., & Bishop, P. L. (2003). Biodegradability of biofilm extracellular polymeric substances. *Chemosphere*, *50*(1), 63–69. https://doi.org/http://dx.doi.org/10.1016/S0045-6535(02)00319-3

Zhao, X., Wang, Y., Shang, Q., Li, Y., Hao, H., Zhang, Y., Guo, Z., Yang, G., Xie, Z., & Wang, R. (2015). Collagen-like proteins (ClpA, ClpB, ClpC, and ClpD) are required for biofilm formation and adhesion to plant roots by Bacillus amyloliquefaciens FZB42. *PLoS ONE*, *10*(2), e0117414–e0117414. https://doi.org/10.1371/journal.pone.0117414

Zhi, Z., Di, J., Javoris, V. H., He, C., & Charles, C. H. (2015). From repulsive to attractive glass: A rheological investigation. *The Journal of Chemical Physics*, *143*(23), 234901. https://doi.org/10.1063/1.4937796

Zhou, Z., Hollingsworth, J. v, Hong, S., Cheng, H., & Han, C. C. (2014). Yielding Behavior in Colloidal Glasses: Comparison between “Hard Cage” and “Soft Cage.” *Langmuir*, *30*(20), 5739–5746. https://doi.org/10.1021/la500866d

Ziemba, C., Shabtai, Y., Piatkovsky, M., & Herzberg, M. (2016). Cellulose effects on morphology and elasticity of Vibrio fischeri biofilms. *Npj Biofilms And Microbiomes*, *2*(1), 1. https://doi.org/10.1038/s41522-016-0001-2

Zong, Y., Yuan, G., Zhao, C., & Han, C. C. (2013). Differentiating bonding and caging in a charged colloid system through rheological measurements. *J Chem Phys*, *138*(18), 184902. https://doi.org/10.1063/1.4803857

Zuidema, J. M., Rivet, C. J., Gilbert, R. J., & Morrison, F. A. (2014). A protocol for rheological characterization of hydrogels for tissue engineering strategies. *Journal of Biomedical Materials Research Part B: Applied Biomaterials*, *102*(5), 1063–1073. https://doi.org/10.1002/jbm.b.33088

Appendix

A) LAOS data pre-processing script

```
clear all
A = dir(''); %This is LAOS raw directory
B = dir(''); %This is Averaged data
saveroute = '' %This is your savepath

%% !!!Do not adjust below!!!
A(1:2,:) = []
B(1:2,:) = []
A = struct2cell(A)';
B = struct2cell(B)';
A = sortrows(A,3,'ascend');
B = sortrows(B,3,'ascend');
MaxStrain = []
cut_mat = []

for i = 1:length(A)
%% Import Files
    flname = strcat(B{i,2},'\',B{i,1});
    d = csv2struct(flname);
    flname = strcat(A{i,2},'\',A{i,1});
    c = csv2struct(flname);
    cut_mat = [d.Time__action__s_];
```

```
%% Determine Colunm numbers
    Ang = find(ismember(fieldnames(c),'Angular_displacement_rad_'));
    Tim = find(ismember(fieldnames(c),'Time__action__s_')); % For stain DOWN
change to Time__sequence__s_
    Torq = find(ismember(fieldnames(c),'Torque_N_m_'));

    A{i,5} = dlmread(flname,',',1,0);
%% Remove y shift
    Torque = A{i,5}(:,Torq)-A{i,5}(1,Torq);

    Q_F = []

%% Segment waves into individual strain events

bg = round(A{i,5}(:,Tim),4);
col = [1:size(A{i,5},2)];
e= 0.2;

    for ii = 1:length(cut_mat)-1
        cut_val = round(cut_mat(ii),4);
        if ii == length(cut_mat)
            Q_F{ii,1} = A{i,5}([find(bg ==cut_val):end],col) ;
        elseif ii == 1
            Q_F{ii,1} = A{i,5}([1:find(bg >=cut_val-e & bg <=cut_val+e)],col) ;
        else
            seq_begin = find(bg <=round(cut_val,4)+e & bg >=round(cut_val,4)-e);
            seq_end = find(bg <=round(cut_mat(ii+1),4)+e & bg>=
round(cut_mat(ii+1),4)-e);
            Q_F{ii,1} = A{i,5}([seq_begin(1):seq_end(1)],col) ;
        end

        Displacement = Q_F{ii,1}(:,Ang);
        Time = Q_F{ii,1}(:,Tim);
        Torque = Q_F{ii,1}(:,Torq);
```

```
%% BoxCar average
    Scale = size(Displacement,1);
    NoPoints = 4000 %6000 for 2Hz, 4000 for 1Hz, 2000 for 0.5Hz
    windowSize = 100; %For 0.5Hz 150 for 1Hz 100
    b = (1/windowSize)*ones(1,windowSize)
    a = 1
    TorqueF = filter(b,a,Torque)
    n = round(Scale/NoPoints) ;
    M = Scale - mod(Scale,n);
    Time_Cut = reshape(Time(1:M),n,[]);
    Time_Cut = transpose(sum(Time_Cut, 1) / n);
    Time_Cut = Time_Cut([50:end])
    Displacement_Cut = reshape(Displacement(1:M),n,[])
    Displacement_Cut = transpose(sum(Displacement_Cut, 1) / n);
    Displacement_Cut =Displacement_Cut([50:end])
    Torque_Cut = reshape(TorqueF(1:M),n,[])
    Torque_Cut = transpose(sum(Torque_Cut, 1) / n);
    Torque_Cut = Torque_Cut([50:end])

        if min(Torque_Cut) < 0
    Y_Shift_T = max(Torque_Cut) -((max(Torque_Cut) + abs(min(Torque_Cut)))/2)
    else
    Y_Shift_T = max(Torque_Cut) -((max(Torque_Cut) - abs(min(Torque_Cut)))/2)
    end

    if min( Displacement_Cut) < 0
    Y_Shift_S = max( Displacement_Cut) -((max( Displacement_Cut) + abs(min(
Displacement_Cut)))/2)
    else
    Y_Shift_S = max( Displacement_Cut) -((max( Displacement_Cut) - abs(min(
Displacement_Cut)))/2)
    end

    if Y_Shift_T > 0
       Torque_Cut = Torque_Cut - Y_Shift_T;
```

```
    else
        Torque_Cut = Torque_Cut - Y_Shift_T
    end

    if Y_Shift_S > 0
        Displacement_Cut = Displacement_Cut - Y_Shift_S;
    else
        Displacement_Cut = Displacement_Cut - Y_Shift_S
    end

    %Torque_Cut = Torque_Cut - Torque_Cut(40)
    %Displacement_Cut = Displacement_Cut + 3.5e-4
    [pks,loc]= findpeaks(Torque_Cut,'MinPeakDistance',50,'MinPeakHeight',0)
%% Filter out low frequencies - if present
%       if size(pks,1) == 0
%           Ts = mean(diff(Time_Cut));                          % Sampling Interval
%           Fs = 1/Ts;                                          % Sampling Frequency
%           Fn = Fs/2;                                          % Nyquist Frequency
%           L = size(Time_Cut,1);                               % Signal Length
%           FTwle = fft([Displacement_Cut Torque_Cut])/L;       % Fourier
Transform
%           Fv = linspace(0, 1, fix(L/2)+1)*Fn;                 % Frequency Vector
%           Iv = 1:numel(Fv);
%           Wp = 0.25/Fn;                                       % Stopband Frequency
(Normalised)
%           Ws = 0.20/Fn;                                       % Passband Frequency
(Normalised)
%           Rp =   1;                                           % Passband Ripple (dB)
%           Rs =  50;                                           % Stopband Ripple (dB)
%           [n,Ws] = cheb2ord(Wp,Ws,Rp,Rs);                     % Filter Order
%           [z,p,k] = cheby2(n,Rs,Ws,'high');                   % Filter Design, Sepcify
Bandstop
%           [sos,g] = zp2sos(z,p,k);
%           Dis_Tor_filtered = filtfilt(sos, g, [Displacement_Cut Torque_Cut]);
```

```
%           [pks,loc]=
findpeaks(Dis_Tor_filtered(:,1),'MinPeakDistance',100,'MinPeakHeight',0)
%           Displacement_Cut = Dis_Tor_filtered(:,1)
%           Torque_Cut = Dis_Tor_filtered(:,2)
%       end

%% Save Proprocessed Data to Savepath
      L_loc = length(loc)

      Begin = loc(L_loc-5)%-41
      Time_Cut = Time_Cut([Begin:loc(L_loc)])
      Strain_Cut = Displacement_Cut([Begin:loc(L_loc)]) * (0.01 /
d.Gap_mm_(1)*0.001);
      Stress_Cut = Torque_Cut([Begin:loc(L_loc)])*6.3662e+05

      Inputfile = [Time_Cut Strain_Cut Stress_Cut];
      file_name = A{i,1};
      file_number = ii
      name = strcat(saveroute,file_name,num2str(file_number),'.mat')
      savename = char(name)
      save(savename,'Inputfile')

   Eq = fit(Time_Cut,Strain_Cut, 'sin1');

   StrainRate_Cut = differentiate(Eq, Time_Cut);

   SPP_In = [Time_Cut Strain_Cut StrainRate_Cut Stress_Cut]

      %% Enter SPP save directory
   file_name = strcat(saveroute,file_name,num2str(file_number))
   fileID = fopen('SPP.txt','w')
   fprintf(fileID,'%6.8f %12.8f %12.8f %12.8f\n',SPP_In )
   save(horzcat(file_name,'SPP','.txt'),'SPP_In','-ascii','-tabs')
   end
   end
```

```
% %% Save Absolute strain for each Proprocessed Dataset
%         MaxStrain{i,1}(ii,1) = max(Displacement_Cut([loc(5):loc(L_loc-2)]))
%     end
```

B) ImageJ preprocessing macroscript

```
path ="";
output = "";
list=getFileList(path);


for(i=1;i<list.length;i++){
        open(path+list[i]);
        filename = list[i];
        filename_Res = list[i];
        run("Enhance Local Contrast (CLAHE)", "blocksize=127 histogram=256
maximum=3 mask=*None* fast_(less_accurate)");
        run("Gaussian Blur...", "sigma=2");
        run("Mexican Hat Filter", "radius=2");
        run("8-bit");
        setAutoThreshold("Otsu dark");
      getThreshold(lower,upper);
      setThreshold(lower,upper);
        run("Convert to Mask");
        setOption("BlackBackground", false);
        run("Dilate");
        saveAs("Tiff", output+filename_Res);
        close();
}
```

C) Matlab quantification – packing fraction from ImageJ processed images

```
A = dir()  %%Input file directory
A(1:2,:)=[]
A = struct2cell(A)
A = A'
for i = 1:length(A)
```

```
    flname = strcat(A{i,2},'\',A{i,1});
    I = imread(flname);
    phi(i,1) = sum(BW(:)==1)/(size(BW,1)^2)
    phi= mean(phi)
    phi= std(phi,0)
end
```

D) Comparison of Mexican hat and dilation processing parameters

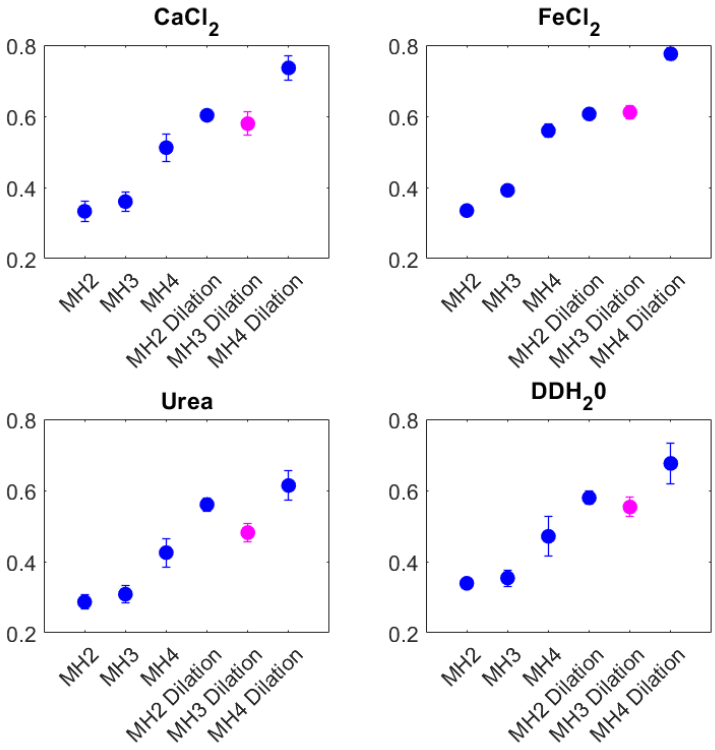

Figure D-1: Plotted is a comparison of image processing parameters used to calculate the packing fraction of P. fluorescens after chemical treatment with respective chemicals. Plotted are the three different radius of mexican hat filter (MH) ranging from radius of 2 to 4 pixels. The same filters where then applied with a dilation step to account for the cell membrane (dilaition). Pink values are the selected processing parameters. Plotted are the mean± standard deviation from n = 5 fields of view taken from z slices from CLSM images.

E) Representative image slices of Syto 63 and FX 1-43 channels

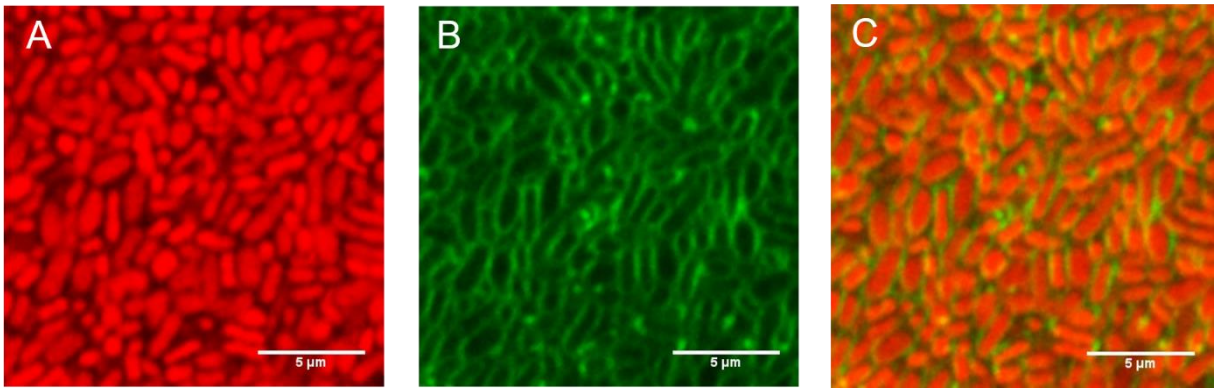

Figure E-1: CLSM depicting the double staining method. This is a representative image slice of *Pantoea* sp. UDP (A) Syto 63 which is a cell permeable DNA stain (B) FX 1-43 which is a cell membrane strain (C) The combined image of intercellular DNA and the cell membrane.

F) *Pantoea* sp. Lissajous Bowditch plots

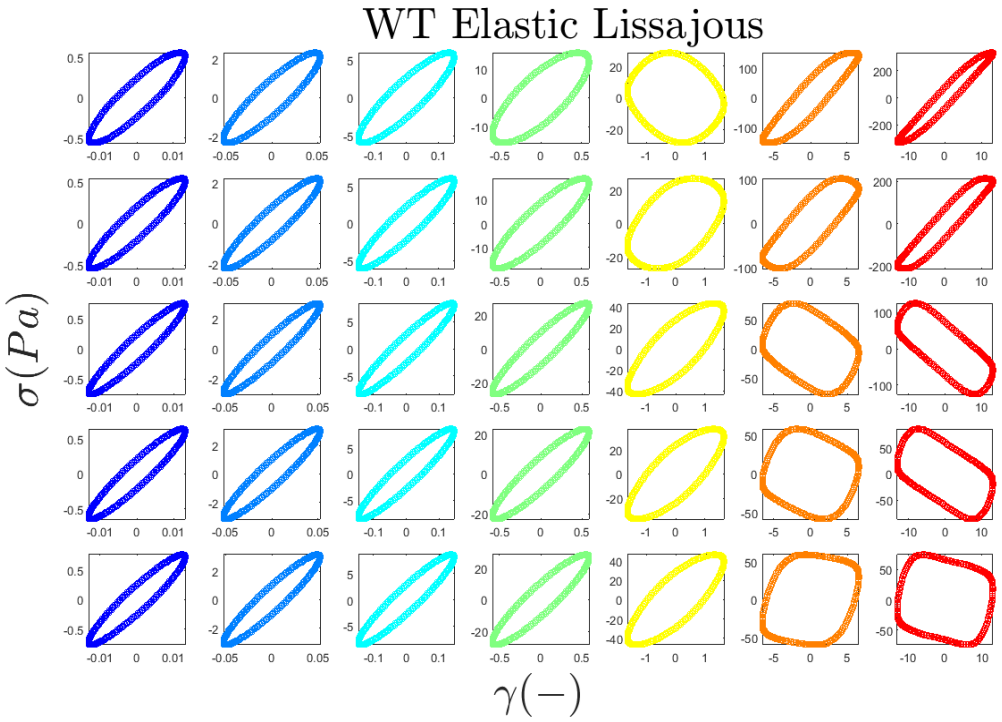

Figure F 1: Lissajous Bowditch Elastic curves of *Pantoea* WT. Columns are increasing left to right in strain, where as rows are increasing bottom to top in frequency.

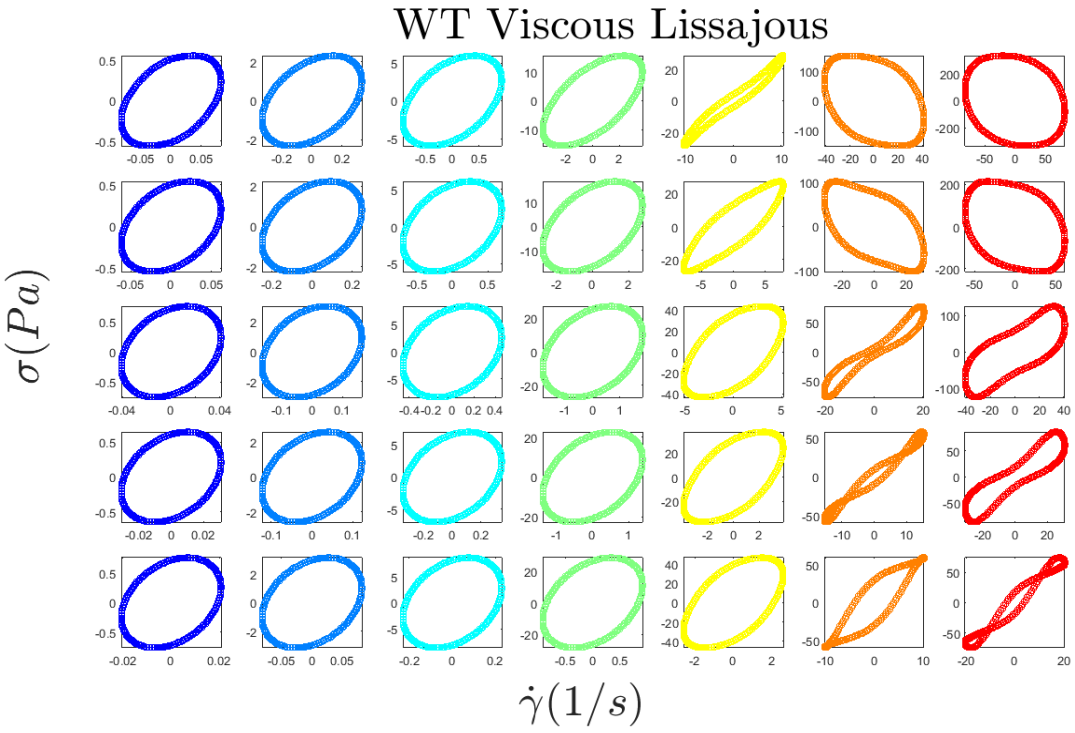

Figure F-2:Lissajous Bowditch Viscous curves of *Pantoea* WT. Columns are increasing left to right in strain, where as rows are increasing from bottom to top in frequency.

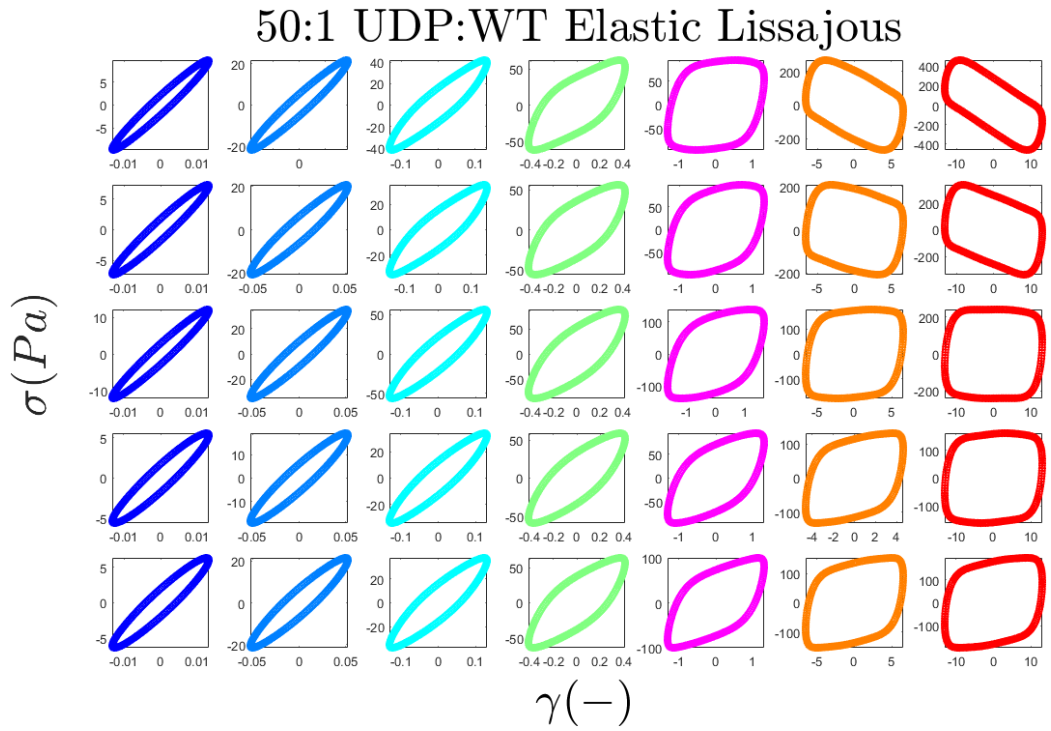

Figure F-3: Lissajous Bowditch Elastic curves of 50:1 UDP:WT. Columns are increasing left to right in strain, where as rows are increasing bottom to top in frequency.

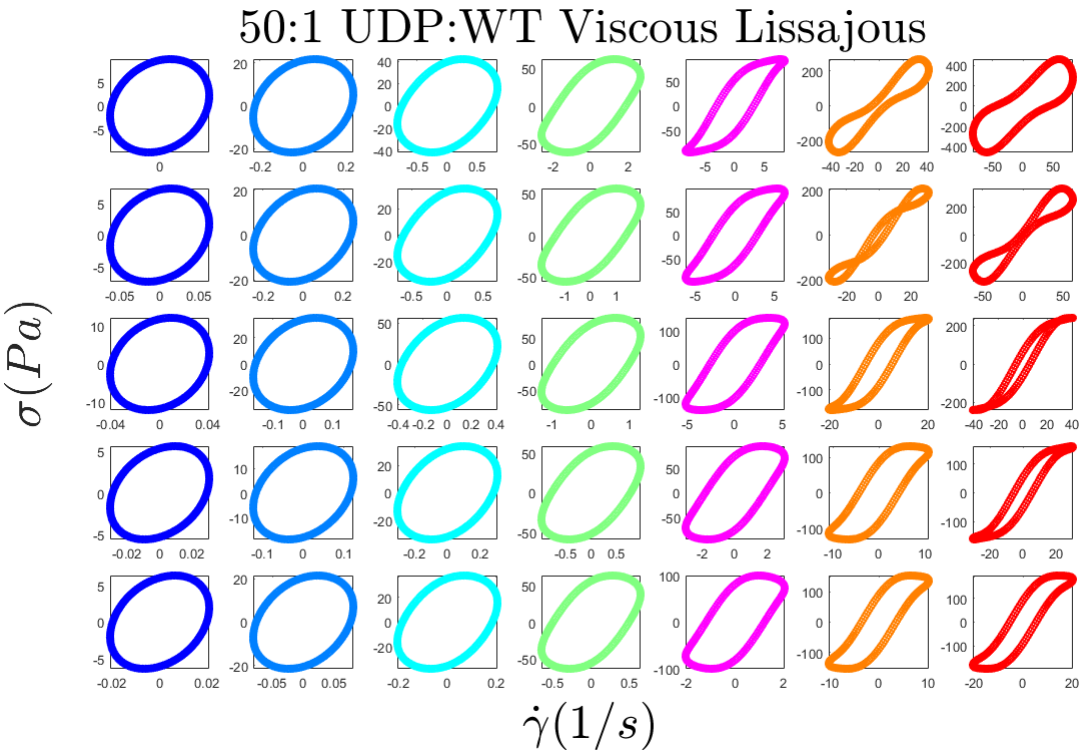

Figure F-4: Lissajous Bowditch Viscous curves of 50:1 UDP:WT. Columns are increasing left to right in strain, where as rows are increasing bottom to top in frequency.

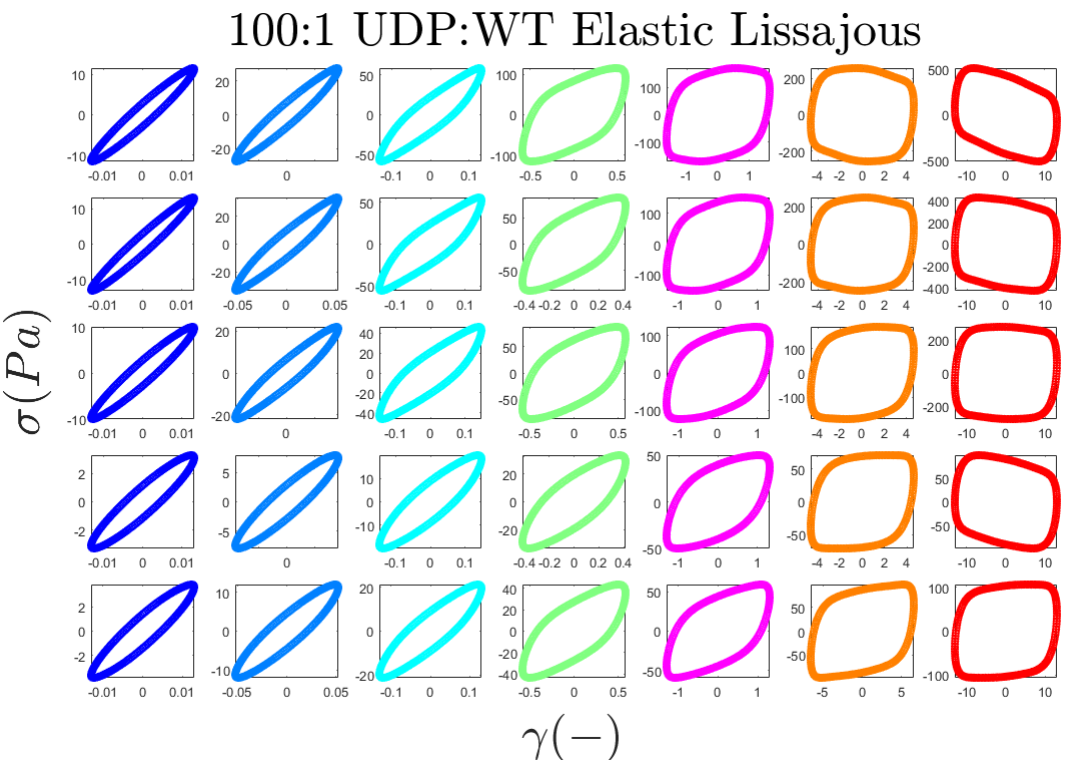

Figure F-5: Lissajous Bowditch Elastic curves of 100:1 UDP:WT. Columns are increasing left to right in strain, where as rows are increasing bottom to top in frequency.

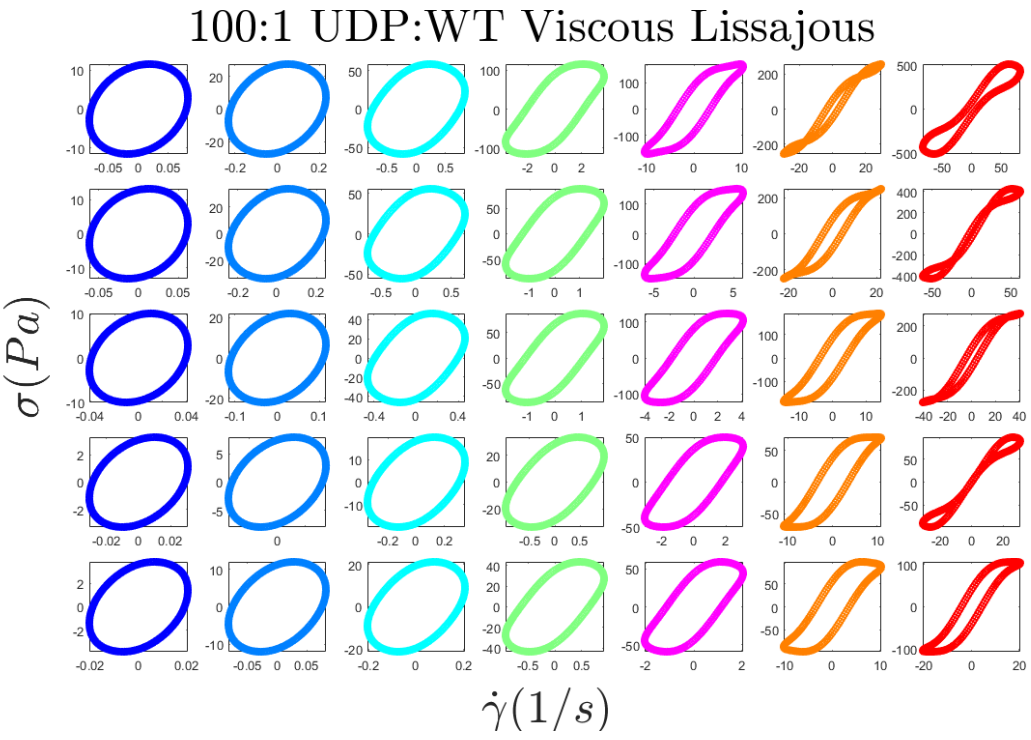

Figure F-6: Lissajous Bowditch Viscous curves of 100:1 UDP:WT. Columns are increasing left to right in strain, where as rows are increasing bottom to top in frequency.

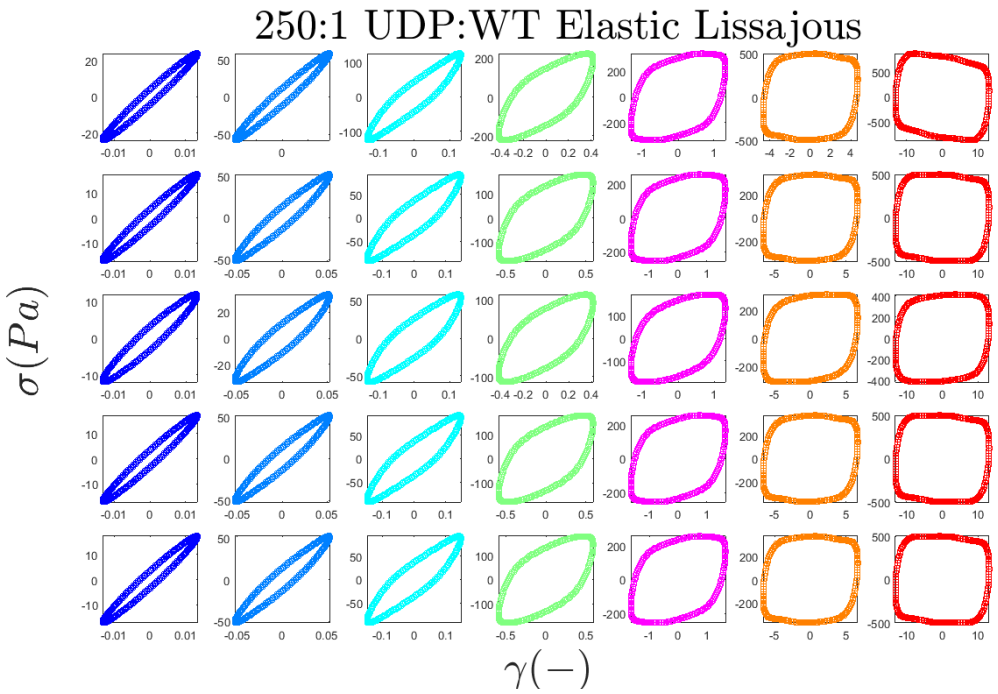

Figure F-7: Lissajous Bowditch Elastic curves of 250:1 UDP:WT. Columns are increasing left to right in strain, where as rows are increasing bottom to top in frequency.

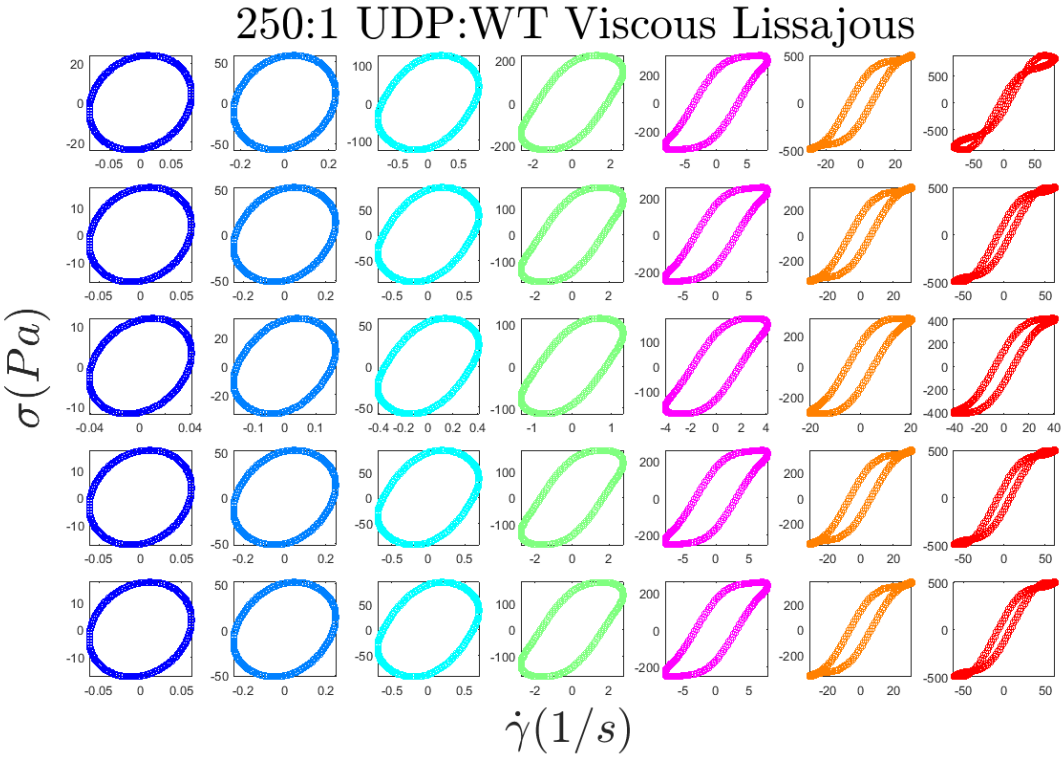

Figure F-8: Lissajous Bowditch Viscous curves of 250:1 UDP:WT. Columns are increasing left to right in strain, where as rows are increasing bottom to top in frequency.

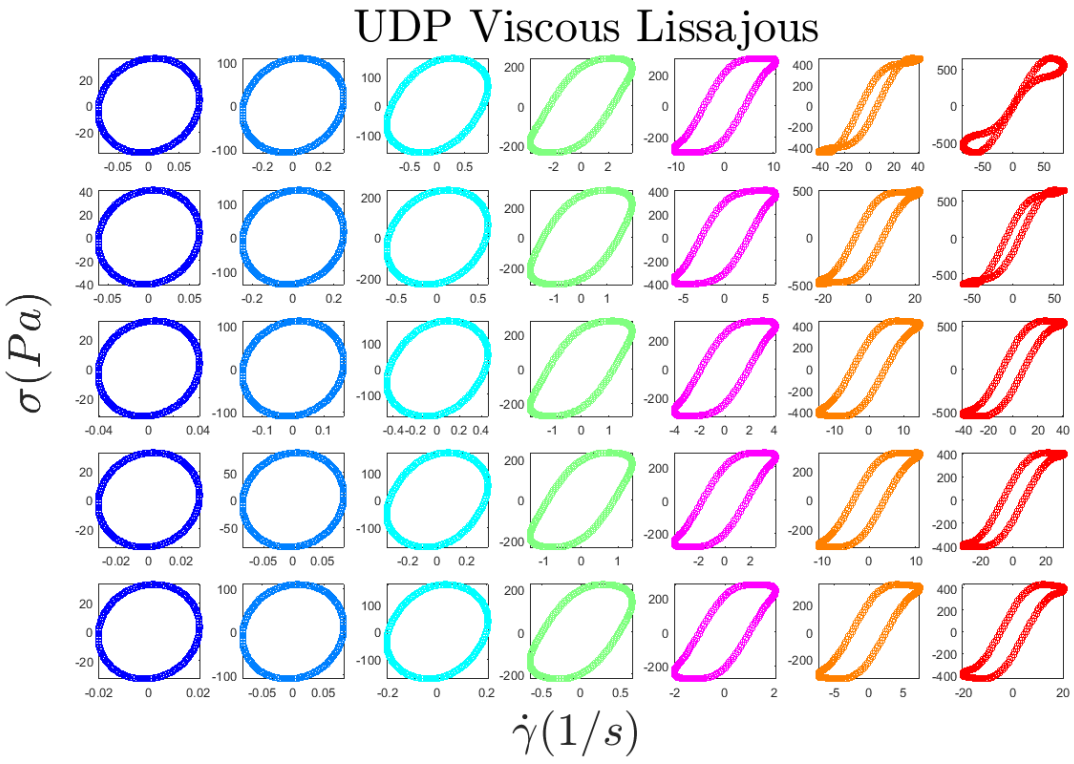

Figure F-9: Lissajous Bowditch Viscous curves of *Pantoea* UDP. Columns are increasing left to right in strain, where as rows are increasing bottom to top in frequency.

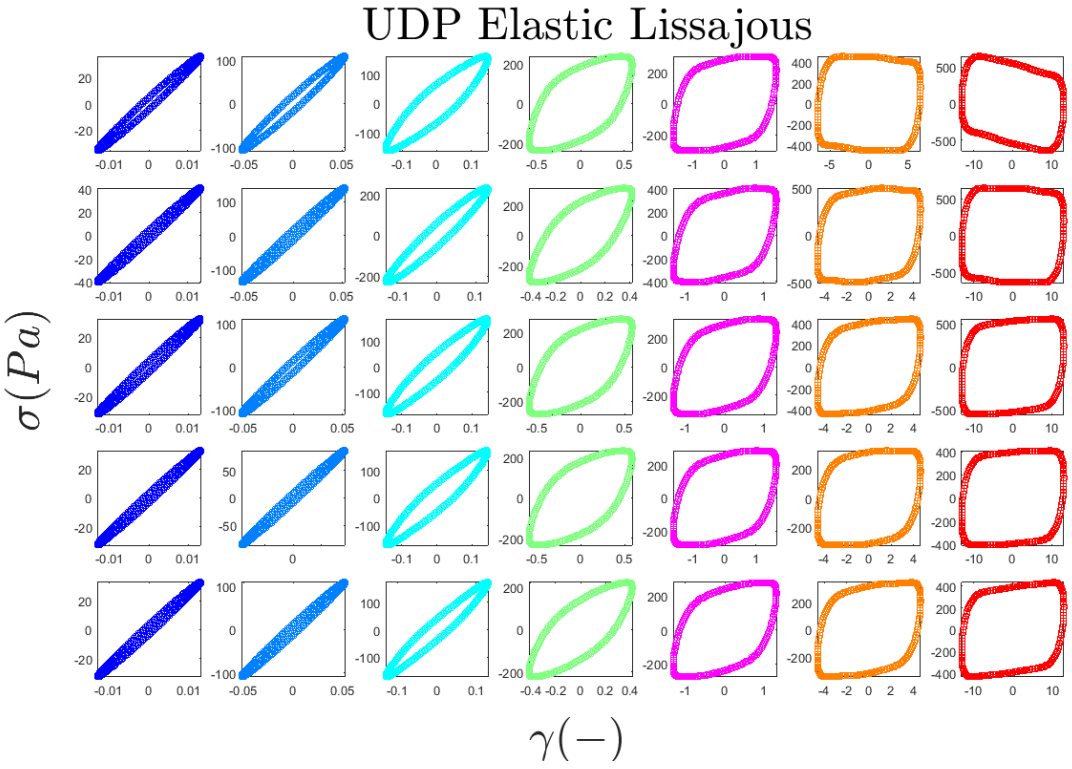

Figure F-10: Lissajous Bowditch Elastic curves of *Pantoea* UDP. Columns are increasing left to right in strain, where as rows are increasing bottom to top in frequency.

G) Lissajous Bowditch plots of *C. denitrificans*, *S. epidermidis*, *N. polysaccharea* and *P. fluorescens*

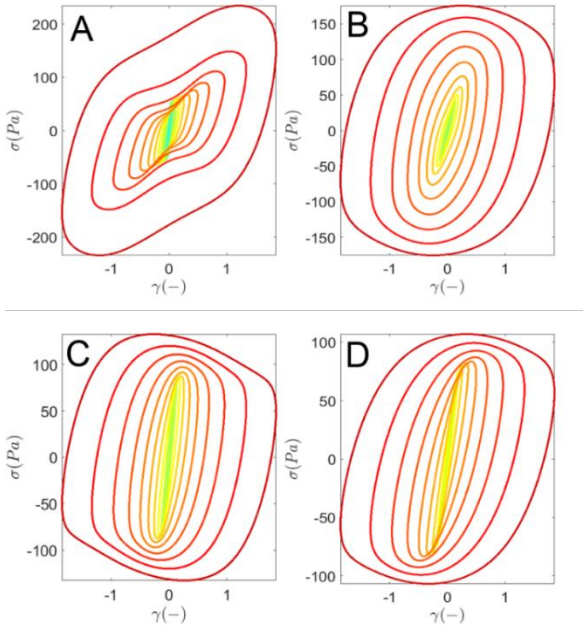

Figure G-1: Elastic Lissajous Bowditch plots acquired at a frequency of 0.5 Hz (A) *Comamonas denitrificans* (B) *Pseudomonas fluorescens*, (C) *Staphylococcus epidermidis* and (D) *Neisseria polysaccharea*. The strain value starts at 0.1 % (Green) to 1000 % (Red)

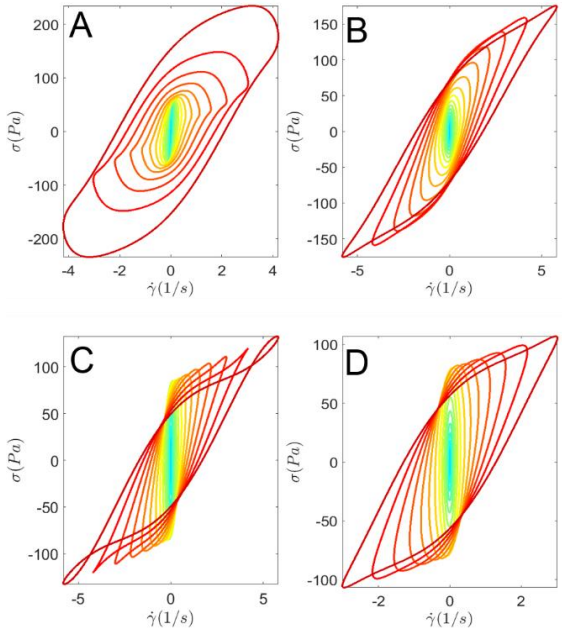

Figure G-2: Viscous Lissajous Bowditch plots acquired at a frequency of 0.5 Hz (A) *Comamonas denitrificans* (B) *Pseudomonas fluorescens*, (C) *Staphylococcus epidermidis* and (D) *Neisseria polysaccharea*. The strain value starts at 0.1 % (Green) to 1000 % (Red)